Probing the Properties of Confined Liquids

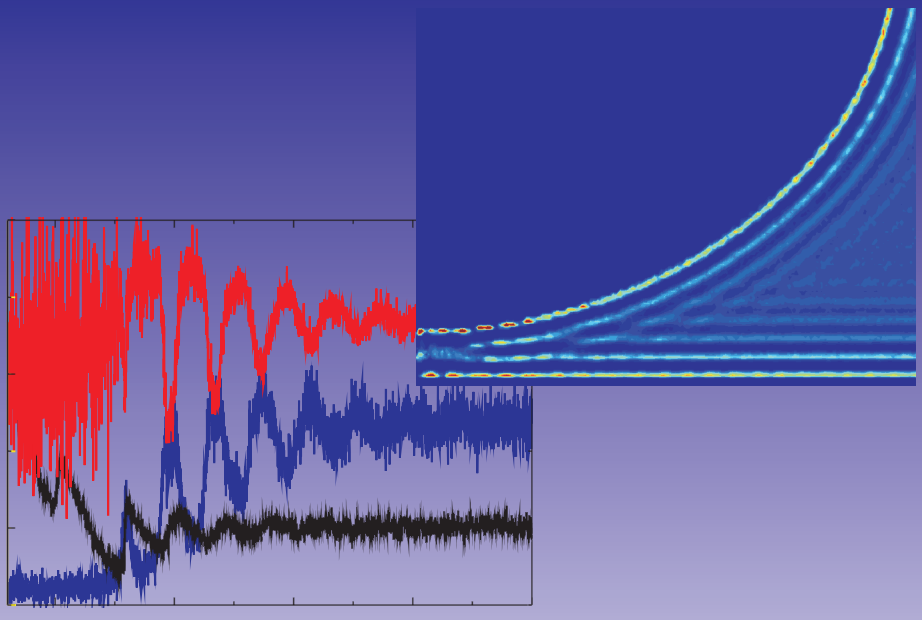

Sissi de Beer

Probing the Properties of Confined Liquids

Sissi de Beer

The research described in this thesis was performed at the Physics of Complex Fluids group within the Mesa+ Institute for Nanotechnology and Department of Science and Technology of the University of Twente. This work has been supported by the Foundation for Fundamental research on Matter (FOM), which is financially supported by the Netherlands Organization for Scientific Research (NWO).

Committee members:

Chairman:	
Prof. Dr. G. van der Steenhoven	University of Twente
Promotor:	
Prof. Dr. F. Mugele	University of Twente
Assistant Promotor:	
Dr. H.T.M. van den Ende	University of Twente
Referee:	
Dr. Ir. W.K. den Otter	University of Twente
Members:	
Prof. Dr. W.J. Briels	University of Twente
Prof. Dr. V. Subramaniam	University of Twente
Prof. Dr. G.J. Vancso	University of Twente
Prof. Dr. E. Charlaix	University Claude Bernard Lyon 1
Prof. Dr. J.W.M. Frenken	University of Leiden

Title: Probing the Properties of Confined Liquids
Author: Sissi de Beer
ISBN: 978-90-365-3198-6
DOI: 10.3990/1.9789036531986

Printed by Gildeprint Drukkerijen, Enschede

PROBING THE PROPERTIES OF CONFINED LIQUIDS

PROEFSCHRIFT

ter verkrijging van
de graad van doctor aan de Universiteit Twente,
op gezag van de rector magnificus,
prof. dr. H. Brinksma
volgens besluit van het College voor Promoties
in het openbaar te verdedigen
op vrijdag 27 mei om 16.45 uur

door

Sissi Jacoba Adrianus de Beer

geboren op 24 oktober 1979

te Bergen op Zoom

This dissertation has been approved by:

Promotor:	Prof. Dr. Frieder Mugele
Assistant Promotor:	Dr. Dirk van den Ende

Table of Contents

Chapter 0

A forerunner

From a personal experience we are all aware that liquids behave differently on large scales from liquids at small scales. For example, the water-surface of a filled bathtub is completely flat. Likewise, on a beautiful windless day, the surface of a lake or pond can be so flat, that it acts as a mirror (Fig. 0.1(a)). On the other hand, when we decide to take a shower instead of a bath, the water will appear to us in the round shape of droplets, just like rain-droplets or dew-droplets (Fig. 0.1(b)).

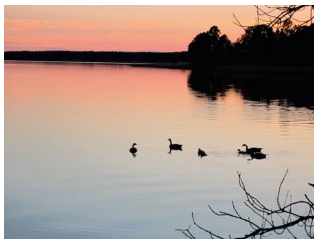

Figure 0.1(a) The flat surface of Lake Hjälmaren, Sweden (courtesy of Kees and Jacintha de Beer) (b) Spherical rain-droplets on the surface of the super-hydrophobic plant, Tropaeolum majus.

So, large amounts of liquid behave different from small amounts of liquids. The reason for this dissimilarity is that, at different length-scales, different forces act on the liquid. On the length-scale larger than a decimeter, volume-forces like gravity dominate. Therefore the liquid surface of a pound is completely flat. For small amounts of liquid, the surface-to-volume ratio increases and surface-forces dominate. So, below the length-scale of centimeters, water will minimize the surface (-energy) and the liquid adopts a spherical droplet-shape.
This thesis describes the study of liquids confined to an even smaller lengthscale: the nanometer (one billionth of a meter) range. On these very small scales again other forces become dominant. Those forces are called inter-molecular forces [1] and are the forces between the molecules of the liquid and or the solid surfaces. Consequently, the liquid behaves completely different from what we observe in Nature.

With the invention of new measurement devices, like the Surface Forces Apparatus (SFA) in 1969 [2] and the Atomic Force Miscroscope (AFM) in 1986 [3], it became possible to measure and to study the properties of liquids at these small length-scales. This resulted in the observation of many peculiar 'new' phenomena, like surface nanobubbles and liquid layering.

Surface nanobubbles
Figure 0.2 shows a typical image of surface nanobubbles. Surface nanobubbles are small gas-filled bubbles at the interface between water and a hydrophobic surface [4]. They have a typical diameter of 10-1000 nm and a height of 5-100nm.

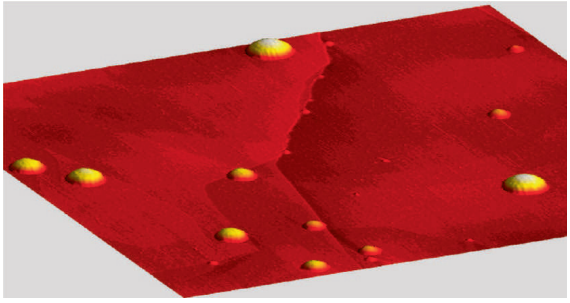

Figure 0.2 Small surface nanobubbles on a graphite surface in water. Image scale: $2000 \cdot 2000 \cdot 40\ nm^3$.

Over the last years these nanobubbles have gained a lot of interest for several reasons. First of all, they should not exist. Bubbles, as small as the surface nanobubbles, have a very high internal Laplace pressure and should therefore immediately dissolve in the water. Second, the surface nanobubbles have properties (e.g. contact angle and surface tension) that are different from the macroscopic liquid-vapor interface properties. At

the moment many research groups all over the world are trying to gain a better understanding of the occurrence of these small bubbles.
A small part of the research described in this thesis has been devoted to the study of surface nanobubbles (Chapter 11). However, the largest part of the thesis describes our study of another peculiar nanoscale phenomenon: liquid layering.

Liquid layering

On a length-scale which is even smaller than the surface nanobubbles (typically below 5 nm), we find another fascinating effect: Close to a solid surface the liquid molecules will assemble into a layered structure. This effect is quit comparable to e.g. marbles in a transparent bucket. At the flat bottom of the bucket the marbles can only position themselves directly above the bottom-surface and will therefore be organized in layers. While at the top of the bucket the marbles are not forced into a plane and the resulting structure looks more disorganized. The same happens for liquid molecules at a solid surface, as is shown in Fig. 0.2(a). The molecules can not penetrate into the solid surface, so they will form a layer directly next to the surface. In this layer the molecular density will be higher. Since molecules can not overlap, additional, although less pronounced, layers are formed adjacent to the first layer. Consequently, from the surface into the liquid, the molecular density oscillates. Only after a few molecular diameters, we find the bulk density of the liquid.

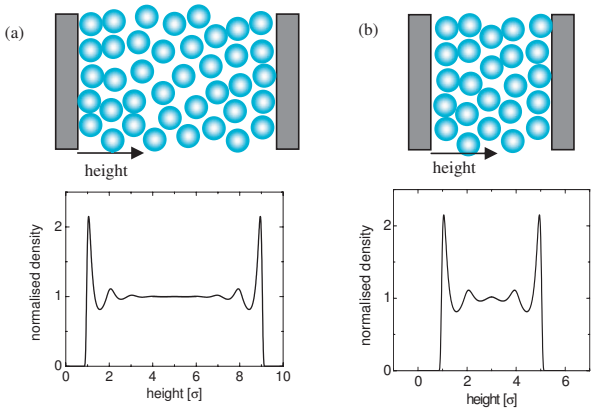

Figure 0.3(a) Close to a solid wall the molecular density varies over several molecular diameters σ. (b) Bringing two solid walls together results in an overlap of the density oscillations of the two walls and thus in a variation in the total density between the two walls.

Upon approach of two solid surfaces towards each other within a few nanometers, the density-oscillations due to both surfaces will overlap (Fig. 0.2(b)). This results in an increase or decrease of the total density between the two surfaces depending on the exact distance between the surfaces. In other words, when the distance between the surfaces is equal to e.g. three molecular diameters σ, the density will be different from

that when the distance is two and a half molecular diameters. Since, understandably, half a molecule does not exist. For a more detailed description of the molecular configuration as a function of distance we refer to Chapter 8 of this thesis.

We can measure liquid layering, because changes in the density will result in changes in the pressure or force on the confining surfaces. The density and thus the force both increase and decrease – or oscillate – as a function of distance between the surfaces. Therefore these forces are called the oscillatory solvation forces. The oscillatory solvation forces were measured for the first time in the 1980's [5] and the existence of liquid layering and the static properties of the layered liquid are by now well-established.

The major goal of this thesis is to understand how liquid layering affects the transport properties of the liquid. In other words: What happens when we move the two solid surfaces, with a layered liquid in-between, with respect to each other? Will the viscosity of the liquid change due to the density variations? Or will the liquid solidify due to the confinement?

These questions have been addressed by other research groups as well. In Chapter 2 we give a literature overview of the current standing in the study of liquids confined between solid surfaces. In the remainder of this thesis we describe our own results of the experiments and simulations performed on confined liquids.
First of all, to obtain trustworthy experimental data, we need to characterize and understand our measurement system. In Chapter 3 and 4 we describe our experimental system and explain our basic modeling steps necessary to extract physical properties from our measurement data. In Chapter 5 and 6 we present our experimental results, which show that the transport properties of a layered liquid indeed change.
Since a confined liquid behaves different from a bulk liquid we can not use continuum theory to understand our experimental results. Therefore we performed Molecular Dynamics (MD) simulations (for an explanation see Chapter 7) of which the results are presented in Chapter 8.
Chapter 9-11 describe other phenomena and research questions that we have been addressed during the course of the thesis. Chapter 9 describes the effect of temperature on liquid layering. Chapter 10 describes the occurrence of nano-droplets when two elastic surfaces with a thin water film are rapidly brought together and eventually in Chapter 11 we present our study on surface nanobubbles.

References:

[1] J. N. Israelachvili, *Intermolecular and Surface Forces* (Academic, London, 1991)
[2] D. Tabor and R.H.S Winterton, *Proc. R. Soc. Lond. A* **312**, 435-450 (1969)
[3] G. Binnig, F.C. Quate and Ch. Gerber, *Phys. Rev. Lett.* **9**, 930 (1986)
[4] J. W. G. Tyrrell, P. Attard, *Phys. Rev. Lett.* **87**, 176104 (2001)
[5] R.G. Horn and J.N. Israelachvili, *Chem. Phys. Lett.* **71**, 192 (1980)

Chapter 1

Introduction

The study of confined liquids is of fundamental importance in many research and engineering areas. For example in the area of biophysics: The exchange of water and nutrients in cells takes place via nano-pores in the cell-membrane [1]. Moreover the joints in e.g. a knee or a shoulder are lubricated with thin liquid films [2]. In chemistry, the study of confined liquids helps in understanding colloid stability and the flow through chromatographic packing. Furthermore, in the research area of geophysics and oil recovery it is important to understand how liquids flow through the small pores in rocks. Additionally, in industry a thorough understanding of thin lubrication films helps reduce friction and wear in production-machines and will therefore help reduce production-costs [3-5]. Moreover, the study of confined liquids also helps the development of new miniature pieces of equipment like the lab-on-a-chip (LOC) [6]. This is a small, chip-sized, device on which laboratory-tests (like blood- or saliva-tests) can be performed. In these LOCs pico-liter volumes of liquid are manipulated and transported via small channels to perform the necessary tests.

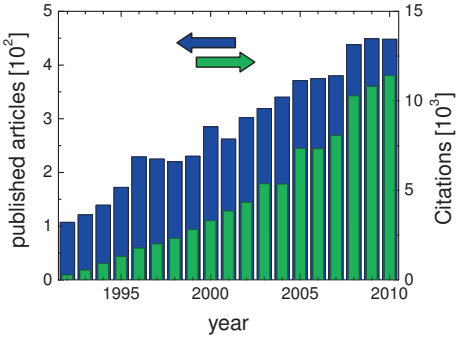

Figure 1.1 The number of articles (blue) published on confined liquids between 1992 and 2010 and the citations to those publications (green).

With the development of high resolution force measurement devices like the Surface Forces Apparatus (SFA) and the Atomic Force Microscope (AFM), the quantitative study of confined liquids became directly feasible. This resulted in a rapidly growing number of publications and citations on the subject of confined liquids. Figure 1.1 shows the number of published articles with the keywords 'confined liquid' and the number of times those publications have been cited between 1992 and 2010 [7].

Since the invention of the SFA and AFM also 'new' fluidic phenomena have been discovered, like:

1) The organization of the liquid molecules into layers close to a solid surface [8-17].
2) Confinement induced freezing and melting [17, 18]
3) Surface nanobubbles at the interface between water and a hydrophobic surface [19].

Moreover, liquid slip over surfaces, an effect long-predicted by many scientists like Bernouilli, Coulomb and Navier, (see e.g. Ref. 5 and references therein), was quantitatively measured for the first time [20, 21].
These phenomena strongly affect the behavior of confined liquids.

In this thesis we mainly focus on liquid layering, which is the organization of liquid molecules confined between two solid surfaces.
The occurrence of liquid layering can intuitively be understood as follows:
In a liquid with density ρ_∞, the relative positions of the molecules with respect to neighboring molecules are correlated. This results in a modulation of the radial density distribution function extending over several molecular lengths σ ($\rho(r) = \rho_\infty g(r)$, with $g(r)$ the pair distribution function, see also Fig. 1.2(a)). In other words, starting from the middle of one molecule, the next molecules are most likely to be found at distances $n \cdot \sigma$ (with n = 1, 2, 3, …). However, since the molecules all randomly move around, for

larger distances, the correlation decreases. In high density liquids the effect dies out for distances larger than 4-5σ.
A similar effect can be observed for liquid molecules close to a solid wall. The wall takes away one degree of freedom for the motion of the liquid molecules. Starting from the wall, the molecules are most likely to be found at distances $h = n \cdot \sigma$ (see also Fig. 1.2(b)), while the correlation strongly decreases after a few layers.

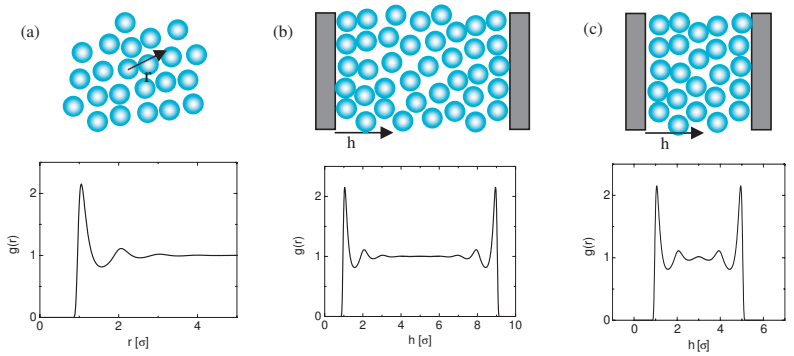

Figure 1.2(a) In a liquid, the position of molecules is strongly correlated resulting in a modulation in the pair distribution function extending over several molecular diameters σ.
(b) Close to a flat solid wall the position of molecules is correlated to the position of the wall.
(c) Bringing two solid walls together results in an overlap over the density distributions of the two walls.

When we bring two solid walls together, the density distributions of both walls overlap (Fig. 1.2(c)). Upon approach this results in an alternating increase and decrease of the total density between the walls. This modulation in the total density between the walls causes the pressure on the walls to oscillate as a function of distance (Fig. 1.3). These pressure oscillations can be measured as the oscillatory solvation forces.
The organization of liquid molecules at solid surfaces is strongly affected by liquid-wall interactions. For a strong attractive force between the liquid molecules and the wall, the correlation will be stronger. This results in larger density-oscillations extending over a larger distance. Automatically, this will give rise to higher oscillatory solvation forces.

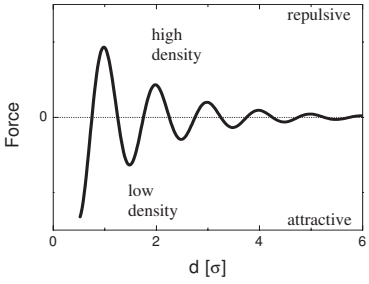

Figure 1.3 Upon approach of two flat surfaces towards each other, the density will oscillate as a function of distance, giving rise to the oscillatory solvation forces.

Both from a fundamental and from an applied perspective the question how the assembly of molecules affects the hydrodynamics and the transport-properties of the confined liquids is particularly interesting and relevant. Although the density variations as a function of distance between the confining surfaces are well-established, the consequences for the dynamics of the system are currently largely unclear.

In SFA measurements confinement induced solidification was reported by Klein et al. [17] for the simple model-liquid octamethycyclotetrasiloxane (OMCTS) for a distance larger than 6 molecular diameters. While other research groups did not find such an effect and observed that the same liquid behaves liquid-like down to the squeeze-out of the last two molecular layers [15, 16]. Moreover, jamming and a glass-transition have been observed by Granick et al. at high approach speeds of the confining surfaces [13].
In AFM measurements also different effects have been reported for simple model liquids: Recently, the damping on the cantilever was found to oscillate as a function of tip-surface distance [9]. On the other hand, earlier measurements had shown a monotonic increase in the damping [22]. Also, a jamming effect at high approach speeds has been observed [10], while others found sharp peaks in the damping [12] or visco-elastic behavior [11].

In this thesis we show that the transport-properties of the confined liquid indeed change depending on the distance between the confining surfaces. Experimentally we find that the damping on the cantilever varies with the distance between the tip and the surface. Moreover, we show via Molecular Dynamics simulations that the variations in the damping are strongly related to the structure and diffusivity of the molecules. The molecules can behave liquid-like or solid-like depending on the distance between the solid walls.

Chapter 2 of this thesis gives an overview of the current state of the research on confined liquids. We discuss the different results measured with different techniques (both SFA and AFM) at different research groups. In our research we often used dynamic AFM Spectroscopy. This technique can be applied in different modes and consequently different methods are needed to extract the forces from the measurement data. We present an overview of the different modes and force-inversion methods in Chapter 3. The most widely used technique in dynamic AFM spectroscopy is to acoustically drive the cantilever and use deflection detection to measure the motion of the cantilever. This technique gives rise to a surprising sensitivity in the phase for tip sample interactions at low frequencies, which is presented in Chapter 4. In Chapter 5 and 6 we present and discuss our measurements performed on the oscillatory solvation forces in confined OMCTS with different techniques, namely:
1) Acoustic drive (Chapter 5)
2) Magnetic drive (Chapter 6)

We show that the conservative forces strongly oscillate as a function tip-surface distance, while the dissipative forces show distinct peaks.
Since we probe the properties of very small amounts of liquid, continuum theories do not apply. Therefore we used Molecular Dynamics (MD) simulations to understand our measurement results. Chapter 7 gives an overview of the techniques used for the simulation, while we presents in Chapter 8 our simulation results on the conservative and dissipative forces. We show that, in agreement with our experimental results, the conservative forces oscillate as function distance. Moreover, we observe peaks in the damping that are very similar to the peaks found in our measurements. Furthermore, we show that the damping correlates with the structure and the dynamics of the confined liquid molecules.
In the remainder of this thesis we describe other research questions that we have addressed during the development of this thesis.
In Chapter 9 we present static squeeze-out force measurements of the effect of temperature and epitaxy on the oscillatory solvation forces. The above described measurements and simulations were performed with model-liquids. In the last two chapters we turn our attention to water. In Chapter 10 we present SFA measurements of confined water and we show that it behaves completely different from the model-liquids described above. In Chapter 11 we present AFM measurements in water on a hydrophobic surface, which results in the presence of surface nanobubbles. Finally, we summarize and conclude our results in Chapter 12.

References:

[1] L. Bocquet and E. Charlaix, *Chem. Soc. Rev.* **39**, 1073 (2010)
[2] W.H. Briscoe, S. Titmuss, F. Tiberg, R.K. Thomas, D.J. McGillivray & J. Klein, *Nature* **444**, 191 (2006)
[3] B.N.J. Persson and F. Mugele, *J. Phys. Condens. Matter* **16**, R295 (2004)
[4] B.N.J. Persson, *Sliding Friction*, Springer-Verlag Berlin Heidelberg, 2nd edition (2000)
[5] B. Bhushan, Nanotribology and Nanomechanics, Springer-Verlag Berlin Heidelberg, 2nd edition (2008)
[6] J.C.T. Eijkel and A. van den Berg, *Microfluid Nanofluid* **1**, 249 (2005)
[7] Database Web of Science, 06-03-2011
[8] J. N. Israelachvili, *Intermolecular and Surface Forces* (Academic, London, 1991)
[9] A. Maali, T. Cohen-Bouhacina, G. Couturier and J-P Aimé, *Phys. Rev. Lett.* **96**, 086105 (2006)
[10] S.H. Khan, G. Matei, S. Patil and P.M. Hoffmann, *Phys. Rev. Lett.* **105**, 106101 (2010)
[11] T.-D. Li and E. Riedo, *Phys. Rev. Lett.* **100**, 106102 (2008)
[12] W. Hofbauer, R.J. Ho, R. Hairulnizam, N.N. Gosvami and S.J. O'Shea *Phys. Rev.* B **80**, 134104 (2009)
[13] Y. Zhu and S. Granick, *Langmuir* **19**, 8148 (2003)
[14] J.N. Israelachvili, P.M. McGuiggan, and A.M. Homola, *Science* **240**, 189 (1988)
[15] T. Becker and F. Mugele, *Phys. Rev. Lett.* **91**, 166104 (2003)
[16] L. Bureau, *Phys. Rev. Lett.* **104**, 218302 (2010)
[17] J. Klein and E. Kumacheva, *Science* **269**, 816 (1995)
[18] H.K. Christenson, *J. Phys. Condens. Matter* **13**, R95 (2001)

[19] J.W.G. Tyrrell, P. Attard, *Phys. Rev. Lett.* **87**, 176104 (2001)
[20] C. Cottin-Bizonne, B. Cross, A. Steinberger and E. Charlaix, *Phys. Rev. Lett.* **94**, 056102 (2005)
[21] O.I. Vinogradova, *Langmuir* **11**, 2213 (1995)
[22] S. J. O'Shea and M. E. Welland, *Langmuir* **14**, 4186 (1998)

Chapter 2

Confined Liquids, the story so far…

Shortly after the invention of the Surface Forces Apparatus (SFA), by Tabor and Winterton [1], confined liquids were studied in the SFA and oscillatory solvation forces in a simple liquid were measured for the first time by Horn and Israelachvili in 1980 [2, 3] (see also Fig. 2.1(a)).
This observation started a whole new research area and gave rise to new fundamental questions, like:

- Why do liquid molecules assemble in layers close to a flat solid surface?
- Do all confined liquids show this phenomenon?
- Are the oscillatory solvation forces affected by solid-liquid interactions and epitaxial effects?
- Are the liquid-molecules in the layers solid- or liquid-like?
- Do we get confinement-induced phase-transitions or glass-transitions?
- How are the oscillatory solvation forces affected by temperature?

Three decades later, the confined liquids community has come a lot closer to answering these fundamental questions. In the following we give a brief overview of the current status of the research in confined liquids, focusing on the oscillatory solvation forces.

What happens when we squeeze-out a model-liquid? Figure 2.1(b) shows SFA measurements of the approach of two mica sheets in octamethylcyclotetrasiloxane (OMCTS) [4]. When the mica sheets are still far (>10 nm) apart, the only force acting on the approaching sheets is the hydrodynamic squeeze-out force or Reynolds-force $F_R = (6\pi\eta R / D)(dD / dt)$ (with η the viscosity, R the radius of curvature of the sheets and D the distance between the sheets). However, as the last few nanometers of liquid are squeezed-out, the distance between the sheets no longer decreases continuously, but via discrete jumps. These discrete jumps represent the layer by layer expulsion of the self-organized liquid-molecules between the two solid surfaces.

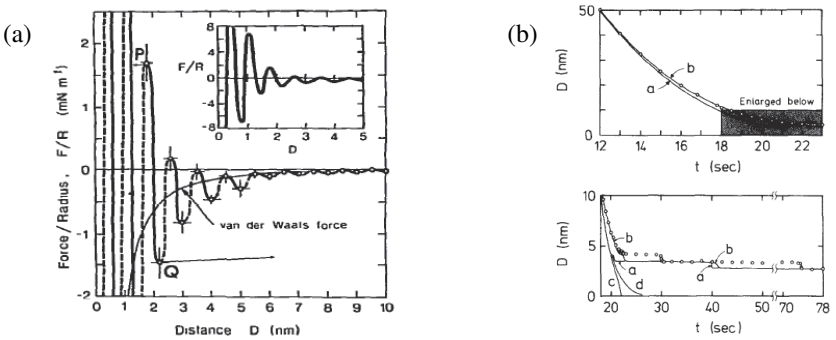

Figure 2.1(a) The first measurement of the oscillatory solvation forces in a simple liquid (OMCTS) (taken from [2]). (b) The squeeze-out of a confined liquid. Far away the dynamic behavior can be explained by the Reynolds drainage force, but at small distances the liquid ruptures in discrete jumps (taken from [4]).

For the last liquid-layers the mica surfaces are locally flattened due to the applied force and the repulsive part of the oscillatory forces. This creates a contact area with a constant thickness and thus a parallel-plate geometry. In this contact area the thickness between the two solid surfaces is approximately $n \cdot \sigma$ (with σ the molecular diameter and n = 1, 2, 3, …).

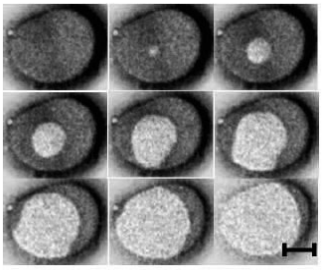

Figure 2.2 The expulsion of a liquid layer confined between two atomically flat mica surfaces. The dark area represents the liquid with a height of $n \cdot \sigma$ and the bright area a height of $(n-1) \cdot \sigma$ (taken from [6], Δt between frames 0.3s, scalebar 25 m).

When the applied force becomes sufficiently high, a hole of thickness $(n-1)\cdot\sigma$ is nucleated, followed by the expulsion of a liquid layer [5]. Figure 2.2 shows the squeeze-out of a liquid layer [6] as imaged by a 2D imaging SFA [7].
Although the assembly of the liquid molecules clearly gives rise to changes in the static properties of the system, it was shown, by studying the expulsion process of the liquid layers, that the dynamics could still be described by continuum theory and bulk viscosity of the liquid down to the squeeze-out of the last two layers [6, 8].
The dynamic properties of a confined liquid have also been studied by moving the two atomically flat mica surfaces relative to each other in parallel (shear-motion).

Via this method, several different phenomena were found:
1) Observation Stick-slip motion [9-11],
2) Measurements interpreted as confinement induced liquid to solid phase transitions [12, 13],
3) Measurements interpreted as approach speed dependent jamming and thus a glass transition [14].

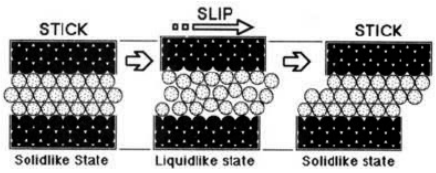

Figure 2.3 Schematic representation of stick-slip motion when two solid surfaces, with a layered liquid in between, are sheared with respect to each other (image taken from [11])

Figure 2.3 shows the schematics of stick-slip in a confined liquid [11]. When the two solid surfaces are sheared with respect to each other, a finite shear stress is needed to bring the top surface is motion. At this shear stress the liquid will slip. However, once the force on the liquid has decreased again, the system will stick again. Consequently, stick-slip motion is observed. Stick-slip motion implies solidification of the liquid, which is shear-melted when the applied force is high enough. This behavior was typically found for the last 2-3 molecular layers confined between the mica surfaces. At larger distances, pure viscous behavior was observed.
On the other hand, in a different laboratory [12, 13], confinement-induced liquid-to-solid phase-transitions were found for confined OMCTS for a surface-to-surface thickness over six molecular layers. In this study the OMCTS was rigorously cleaned using double distillation and dried with molecular sieves. Figure 2.4 shows the measurements, which are considered to be a phase-transition. When one of the solid surfaces is approached towards the other in OMCTS, the characteristic average oscillatory solvation forces are measured. Moreover, upon monitoring the noise of the force-sensor it was found that the noise dramatically drops as the system goes from seven to six layers (Fig. 2.4(b)). Via shear measurements of the system described in

Fig. 2.4 it was shown that the viscosity of the confined liquid increases with more than seven orders of magnitude.

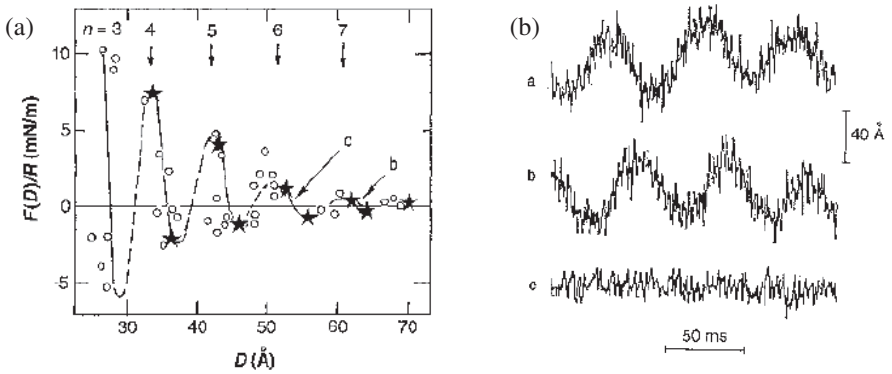

Figure 2.4 Liquid to solid phase transition due to confinement in OMCTS. (a) The normal force upon approach and retract of the two solid surfaces. (b) The noise on the lateral force-sensor, displaying an abrupt transition at $D = 6\sigma$ (curve c, also denoted by the arrow in (a)). Just above $D = 6\sigma$ the response in the noise (curve b) is the same as in the bulk liquid (curve a). (taken from [13])

In later experiments in the same laboratory also stick-slip motion was studied in which the dynamics of slip motion was analyzed in detail [14]. With use of a model based on a harmonic oscillator and simple shear flow, it was found that the viscosity increases by four orders of magnitude. Nevertheless, recently a new model was proposed to describe slip dynamics [15]. This model is based on the earthquake model extended by Bo Persson and assumes that slip occurs via melting of different domains instead of one massive melt. With use of this model the results of Ref. [14] can be described using the bulk viscosity of OMCTS.
Also, in a different lab, shear measurements were performed on the same system (OMCTS between mica), which resulted in a bulk-like response [17] unless the approach speed was high enough to cause jamming. A similar approach speed effect has been observed in recent Atomic Force Microscopy measurements for both water and OMCTS [18, 19]. Dynamic AFM measurements do not suffer from the notorious snap-in instability and therefore the liquid properties can be studied for arbitrary tip-surface distance. In the experiments of Ref. [18, 19] a variation was observed in the amplitude and phase response of the cantilever as the approach speed was varied. At low approach speeds the extracted elastic and the viscous response oscillate in phase as a function of the tip-surface distance. However, at large approach speeds the stiffness and damping were observed to be out-of-phase. Moreover the relaxation-time was found to increase with decreasing stiffness. The latter results were interpreted as an elastic / solid response for an integer number of layers between the tip and the

surface and a viscous response (with dramatically increased viscosity) at distances where an integer number of molecules does not fit between the tip and the surface.

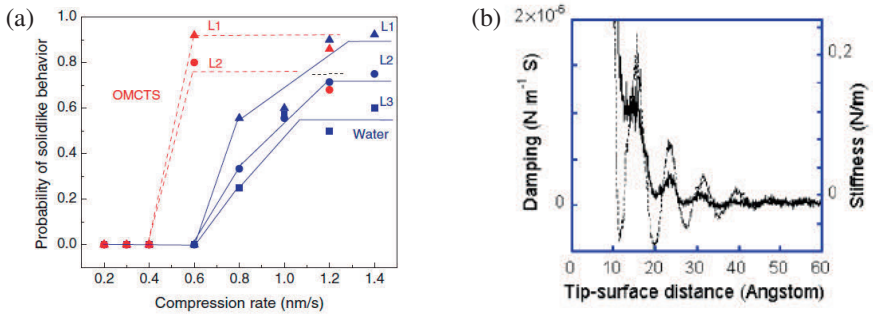

Figure 2.5(a) Depending on the compression rate a confined liquid can respond solid-like or liquid-like (taken from [19]) (b) Oscillations in the stiffness and the damping on an AFM cantilever upon decreasing the distance between the tip and the surface (taken from [20]).

In another research lab, similar oscillations in the stiffness and the damping were observed [20]. However, they interpreted these results, by approximating the damping with a Reynolds squeeze-out force, as an increase in the effective viscosity by four orders of magnitude for the last liquid layer.

Nevertheless, the measurements described in Ref. [18-20] are performed using an acoustic driving scheme (see Chapter 3). This technique is frequently disputed for its sensitivity to modeling errors [21, 22] and the difficulty of obtaining a trustworthy spectral response of the cantilever without spurious resonances [23]. In fact, wrongful modeling can result in artificial oscillations in the viscous response (or damping) [21, 24].

The authors of Ref. [22] claimed to have performed artifact-free measurements using a magnetic driving scheme in which they observed a monotonic increase in the damping without oscillations. Nonetheless, in other recent magnetic drive AFM measurements, in a different laboratory, peaks in the damping were observed at tip-surface distances of non-integer molecular diameters [25] with a slightly different model system (1-dodecanol).

In shear AFM measurements [26] a strain rate dependence of the elastic and viscous response was found for water and OMCTS. From these results the authors of Ref. [26] concluded that the confined liquid behaves like a gel or metastable complex fluid.

All the observations and interpretations described above seem to contradict each other. However, different measurement techniques and methods were used in the different research labs. It was recently shown in simultaneous squeeze-out and shear measurement that the extracted shear viscosity can deviate from the viscosity derived from squeeze-out experiments [27].

The experiments described above were mainly performed in OMCTS (simple, spherical model liquid). However, more complex liquids can result in an even more complex response to confinement:
For example for alkanes it was found that the oscillatory forces in SFA experiments are strongly affected by the approach speed [28]. For high approach speeds the carbon-chains can be quenched in a metastable state which relaxes back to equilibrium; a layered configuration. Nevertheless, a consistent viscous dissipation was extracted from the Reynolds drainage force independent of the approach speed, which shows an increase compared to the bulk response below 10nm up to many orders of magnitude for small distances. Moreover, alkanes show an interesting shear response. A maximum in the viscous dissipation is measured at a characteristic shear velocity depending on the molecular length [29]. This effect is blamed on bridging of the carbon-chain between layers. At low velocities the bridging molecules have time to diffuse in line with the shear motion and at high velocities the molecules are shear-aligned. The latter effect was also observed via freeze-fraction AFM measurements [30] and non-equilibrium Molecular Dynamics (MD) simulations [31-34]. At intermediate velocities, the dissipation is caused by the tension on the bridges. The data points in Fig. 2.6 show the experimental results. The two curves represent the calculated friction force for thermal fluctuating bridges (solid) and an assumed Boltzmann distribution of the bridges (dashed).

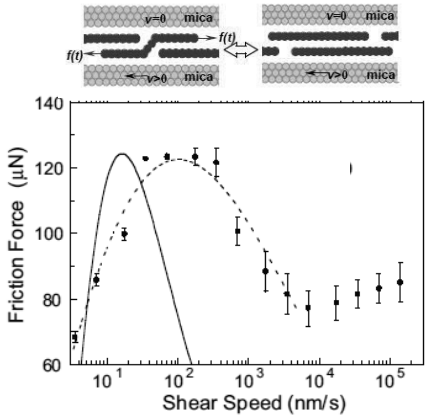

Figure 2.6 Due to bridging between layers, the friction force of sheared linear alkane molecules shows a maximum at a characteristic shear-velocity (taken from Ref. [29]).

The linear molecules described above, all assemble flat on the surfaces. However, linear molecules can also orient perpendicular to the surface (e.g. alcohols on mica [35]) depending on the solid-liquid interactions. Such orientation gives rise to another shear-response [36, 37]. Creep processes, due to interconnection of the molecules at

the top and the bottom surfaces, affect the stick-slip motion for the last two layers. For distances larger than two molecular layers a bulk-like lubrication was observed [36].
Liquid crystals are specifically interesting molecules, since they can already be oriented in the bulk liquid in a smectic or nematic phase [38]. Close to solid surfaces pre-smectic phases have been observed [39] also depending on temperature [40]. From resonance shear measurements was concluded that 6CB shows an increased viscosity by orders of magnitude due to confinement [41].
Recently, ionic liquids have gained a lot of interest, since they are assumed to be 'green' solvents [42] and hold potential application in electrochemistry [43] and solar cells [44]. For ionic liquids on mica a strong oscillatory force profile was observed [45-49], while the oscillatory solvation forces strongly reduce for ionic liquids on HOPG [45] or mica covered with a CH_3 terminated SAM (self-assembled monolayer) [46]. The surface charge of bare mica attracts the ionic liquid molecules and strongly increases the oscillatory forces. Moreover, the viscous dissipation in the confined ionic liquid also strongly depends on the surface charge [46] and can on mica increase by orders of magnitude [47] compared to the bulk value.
Last but not least, we discuss the studies performed on confined water. Water is specifically interesting because of it presence everywhere in nature. Moreover, the strong intermolecular interactions within water (hydrogen-bonds) can, already in the bulk liquid, cause exciting phenomena, like ion-specific changes in the relaxation-time [50].Whether an oscillatory force profile can be observed in water confined between hydrophilic mica surfaces strongly depends on the ion-concentration [51, 52] (~10^{-3} M KCl). For other concentrations a monotonic repulsion is observed, which is also called the hydrophilic repulsion or repulsive hydration force. For water on hydrophobic surfaces often nanobubbles are observed [53] and for water confined between two hydrophobic surfaces a strong attractive force was measured, called the hydrophobic attraction [54-56]. This, until recently, unexplained attractive force had puzzled scientists for years. However, it was only recently discovered that the attractive force could be explained by counterions in the water resulting in an attractive double layer force [57]. For the dynamic response of confined water different phenomena have been observed. From SFA shear measurements before and during the snap-to-contact between mica surfaces in water was concluded that the viscous dissipation in confined water is bulk-like down to the last liquid-layers [58]. Moreover, water was found to be a perfect bio-lubricant [59]. On the other hand, recent AFM measurements in water have shown strong variations in the structural forces and viscous dissipation [19, 26, 60-62] and significant changes in the liquids relaxation time [19, 26]. The structural forces and liquid-to-solid phase transitions were also found in numerical simulations [63, 64]. By studying the periodicity of the oxygen atoms in water, it was shown that the water molecules all orient in the same direction with respect to the surface [65]. Moreover, scanning polarization AFM measurements of monolayers of water absorbed on mica have also shown liquid-to-solid phase transitions [66], which were reproduced with numerical simulations [67]. Furthermore, friction force microscopy studies under ambient conditions have indicated ice formation on the surface within the water-

meniscus formed between the tip and a graphite surface [68, 69]. On the other hand, measurements of the snap-to-contact of two hydrophilic surfaces in water using AFM with an active force-feedback had shown a liquid-like response of the confined water. Nevertheless, the viscosity of the water meniscus was found to be seven orders of magnitude higher than the bulk [70]. Monte Carlo simulations by the same authors revealed that most likely a cooperative effect of the hydrogen-bonding of the water to both surfaces is responsible for the increased viscosity.
In short, as for simple model liquids, also for confined water various phenomena have been reported and a consistent picture still lacks.

As already mentioned above, the oscillatory solvation forces have also been studied extensively with theoretical and numerical techniques. Already before the first observation of the oscillatory solvation forces, layering was predicted in hard-sphere- and Lennard-Jones liquids close to solid walls from the Percus-Yevick theory and Monte Carlo simulations [71-74]. Moreover, upon confinement the average solvation force was found to oscillate with the distance between the walls [75]. Later, direct comparison of the static response of confined OMCTS via experiments and Percus-Yevick theory showed excellent quantitative agreement [76].
Although liquid-to-solid phase transitions in confinement were already predicted by equilibrium theory [77], to study the dynamic and dissipative response of confined liquids and to reproduce the dynamic experimental techniques often non-equilibrium numerical techniques were applied. Early combined Monte Carlo – Molecular Dynamics (MD) simulations gave a first indication that the confined liquid can solidify depending on the distance between the walls [78] and that, for the distances at which the liquid solidifies, a finite shear stress is needed to bring the system in (shear-) motion. In this study the walls were commensurate with the liquid and solidification already occurred at distance larger than 6 molecular layers. However, it was soon realized that commensurability has a very significant effect on the dynamic response of confined liquids [79]. Nevertheless, a finite shear stress was still needed when sliding the last confined liquid layers for non-commensurate surfaces. Later, in other Monte Carlo simulations, it was found, that shear-induced melting can create an unstable system resulting in the squeeze-out of a liquid layer [80]. The latter was also observed in experimental studies [10]. Other non-equilibrium MD simulations showed that the forces due to layering can be so high that it can elastically deform the solid surfaces [81] and thus that the elasticity of the walls needs to be taken into account to quantitatively reproduce the experimental results.
In view of the SFA squeeze-out experiments [6-8] also MD simulations have been performed to study the drainage and layering transitions upon confinement [82, 83]. In agreement with the experimental observation, this study showed that the increased pressure during approach induces a nucleation of a hole of n-1 layers, which grows and results in the expulsion of the liquid.

Although often a qualitative agreement was found with the experiments, the disadvantage of non-equilibrium MD is the large approach or shear velocity inherent to these short time-scale simulations. These short time-scales are close to the characteristic time of the molecules and so the studied properties are non-equilibrium properties. In the experiments the characteristic timescales are much slower and can therefore be assumed to be quasi-static. For that reason, more recently, also equilibrium MD simulations are applied to study the dynamics in confined liquids. Upon examination of the confined molecules it was found that the diffusion of the molecules is anisotropic [84], strongly varies with the distance between the confining surfaces and also varies with the distance from the walls [85]. This is in qualitative agreement with recent studies on colloidal suspensions, which are often used as a large-scale model-system for molecular systems [86, 87]. Via the Stokes-Einstein equation the diffusion is related to the viscosity, but the viscosity of the confined can also be calculated directly using the Green-Kubo relations [88]. In the latter method the distance between the walls was not varied, but the results from the former method imply that the viscosity of the liquid varies with the distance between the walls. Similar correlations have been used to study slip from equilibrium MD simulations [89].
Nowadays, the computational power is a lot larger than 10-20 years ago and the simulation of all-atom systems becomes feasible. All atom simulations are more realistic than united atom simulations, because the internal structure of the molecules is crucial for a quantitative comparison of the internal dissipation derived from experiments and simulations. Recent all-atom simulations of cyclohexane of mica have shown confinement-induced solidification depending on the distance between the walls [90].
Nevertheless, upon comparison of the experiments to numerical simulations, one always needs to be aware that in experiments a system-property is probed, while in most simulations the liquid-properties are probed. This is not necessarily the same [91].

Although there is so far no complete consistent picture on the *dynamic* response or the transport properties of confined liquids, for the *static* response the results converge into an agreement independent of the measurement technique. The following conclusions have been drawn:

1) Shape of the oscillatory solvation forces

Although there is no theoretical ground, the oscillatory solvation forces $f(D)$ are often well described by the empirical relation [92]:

$$f = f_0 \cos\left(\frac{2\pi D}{\sigma}\right)\exp\left(-D/\lambda\right), \qquad (1)$$

where f_0 is the amplitude of the forces, D is the distance between the confining surfaces, σ is the periodicity of the forces and λ is the decay length of the interactions.

The force amplitude f_0 of the oscillatory solvation forces strongly depends on the solid-liquid interactions and on the area of the probing surface. For example, on HOPG the oscillatory forces are much stronger in hexadecane than in OMCTS see e.g. [93]. This is due to epitaxial effects between the hexadecane molecules and the HOPG surface. Layering occurs for liquids wetting the solid surface. For non-wetting situations the oscillatory forces are strongly reduced or not observed at all [61]. A non-wetting surface gives rise to a different nanoscale phenomenon: slip [94]. The magnitude of the oscillatory forces in *layered* liquids exceeds generally the van der Waals forces [92]. In SFA and AFM experiments the forces are probed with spherical surfaces. This implies that the force also depends on the radius of curvature R of the tip (AFM) and cylinders (SFA). However, using the Derjaguin approximation [3, 92, 95]:

$$F(D) = 2\pi R W(D), \qquad (2)$$

with W the free energy between two planar surfaces, one can assume that $F / R =$ constant.
It was numerically shown that the Derjaguin approximation holds as long as the characteristic lengthscale of the interactions is smaller than the tip radius [96]. Nevertheless, in AFM experiments it was observed that, for the oscillatory forces, F / R is only constant for small tip radii [97]. For larger tip radii and colloidal probes the liquid is most likely squeezed out by nano-asperities due to the local roughness of the tip.

The periodicity of the oscillatory solvation forces σ represents the size and shape of the molecules. The measured periodicity can be different for the same liquid depending on the solid liquid interactions. For OMCTS on Highly Oriented Pyrolytic Graphite (HOPG) often a periodicity is measured of 0.7-0.8 nm [18, 20-23] which equals the minor diameter of the molecule. On the other hand, for OMCTS on mica often a periodicity of 0.9-1.1 nm (equal to the major diameter) is measured [2-4, 9-13, 17]. This is because surface specific interactions can orient the molecules (see also alcohols on mica [35-37] vs HOPG [25]). When a liquid is strongly layered at the surface, the measured periodicity can also be smaller than the molecular size [98]. Before the rupture process the molecular layers can be significantly compressed.
The decay length λ of the interaction also depends on the liquid-surface interactions, but has typically been measured to be 1.0 - 2.0 σ.

2) The effect of temperature

Over the years many reports indicated confinement-induced shifts in the melting point of the liquid (for a review see [99]). So, one might expect the oscillatory solvation

forces to be affected by temperature. Nevertheless, surprisingly, early SFA measurements have shown that the static response / conservative oscillatory forces of OMCTS are independent of the temperature between 10 ºC above down to 3 ºC below the liquids melting point (17.5ºC) [100]. From later AFM experiments over a larger temperature range (20 - 60 ºC) was derived that the *measured* amplitude of the oscillatory forces decreases with temperature [101]. These results were attributed to a temperature-dependent reduction in the entropic energy-barrier of the system that needs to be overcome for the liquid-layer to rupture. Nevertheless in Chapter 9 we will show that specific liquid-surface interactions can result in surprising temperature-effects.

3) Effect of contamination, poly-dispersity and mixing

In non-polar liquids, contamination with water and other polar components is known to have a huge effect on the amplitude of the oscillatory forces [102], especially on hydrophilic surfaces. The polar molecules disturb the layering. Moreover, they can create a capillary neck, causing an artificial attractive force on top of the oscillatory forces. Therefore non-polar liquids are often dried with molecular sieves; see e.g. [2-4, 6-14]. Contamination with similar molecules has a much lower effect [103, 104]. For mixtures of different non-polar liquids, the forces will be the same as for a pure liquid as long as the fraction of the dominant component exceeds 90% [105]. The latter only holds for liquids with comparable liquid-surface interactions. For a 50-50 mixture the oscillations in the force are less well-defined and often combinations of periodicities are observed [104, 105].

4) Effect surface roughness and commensurability

As already mentioned above, surface roughness has a dramatic effect on the oscillatory solvation forces. When the lengthscale of the roughness is random, but comparable to the molecular size, the oscillatory forces can completely disappear [106]. On the other hand, when the lengthscale of the roughness is not random and exactly matches the molecular size (i.e. the surfaces are commensurate with the liquid molecules) the oscillatory forces will significantly increase and it will be impossible to squeeze-out the last layers of liquid; see e.g. [82].

In summary, we have described that over the last three decades a lot has been learned on the oscillatory solvation forces. Especially, the conservative part of the oscillatory forces is by now well-established. However, on the viscous dissipation in confined layered liquids, which is also the subject of this thesis, there is so far not yet an agreement.

References:

[1] D. Tabor and R.H.S Winterton, *Proc. R. Soc. Lond. A* **312**, 435-450 (1969)
[2] R.G. Horn and J.N. Israelachvili, *Chem. Phys. Lett.* **71**, 192 (1980)
[3] R.G. Horn and J.N. Israelachvili, *J. Chem. Phys.* **75**, 1400 (1981)
[4] D.Y.C. Chan and R.G. Horn, *J. Chem. Phys.* **83**, 5311 (1985)
[5] B.N.J. Persson and E. Tossatti, *Phys. Rev. B* **50**, 5590 (1994)
[6] T. Becker and F. Mugele, *Phys. Rev. Lett.* **91**, 166104 (2003)
[7] T. Becker and F. Mugele, *J. Phys. Cond. Matt.* **17**, S319 (2005)
[8] L. Bureau and A. Arvengas, *Phys. Rev. E* **78**, 061501 (2008)
[9] M.L. Gee, P.M. McGuiggan and J.N. Israelachvili, *J. Chem. Phys.* **93**, 1895 (1990)
[10] H. Yoshizawa, P. M. McGuiggan and J.N. Israelachvili, *Science* **259**, 1305 (1993)
[11] H. Yoshizawa and J.N. Israelachvili, *J. Chem. Phys.* **97**, 11300 (1993)
[12] J. Klein and E. Kumacheva, *Science* **269**, 816 (1995)
[13] J. Klein and E. Kumacheva, *J. Chem. Phys.* **108**, 6996 (1998)
[14] J. Klein, *Phys. Rev. Lett.* **98**, 056101 (2007)
[15] O.M. Braun and E. Tosatti, *EPL* **88**, 48003 (2009)
[16] B.N.J. Persson, *Phys. Rev.* B **51**, 13568 (1995)
[17] Y. Zhu and S. Granick, *Langmuir* **19**, 8148 (2003)
[18] S. Patil, G. Matei, A. Oral and P.M. Hoffmann, *Langmuir* **22**, 6485 (2006)
[19] S.H. Khan, G. Matei, S. Patil and P.M. Hoffmann, *Phys. Rev. Lett.* **105**, 106101 (2010)
[20] A. Maali, T. Cohen-Bouhacina, G. Couturier and J.-P. Aimé, *Phys. Rev. Lett.* **96**, 086105 (2006)
[21] S.J. O'Shea, *Phys. Rev. Lett.* **97**, 179601 (2006)
[22] G.B. Kaggwa, J.I. Kilpatrick, J.E. Sader and S.P. Jarvis, *Appl. Phys. Lett.* **93**, 011909 (2008)
[23] S.J. O'Shea and M.E. Welland, *Langmuir* **14**, 4186 (1998)
[24] J.E. Sader and S.P. Jarvis, *Phys. Rev.* B **74,** 195424 (2006)
[25] W. Hofbauer, R.J. Ho, R. Hairulnizam, N.N. Gosvami and S.J. O'Shea, *Phys. Rev.* B **80**, 134104 (2009)
[26] T.-D. Li and E. Riedo, *Phys. Rev. Lett.* **100**, 106102 (2008)
[27] L. Bureau, *Phys. Rev. Lett.* **104**, 218302 (2010)
[28] L. Bureau, *Phys. Rev. Lett.* **99**, 225503 (2007)
[29] L.-M. Qian, G. Luengo and E. Perez, *EPL* **61**, 268 (2003)
[30] C. Drummond, N. Alcantar and J. Israelachvili, *Phys. Rev.* E **66**, 011705 (2002)
[31] A. Jabbarzadeh, P. Harrowell and R.I. Tanner, *Phys. Rev. Lett.* **96**, 206102 (2006)
[32] A. Jabbarzadeh, P. Harrowell and R.I. Tanner, *Phys. Rev. Lett.* **94**, 126103 (2005)
[33] I.M. Sivebaek, V.N. Samoilov, B.N.J. Persson, *Eur. Phys. J.* E **27**, 37 (2008)
[34] I.M. Sivebaek, V.N. Samoilov, B.N.J. Persson, *Langmuir* **26**, 8721 (2010)
[35] F. Mugele, S. Baldelli, G.A. Somorjai and M. Salmeron, *J. Phys. Chem.* B **104**, 3140 (2000)
[36] F. Mugele and M. Salmeron, *J. Chem. Phys.* **114**, 1831 (2001)
[37] F. Mugele, B.N.J. Persson, S. Zilberman, A. Nitzan and M. Salmeron, *Tribol. Lett.* **12**, 123 (2002)
[38] P.G. DeGennes, The physics of liquid crystals (1974, Clarendon Press, Oxford, UK)
[39] P.G. DeGennes, *Langmuir* **6**, 1448 (1990)
[40] G. Carbone, R. Barberi, I. Musevic and U. Krzic, *Phys. Rev. E* **71**, 051704 (2005)
[41] M. Mizukami and K. Kurihara, *Rev. Sci. Instrum.* **79**, 113705 (2008)
[42] Ionic Liquids as Green Solvents: Progress and Prospects, ACS Symposium series 856, ed. R.D. Rogers and K.R. Seddon (2003, American Chemical Society, Washington DC)

[43] M. Armand, F. Endres, D.R. MacFarlane, H. Ohno and B. Scrosati, *Nat. Mater.* **8**, 621 (2009)
[44] Y. Bai, Y. Cao, J. Zhang, M. Wang, R. Li, P. Wang, S.M. Zakeeruddin and M. Gratzel, *Nat. Mater.* **7**, 626 (2008)
[45] R. Atkin and G.G. Warr, *J. Chem. Phys.* C **111**, 5162 (2007)
[46] I. Bou-Malham and L. Bureau, *Soft Matter* **6**, 4062 (2010)
[47] K. Ueno, M. Kasuya, M. Watanabe, M. Mizukami, *Phys. Chem. Chem. Phys.* **12**, 4066 (2010)
[48] S. Perkin, T. Albrecht and J. Klein, *Phys. Chem. Chem. Phys.* **12**, 1243 (2010)
[49] R. Hayes, S. Z. E. Abedin and R. Atkin, *J. Chem. Phys.* B **113**, 7049 (2009)
[50] K.J. Tielrooij, N. Garcia-Araez, M. Bonn and H.J. Bakker, *Science* **328**, 1006 (2010)
[51] R.M. Pashley and J.N. Israelachvili, *J. Colloid Interface Sci.* **101**, 511 (1984)
[52] J.N. Israelachvili and R.M. Pashley, *Nature* **306**, 500 (1984)
[53] J. W. G. Tyrrell and P. Attard, *Phys. Rev. Lett.* **87**, 176104 (2001)
[54] R.M. Pashley, P.M. McGuiggan, B.W. Ninham and D.F. Evans, *Science* **229**, 1088 (1985)
[55] S. Perkin, N. Kampf and J. Klein, *Phys. Rev. Lett.* **96**, 038301 (2006)
[56] A.J. Katan, T.H. Oosterkamp, *J. Chem. Phys.* C **112**, 9769 (2008)
[57] G. Silbert, J. Klein and S. Perkin, *Faraday Discuss.* **146**, 309 (2010)
[58] U. Raviv, P. Laurat and J. Klein, *Nature* **413**, 51 (2001)
[59] W.G. Briscoe, S. Titmuss, F. Tiberg, R.K. Thomas, D.J. McGillivray and J. Klein, *Nature* **444**, 191 (2006)
[60] S. Jeffrey, P.M. Hoffmann, J.B. Pethica, C. Ramanujan, H.O. Ozer and A. Oral, *Phys. Rev.* B **70**, 054114 (2004)
[61] T.D. Li, J.P. Gao, R. Szoszkiewicz, U. Landman and E. Riedo, *Phys. Rev.* B **75**, 115415 (2007)
[62] T. Uchihashi, M. Higgins, Y. Nakayama, J.E. Sader and S.P Jarvis, *Nanotechnology* **16**, S49 (2005)
[63] N. Giovambattista, P.J. Rossky and P.G. Debenedetti, *Phys. Rev. Lett.* **102**, 050603 (2009)
[64] R. Zangi and A.E. Mark, *Phys. Rev. Lett.* **91**, 025502 (2003)
[65] L. Cheng, P. Fenter, K.L. Nagy, M.L. Schlegel and N.C. Sturchio, *Phys. Rev. Lett.* **87**, 156103 (2001)
[66] P.B. Miranda, L. Xu, Y.R. Shen and M. Salmeron, *Phys. Rev. Lett.* **81**, 5876 (1998)
[67] S.-H. Park and G. Sposito, *Phys. Rev. Lett.* **89**, 085501 (2002)
[68] K.B. Jinesh and J.W.M. Frenken, *Phys. Rev. Lett.* **96**, 166103 (2006)
[69] K.B. Jinesh and J.W.M. Frenken, *Phys. Rev. Lett.* **101**, 036101 (2008)
[70] R.C. Major, J.E. Houston, M.J. McGrath, J.I. Siepmann and X.-Y. Zhu, *Phys. Rev. Lett.* **96**, 1777803 (2006)
[71] D. Henderson, F.F. Abraham and J.A. Barker, *Mol. Phys.* **31**, 1291 (1976)
[72] E. Waisman, D. Henderson and J.L. Lebowitz, *Mol. Phys.* **32**, 1373 (1976)
[73] I.K. Snook and D. Henderson, *J. Chem. Phys.* **68**, 2134 (1978)
[74] I.K. Snook and W. van Megen, *J. Chem. Phys.* **70**, 3099 (1979)
[75] W. van Megen and I.K. Snook, *J. Chem. Soc., Faraday Trans.* **2**, 1095 (1979)
[76] P. Attard and J.L. Parker, *J. Phys. Chem.* **96**, 5086 (1992)
[77] A.V. Tkachenko and Y. Rabin, *Sol. Stat. Comm.* **103**, 361 (1997)
[78] M. Schoen, C.L. Rhykerd, D.J. Diestler and J.H. Cushman, *Science* **245**, 1223 (1989)
[79] P.A. Thompson and M.O. Robbins, *Science* **250**, 792 (1990)
[80] D.J. Diestler, M. Schoen, J.H. Cushman, *Science* **262**, 545 (1993)
[81] J. Gao, W.D. Luedtke and U. Landman, *Science* **270**, 605 (1995)

[82] B.N.J. Persson and P. Ballone, *J. Chem. Phys.* **112**, 9524 (2000)
[83] B.N.J. Persson, V.N. Samoilov, S. Zilberman and A. Nitzan, *J. Chem. Phys.* **117**, 3897 (2002)
[84] J. Gao, W.D. Luedtke and U. Landman, *Phys. Rev. Lett.* **79**, 705 (1997)
[85] J. Mittal, T.M. Truskett, J.R. Errington and G. Hummer, *Phys. Rev, Lett.* **100**, 145901 (2008)
[86] C.R. Nugent, K.V. Edmond, H.N. Patel and E.R. Weeks, *Phys. Rev, Lett.* **99**, 025702 (2007)
[87] H.B. Eral, D. van den Ende, F. Mugele and M.H.G. Duits, *Phys. Rev.* E **80**, 061403 (2009)
[88] J. Delhommelle and P.T. Cummings, *Phys. Rev.* B **72**, 172201 (2005)
[89] L. Bocquet and J.-L. Barrat, *Phys. Rev.* E **49**, 3079 (1994)
[90] H. Docherty and P.T. Cummings, *Soft Matter* **6**, 1640 (2010)
[91] M.H. Müser and M.O. Robbins, *Phys. Rev.* B **61**, 2335 (2000)
[92] J.N. Israelachvili, *Intermolecular and Surface Forces* (Academic London 1991)
[93] S. de Beer, P. Wennink, M. Van der Weide-Grevelink & F. Mugele, *Langmuir* **26**, 13245 (2010)
[94] C. Cottin-Bizonne, B. Cross, A. Steinberger and E. Charlaix, *Phys. Rev. Lett.* **94**, 056102 (2005)
[95] S.J. O'Shea, M.E. Welland and J.B. Pethica, *Chem. Phys. Lett.* **223** 336 (1994)
[96] L.D. Gelb, R.M. Lynden-Bell, *Phys. Rev. B* **49**, 2058 (1994)
[97] L.T.W. Lim, A.T.S. Wee and S.J. O'Shea, *Langmuir* **24**, 2271 (2008)
[98] N.N. Gosvami, S.K. Sinha, W. Hofbauer and S.J. O'Shea, *J. Chem. Phys.* **126**, 214708 (2007)
[99] H.K. Christenson, *J. Phys.: Condens. Matter* **13,** R95 (2001)
[100] H.K. Christenson, J.N. Israelachvili, *J. Chem. Phys.* **80**, 9 (1984)
[101] L.T.W. Lim, A.T.S. Wee, S.J. O'Shea, *J. Chem. Phys.* **130**, 134703 (2009)
[102] H.K. Christenson and C.E. Blom, *J. Chem. Phys.* **86** 419 (1987)
[103] J.N. Israelachvili, S.J. Kott, M.L. Gee, T.A. Whitten, *Macromolecules* **22**, 4247-4253 (1989)
[104] R.Y.H. Lim and S.J. O'Shea, *Langmuir* **20**, 4916 (2004)
[105] H.K. Christenson, *Chem. Phys. Lett.* **18**, 455 (1985)
[106] H.K. Christenson, *J. Phys. Chem.* **90**, 4 (1986)

Chapter 3

Small Amplitude Atomic Force Spectroscopy

The measurements described in this thesis have mainly been performed with the Atomic Force Microscope (AFM). In the experiments we oscillate our cantilever with a small amplitude (sub-angstrom) and monitor the amplitude and phase response to obtain the conservative and dissipative tip-sample forces. To extract the correct properties of the studied samples, we first need to characterize our measurement system. This chapter provides a general introduction to small amplitude Atomic Force Spectroscopy. Moreover, we explain the basic modeling steps necessary to extract the conservative and dissipative interaction forces for the different methods available in AFM spectroscopy.[1]

[1] Part of the chapter has been published as: S. de Beer, D. van den Ende, D. Ebeling, F. Mugele, *Small Amplitude Atomic Force Spectroscopy*, Chapter 2 in Scanning Probe Microscopy in Nanoscience and Nanotechnology 2, p 39-58, ed. Bharat Bhushan, Springer-Verlag Berlin Heidelberg (2011)

3.1 Atomic Force Microscope & Surface Forces Apparatus

To quantitatively probe the properties of the oscillatory solvation forces in confined liquids, two measurement-systems dominate the research field: (1) the Surface Forces Apparatus (SFA) and (2) the Atomic Force Microscope (AFM). Figure 3.1 shows a schematic representation of the measurement principle of both (a) the SFA and (b) the AFM.
In the SFA two large mica surfaces are approached via a piezo. The surfaces are in a crossed-cylinder geometry with a radius of approximately 1cm. One of the cylinders is attached to a cantilever. The distance between the mica surfaces can be accurately measured (within 0.2nm) using interferometry (for more details see Chapter 10). By comparing the distance between the cylinders to the piezo displacement, the deflection of the cantilever can be determined. From the deflection the force can be calculated.
In the AFM a cantilever, with a small tip (radius 6-100nm), and a flat surface are approached towards each other with a piezo. The deflection of the cantilever is in most measurement setups measured with a laser aligned at the backside of the cantilever. The reflection of the laser is monitored on a quadrant photo-detector. The deflection of the cantilever is converted into a force.

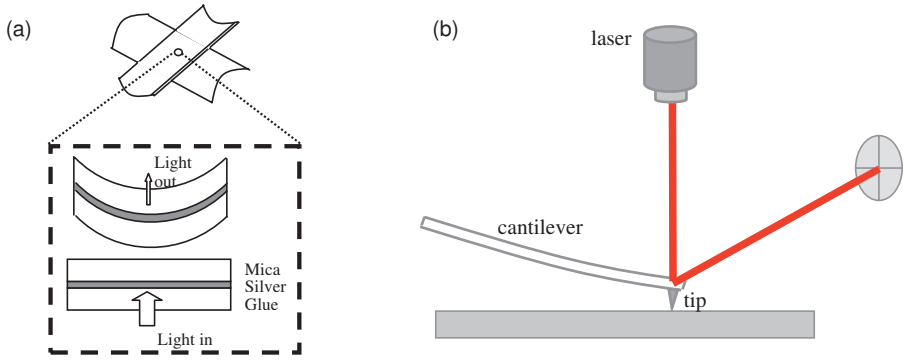

Figure 3.1 (a) Schematic representation of the SFA setup (b) Schematic representation of the AFM setup.

Most of the experiments described in this thesis have been performed with the AFM. The major differences between SFA and AFM measurements are:
1) The technique to determine the surface-to-surface distance.
2) The geometry.
3) The surfaces employed for the experiments.

In SFA, two large, transparent, very-well defined, atomically flat mica surfaces are used. Because interferometry is used to determine the distance between the surfaces, there is (within 0.2nm) no uncertainty when the surfaces make contact. On the other

hand in AFM, where the tip-surface separation is measured indirectly via the deflection, the point of real tip-surface contact is always less well-defined (although, this can be circumvented by combining AFM with conduction measurements, see also Chapter 9). Nevertheless, in SFA the surfaces need to be transparent for the interferometric detection, which makes the SFA a lot less flexible with respect to the use of different kinds of surfaces like in AFM. However, in AFM a small less well-defined tip is approached towards an atomically flat surface. This makes the AFM a less well-defined model-system than the SFA. But, in most technological applications the surfaces are nanoscopically bad-defined and rough and so contact is made via many nano-asperities. Understanding a (small) single-asperity contact (as in AFM) is for that reason more relevant in the applied research of e.g. friction and wear.

3.2 Introduction to Atomic Force Microscopy

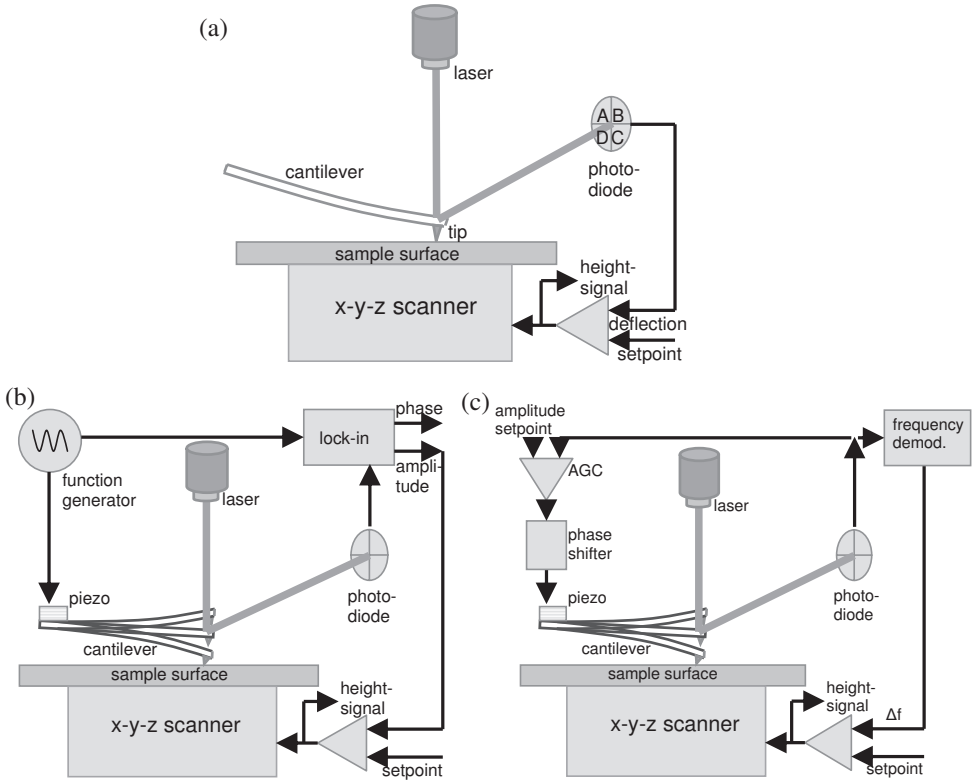

Figure 3.2 Feedback mechanisms for: (a) Contact mode, the deflection is measured by the photo-diode and kept constant by adjusting the z piezo (b) Amplitude modulation, via the lock-in amplifier the amplitude and the phase response of the cantilever is measured and the amplitude is kept constant by adjusting the z piezo (c) Frequency modulation, via the frequency demodulator the frequency shift is measured and kept constant by adjusting the z piezo.

Since its invention by Binnig et al [1] in the 1980's, the atomic force microscope (AFM) has evolved into one of the most powerful tools for nanotechnology. Nowadays, the AFM is used in numerous research fields varying from biology to solid state physics and in many industries, like the semi-conductor or the automotive industry.

The AFM is most commonly used for topographical imaging of surfaces, where a static or dynamic feedback mechanism on the cantilever (Fig. 3.2) is applied to follow the surface in great detail (down to atomic resolution).In contact mode imaging (as the static feedback is often called) the tip of the cantilever is kept in contact with the surface (Fig. 3.2(a)). Due to the repulsive or adhesive forces between the tip and the surface, the cantilever bends upwards or downwards as soon as the topography of the surface resp. increases or decreases in height. While the tip scans the surface (in x and y), the bending of the cantilever is measured by the quadrant photo-detector (or sometimes by interference detection, for a review on detection-techniques see Ref.2). The deflection is given by detector signals $a + b$, minus $c + d$ (see Fig. 3.2(a)) and kept constant by adjusting the z piezo below the sample surface. The change in feedback-voltage applied to the z piezo is the measured height signal and gives the topography of the scanned surface. Note that in AFM the feedback is on the force and therefore artificial height differences might be observed due to changing surface properties over the sample (e.g. elasticity). Next to a static feedback mechanism (like contact mode) also dynamic methods are used: Amplitude Modulation (AM-) and Frequency Modulation (FM-) AFM. The advantage of dynamic AFM is that the tip is not necessarily in contact with the surface and so during imaging the (lateral, but sometimes also nomal) forces between tip and sample are much less than in contact mode. In both dynamic methods, the cantilever is driven with an amplitude of typically 0.5-100 nm. This can be accomplished by a drive piezo (as in Fig. 3.2(b) and (c)) or magnetic actuation. In contrast to simply measuring the static deflection, one now measures the amplitude and phase or frequency shift with respect to the driving signal of the cantilever oscillation. As will be explained in more detail below, upon approach of the cantilever towards the surface, the response (amplitude, phase and resonance frequency) will change due to tip-surface interactions. For AM-AFM (Fig. 3.2(b)), the drive frequency and the drive amplitude are kept constant, while the amplitude and phase response of the cantilever are monitored via a lock-in amplifier. Subsequently the amplitude is compared to the set-point value and kept constant by adjusting the z piezo. Like in contact mode the feedback voltage gives the height-signal. A disadvantage of AM-AFM is the notorious bi-stability due to the non-linear response of the cantilever caused by non-linear tip-sample forces [3], which can be overcome using a phase-feedback [4] or FM-AFM [5]. FM-AFM can be applied in two modes, constant amplitude (CA) [6] and constant excitation (CE) mode [7]. In the following we will focus on the constant amplitude mode, since this technique is most widely used. Figure 3.2(c) shows a typical driving scheme for FM-AFM. In FM-AFM the cantilever is driven with a fixed phase lag (normally close to resonance, i.e. -90˚). This can be accomplished by self-excitation ([5], Fig. 3.2(c)) or a phase locked loop (PLL)

[8]. In self-excitation the signal from the photo-detector is amplified, phase-shifted by 90° and then used to driven the cantilever for a guaranteed driving at resonance, while with a PLL the cantilever is driven at the actual measured resonance frequency. At the same time the measured amplitude response of the cantilever is kept constant with the Automatic Gain Controller (AGC). Due to changes in the height of the scanned surface, the resonance frequency will change. The shift in resonance frequency is compared to the set-point value and kept constant by adjusting the z piezo. Again the z piezo voltage gives the height signal.

Even though the force on the sample can be significantly reduced using dynamic AFM, for some specific samples (e.g. liquid-air interfaces [9]), and especially in a liquid environment, it can still be too large to image features without deforming them. In this case, a Q-control [10, 11] can be used to reduce the force on the sample even more. For a good review on the different imaging feedback methods see Ref. 12.

Although imaging was the number one application of the AFM, over the years, more and more people realized that the AFM can also be used to quantitatively study surface or sample properties, which can be done via either force spectroscopy or one of the imaging modes.

During imaging in contact mode the friction forces can be studied by monitoring the torsional bending of the cantilever [13], (a + c) - (b + d) in Fig. 3.2(a), while in AM-AFM the phase signal can, although not straightforward, be related to the energy dissipation [14]. Recently also imaging methods have been developed involving the analysis of higher harmonics [15] and higher oscillation modes [16] of the AFM cantilever. These techniques give access to sample properties such as elasticity and adhesion.

In force distance mode, the topography of the sample surface is no longer studied, but the response of the cantilever is monitored while it is approached and retracted from the surface. From the response of the cantilever the tip-sample forces are extracted as a function of tip-surface distance. This can be done in contact mode, where the deflection z of the cantilever is translated into a force F using $F = -k_c z$, with k the spring-constant of the cantilever. Although this method is simple and straightforward to apply, it has some disadvantages, like the snap-to-contact as soon as the attractive force gradient $dF(z_c)/dz = k_{\text{int}}$ is larger then the spring constant k_c, which implies that only a small part of the attractive tip-sample force can be measured. This can be overcome using stiffer cantilevers, at the expense of sensitivity loss in the force. Nevertheless, also with stiff cantilevers complete high-resolution conservative force profiles can be extracted [17] in contact mode. This is accomplished by monitoring the Brownian noise instead of the average deflection of the relatively stiff cantilever upon approach and retracts.

Another method to extract the complete force-profile is via dynamic AFM, which has the additional advantage that next to the conservative forces also the dissipative forces can be measured. This can again be done in AM- or FM-AFM mode. Over the years many techniques have been developed to extract the conservative and dissipative

forces, varying from small to large amplitude or even universal methods for both AM [18-25] - and FM-AFM [26-28].
In remainder of this Chapter we will discuss the small amplitude force-inversion techniques developed for AM [22-25] - and FM-AFM [28]. The exact force-inversion methodology depends on the driving scheme used in the experiments, as will be discussed in the next sections.

3.3 Small amplitude spectroscopy

Small amplitude spectroscopy is a method of dynamic force spectroscopy in which the amplitude response of the cantilever is kept small enough to justify linearization of the conservative and dissipative tip-sample forces. In atomic force spectroscopy the cantilever is usually modeled as a simple harmonic oscillator affected by the tip-sample interactions F_{ts}:

$$m \cdot \ddot{z} + \gamma_c \cdot \dot{z} + k_c \cdot z = F_{dr} + F_{ts} \tag{1}$$

Here, z (t) describes the displacement of the cantilever, k_c is the cantilevers spring constant, m is the total effective mass (when relevant including the added mass caused by the motion of the surrounding liquid), γ_c is the viscous damping around (or of) the cantilever and F_{dr} is the driving force applied to the cantilever and F_{ts} is the tip sample force.

The system properties k_c, m and γ_c can be found using a thermal noise spectrum of the cantilever. Integration of the thermal noise spectrum results in the spring constant k_c [29,30] and fitting the thermal noise spectrum with

$$A = A_{white} + \frac{A_0 f_0^4}{\left(f^2 - f_0^2\right)^2 + \left(\frac{f\, f_0}{Q}\right)^2}$$

results in the calibration constants Q and $\omega_0 = 2\pi f_0$. From these calibration constants and the spring constant we can calculate the mass via $m = \omega_0^2 / k_c$ and the damping via $\gamma_c = m\omega_0 / Q$. How the driving force is determined depends on the actuation and detection method and will therefore be explained in the different sub-sections below. In our measurements we do not know the absolute value of the phase (there are also phase-lags due to e.g. electronics). So before analyzing the results, the phase (far away, i.e without interactions) needs to be shifted to the correct value. This phase-shift also depends on the actuation and detection method. The correct value of the phase can be found using the equations for the phase given below (with the interactions set to zero).

In small amplitude spectroscopy the tip sample force F_{ts} at the (quasi-statically moved) average cantilever position z_c is rewritten using a Taylor expansion:

$$F_{ts}(z_c + z, \dot{z}) = F_{ts}(z_c, 0) - k_{\text{int}} z - \gamma_{\text{int}} \dot{z} - \frac{1}{2} k'_{\text{int}} z^2 - \frac{1}{2} \gamma'_{\text{int}} z\dot{z} + H.O.T. \qquad (2)$$

where H.O.T. are the Higher Order Terms, $k_{\text{int}} = -dF_{ts}(z_c)/dz$ is the interaction stiffness, γ_{int} is the interaction damping and $F_{ts}(z_c,0)$ is the equilibrium force on the cantilever. Note that these tip-sample force parameters k_{int} and γ_{int} are independent of the specific measurement technique and should be identical for all data extracted by the different techniques described below. When applying a linearization only the first order terms of eq. 2 are taken into account. This approximation is therefore only valid as long as the amplitude $A << 2k_{\text{int}}/k'_{\text{int}}$ and $A << 2\gamma_{\text{int}}/\gamma'_{\text{int}}$ [24]. After substitution of the linearised tip-sample force, eq. 1 can be solved for the conservative interaction stiffness and the dissipative interaction damping. The resulting equations we call the force-inversion formulae. The exact form of these formulae depends on the actuation and detection technique. In a liquid (low $Q = m\omega_0/\gamma_c$, where $\omega_0 = \sqrt{k_c/m}$) environment the differences between these techniques become more pronounced and can no longer be neglected. Therefore we will explain the different techniques using typical AFM-in-liquid characteristics and (cantilever-) properties (spring constant k_c = 2 N/m, quality factor Q = 3, measured frequency at the amplitude maximum $f_{res} = \omega_0/2\pi\sqrt{1-1/2Q^2} = 40kHz$).

3.3.1 Actuation techniques

To perform dynamic AFM spectroscopy several driving schemes can be used. The by far most widely used technique is acoustic driving (see e.g. [21, 23, 24, 26]), where a small piezo is used to drive the cantilever at the backside. The downside of this technique is that spurious resonances are produced next to the fundamental resonance [31]. Although, this is not necessarily a problem for imaging, for spectroscopy a clean cantilever response (resonance curve) is needed for a correct characterization of the system. This problem can be overcome by applying a more direct force to the cantilever, like in sample modulation [25] or a magnetic driving scheme [22, 27]. The exact driving and detection method determines the *measured* amplitude / phase versus frequency response and the shift in resonance frequency of the cantilever [32] and therefore the force-inversion formulae, which will be discussed in more detail below.

3.3.1a Sample Modulation

In sample modulation [25] the z piezo (on which the sample is mounted) is oscillated with a small amplitude. Due to tip-sample interactions the motion of the cantilever is

coupled to the motion of the sample. Consequently the cantilever will only respond close to the surface where the tip-sample forces come into play.

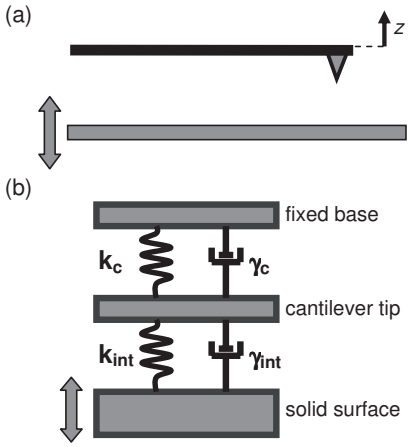

Figure 3.3 (a) In sample modulation the response of the cantilever is monitored while the sample is oscillated (b) Spring-dashpot representation of sample modulation.

For small amplitude spectroscopy the equation describing the dynamics of the cantilever is given by:

$$m \cdot \ddot{z} + \gamma_c \cdot \dot{z} + k_c \cdot z = k_{\text{int}}(d - z) + \gamma_{\text{int}}(\dot{d} - \dot{z}) \tag{3}$$

In which $z(t)$ is the measured response of the cantilever and $d(t)$ is the driving motion of the sample. Using the Ansatz $z = Ae^{i(\omega t+\varphi)}$ and $d = A_d e^{i\omega t}$ (with ω is the drive frequency, A is the measured amplitude, φ the measured phase and A_d is the drive amplitude), eq. 3 can be solved for the amplitude A and the phase φ:

$$\frac{A}{A_d} = \frac{k_{\text{int}}\sqrt{1+(\omega\gamma_{\text{int}}/k_{\text{int}})^2}}{\sqrt{(k_{\text{int}}+k_c-m\omega^2)^2+\omega^2(\gamma_{\text{int}}+\gamma_c)^2}} \tag{4a}$$

and

$$\tan\varphi = \frac{-\omega(\gamma_{\text{int}}(m\omega^2-k_c)+\gamma_c k_{\text{int}})}{k_{\text{int}}(k_{\text{int}}+k_c-m\omega^2)+\omega^2\gamma_{\text{int}}(\gamma_{\text{int}}+\gamma_c)} \tag{4b}$$

Figure 3.4 shows the amplitude and phase response of the cantilever for a typical sample modulation configuration in liquid. Figure 3.4 shows that for a positive interaction stiffness the resonance frequency of the system shifts up, while for a negative interaction stiffness the resonance frequency goes down. A positive interaction stiffness will increase the total stiffness and therefore increase the resonance frequency of the system, while a negative interaction stiffness will decrease the total stiffness and the resonance frequency of the system.
Also note that the phase is negative for a positive interaction stiffness and positive for a negative interaction stiffness. This implies an increased sensitivity in the phase physical systems with an oscillatory stiffness (like the oscillatory solvation forces).

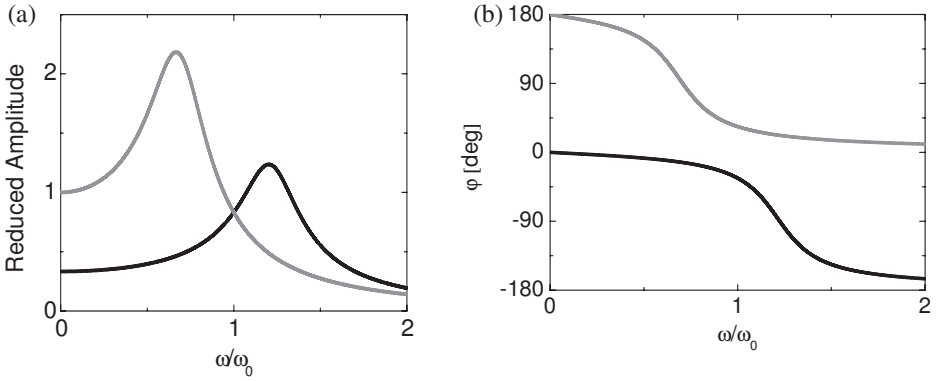

Figure 3.4 The effect of a positive and a negative interaction stiffness (k_{int} = + 0.5 k_c black and - 0.5 k_c gray) on the amplitude (a) and phase (b) spectra of the cantilever in a sample modulation system.

Figure 3.5 show the effect of an increasing interaction damping on the spectra of a typical sample modulation configuration in liquid. For an increasing damping the amplitude response increases, due to the larger coupling with the modulating sample surface. The frequency f_{res} at which we find a maximum in the amplitude is, for a simple harmonic oscillator, expected to go down for an increasing damping coefficient (decreasing Q) with: $f_{res} = \omega_0 / 2\pi\sqrt{1-1/2Q^2}$. This behavior can also qualitatively be observed in Fig. 3.5(a). The phase response is 90˚ for $\omega \rightarrow 0$ and decreases to -90˚ for $\omega \rightarrow \infty$. This decrease is more gradual for a higher damping.

In Amplitude Modulation (AM) sample modulation atomic force spectroscopy the sample is driven with a fixed drive amplitude A_d and drive frequency ω. The amplitude A and phase φ response of the cantilever are monitored upon approach and retract towards and from the oscillating sample surface. To extract the interaction stiffness k_{int} and the damping γ_{int} from the measured amplitude and phase response we need to solve eq. 3 for k_{int} and γ_{int}.

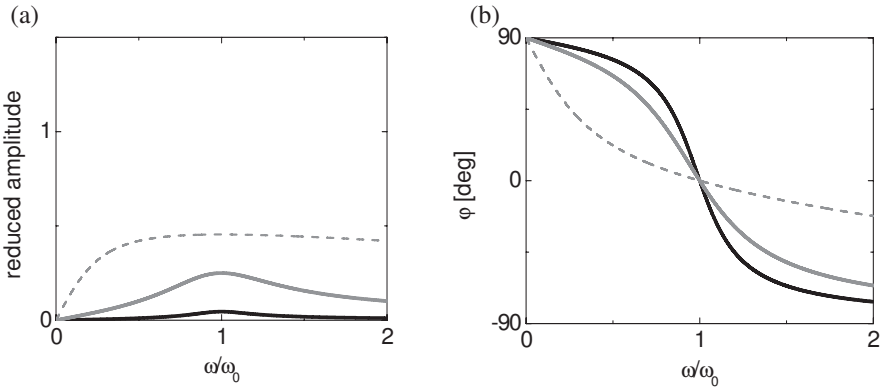

Figure 3.5 The effect in an increasing interaction damping ($\gamma_{int} = 0.1\gamma_c$ black, $1\gamma_c$ gray and $10\gamma_c$ dashed) on the amplitude (a) and phase (b) spectra of the cantilever in a sample modulation system.

After substituting the Ansatz $z = Ae^{i(\omega t+\varphi)}$ and $d = A_d e^{i\omega t}$ and their derivatives in eq. 3 we find: (See Appendix 3.A for the complete derivation. For the limit $\omega \to 0$ see Ref. [32])

$$k_{\text{int}} = -k_c + m\omega^2 + \frac{\left(k_c - m\omega^2\right)\left(1 - \frac{A}{A_d}\cos\varphi\right) - \gamma_c\omega\frac{A}{A_d}\sin\varphi}{1 - 2\left(\frac{A}{A_d}\right)\cos\varphi + \left(\frac{A}{A_d}\right)^2} \tag{5a}$$

and

$$\gamma_{\text{int}} = -\gamma_c + \frac{\gamma_c\omega\left(1 - \frac{A}{A_d}\cos\varphi\right) + \left(k_c - m\omega^2\right)\frac{A}{A_d}\sin\varphi}{\omega\left(1 - 2\left(\frac{A}{A_d}\right)\cos\varphi + \left(\frac{A}{A_d}\right)^2\right)} \tag{5b}$$

From the calibration constants k_c, Q and f_{res}, the damping γ_c and the mass m can be calculated and together with the measured amplitude A and phase φ be used to extract the distance dependent conservative and dissipative interaction forces. The drive amplitude A_d can be determined from the measured amplitude of the cantilever in full contact with the sample surface. In FM atomic force spectroscopy we want to extract the interaction stiffness and interaction damping from the measured frequency shift and change in applied drive amplitude to keep the measured amplitude constant. For this we can use the same formulae as derived for AM AFM. In contrast to AM AFM, where the amplitude A and phase φ are monitored while the drive frequency ω and the

drive amplitude A_d are kept constant, now ω and A_d are monitored while A and φ are kept constant. When the phase is locked on -90°, eq. 5a and b reduce to:

$$k_{\text{int}} = -k_c + m\omega^2 + \frac{\left(k_c - m\omega^2\right) + \gamma_c \omega \frac{A}{A_d}}{1 + \left(\frac{A}{A_d}\right)^2} \tag{6a}$$

and

$$\gamma_{\text{int}} = -\gamma_c + \frac{\gamma_c \omega - \left(k_c - m\omega^2\right)\frac{A}{A_d}}{\omega\left(1 + \left(\frac{A}{A_d}\right)^2\right)} \tag{6b}$$

3.3.1b Magnetic Actuation

In magnetic driving either the cantilever is coated with a magnetic or magneto-restrictive material or a small magnetic particle is attached to the end of the cantilever. With a coil an oscillating magnetic field is applied in order to drive the cantilever (Fig. 3.6(a)). The forcing of the cantilever is direct and with deflection detection (or interferometric detection) the total motion of the cantilever is measured.

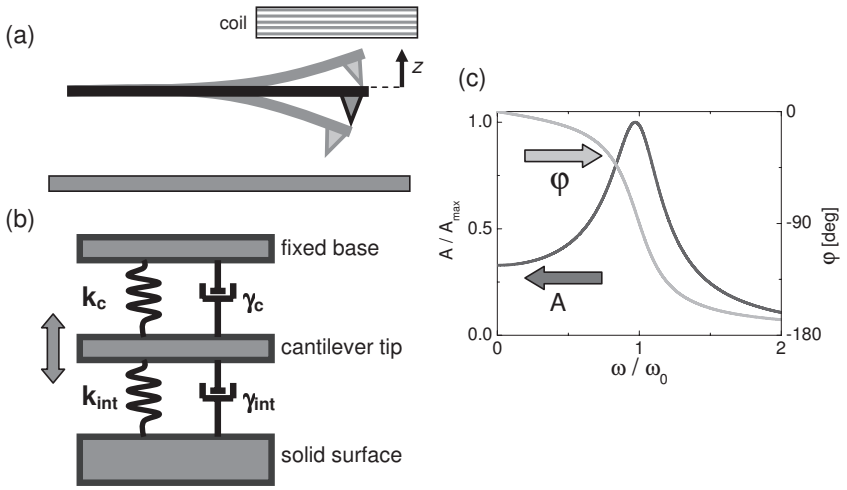

Figure 3.6 (a) In magnetic actuation the response of a magnetic cantilever is monitored while an oscillating magnetic field is applied (b) Spring-dashpot representation of magnetic actuation. (c) Amplitude and phase response for magnetic driving with a typical AFM configuration in liquid without interactions.

The equation of motion for this system is described by:

$$m \cdot \ddot{z} + \gamma_c \cdot \dot{z} + k_c \cdot z = F_0 e^{i\omega t} - \gamma_{\text{int}} \dot{z} - k_{\text{int}} z \tag{7}$$

Using the Ansatz $z = Ae^{i(\omega t+\varphi)}$ eq. 7 can be solved for the amplitude A and phase φ:

$$A = \frac{F_0}{\sqrt{\left(k_{tot} - m\omega^2\right)^2 + \left(\omega\gamma_{tot}\right)^2}} \tag{8a}$$

and

$$\tan\varphi = \frac{-\omega\gamma_{tot}}{-m\omega^2 + k_{tot}} \tag{8b}$$

Figure 3.6(c) shows the amplitude and phase response as a function of frequency for a magnetically driven cantilever in liquid without tip-sample interactions. Here we see the well-established typical response of a harmonic oscillator. Due to the damping the amplitude-maximum is at a lower frequency then the resonance frequency $\omega_0 = \sqrt{k_c / m}$ and the phase shows a gradual decrease from 0 to -180˚. The phase is exactly -90˚ for ω_0.

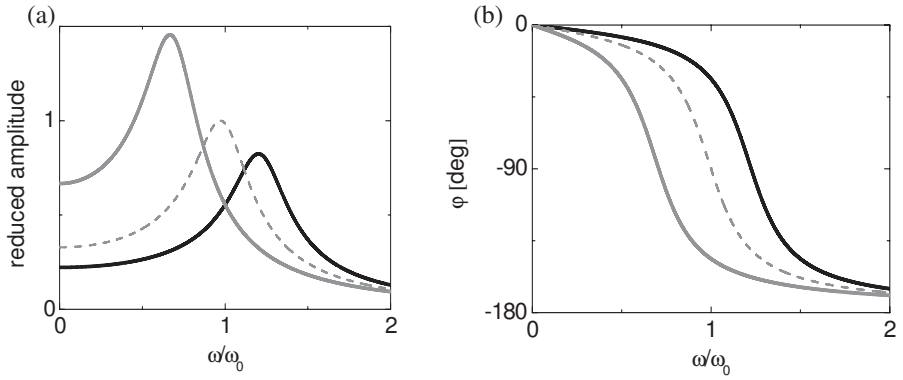

Figure 3.7 The effect of a positive and a negative interaction stiffness (k_{int} = + 0.5 k_c black and - 0.5 k_c gray) on the amplitude (a) and phase (b) spectra of the cantilever using magnetic actuation.

Figure 3.7 shows the effect of a positive and a negative interaction stiffness on the amplitude and phase response for a typical magnetic drive configuration in liquid (spring constant k_c = 2 N/m, quality factor Q = 3, amplitude resonance frequency $f_{res} = 40kHz$).
The resonance frequency increases for a positive interaction stiffness and the resonance frequency decreases for a negative interaction stiffness, which is also

expected from its definition: $\omega_0 + \Delta\omega = \sqrt{k_{tot}/m}$, where k_{tot} is the total stiffness (cantilever stiffness + interaction stiffness). Since the forcing is constant and the static deflection z is given by $z = -F/k_{tot}$ the amplitude response for $\omega \rightarrow 0$ is higher for a negative stiffness. This effect can qualitatively be observed for all frequencies.

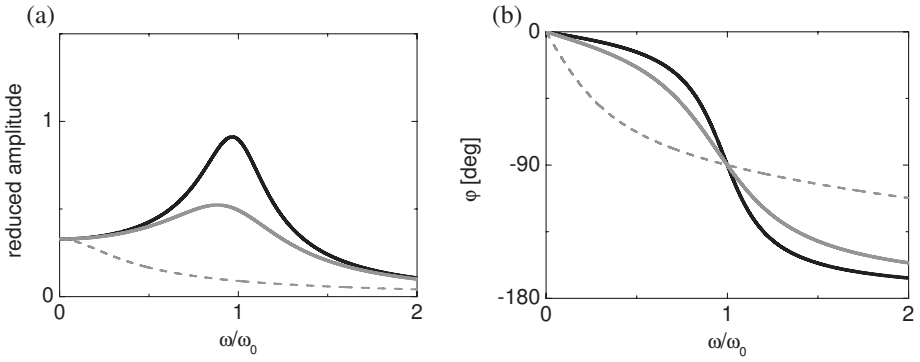

Figure 3.8 The effect in an increasing interaction damping ($\gamma_{\mathrm{int}} = 0.1\gamma_c$ black, $1\gamma_c$ gray and $10\gamma_c$ dashed) on the amplitude (a) and phase (b) spectra of the cantilever using magnetic actuation.

Figure 3.8 shows the effect of an increasing interaction damping on the amplitude and phase response of an magnetically driven cantilever in liquid. Since an increasing interaction damping increases the total damping the frequency at which we find the maximum amplitude is expected to go down according to $f_{res} = \omega_0 / 2\pi\sqrt{1 - 1/2Q^2}$. The phase shows for a higher damping a more gradual decrease from 0˚ at $\omega \rightarrow 0$ to -180˚ at $\omega \rightarrow \infty$, but for all values of the interaction damping the phase is -90˚ at ω_0.

In order to extract the physical interaction forces from the calibration constants and the measured amplitude and phase response, we need to solve eq. 7 for the interaction stiffness k_{int} and damping γ_{int}, yielding (see, e.g. [22, 33]):

$$k_{\mathrm{int}} = -k_c + m\omega^2 + \frac{F_0}{A}\cos\varphi \tag{9a}$$

and

$$\gamma_{\mathrm{int}} = \frac{-F_0}{A\omega}\sin\varphi - \gamma_c \tag{9b}$$

Where F_0 can be determined from the amplitude far away from the surface (where the interactions are zero) using eq. 8a.
For the derivation of the force inversion formulae in FM AFM (magnetic drive) we use the fact that the phase is locked at -90˚. When the phase is -90˚, the system is driven at

resonance. As shown above in Fig. 3.7 and 3.8, the shift in the resonance frequency is only determined by the interaction stiffness and not by the interaction damping. So using $\omega_0 + \Delta\omega = \sqrt{k_{tot}/m}$ we can directly calculate the interaction stiffness from the frequency shift:

$$k_{\text{int}} = m(\omega_0 + \Delta\omega)^2 - k_c = m\omega_0^2\left(\frac{2\Delta\omega}{\omega_0} + \left(\frac{\Delta\omega}{\omega_0}\right)^2\right) \tag{10a}$$

For $k_{\text{int}} << k_c$ eq. 10a reduces to [28]: $k_{\text{int}} = \frac{2k_c\Delta\omega}{\omega_0}$

$$\gamma_{\text{int}} = \frac{F_0}{A(\omega_0 + \Delta\omega)} - \gamma_c \tag{10b}$$

Another way to characterize the dissipation in the system is by determining the dissipated energy per cycle E_{dis}. To do so the amplitude of the oscillating cantilever is kept constant by adjusting the driving force F, and E_{dis} is calculated using

$$E_{dis} = \int_0^T F v dt$$

resulting in [34]:

$$E_{dis} = \frac{\pi k_c A^2}{Q}\frac{F}{F_0} \tag{10c}$$

where F / F_0 is the relative change in driving force to keep the measured amplitude constant.

3.3.1c Acoustic Actuation

Acoustic driving is the most widely used actuation technique. In acoustic driving a small drive piezo at the back of the cantilever (Fig. 3.9(a)) is used to oscillate the cantilever. When using deflection detection modelling the system is not as straightforward as for magnetic driving. Since in deflection detection only the motion relative to the driving motion $d(t)$ is measured, the actual motion of the cantilever $z(t)$ can be significantly different from the measured signal (Compare Fig. 3.9(c) to 3.6(c)). This can be circumvented by using an interferometric detection setup, where the total motion of the cantilever is measured. (Although one still needs to be alert for the

spurious resonances characteristic for acoustic driving). When using interferometric detection the forces can be extracted using the equations given in Section 3.3.1c.

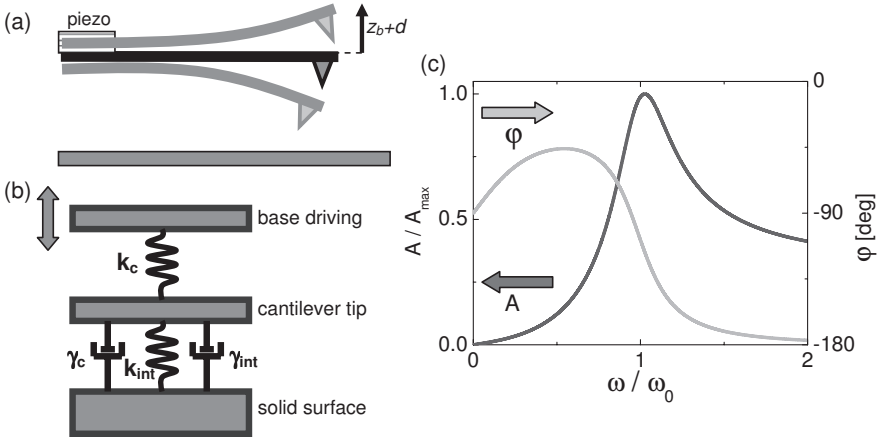

Figure 3.9 (a) In acoustic driving the deflection (for deflection detection) or the total motion (for interference detection) of the cantilever is monitored while it is driven with a small piezo at the backside (b) Spring-dashpot representation of acoustic actuation with deflection detection (c) Amplitude and phase response for acoustic driving and deflection detection for a typical AFM configuration in liquid without interactions.

For acoustic driving with deflection detection the equation of motion is given by:

$$m \cdot \ddot{z} + \gamma_{tot} \cdot \dot{z} + k_{tot} \cdot z = k_c \cdot z_d \tag{11}$$

where $k_{tot} = k_c + k_{\text{int}}$ and $\gamma_{tot} = \gamma_c + \gamma_{\text{int}}$ are the total stiffness and damping, respectively, while the measured deflection will be given by $d(t) = z(t) - z_d(t)$.
To find the measured amplitude and phase response we solve eq. 11 using the Ansatz $z(t) = A_{tot} \exp(i(\omega t + \psi_{tot})) = d(t) + z_d(t) = A\exp(i(\omega t + \varphi)) + A_d \exp(i\omega t)$, in which ω is the drive frequency, A and φ are the measured deflection amplitude and phase of the deflection *d(t)* and A_d is the amplitude of the base-motion (see e.g. [24]):

$$A = \frac{A_d \sqrt{\left(k_c - k_{tot} + m\omega^2\right)^2 + \left(\omega\gamma_{tot}\right)^2}}{\sqrt{\left(k_{tot} - m\omega^2\right)^2 + \left(\omega\gamma_{tot}\right)^2}} \tag{12a}$$

and:

$$\tan\varphi = \frac{-k_c\omega\gamma_{tot}}{k_c\left(-m\omega^2 + k_{tot}\right) - \left(-m\omega^2 + k_{tot}\right)^2 - \left(\omega\gamma_{tot}\right)^2} \tag{12b}$$

Note that the total amplitude A_{tot} of the tip motion, given by $A_{tot} = \sqrt{\left((A\sin\varphi)^2 + (A\cos\varphi + A_d)^2\right)}$, can be substantially different from the measured deflection amplitude A in eq. 4a. Please be warned: The linearization of eq. 2 is only justified when $A_{tot} << 2k_{\mathrm{int}} / k'_{\mathrm{int}}$ and $A_{tot} << 2\gamma_{\mathrm{int}} / \gamma'_{\mathrm{int}}$ [24]. Figure 3.9(c) shows the amplitude and phase spectra for a typical configuration in liquid without interactions. Note that Fig. 3.9(c) is significantly different from Fig. 3.6(c). Figure 3.9(c) shows that the amplitude reduces to zero for $\omega \rightarrow 0$ and a finite value for $\omega \rightarrow \infty$. Moreover the phase reduces again to -90° for $\omega \rightarrow 0$.

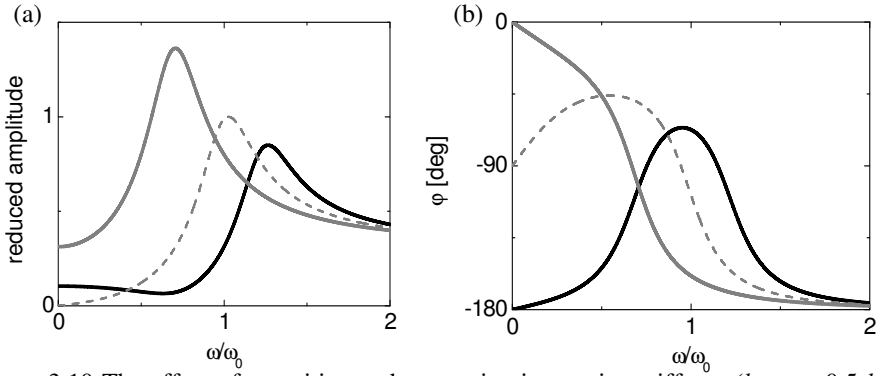

Figure 3.10 The effect of a positive and a negative interaction stiffness (k_{int} = + 0.5 k_{c} black and - 0.5 k_{c} gray) on the amplitude (a) and phase (b) spectra of the cantilever for acoustic driving using deflection detection.

Figure 3.10 shows how the amplitude and phase spectra of Fig. 3.9(c) are affected by a positive or negative interaction stiffness. Note that the amplitude for $\omega \rightarrow 0$ increases both for a negative and for a positive interaction stiffness. Moreover, the phase becomes extremely sensitive for variations of k_{int} at $\omega \rightarrow 0$.

Figure 3.11 shows the effect of an increasing interaction damping on the spectra. In contrast to the magnetically driven system the amplitude resonance frequency does not go down for an increasing damping. Again, the phase at low frequencies is very sensitive for variations in γ_{int}.

In order to extract the physical interaction forces from the calibration constants and the measured amplitude and phase response, we need to solve eq. 11 for the interaction stiffness k_{int} and damping γ_{int}, yielding [23, 24]:

$$k_{\mathrm{int}} = -k_c + m\omega^2 + \frac{k_c A_d\left(A_d + A\cos\varphi\right)}{A_d^2 + A^2 + 2A_d A\cos\varphi} \tag{13a}$$

and:

$$\gamma_{\text{int}} = \frac{-k_c A_d A \sin\varphi}{\omega\left(A_d^2 + A^2 + 2A_d A\cos\varphi\right)} - \gamma_c \tag{13b}$$

where A_d can be calculated from the measured free amplitude A far away from the surface (at e.g.10nm) using eq. 12a with the interactions set to zero.

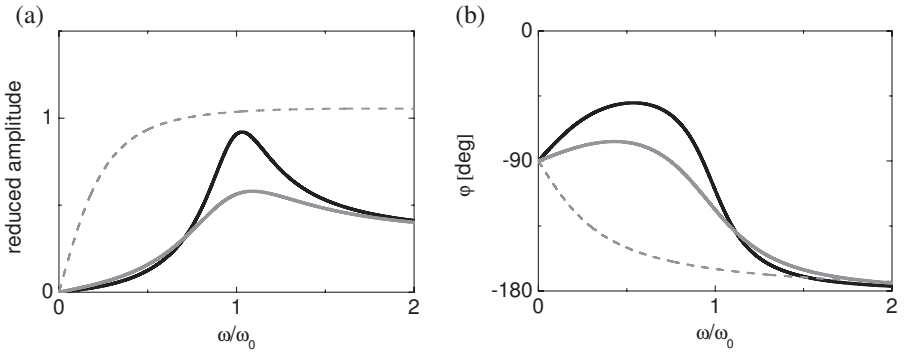

Figure 3.11 The effect in an increasing interaction damping (γ_{int} = 0.1γ_c black, 1γ_c gray and 10γ_c dashed) on the amplitude (a) and phase (b) spectra of the cantilever for acoustic driving using deflection detection.

To extract the interaction forces from the frequency shift and change in drive amplitude we can (as described above) use the same formulae as derived for AM AFM. When the phase is locked on -90°, eq. 13a and b reduce to:

$$k_{\text{int}} = -k_c + m\omega^2 + \frac{k_c {A_d}^2}{A_d^2 + A^2} \tag{14a}$$

and:

$$\gamma_{\text{int}} = \frac{k_c A_d A}{\omega\left(A_d^2 + A^2\right)} - \gamma_c \tag{14b}$$

3.3.2 Effect frequency dependent damping

In our derivations we assumed that the viscous damping γ_c and the total mass m due to the liquid surrounding the cantilever are constant. But is this assumption justified?
The interaction of a solid object oscillating in a viscous fluid does in fact depend on the frequency [35]. Following Sader [36], we describe the hydrodynamic loading on

the cantilever by a hydrodynamic function $\Gamma = \Gamma' + i\Gamma''$, which yields an added mass and a damping given by $m_{added} = m - m_{cant} = (\pi/4)\rho w^2 L\Gamma'$ and $\gamma_c = (\pi/4)\rho w^2 L\omega\Gamma''$ [32]. Here, ρ, w and L denote resp. the density of liquid, and the width and the length of the cantilever. Γ depends on the viscous penetration depth $\delta = \sqrt{2\eta/\rho\omega}$ (η: viscosity of the liquid) and the cantilever geometry as $\Gamma' = a_1 + a_2\delta/w$ and $\Gamma'' = b_1\delta/w + b_2(\delta/w)^2$ with a_1 = 1.0533, a_2 = 3.7997, b_1 = 3.8018 and b_2 = 2.736. With the calibration constants (k, Q, $\omega_{0,air}$ and $\omega_{0,liquid}$) applied at resonance, the frequency independent prefactor in both the frequency-dependent added mass and damping can be calculated.

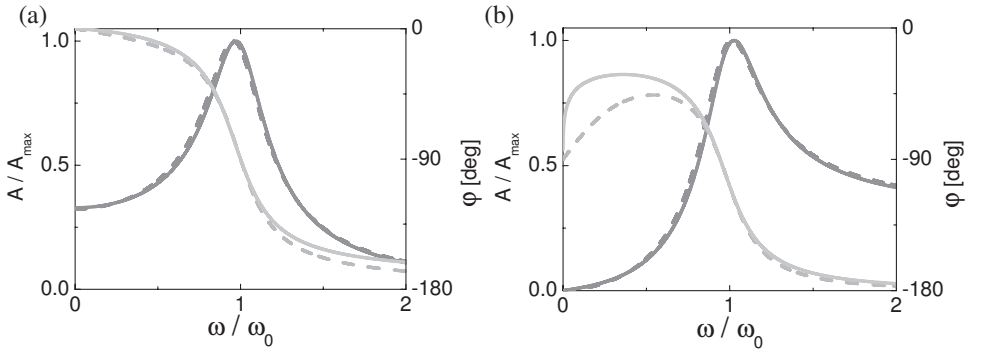

Figure 3.12 The effect of including a frequency dependent added mass and damping (dashed) on the spectra of a) a magnetically driven cantilever and b) an acoustically driven cantilever.

Figure 3.12(a) shows typical spectra for a *magnetically* driven cantilever in Octamethylcyclotetrasiloxane (spring constant k_c = 2 N/m, quality factor Q = 3, amplitude resonance frequency $f_{res} = 40kHz$, ρ = 956 kg/m^3, η = 22 mPas) calculated for a constant damping and added mass and for a frequency dependent damping and added mass (dashed). The amplitude response curves appear similar. But for the phase response above resonance some deviations occur. Since phase-offsets are known to cause cross-coupling between the extracted conservative and dissipative forces [23], these deviations can not be neglected. So, for a cantilever magnetically driven above resonance the frequency dependent added mass and damping need to be taken into account. Figure 3.12(b) shows the spectra for an *acoustically* driven cantilever (with the same properties as in Fig. 3.12(a)) and again calculated for a constant damping and added mass and for a frequency dependent damping and added mass (dashed). Once more, the amplitude response is the same in both situations. Nevertheless the phase response significantly deviates now below resonance. So, for a cantilever acoustically driven (using deflection detection) below resonance the frequency dependent added mass and damping definitely need to be taken into account. We would like to mark that the conclusions described above are only guidelines. To reduce systematic errors in your analysis it is always recommended to include the frequency dependent added

mass and damping in the equations for the amplitude, phase and force-inversion formulae described in the sections above.

3.4 Summary

In this chapter we have presented and discussed the different driving schemes and the resulting force inversion formulae for AM and FM small amplitude atomic force spectroscopy. We have shown that in liquid (low Q environment) the measured response of the cantilever strongly depends on the actuation and detection technique. Moreover, to avoid phase-errors a frequency dependent damping should be taken into account for the calculation of the calibration constant.
So, in order to extract the correct forces from our dynamic AFM measurements, we have to:

1) Determine our actuation and detection method
2) Find the accompanying force inversion formulae (depending on the actuation / detection method used)
3) Take into account the frequency dependent added mass and damping
4) Do a correct calibration (depending on the actuation / detection method used)
5) Shift the phase to the correct value (depending on the actuation / detection method used)

References:

[1] G. Binnig, F.C. Quate and Ch. Gerber, *Phys Rev Lett* **9**, 930 (1986)
[2] Marti, O. (1999), *AFM Instrumentation and Tips*, in Handbook of Micro/Nanotribology (B. Bhushan, eds), pp. 81-144, CRC Press, 2nd Edition.
[3] R. Garcia and R. Perez, *Surf. Sci. Reports* **47**, 197-301 (2002)
[4] Yasuhiro Sugawara, Naritaka Kobayashi, Masayo Kawakami, Yan Jun Li, Yoshitaka Naitoh, and Masami Kageshima, *Appl. Phys. Lett.* **90**, 194104 (2007)
[5] H. Hoelscher, A. Schwarz, W. Allers, U. D. Schwarz, and R. Wiesendanger, *Phys. Rev.* B **61**, 12678 (2000)
[6] T.R Albrecht, P Grutter, D. Horne, D. Rugar, *J. Appl. Phys.* **69**, 668 (1991)
[7] H. Ueyama, Y. Sugawara, S. Morita, *Appl. Phys.* A **66**, s295 (1998)
[8] Ch. Loppacher, M. Bammerlin, F. Battiston, M. Guggisberg, D. Müller, H.R. Hidber, R. Lüthi, E. Meyer, H.J. Güntherodt, *Appl. Phys.* A **66**, S215–S218 (1998)
[9] B.M. Borkent, S. de Beer, F. Mugele, D. Lohse, *Langmuir* **26**, 260-268 (2010)
[10] B. Anczykowski, J.P. Cleveland, D. Krueger, V. Elings, and H. Fuchs, *Appl. Phys. A: Mater. Sci. Process.* **66**, S885 (1998)
[11] D. Ebeling, H. Hoelscher, B. Anczykowski, *Appl. Phys. Lett.* **89**, 203511 (2006)
[12] H. Hoelscher, A Schirmeisen, *Dynamic Force Microscopy and Spectroscopy*, in ADVANCES IN IMAGING AND ELECTRON PHYSICS, VOL. 135 (2005)
[13] C.M. Mate, G.M. McClelland, R. Erlandsson, S. Chiang, *Phys. Rev. Lett.* **59**, 1942-1945 (1987)
[14] J.P. Cleveland, B. Anczykowski, A.E. Schmid, V.B. Elings, *Appl. Phys. Lett.* **72**, 2613-

2615 (1998)
[15] O. Sahin, S. Magonov, C. Su, C. F. Quate and O. Solgaard, *Nature Nanotechnology* **2**, 507 (2007)
[16] X. Xu, J. Melcher, S. Basak, R, Reifenberger and A. Raman, *Phys. Rev. Lett.* **102**, 060801 (2009)
[17] P. D. Ashby and C. M. Lieber, *J. Am. Chem. Soc.* **126**, 16973 (2004)
[18] H. Hoelscher, *Appl. Phys. Lett.* **89**, 123109 (2006)
[19] M. H. Lee and W. H. Jhe, *Phys. Rev. Lett.* **97**, 036104 (2006)
[20] S. Q. Hu and A. Raman, *Nanotechnology* **19**, 375704 (2008)
[21] A. J. Katan, M. H. van Es and T. H. Oosterkamp, *Nanotechnology* **20**, 165703 (2009)
[22] S. J. O'Shea and M. E. Welland, *Langmuir* **14**, 4186 (1998)
[23] C. Jai, T. Cohen-Bouhacina and A. Maali, *Appl. Phys. Lett.* **90,** 113512 (2007)
[24] S. de Beer, D. van den Ende, F. Mugele, *Nanotechnology* **21**, 325703 (2010)
[25] R. Lim, S.F.Y. Li, S.J. O'Shea, *Langmuir* **18**, 6116 (2002)
[26] D. Ebeling and H. Hoelscher, *J. Appl. Phys.* **102**, 114310 (2007)
[27] J. E. Sader and S. P. Jarvis, *Appl. Phys. Lett.* **84**, 1803 (2004)
[28] F.J. Giessibl, *Rev. Mod. Phys.* **75**, 949 (2003)
[29] J. L. Hutter and J. Bechhoefer, *Rev. Sci. Instrum.* **64**, 1868 (1993)
[30] Veeco Application note: *Practical Advice on the Determination of Cantilever Spring Constants*, Ben Ohler (2007)
[31] A Maali, C Hurth and T Cohen-Bouhacina, *Appl. Phys. Lett.* **88**, 163504 (2006)
[32] N.A. Burnham, G. Gremaud, A.J. Kulik, P.-J. Gallo and F. Oulevay, *J. Vac. Sci. Technol.* B **14**, 1308-1312 (1996)
[33] A. Maali, T. Cohen-Bouhacina, G. Couturier and J.-P. Aimé, *Phys. Rev. Lett.* **96**, 086105 (2006)
[34] W. Hofbauer, R.J. Ho, R. Hairulnizam, N.N. Gosvami, S.J. O'Shea, *Phys. Rev.* B **80**, 134104 (2009)
[35] L. Landau and F. Lifshitz, *Fluid Mechanics*, Theoretical Physics Vol.6 (Mir, Moscow, 1971)
[36] J. E. Sader, *J. Appl. Phys* **84**, 64 (1998)
[37] A. Maali, C. Hurth, R. Boisgard, C. Jai, T. Cohen-Bouhacina and J.-P. Aime, *J. Appl. Phys.* **97**, 074907 (2005)

Appendix 3A

To find the interaction stiffness k_{int} and damping γ_{int} for a sample modulation setup we solve the equation of motion:

$$m \cdot \ddot{z} + \gamma_c \cdot \dot{z} + k_c \cdot z = k_{\text{int}}(d - z) + \gamma_{\text{int}}(\dot{d} - \dot{z}) \tag{A1}$$

We use the ansatz $z_d = A_d e^{i\omega t}$, $z = Ae^{i\varphi} e^{i\omega t}$ and obtain:

$$\left(k_{tot} - m\omega^2 + i\gamma_{tot}\omega\right)A(\cos\varphi + i\sin\varphi) = \left(k_{\text{int}} + i\gamma_{\text{int}}\omega\right)A_d \tag{A2}$$

where $k_{tot} = k_c + k_{\text{int}}$ and $\gamma_{tot} = \gamma_c + \gamma_{\text{int}}$ are the total stiffness and damping, respectively. With:

$$\begin{aligned} K &= k_{tot} - m\omega^2 \qquad & \Gamma &= \gamma_{tot}\omega \\ K_c &= k_c - m\omega^2 \qquad & \Gamma_c &= \gamma_c\omega \end{aligned} \tag{A3}$$

We express k_{int} and γ_{int} as:

$$k_{\text{int}} = K - K_c \qquad \gamma_{\text{int}} = (\Gamma - \Gamma_c)/\omega \tag{A4}$$

To derive equations for k_{int} and γ_{int}, we solve for K and Γ:

$$\frac{z}{z_d} = H(\cos\varphi + i\sin\varphi) = \frac{k_{\text{int}} + i\gamma_{\text{int}}\omega}{k_{tot} - m + i\gamma_{tot}\omega} = \frac{(K - K_c) + i(\Gamma - \Gamma_c)}{K + i\Gamma} \tag{A5}$$

With:

$$H = A/A_d \tag{A6}$$

Hence

$$\begin{aligned} H\cos\varphi + iH\sin\varphi &= \frac{\left((K - K_c) + i(\Gamma - \Gamma_c)\right) - (K - i\Gamma)}{K^2 + \Gamma^2} \\ &= 1 - \frac{KK_c + \Gamma\Gamma_c}{K^2 + \Gamma^2} + i\frac{\Gamma K_c - K\Gamma_c}{K^2 + \Gamma^2} \end{aligned} \tag{A7}$$

Or

$$\begin{aligned} \frac{KK_c + \Gamma\Gamma_c}{K^2 + \Gamma^2} &= 1 - H\cos\varphi \\ \frac{\Gamma K_c - K\Gamma_c}{K^2 + \Gamma^2} &= H\sin\varphi \end{aligned} \tag{A8}$$

The set of equations in A8 are quadratic in K and Γ but linear in:

$$\tilde{K} = \frac{K}{K^2 + \Gamma^2}$$
$$\tilde{\Gamma} = \frac{\Gamma}{K^2 + \Gamma^2} \tag{A9}$$

So one obtains:

$$\begin{pmatrix} K_c & \Gamma_c \\ -\Gamma_c & K_c \end{pmatrix} \begin{pmatrix} \tilde{K} \\ \tilde{\Gamma} \end{pmatrix} = \begin{pmatrix} 1 - H\cos\varphi \\ H\sin\varphi \end{pmatrix} \tag{A10}$$

Inversion of A10 results in:

$$\begin{pmatrix} \tilde{K} \\ \tilde{\Gamma} \end{pmatrix} = \begin{pmatrix} \tilde{K}_c & -\tilde{\Gamma}_c \\ \tilde{\Gamma}_c & \tilde{K}_c \end{pmatrix} \begin{pmatrix} 1 - H\cos\varphi \\ H\sin\varphi \end{pmatrix} \tag{A11}$$

Where,

$$\tilde{K}_c = \frac{K_c}{{K_c}^2 + {\Gamma_c}^2}$$
$$\tilde{\Gamma}_c = \frac{\Gamma_c}{{K_c}^2 + {\Gamma_c}^2} \tag{A12}$$

From A11 one obtains:

$$\tilde{K} = \tilde{K}_c\left(1 - H\cos\varphi\right) - \tilde{\Gamma}_c H\sin\varphi$$
$$\tilde{\Gamma} = \tilde{\Gamma}_c\left(1 - H\cos\varphi\right) + \tilde{K}_c H\sin\varphi \tag{A13}$$

Using A9 and A12 or the inverse transformations:

$$K = \frac{\tilde{K}}{\tilde{K}^2 + \tilde{\Gamma}^2}$$
$$\Gamma = \frac{\tilde{\Gamma}}{\tilde{K}^2 + \tilde{\Gamma}^2} \tag{A14}$$

we rewrite A13 into:

$$K = \frac{K_c\left(1 - H\cos\varphi\right) - \Gamma_c\left(H\sin\varphi\right)}{\left(1 - H\cos\varphi\right)^2 + \left(H\sin\varphi\right)^2}$$
$$\Gamma = \frac{\Gamma_c\left(1 - H\cos\varphi\right) + K_c\left(H\sin\varphi\right)}{\left(1 - H\cos\varphi\right)^2 + \left(H\sin\varphi\right)^2} \tag{A15}$$

Now we know K and Γ, we use A4 to eventually obtain:

$$k_{\text{int}} = K - K_c = \frac{K_c(1 - H\cos\varphi) - \Gamma_c(H\sin\varphi)}{(1 - H\cos\varphi)^2 + (H\sin\varphi)^2} - K_c$$
$$\gamma_{\text{int}} = (\Gamma - \Gamma_c)/\omega = \left(\frac{\Gamma_c(1 - H\cos\varphi) + K_c(H\sin\varphi)}{(1 - H\cos\varphi)^2 + (H\sin\varphi)^2} - \Gamma_c \right) / \omega \qquad \text{(A16)}$$

Using A3 and A6 we obtain the results of eq. 5a and b:

$$k_{\text{int}} = -k_c + m\omega^2 + \frac{\left(k_c - m\omega^2\right)\left(1 - \frac{A}{A_d}\cos\varphi\right) - \gamma_c\omega\frac{A}{A_d}\sin\varphi}{\left(1 - \frac{A}{A_d}\cos\varphi\right)^2 + \left(\frac{A}{A_d}\sin\varphi\right)^2}$$

and

$$\gamma_{\text{int}} = -\gamma_c + \frac{\gamma_c\omega\left(1 - \frac{A}{A_d}\cos\varphi\right) + \left(k_c - m\omega^2\right)\frac{A}{A_d}\sin\varphi}{\omega\left(\left(1 - \frac{A}{A_d}\cos\varphi\right)^2 + \left(\frac{A}{A_d}\sin\varphi\right)^2\right)}$$

Chapter 4

Acoustically driven cantilever dynamics in the presence of tip sample interaction

In Chapter 3 we have shown that the observed dynamic response of an Atomic Force Microscope (AFM) cantilever depends on the actuation and detection technique. In this chapter we describe an effect for the specific (however, most frequently used) setup of acoustic driving with deflection detection. We show that – in contrast to the general belief – the cantilever's phase response is extremely sensitive to variations in the conservative tip-sample interactions.[1]

[1] This chapter has been published as: S. de Beer, D. van den Ende & F. Mugele, *Appl. Phys. Lett.* **93**, 253106 (2008).

4.1 Introduction

Atomic Force Microscopy (AFM) is more and more evolving from a pure imaging technique to a tool for measuring quantitative tip-sample interaction forces. While experiments performed in vacuum and air played a dominant role in earlier stages, research fields such as soft matter science, biology, and nanofluidics generate an increasing demand for quantitative atomic force spectroscopy techniques operating in liquid environments in recent years. Hydrodynamic damping of the cantilever motion due to the ambient liquid, however, dramatically reduces the cantilevers quality factor and thereby poses a challenge to quantitative AFM spectroscopy. In particular, established methods for extracting conservative and dissipative tip-sample interaction forces from the cantilever oscillation dynamics either require low damping [1-3] and thus can not be readily adopted. For instance, it has been pointed out that the motion of the base of the cantilever (which is negligible in air or vacuum) has to taken into account in a proper description of acoustically driven AFM cantilevers in liquid [4-6]. However, the consequences of this effect for the quantitative analysis of the cantilever dynamics in the presence of tip-sample interaction forces have not been explored so far.

In this chapter we present a harmonic oscillator model which includes explicitly the finite amplitude of the base movement and includes the effect of tip-sample interactions. We compare the frequency-dependent amplitude and phase response of the model to measurements of oscillatory solvation forces due to molecular layering [7]. These forces were measured in Octamethylcyclotetrasiloxane (OMCTS), a non-polar quasi-spherical model liquid, at various frequencies close to and below resonance. For an AFM setup with acoustic driving and beam deflection detection both the experiments as well as the analytical solution to the model display a strong phase-response in the cantilever dynamics for low frequencies.

4.2 Materials and Methods

The measurements described in this chapter were performed on a Veeco Multimode with Nanoscope V controller equipped with a very stable small piezo scanner ("A scanner") using long rectangular gold coated cantilevers (Mikromasch) with a nominal spring constant of
k_c = 3 N/m and a resonance frequency of $f \approx 90$ kHz in air. Prior to the measurements the cantilevers were cleaned in a plasma-cleaner for 30 minutes and after the measurements the tip was characterized using high resolution SEM imaging (yielding a tip radius $R_{tip} = 50nm$). Acoustic driving was realized using an adapted cantilever holder, as described in ref. [8], which reduces spurious resonances characteristic of the conventional commercial liquid cell. The spring constant was determined in air using the thermal calibration method, as first described by Hutter [9]. The resonance frequency (f_0 = 43±1kHz) and quality factor Q (3.1 ± 0.5) in liquid were determined

with the same method, 100nm above the sample surface, for a correct characterization of the added mass of the system. The OMCTS used in the measurements was dried using 4 Å molecular sieves. The highly oriented pyrolitic graphite (HOPG) was freshly cleaved just before depositing the OMCTS on the surface.

4.3 Experimental results

Figure 4.1 shows the measured Amplitude and Phase Distance curves for 3 different drive frequencies close to and well below the cantilever resonance ($\omega_0 = \sqrt{k_c / m}$, with *m* being the effective mass) upon approaching the HOPG surface. Far away from the surface the amplitude and phase response are constant. (The absolute value of the phase far away from the surface is shifted such in accordance with Fig. 4.3(b); see below.) At a distance of 5 to 6 nm the response changes due to the tip-sample interaction. For a driving frequency ω close to resonance (top panel) both amplitude and phase display clear modulations due to the oscillating tip-sample interaction. The periodicity of these oscillations (≈0.76nm) reflects the molecular size of OMCTS (0.9nm), as reported before by others [10-13]. The oscillations are superimposed on an overall decrease in amplitude, as usual. The curves shown in the middle panel were measured at an intermediate drive frequency on the wing of the resonance peak. Compared to the top panel, the oscillations are more pronounced in the amplitude and less pronounced in the phase. All these observations expected from the standard harmonic oscillator model: for $\omega \approx \omega_0$, the amplitude is close to its maximum and hence not very sensitive to small shifts of the resonance curve (as induced by the tip-sample interaction), whereas the variation of the phase is maximum [14]. If ω is chosen on the wing of the resonance peak, the sensitivity of the amplitude becomes maximized whereas the phase sensitivity continuously decreases (see also the thin gray lines in Fig. 4.3(a) and (b)). However for $\omega << \omega_0$ (bottom panel) we find substantial deviations from the standard picture: first, we observe an overall increase of the amplitude upon approaching the surface. Second, the periodicity in the amplitude oscillations doubles at separations below 2nm. Third – and most strikingly – the oscillations in the phase become more pronounced again – even more pronounced than at $\omega \approx \omega_0$. These observations have important consequences for the quantitative interpretation of amplitude-force-distance curves.

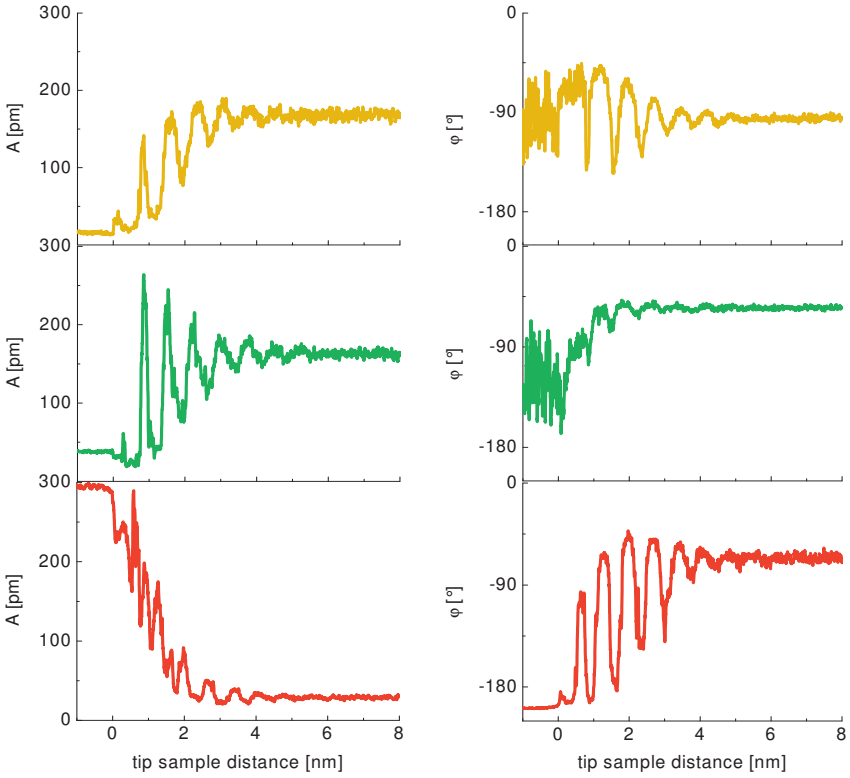

Figure 4.1 Amplitude and Phase of the AFM-cantilever versus separation between the solid HOPG surface and the cantilever-tip for different drive frequencies (top / yellow 41kHz (ω/ω_o=0.95), middle / green 32kHz (ω/ω_o=0.75) and bottom / red 6kHz (ω/ω_o=0.15)) relative to resonance (43kHz). The periodicity of the oscillations reflects the size of the molecules (Octamethyltetrasiloxane).

4.4 Model results

Figure 4.2(a) shows the schematic representation of the cantilever and its motion, which we treat within the harmonic oscillator approximation. As will become clear in the following, our observations are caused by a combination of two – in principle well-known – effects:

In a highly damping environment (i.e. for low Q) the dynamics of an acoustically driven cantilever can only be understood by properly including the base motion z_d. (This is in contrast to magnetically driven cantilevers, where the measured motion is the only motion. [10,13])

Beam deflection systems measure the deflection x of the cantilever with respect to the position z_d of the base and not with respect to the average position z_c. (This implies immediately that the amplitude measured via beam deflection goes to zero for $\omega \to 0$, in contrast e.g. to an interferometric detection system [11]; see also Fig. 4.3.)

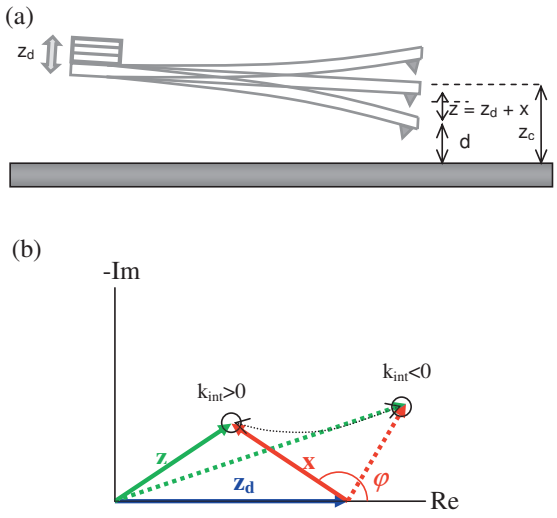

Figure 4.2 (a) Scheme of the cantilever dynamics, which can is described by a simple harmonic oscillator including the base-motion. In (b) the difference between the drive signal z_d (blue), the motion of the cantilever z (green) and the measured deflection x (red) is drawn. The solid lines show the response for a positive interaction stiffness and the dashed lines for a negative stiffness. The measured amplitude is the length of the vector x and the phase is the angle between the Re-axis and the vector x.

Including the motion of the cantilever base z_d results in the following equation of motion for the cantilever:

$$m \cdot \ddot{z} + \gamma_c \cdot \dot{z} + k_c \cdot z = k_c \cdot z_d + F_{ts}, \qquad (1)$$

where γ_c is the damping of the cantilever, k_c is the spring constant and m is the effective mass of cantilever including the added mass caused by the motion of the surrounding liquid ($\omega_0 = \sqrt{k_c / m}$). Far away from the surface ($d \geq 6nm$, in the present experiments) F_{ts} is zero. For smaller d, F_{ts} is finite and changes the resonance behavior of the system. For sufficiently small cantilever amplitude, F_{ts} can be linearized to $F_{ts}(z,\dot{z}) = F_{ts}(z_c,0) - k_{\text{int}}(z_c)z + -\gamma_{\text{int}}(z_c)\dot{z}$.

Using the ansatz that z is described by $z = x + z_d = Ae^{i(\omega t+\varphi)} + A_d e^{i\omega t}$, where A and φ are the amplitude and phase measured in the experiments, A_d is the amplitude of the driving mechanism and ω is the drive frequency, equation (1) can be solved for A and φ:

$$A = \frac{A_d\sqrt{\left(k_c - k_t + m\omega^2\right)^2 + \left(\omega\gamma_t\right)^2}}{\sqrt{\left(k_t - m\omega^2\right)^2 + \left(\omega\gamma_t\right)^2}} \approx \frac{|k_{\text{int}}|}{k_t}A_d \tag{2a}$$

and:

$$\tan\varphi = \frac{-k_c\omega\gamma_t}{k_c\left(-m\omega^2 + k_t\right) - \left(-m\omega^2 + k_t\right)^2 - \left(\omega\gamma_t\right)^2} \approx \frac{\omega\gamma_t}{k_{\text{int}}(1 + k_{\text{int}}/k_c)}, \tag{2b}$$

where the approximations hold for $\omega << \omega_0$. $k_t = k_c + k_{\text{int}}$ and $\gamma_t = \gamma_c + \gamma_{\text{int}}$ are the total stiffness and damping, respectively.

Figures 4.3(a) and (b) show the calculated amplitude and phase spectra for the cantilever used in the experiments. In the absence of tip-sample interaction, the curves are similar to those calculated by others, displaying in particular a decrease of the amplitude to zero [5,6] and a reduction of the phase to -90° for $\omega \to 0$ [4]. It is particularly interesting to analyze the behavior of the curves in the presence of a finite tip-sample interaction, as shown here for two examples with a positive and negative interaction stiffness of $+0.1k_c$ and $-0.1k_c$, respectively. In line with the asymptotic expressions in eq. (2), the phase becomes increasingly sensitive to variations of k_{int} for $\omega \to 0$. This explains the experimental behavior of the phase shown in Fig. 4.1: for the oscillatory tip-sample interaction due to the confined OMCTS, the interaction stiffness varies between positive and negative values and thereby gives rise to dramatic oscillations of the phase. The physical origin of this behavior becomes clear from Fig. 4.2(b), where we indicate the position of the cantilever base z_d and the tip z in the complex plane. As explained above, the quantity measured by beam deflection in an acoustically driven AFM is the cantilever deflection, i.e. the difference vector $x = z - z_d$. For low frequencies, the tip displacement z (which is correctly described by the standard harmonic oscillator; dotted lines in Fig. 4.3(a) and (b)) displays very little variation in the phase but a finite amplitude variation (as a function of F_{ts}). As a consequence, the phase of the difference-vector varies a lot, as found in the experiments. Figure 4.2(b) also shows why the periodicity in the low frequency amplitude response doubles in Fig. 4.1: when the interaction stiffness varies back and forth between a positive and a negative value, z moves along the trajectory in the complex plane that is indicated by the dotted line. The measured amplitude of the difference vector x, however, displays twice as many maxima and minima – in agreement with the asymptotic expression in eq. (2). Finally, Figure 4.3(c) shows an experimental frequency response curve measured far away from the surface together with a thermal noise spectrum. While the response curves display several spurious resonances at $\omega > \omega_0$ (which are related to the usual resonances in the driving piezo [8]), the low frequency behavior corresponds nicely with the model curves shown in

Fig. 4.3(a) and (b). In particular, the phase displays the marked decrease that the model predicts for $\omega \to 0$.

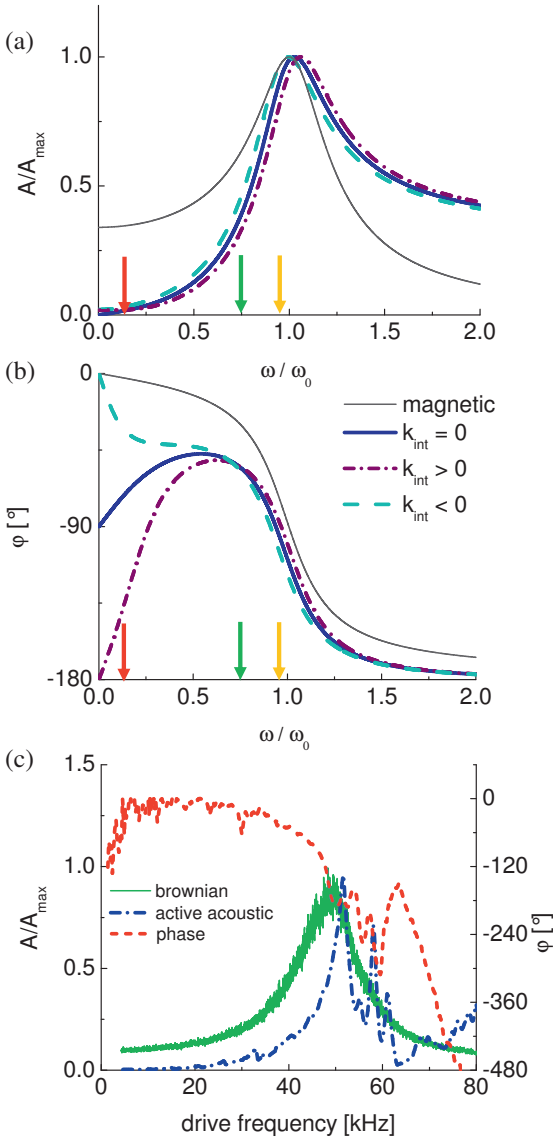

Figure 4.3 Amplitude and phase versus frequency. (a) and (b): thick lines: calculated model curves following eqns. (2a) and (2b) for variable interaction stiffness $k_{int} = 0, \pm 0.1\ k_c$ (at $\gamma_{int} = 0$) thin dotted lines: standard harmonic oscillator model. Colored arrows indicate the drive frequencies for the data in Fig. 4.1. (c) Measured amplitude and phase response as well as thermal response vs. frequency. (k_c = 3.7 N/m and the resonance frequencies is f = 49 kHz). The spurious peaks above resonance are due to the response of the drive-piezo.

4.5 Summary

In summary we have shown that the combination of beam deflection detection and acoustic driving gives rise to a very strong sensitivity of the cantilever's phase to the tip-sample interaction for low driving frequencies. The effects described here are relevant for any experiment attempting to measure quantitative tip-sample interaction forces, including non-oscillatory ones, in low Q environments with an AFM that makes use of this (by far most widely spread) design. The consequences of the present observations for quantitative force inversion procedures will be reported in Chapter 5.

Acknowledgement

We thank A. Maali for his assistance during the early stages of the experiment and we thank K. Smit and P. Markus (Veeco) for the technical support. This work has been supported by the Foundation for Fundamental research on Matter (FOM), which is financially supported by the Netherlands Organization for Scientific Research (NWO).

References

[1] H. Hoelscher, *Appl. Phys. Lett.* **89**, 123109 (2006)
[2] A.J. Katan, PhD thesis, Leiden (2007)
[3] F. J. Giessibl, *Phys. Rev.* B **56**, 16010 (1997)
[4] X. Xu and A. Raman, *J. Appl. Phys.* **102**, 034303 (2007)
[5] E. T. Herruzo and R. Garcia, *Appl. Phys. Lett.* **91**, 143113 (2007)
[6] C. Jai, T. Cohen-Bouhacina and A. Maali, *Appl. Phys. Lett.* **90**, 113512 (2007)
[7] J. N. Israelachvili, Academic Press London (1991).
[8] A. Maali, C. Hurth and T. Cohen-Bouhacina, *Appl. Phys. Lett.* **88**, 163504 (2006)
[9] J. L. Hutter and J. Bechhoefer, *Rev. Sci. Instrum.* **64**, 1868 (1993)
[10] W. H. Han and S. M. Lindsay, *Appl. Phys. Lett.* **72**, 1656-1658 (1998)
[11] S. Patil, G. Matei, A. Oral and P. M. Hoffmann, *Langmuir* **22**, 6485-6488 (2006)
[12] R. Lim, S. F. Y. Li and S. J. O'Shea, *Langmuir* **18**, 6116-6124 (2002)
[13] J. E. Sader, T. Uchihashi, M. J. Higgins, A. Farrell, Y. Nakayama and S. P. Jarvis, *Nanotechnology* **16**, S94-S101 (2005)
[14] R. Garcia and R. Perez, *Surf. Sci. Reports* **47**, 197-301 (2002)

Chapter 5

Oscillatory solvation forces measured with acoustic actuation

In this chapter we elaborate on the work presented Chapter 4. While in Chapter 4 we presented and discussed the model to describe the cantilever dynamics for acoustic actuation and deflection detection, we now address both the technical question of obtaining reliable tip-sample interaction forces from small amplitude, Amplitude-Modulation Atomic Force Microscopy (AM-AFM) measurements and the physical question regarding the effect of confinement on the stiffness and dissipation in confined layers of octamethylcyclotetrasiloxane (OMCTS).[1]

To do so, we measure and model the response curve of the AFM cantilever as a function of the drive frequency incorporating (in addition to the motion of the cantilever base which was already discussed in Chapter 4) the frequency-dependent

[1] This chapter has been published as: S. de Beer, D. van den Ende & F. Mugele, *Nanotechnology* **21**, 325703 (2010).

added mass and dissipation of the cantilever. Subsequently, we measure the amplitude-phase-distance (APD) curves over a wide range of driving frequencies and extract the corresponding conservative and dissipative tip-sample interaction forces. Eliminating the effect of finite drive amplitudes, we obtain consistent conservative tip-sample interactions over the entire range of drive frequencies. The corresponding dissipative tip-sample forces display peaks at tip-surface distances corresponding to the expulsion of the last two molecular layers. The physical origin of (apparent) superimposed oscillations observed at certain drive frequencies is discussed analyzing the relative strength of various contributions to the cantilever damping. We identify an upper limit for the possible confinement-induced enhancement of the effective viscosity.

5.1 Introduction

The properties of liquids confined between solid surfaces are crucial for understanding numerous technological problems including lubrication and nanotribology, porous media and nanofluidic devices for biotechnological applications [1]. The key question is to what extent macroscopic continuum physics – in particular hydrodynamics – can be applied to describe the systems at such small scales and, if not, how deviations from the macroscopic behaviour manifest themselves.
It is by now well established that the structure of the liquid is altered close to the solid-liquid interface is such a way that the liquid molecules assume a layer structure parallel to the interface. This gives rise to oscillations in the average density and to (conservative) oscillatory solvation forces upon confining the liquid between two solid surfaces [2]. In addition to this structuring, some studies also report a strongly increased dissipation and in some cases even solid-like friction for liquid films with a thickness of several molecular layers [3, 4]. In contrast other studies find essentially bulk-like viscous dissipation, except for the molecular layers directly adjacent to the solid, which behave more rigidly [5,6]. According to molecular simulations both solidification and liquid-like behaviour can be achieved, depending on the interaction potentials between the solid and the liquid. While most simulations focused on equilibrium properties and the resulting conservative forces, Gao and Landman [7] also reported that the diffusivity in confined liquids is maximum for surface separations corresponding to a non-integer number of molecular layers corresponding to states with a reduced density. The fluctuation-dissipation theorem – if applicable to these systems – then suggests periodic variations in the (viscous) dissipation for strongly layered liquids.
Do such periodic variations exist? A number of recent Atomic Force Microscopy (AFM) experiments addressed this question using various measurement techniques, including conventional amplitude modulation (AM)-AFM and frequency-modulation (FM)-AFM and different driving schemes (acoustic/base drive vs. magnetic drive). While studies using the acoustic scheme [8, 9] reported oscillations in the dissipation, a continuous increase by several orders of magnitude was reported in the magnetically driven systems [10, 11]. (Very recently a sharply peaked and periodic dissipation was

also reported in a very careful experiment using the magnetic scheme [12].) Thus, even for simple (Lennard Jones-like) model systems, such as the most widely used Octamethylcyclotetrasiloxane (OMCTS), the question how confinement affects dissipation has yet to be answered.
From a technical perspective, the acoustic driving scheme in AFM is frequently criticized for its known sensitivity to experimental and modelling errors (see [13] in the present context). Yet, AFM cantilevers driven at sufficiently small amplitudes are known to behave as harmonic oscillators and are therefore in principle straightforward to model. This rises the – given the dominance of acoustically driven AFMs: important – technical question under which conditions and to what extent reliable interaction forces can be extracted from AM-AFM measurements. Despite the fact that the relevance of taking into account the motion of the cantilever base has been known for a long time [14], it was noticed only recently (see Chapter 4) that the acoustic driving scheme gives rise to a particularly strong phase response at *low* driving frequencies, which offers the potential of an increased sensitivity.

5.2 Materials and Methods

5.2.1 Materials

Amplitude-phase distance (APD) curves were measured in Octamethylcyclotetrasiloxane (OMCTS purum, ≥ 99.0%, Sigma Aldrich), a non-polar liquid of slightly spheroid molecules with a major diameter of 1.0-1.1 nm and a minor diameter of 0.7-0.8 nm, which is known to display pronounced layering when confined between two solid surfaces [2-11,15]. To minimize the detrimental effect of residual water [16] we dried the liquid using 4 Å molecular sieves (Sigma Aldrich) for several days prior to the measurement. To test whether water-contamination influenced our results, we repeated the measurements in a closed chamber with a dry nitrogen atmosphere, which gave the same results (within the experimental error). As a substrate hydrophobic Highly Ordered Pyrolytic Graphite (HOPG, Mikromasch grade ZYA) was used, which was cleaved using adhesive tape just prior to the deposition of the liquid (OMCTS). Before each spectroscopy experiment, the freshly cleaved HOPG substrate was imaged in the liquid to ensure that the surface was clean and atomically smooth and that the system was stable.

5.2.2 AFM measurements

The measurements were performed on a commercial Veeco Multimode with Nanoscope V controller equipped with a low-noise head using deflection detection and a stable small piezo scanner (“Veeco A scanner”). We used rectangular cantilevers (Mikromasch NSC36, manufactured of bare silicon or gold coated silicon) with

various stiffnesses of k_c = 3-7 N/m and resonance frequencies of $f \approx$ 80-120 kHz (in air), as determined using the thermal calibration method [17, 18]. The resonance frequency ($f \approx$ 30-60 kHz) and quality factor Q (~ 3) in liquid were determined with the same method at a reference distance of 100nm above the sample surface (with a relative uncertainty of < 5%). The specific cantilevers were chosen for their long tip-height (h ~ 25 μm), in order to minimize the change in hydrodynamic squeeze-out damping between the cantilever and the solid surface. We verified that possible variations of the added mass and hydrodynamic damping of the cantilever were below the detection limit between the reference distance and 10nm above the surface. Prior to the measurements the cantilevers were treated in a plasma-cleaner (Harrick Plasma) for 1 minute. After the measurements the tip was imaged using high resolution SEM (HR- SEM Zeiss LEO 1550) yielding tip radii of R_{tip} = 15 – 30 nm. The cantilever oscillation was driven at the base using a modified Tapping holder (Veeco MMMC), as described in ref. [19]. This yields stable drive amplitudes for several hours and reduces the spurious resonance peaks that are typical of commercial liquid cells.
APD curves including the average (Tapping mode, TM) deflection signal were recorded over 10nm tip surface distance for variable free oscillation amplitudes and drive frequencies from 0.07 to 0.5 nm at large distance (corresponding to peak-to-peak amplitudes of 0.14 to 1 nm) and 5…60 kHz, respectively. For each setting a minimum of 25 measurement curves were recorded and analyzed. The deflection signal in contact with the substrate was used to calibrate the deflection signal, which is appropriate for both static and dynamic deflection since we use small cantilevers compared the size of the laser-spot [20] (see also Fig. 1 Appendix 5.A). Thanks to the small drive amplitudes, no higher harmonics were generated within the (Brownian) noise limit of our system, as verified using a spectrum analyzer.
Typically, all APD curves in a set of measurements displayed several oscillations in the amplitude and phase response (see also section 5.4.1) over a period of several hours. Cantilevers that did not display this stability (e.g. due to a bad tip or contamination) were discarded. Test measurements did not display any significant dependence of the results on the approach speed within a range of 1 and 10 nm/s. Therefore a convenient standard approach speed between 1-2 nm/s was chosen for all the experimental data presented here. The drift normal to the surface was typically 0.08 ± 0.03 nm/s, as determined from the change in z piezo voltage at tip-surface contact. All measurements were performed at a room-temperature of 22±1°C. The temperature next to the sample was measured to be 27°C, presumably due to local heating from the electronics in the AFM head.

5.2.3 Numerical calculations

We simulated the dynamics of the AFM cantilever numerically using the approach of Garcia and Perez [21]. The programs for the simulations were written and run in Matlab based on the code used in ref. [22]. The ordinary differential equation for the cantilever dynamics including the tip-sample forces (see below) was solved using a 4th

order Runge-Kutta scheme. Numerical APD curves for various drive amplitudes were calculated starting 10 nm above the sample surface down to 1 nm in 250 discrete steps. At each step, the steady state amplitude and phase of the oscillation were extracted from the oscillatory cantilever motion via a Fast Fourier Transform. For fitting and validation purposes, the resulting numerical amplitude and phase versus distance curves were converted into a distance-dependent stiffness using the same force inversion formulae (to be described in section 5.3) as for the experimental data.

5.3 Cantilever dynamics and Force inversion

Over more then a decade many methods have been developed to quantitatively map both the conservative as dissipative interaction forces in dynamic AFM based on different methods and techniques, varying from small [14] to large amplitude [23] AFM as well as universal methods for both amplitude modulation (AM) [24-26] as frequency modulation (FM) AFM [27]. In our measurements we used AM small amplitude spectroscopy.
For typical base-driven atomic force microscopes the vertical motion $z(t)$ of the cantilever tip can be modelled as a harmonic oscillator affected by the tip-sample interactions F_{ts}:

$$m \cdot \ddot{z} + \gamma_c \cdot \dot{z} + k_c \cdot z = k_c \cdot z_b + F_{ts} \tag{1}$$

Here, k_c is the cantilevers spring constant, z_b (t) describes the displacement of the cantilever base, m is the total effective mass (including the added mass caused by the motion of the surrounding liquid), and γ_c is the viscous damping around the cantilever. The usual deflection detection scheme measures the deflection $d(t)$ of the cantilever, which is related to the vertical tip position by $z(t) = d(t) + z_b(t)$ (see also Fig. 5.1). Since the quality factor Q is low in a liquid environment, both $d(t)$) and $z_b(t)$ can be comparable (see e.g. [14]). In particular for driving frequencies off resonance the absolute motion of the tip with respect to the sample surface can be significantly larger than the measured deflection amplitude, which has important consequences for the amplitude and phase response of the cantilever (see also [15, 28]).
Since we use for our measurements very small amplitudes (much smaller than the characteristic length-scale of the changes in the interactions), we can linearize the tip-sample force F_{ts} around the (quasi-statically moved) average cantilever position z_c. Taylor expansion of F_{ts} yields:

$$F_{ts}(z_c + z, \dot{z}) = F_{ts}(z_c, 0) - k_{\text{int}} z - \gamma_{\text{int}} \dot{z} - \frac{1}{2} k'_{\text{int}} z^2 - \gamma'_{\text{int}} z\dot{z} + H.O.T. \tag{2}$$

where H.O.T. are the Higher Order Terms, $k_{\text{int}} = dF_{ts}/dz$ is the interaction stiffness, γ_{int} is the interaction damping (see Fig. 5.1) and $F_{ts}(z_c,0)$ is the equilibrium force on the cantilever, which shows up in the average deflection.

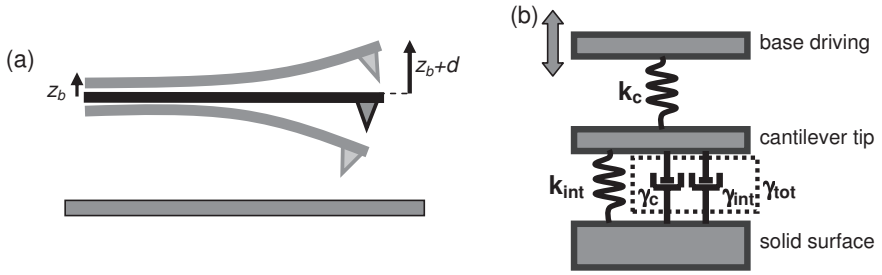

Figure 5.1 Illustration of the cantilever, where the total motion z of the cantilever consists of the measured deflection d plus the base motion z_b due to the acoustic driving mechanism. (b) Spring-dashpot representation of the harmonic oscillator model for acoustic driving with deflection detection and linearized tip-sample forces.

For small static forces and small drive amplitudes, only the linear terms need to be considered, $F_{ts}(z_c + z, \dot{z}) = -k_{\text{int}}(z_c)\, z - \gamma_{\text{int}}(z_c)\, \dot{z}$, leading to a simplified version of eq. 1:

$$m \cdot \ddot{z} + \gamma_{tot} \cdot \dot{z} + k_{tot} \cdot z = k_c \cdot z_b \tag{3}$$

where $k_{tot} = k_c + k_{\text{int}}$ and $\gamma_{tot} = \gamma_c + \gamma_{\text{int}}$ are the total stiffness and damping, respectively.

Using the Ansatz $z(t) = A_{tot} \exp(i(\omega t + \varphi_{tot})) = d(t) + z_b(t) = A\exp(i(\omega t + \varphi)) + A_b \exp(i\omega t)$ (in which ω is the drive frequency, A and φ are the measured deflection amplitude and phase of the deflection and A_b is the amplitude of the base-motion) we can solve eq.3 for the A and φ (see Chapter 4). As noted earlier, the total amplitude A_{tot} of the tip motion, given by $A_{tot} = \sqrt{(A\sin\varphi)^2 + (A\cos\varphi + A_b)^2}$, can be substantially different from the measured deflection amplitude A in eq. 2a in Chapter 4.
In order to extract the physical interaction forces we need to solve eq. 3 for the interaction stiffness k_{int} and damping γ_{int}, yielding:

$$k_{\text{int}} = -k_c + m\omega^2 + \frac{k_c A_b (A_b + A\cos\varphi)}{A_b^2 + A^2 + 2A_b A\cos\varphi} \tag{4a}$$

and:

$$\gamma_{\text{int}} = \frac{-k_c A_b A \sin\varphi}{\omega\left(A_b^2 + A^2 + 2A_b A\cos\varphi\right)} - \gamma_c \tag{4b}$$

where A_b is calculated from the measured free amplitude A far away from the surface (at 10nm) using eq. 2a of Chapter 4 with the interactions set to zero[2]. Note that these physical tip-sample forces k_{int} and γ_{int} are independent of the specific measurement technique and should, in particular, look identical as equivalent data extracted from e.g. frequency modulation AFM measurements. Close to resonance, these formulae can be applied using frequency-independent calibration constants (k_c, m, and γ_c) as determined from calibration measurements of the resonance frequency and the Q factor far away from the surface (at 100 nm). For drive frequencies varying over a substantial range, however, one needs to take into account the frequency-dependence of the motion of the fluid around the oscillating cantilever [30], which can be achieved by replacing m and γ_c by their frequency-dependent counterparts without changing the structure of eq. 4. Following Sader [36], we describe the hydrodynamic loading on the cantilever by a hydrodynamic function $\Gamma = \Gamma' + i\Gamma''$, which yields an added mass and a damping given by $m_{added} = m - m_{cant} = (\pi/4)\rho w^2 L\Gamma'$ and $\gamma_c = (\pi/4)\rho w^2 L\omega\Gamma''$ [32]. Here, ρ, w and L denote resp. the density of liquid, and the width and the length of the cantilever. Γ depends on the viscous penetration depth $\delta = \sqrt{2\eta/\rho\omega}$ (η: viscosity of the liquid) and the cantilever geometry as $\Gamma' = a_1 + a_2\delta/w$ and $\Gamma'' = b_1\delta/w + b_2(\delta/w)^2$ with a_1 = 1.0533, a_2 = 3.7997, b_1 = 3.8018 and b_2 = 2.736. With the calibration constants (k, Q, $\omega_{0,air}$ and $\omega_{0,liquid}$) applied at resonance, the frequency independent prefactor in both the frequency-dependent added mass and damping can be calculated.

The relevance of this frequency-dependent correction becomes apparent from the amplitude and phase response of the cantilever far away from the surface. Fig. 5.2 shows a comparison between the experimental frequency response (thick black solid lines) and various implementations of the model. Above the resonance frequency, the experimental data are distorted by various spikes, which are typical for AFMs with acoustic driving. To avoid interference with these features, all measurements described in this Chapter are carried out at drive frequencies below the lowest spike. We therefore also limit the comparison of the model curves to the frequency range below resonance. The dashed lines show the response curve of a simple harmonic oscillator (ignoring the base motion), which is shown for reference and which is obviously not suitable in the present case of a low Q environment [14, 15, 28]. The thin solid curves represent the frequency response according to eq. 2a in Chapter 4 (i.e. including the base motion) for constant m and γ_c. As described in Chapter 4, this correction captures the most important features of the experimental curves, namely the vanishing amplitude and the non-zero phase at low frequencies. Yet, the phase decreases much more quickly towards -90° than observed experimentally, which was left unnoticed previously. This deviation leads to a substantial phase error if the model is used to

[2] Somewhat differently looking but equivalent force inversion formulae were derived by Jai et al. [29].

extract tip sample interaction forces from measured APD curves at low frequencies. In contrast, the dash-dotted model curve, which incorporates the frequency-dependence of m and γ_c, produces a much more satisfying agreement also at the lowest frequencies and thus reproduces the global shape of both amplitude and phase response over the entire frequency range – notwithstanding some residual deviations.

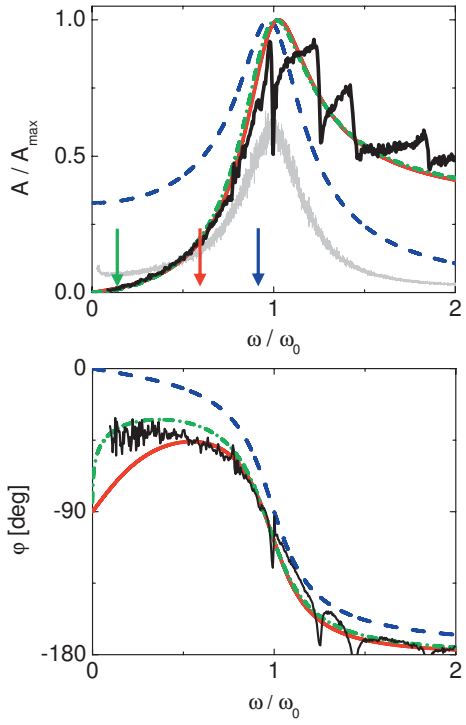

Figure 5.2 Amplitude and Phase response of the cantilever versus normalized drive frequency for ambient liquid (Q = 3). Blue dashed lines: conventional harmonic oscillator (H.O.). Red solids lines: deflection signal including base-drive (constant damping and added mass). Green dash-dot lines: deflection signal including base-drive with frequency-dependent damping and added mass. Black lines: experimental response (Au coated Si cantilever, $\omega_{res}/2\pi$ = 38 kHz, the spurious peaks above ω/ω_0 = 0.95 are due to the piezo response). Grey line: Thermal noise spectrum (Si cantilever, $\omega_{res}/2\pi$ = 42 kHz). Coloured arrows indicate the measurement frequencies of the data shown in Fig. 5.3.

5.4 Results

5.4.1 Measurements

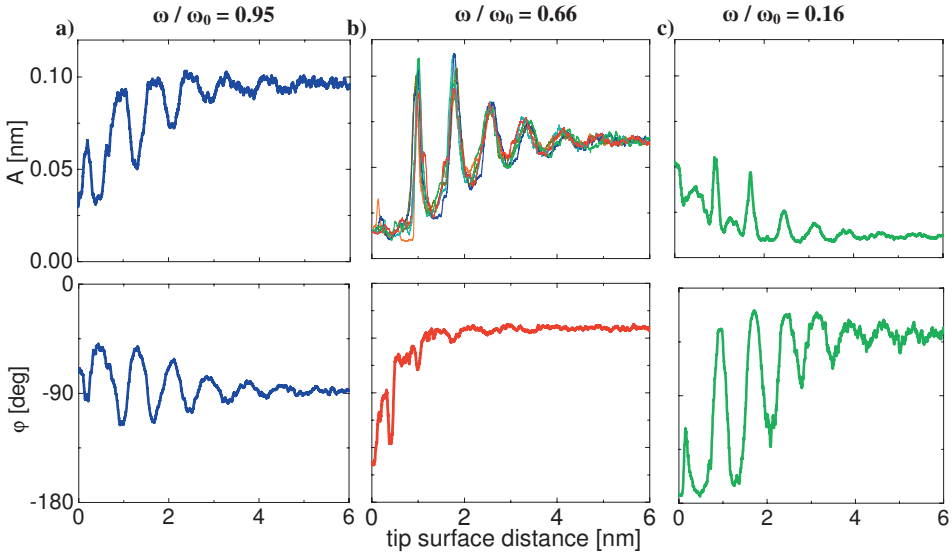

Figure 5.3 Amplitude A and phase φ versus distance curves upon approaching the surface, (total free amplitude (a) 0.117 nm (b) 0.129 nm (c) 0.320 nm; resonance frequency $\omega_{res}/2\pi$ = 38 kHz, Au-coated Si cantilever) for three different driving frequencies: (a) ω/ω_0 = 0.95, (b) ω/ω_0 = 0.66, (c) ω/ω_0 = 0.16. The different curves in b) indicate the reproducibility of the measurements. (a smoothing filter was applied to eliminate high frequency noise)

Figure 5.3 shows APD curves measured with the same cantilever at three different frequencies close to and below resonance. We chose these frequencies with special care. At these frequencies the calculated cantilever response matches the measured response very well and no spurious peaks were observed in the spectra (Fig. 5.2)). For all driving frequencies, both the amplitude and the phase display oscillations with a periodicity varying from 0.7-0.9 nm from curve to curve reflecting the diameter of the OMCTS molecules. For a detailed description and explanation of the frequency-dependent cantilever response we refer to Chapter 4. The same trends as a function of frequency are observed for all free amplitudes. For the highest free amplitudes, the amplitude and phase modulations decrease systematically, as noted earlier by others [8]. Using the results of Fig. 5.2 we can qualitatively understand the frequency dependent response in Fig. 5.3, as discussed in Chapter 4.
The data in Fig. 5.3 represent typical APD curves selected from a large data set. The overall behaviour of the curves is very reproducible, as evidenced by the selection of

amplitude curves shown in Fig. 5.3(b)). Yet, details such as the number of visible oscillations cycles can vary from curve to curve. Fig. 5.4 shows the distribution of the number of oscillations observed in a number of consecutive APD curves at several locations on the sample surface under otherwise identical conditions. Regarding the fact that the tip-sample interaction is mediated by merely a few hundred molecules under the tip, we attribute the variations in the number of oscillations to the stochastic nature of the molecular motion. This distribution does not affect validity of the qualitative trends as a function of frequency shown in Fig. 5.3.

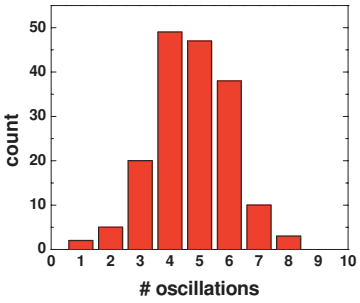

Figure 5.4 Frequency of the number of oscillations in amplitude-distance curves from 174 measurements at 6 different positions on different terraces of the HOPG ($\omega/\omega_0 = 0.75$).

5.4.2 Analysis of the results

5.4.2.1 Tip sample interaction forces

To extract the tip-sample interaction forces from the measured data, we apply eq. 4 to the measured APD curves shown in Fig. 5.3. Before doing so, we need to realize that the measured phase is affected by a phase offset due to the measurement system. The agreement between the experimental phase response and the model curve in Fig. 5.2 shows that (except for the spurious peaks at high frequencies) this phase offset is a frequency-independent constant. To account for it, we measure the phase at a distance of 10nm above the surface (i.e. outside the range of the tip-sample interaction) and shift this value manually to the value obtained from the model curve following a procedure suggested by Sader and Jarvis [33] in the context of frequency modulation AFM measurements. Failure to carry this procedure correctly leads to cross coupling between the phase and amplitude signal and thereby induces two main effects:
i) the interaction stiffness and the interaction damping do not decay to zero at large distance ii) artificial oscillations in the dissipation are created in the case of oscillatory conservative tip-sample forces (see [8,13]).

Figure 5.5 shows the interaction stiffness and damping extracted by inverting the curves shown in Fig. 5.3 using eq. 4 using the full frequency-dependent m and γ_c. The conservative forces display a strongly oscillatory behaviour that decays to zero within a few molecular layers, independent of the applied frequency. The only significant trend (i.e. beyond typical variations from curve to curve), is a slight reduction of the amplitude of the force oscillations at the lowest frequencies. Yet, as we will discuss below, this effect is caused by the somewhat larger drive amplitude required in off-resonance measurements.

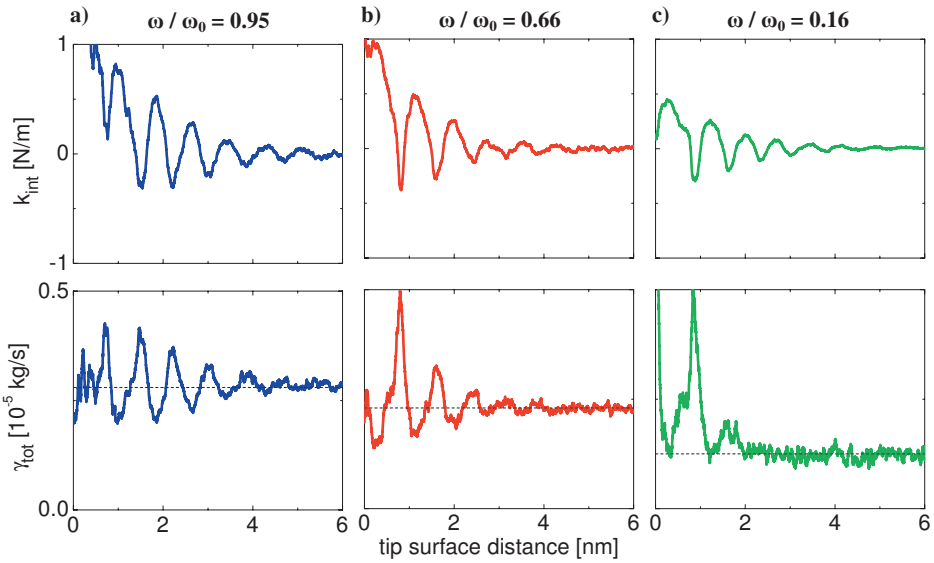

Figure 5.5 The interaction stiffness k_{int} and total damping γ_{tot} vs. tip-surface distance extracted from the amplitude and phase response of the cantilever (curves in Fig. 5.3) using eq. 4 with frequency-dependent damping and added mass. Left column: ω/ω_0 = 0.95; middle: ω/ω_0 = 0.66; right: ω/ω_0 = 0.16. The black dashed lines denote the damping of the cantilever γ_c.

The extracted total damping shows more variability between the different drive frequencies. For ω/ω_0 = 0.95 and 0.66, an oscillatory behaviour appears, similar to and exactly out-of-phase with the interaction stiffness with superimposed peaks. For the lowest drive frequency, the oscillatory behaviour is absent, yet the peaks at $d \approx 0.9$ nm and 1.7 nm remain visible. Such sharp peaks in the total damping were consistently found in many independent experiments with various cantilevers (Si or gold-coated Si and for various tip radii and spring constants). Note that the total damping at large distance approaches a constant value γ_{tot}^{∞}, which decreases with decreasing frequency as expected from the expressions given in Section 5.3.

The degree of consistency shown in Fig. 5.5 can only be achieved using the complete mechanical model for acoustic driving with deflection detection (see Fig. 5.1) including the frequency-dependent damping and added mass presented in the previous section. Neglecting the frequency-dependence of the added mass and damping leads to substantial deviations of the damping forces at low frequencies. If the base-motion is neglected (i.e. upon using a simple harmonic oscillator model) both conservative and dissipative forces are completely inconsistent between low and high frequencies, as expected (see [14]). Both of these findings are obviously consistent with the deviations found for the modelled frequency response curves (Fig. 5.2).

5.4.2.2 Conservative forces and amplitude dependence

For tip-surface distances beyond 1 nm, the conservative force curves can be fitted rather well with an exponentially decaying cosine profile (see Fig. 2, Appendix 5.A), which is known to approximate the shape of oscillatory solvation forces rather well [2]:

$$k_{\mathrm{int}}(z_c) = K_{\mathrm{int}} \cos\left(2\pi \cdot z_c / \sigma\right) \cdot \exp\left(-z_c / \xi\right) \qquad (5)$$

Fitting eq. 5 to the experimental data at variable frequency, we find an average periodicity σ = 0.78 ± 0.1 nm and a decay length ξ = 1.2 ± 0.2 nm. Interestingly, eq. 5 provides a good fit to the experimental data for distances beyond the first molecular layer, as illustrated in Appendix 5.A (Fig.2). (The region d < ~0.75 nm was excluded in the fitting process.) The fit parameter K_{int} yields a measure for the strength of the oscillatory solvation forces.

Before comparing the data at variable frequencies, we note that the (apparent) strength of the oscillatory solvation forces depends on the amplitude of the cantilever oscillation. If the free amplitude of the cantilever becomes comparable to the characteristic length-scale of the interactions the amplitude of the oscillations in both the amplitude and phase as well as in the resulting interaction forces decreases, as shown in Fig. 5.6 (see also [8]). Converting experimentally obtained APD curves for variable A_{tot}^{∞} between 0.09 nm and 0.4 nm at a fixed frequency into interaction forces and fitting the conservative forces using eq. 5, we find that the amplitude of the interaction stiffness gradually decreases approximately from 1.2 N/m for the smallest amplitude to 0.3 N/m for the largest amplitude (see symbols in Fig. 5.7)[3].

In the context of the force inversion method used here, the linearization of the tip-sample interaction forces, as described in eq. 2 provides a criterion for the maximum acceptable total amplitude A_{tot}^{∞}. For typical numbers for the periodicity σ = 0.8 nm and

[3] To exclude the possibility of systematic changes in the experimental conditions with time, e.g. due to contamination or temperature variation, the free amplitude was increased and decreased in random order during the experiments.

for the decay length ξ = 1.1 nm, we find the requirement $A_{tot}^{\infty} << 2k_{int} / k'_{int}$, so $A_{tot}^{\infty} <<$ 0.29 nm.

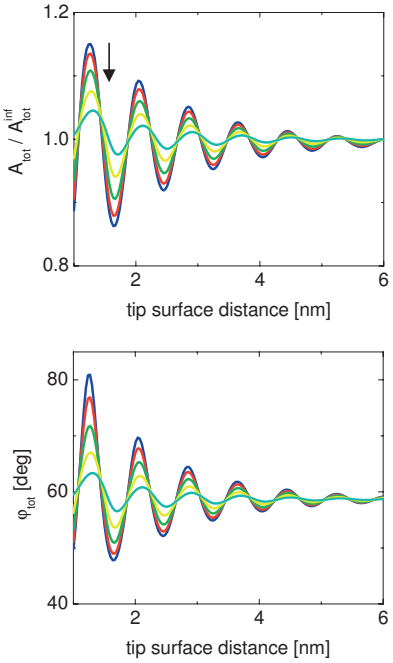

Figure 5.6 Numerically calculated amplitude and phase response of the cantilever (ω/ω_0 = 0.93, k_c = 1.9 N/m and Q = 2.7) versus tip-surface distance in the presence of oscillatory tip-sample forces (K_{int} = 0.3 N/m, σ = 0.8 nm and ξ = 1.1 nm) for variable free amplitude (80 pm, 160 pm, … 400 pm) increasing along the arrow from dark blue to turquoise.

To quantify the expected reduction for larger amplitudes, we numerically calculated APD curves by inserting the full non-linear tip-sample interaction force according to eq. 5 into eq. 1 for variable driving amplitude at a fixed drive frequency close to resonance. (For simplicity the interaction damping was left out in these calculations.)
As shown in Fig. 5.6, the amplitude of the oscillations in A_{tot} and φ_{tot} decreases strongly with increasing A_{tot}^{∞}, in qualitative agreement with the experimental data. Note that appreciable smoothing effects can already be observed for A_{tot}^{∞} = 0.16 nm.
Inserting the numerically calculated cantilever response into eq. 4 leads to the apparent interaction stiffness as a function of the free cantilever amplitude. The solid line in Fig. 5.7 shows the corresponding stiffness amplitude K_{int} decreases as a function of A_{tot}^{∞}, in excellent agreement with experimental measurements.

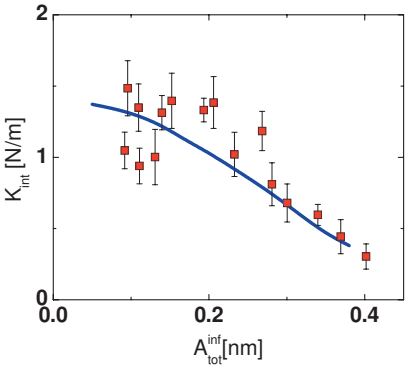

Figure 5.7 Apparent Amplitude K_{int} of the fitted interaction stiffness vs. total cantilever-amplitude A_{tot}^{∞} extracted from the amplitude and phase response (ω/ω_0 = 0.92, resonance frequency $\omega_0/2\pi$ = 36 kHz). Symbols: experimental results (Si cantilever); error bars denote the standard error with 95% confidence interval. Solid line: numerical calculation (see text for details).

This result explains the apparent reduction of the oscillatory interaction forces in Fig. 5.5(c) (recorded far below resonance) compared to Fig. 5.5(a) and (b) (recorded on resonance): the off resonance measurements were performed using a relatively large amplitude $A_{tot}^{\infty} \approx 0.3$ nm (see Fig. 5.3) in order to achieve a similar signal-to-noise ratio as for the on resonance measurements. For such large amplitudes, linearization of the tip-sample interaction forces is no longer justified, causing the observed apparent reduction of K_{int}. This observation may explain some of the discrepancies between different dynamic AFM measurements carried out with different free amplitudes.

5.4.2.3 Conservative forces at variable drive frequency

Using the result of Fig. 5.7, we can correct the extracted apparent values of the amplitude of the interaction stiffness K_{int} and extrapolate them to their intrinsic value for small drive amplitudes. Fig. 5.8 shows the result for a data set consisting of various different cantilevers and types of cantilevers for a range of drive frequencies from 5 kHz to 58 kHz. Within the experimental error, we find that the strength of the oscillatory solvation forces is identical, irrespective of the drive frequency and of the material of the cantilever.

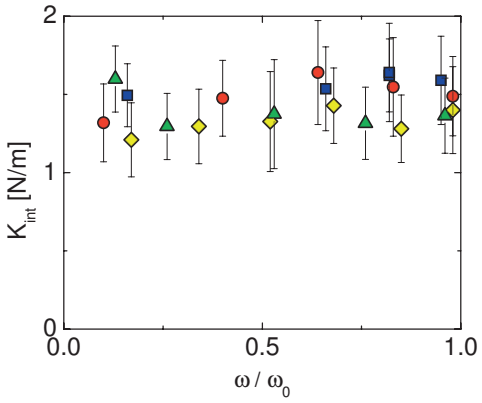

Figure 5.8 Extrapolated Amplitude K_{int} of the fitted interaction stiffness vs. measurement frequency for various cantilevers. (red circles: Au coated Si, $\omega_{\text{res}}/2\pi$ = 51 kHz); green triangles: Si, $\omega_{\text{res}}/2\pi$ = 37 kHz; yellow diamonds: Si, $\omega_{\text{res}}/2\pi$ = 59 kHz; blue squares: Au coated Si, $\omega_{\text{res}}/2\pi$ = 38 kHz); error bars denote the standard error with 95% confidence interval)

5.5 Discussion

5.5.1 Conservative tip-sample interactions

To compare the present results to previous SFA and AFM measurements, we convert the interaction stiffness k_{int} into the normalized force f / R using the Derjaguin approximation [20, 34, 35]. f / R is proportional to the interaction energy per unit area of two parallel surfaces at separation z_c. Approximating the local oscillatory pressure by $P(z_c) = P_0 \cos(2\pi \cdot z_c / \sigma) \cdot \exp(-z_c / \xi)$, the resulting *amplitude* F / R of the distance dependent oscillatory force f / R is related to the *amplitude* K_{int} of the distance dependent oscillatory stiffness k_{int} (fitted using eq. 5) by:

$$\frac{F}{R} = \frac{K_{\text{int}}}{2\pi R \sqrt{\left(\frac{1}{2\pi\xi}\right)^2 + \left(\frac{1}{\sigma}\right)^2}} \tag{6}$$

where R is the tip radius. For small drive amplitudes and using the fitted interaction stiffness, we find a force amplitude F/R = 9 ± 2 mN/m, in agreement with earlier measurements in SFA and AFM [2, 34]. Based on the fact that tip-sample distances of about one molecular layer and below need to be excluded from the fitting procedure, one may speculate that the molecules immediately adjacent to the substrate surface are in a different, perhaps solidified state, as compared to the other molecular layers.

The fact that the strength of the solvation forces extracted from distances beyond the first molecular layer is independent of the drive frequency indicates that the system does not have any relevant relaxation times within the corresponding time interval of 0.02 to 0.2 ms. For a fluid this is not surprising since typical molecular relaxation times are substantially faster.

5.5.2 Dissipative tip-sample interactions

Compared to the conservative interactions, the picture emerging from the dissipation extracted for various frequencies is somewhat less consistent. For all frequencies the dissipation decays to a constant frequency-dependent asymptotic value $\gamma_{tot}^{\infty}(\omega)$, as expected. Yet, the data recorded close to resonance (Fig. 5.5(a) and (b)) display oscillations involving both enhancements and reductions of γ_{tot} by several tens of percents of γ_{tot}^{∞}, while the low frequency data (Fig. 5.5(c)) only display positive peaks at distances corresponding to the minima in k_{int}.

To elucidate whether oscillations in the damping are realistic and to what extent confinement may enhance the local dissipation, we consider the dynamics of the cantilever in the framework of hydrodynamics. The experimental observation that A and φ (as well as k_{int} and γ_{tot}) are constant within several tens of nanometers from the surface (see section 5.2 and Fig. 3 of Appendix 5.A) suggests that it is justified to split the dissipation into a background contribution due to the global motion of the cantilever, which is constant within the distance range covered by the APD curves, and a distance-dependent contribution arising from the local dynamics in the vicinity of the tip. This idea is consistent with an approach by O'Shea and Welland [11], who decomposed the total damping into separate contributions arising from the motion of different parts of the cantilever, namely the cantilever beam, the cone of the tip (modelled as an effective sphere), and the nano-scale tip itself. For each of these components separate solutions of the time-dependent Stokes equations for the respective idealized geometry are known and allow for estimating their relative importance. The analysis, which we describe for our experimental situation in Appendix 5.B, shows that the total damping is dominated by the damping of the cantilever beam in the fluid rather than the squeeze-out damping at the tip. This is due to the much larger characteristic size of the former (typically 100 µm vs. 20 nm). Inserting numerical values, one finds indeed that this background contribution is expected to be constant, within ~ 0.25%, over the range of the APD curves. The most interesting distance-dependent contribution is obviously the squeeze-out damping due to the confined fluid the between tip and sample. It can be described by Reynolds' classical expression:

$$\gamma_R = 6\pi\eta_{loc}\frac{R_{tip}^2}{d} \qquad (7)$$

For distances d of a few nanometers and for a local viscosity η_{loc} under the tip equal to the bulk viscosity, this tip damping is several orders smaller than the beam damping [11]. Only for $d \rightarrow 0$ (i.e. << 1 nm) and/or if the local viscosity is dramatically enhanced, e.g. due to confinement effects, this contribution can lead to a substantial and measurable excess damping.

The above considerations have important consequences regarding the nature of variations in the damping, which – to our knowledge – have not been expressed explicitly so far: Since the background damping is constant within the experimental error and a few orders of magnitude larger than the tip damping, γ_{tot} can only increase but never significantly decrease within the uncertainty of AFM measurements (typically a few percent). This conclusion results directly from the relative order of magnitude of the global and the local dissipation and therefore applies to all AFM measurements independent of the specific measurement technique (AM-AFM vs. FM-AFM; base-drive vs. magnetic drive). As a consequence, we conclude that any reduction of the global damping, such as the ones shown in Fig. 5.5(a) and (b), must be artificial and caused by either uncertainties in calibration constants and/or imperfections in the model of the cantilever dynamics. (For the present case of AM-AFM, the experimental uncertainties include in particular errors in the absolute phase [8, 13], in addition to Q and ω_0, which are also important in FM-AFM.)

Since the background damping of the cantilever is constant within the experimental errors, it is justified to subtract that contribution and consider the remaining interaction damping $\gamma_{int} = \gamma_{tot} - \gamma_{tot}^{\infty}$. Using hydrodynamics as a reference framework, we compare the resulting γ_{int} to the expectations based on eq. 7 (see Fig. 5.9).

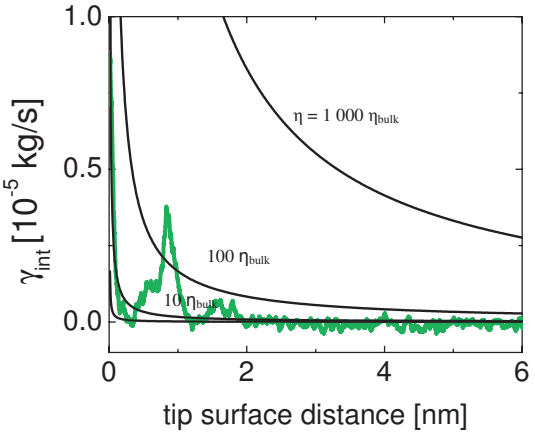

Figure 5.9 The extracted interaction damping for $\omega/\omega_0 = 0.16$ (green curve). The black curves show the calculated Reynolds damping γ_R for increasing viscosity ($R_{tip} = 20$ nm).

We plot the low frequency data from Fig. 5.5(c) in Fig. 5.9 because they do not display artificial negative values of γ_{int}, caused by excessive reductions of γ_{tot} as discussed

above. Moreover, the low frequency measurements are less sensitive to calibration errors, while the amplitude and phase response (as mentioned above) is equally sensitive to variations in the stiffness and damping (see also Appendix 5.A and partially ref. [15]).

Figure 5.9 also shows the calculated Reynolds squeeze-out damping under the tip (eq. 7), for increasing values of the viscosity. For $\eta_{loc} = \eta_{bulk}$ (Fig. 5.9), the Reynolds damping under the tip γ_R is negligible for all realistic values of d, in agreement with the discussion above. Yet, the Reynolds damping resulting from already a 100 times enhanced local viscosity lies above the experimental data at all distances. In the damping measured for $d > 2$ nm, the data are consistent with the bulk viscosity and approximately 10x the bulk viscosity (within the experimental error), corresponding to 22 mPa s. Larger enhancement factors are incompatible with our experimental data. Note that the same conclusion can also be drawn on the basis of all our data recorded, irrespective of the drive frequency. (including the artificial oscillations visible close to resonance)

A direct conversion of the measured damping into an effective viscosity seems to provide a reasonable description of the system down to distances of 2 to 3 nanometers. At smaller separations, the hydrodynamic picture becomes progressively more questionable given the small number of molecules involved (a few hundred) and the discrete layer structure of the confined liquid. The position of the maxima at $d \approx 0.9$ nm and 1.7 nm in the damping in Fig. 5.9 coincides with the minima in the interaction stiffness. It also coincides with a region of (small) negative slope of the average deflection of the cantilever (data not shown). The maxima in the damping thus occur at distances corresponding to attractive forces, where according to a standard hard sphere-like model as well as numerical simulations, the average density of the fluid inside the gap is reduced compared to the bulk value. Such a reduced density implies more free volume for the molecules and thus more freedom to exchange sites, which may enhance the opportunities to dissipate energy compared to the more compact configuration of completely filled layers that provide a more elastic response. Hofbauer et al. [12] recently proposed a similar mechanism to explain similar (yet more pronounced) peaks in the dissipation for confined dodecanol.

Finally, we note that for all distances, except for the minima in the interaction stiffness, (corresponding to the attractive part of the conservative forces), the damping always assumes values that are compatible with the bulk viscosity indicating that the "effective viscosity" in complete layers of OMCTS is similar to the value found in the bulk. Notwithstanding the differences in the confinement geometry between the surface forces apparatus and the AFM, it is remarkable how this result agrees with some of the earlier SFA measurements [5, 6].

The fact that the conservative tip-sample interaction forces follow the behavior of hard sphere fluids (eq. 5) and the fact that the effective viscosity is compatible with the bulk viscosity down to a thickness of three mono-layers clearly suggest that the system behaves liquid-like. The consistency of the behavior (including in particular the absence of artificial negative interaction damping) for the various experimental

conditions investigated support this conclusion. We note that this finding is at variance with the conclusion of Patil et al. [9] who reported signs of a jamming-like solidification for confined OMCTS for the range of approach rates used in the present study and liquid-like behavior only for approach rates below 0.6nm/s. Their interpretation is based on a Maxwellian model of a visco-elastic liquid, yet, they do not provide any details regarding the modeling of the cantilever dynamics. We currently have no explanation for the deviation with our data.

5.6 Conclusions

In summary, the results presented in this Chapter show that it is indeed possible to extract consistent tip-sample interaction forces over a wide range of driving frequencies from amplitude-modulation AFM measurements provided that three elements are correctly taken into account, namely:
i) the motion of the cantilever base,
ii) the frequency-dependence of the added mass and the viscous damping of the cantilever,
iii) the finite oscillation amplitude of the cantilever.
While the consistency with respect to the conservative forces is very satisfying, known residual discrepancies due to cross coupling with conservative forces limit the accuracy of dissipative forces measured at AFM drive frequencies close to resonance. This problem can be circumvented by choosing drive frequencies substantially below resonance, where the measurement system is less sensitive to errors in the phase and/or uncertainties in the calibration constants.
The dissipative forces extracted in this way show that the “effective” viscosity of the liquid confined between tip and sample is bulk-like down to approximately three molecular layers. Only for the last two layers, local maxima in the dissipation are found at tip-sample distances corresponding to minima in the interaction stiffness where the average density of the confined fluid is expected to be minimal from molecular simulations.

Acknowledgement

We thank J. E. Sader for his comments at SPM-UK 2009. We thank P. Markus (Veeco) and K. Smit for the technical support and M. Smithers for his help on the SEM images. This work has been supported by the Foundation for Fundamental research on Matter (FOM), which is financially supported by the Netherlands Organization for Scientific Research (NWO).

References

[1] B. Bhushan, J.N. Israelachvili and U. Landman, *Nature* **374**, 607 (1995)
[2] J.N. Israelachvili, *Intermolecular and Surface Forces,* 2nd ed. (1992)
[3] J. Klein and E. Kumacheva, *Science* **269** 816 (1995)
[4] M.L. Gee, P.M. McGuiggan, J.N. Israelachvili and A.M. Homola, *J. Chem. Phys.* **93** 1895 (1990)
[5] T. Becker and F. Mugele, *Phys. Rev. Lett.* **91** 166104 (2003)
[6] L. Bureau L and A. Arvengas, *Phys. Rev*. E **78** 061501 (2008)
[7] J. Gao, W.D. Luedtke and U. Landman, *Phys. Rev. Lett.* **79** 4 (1997)
[8] A. Maali, T. Cohen-Bouhacina, G. Couturier and J.-P. Aimé, *Phys. Rev. Lett.* **96** 086105 (2006)
[9] S. Patil, G. Matei, A. Oral and P.M. Hoffmann, *Langmuir* **22** 6485 (2006)
[10] G.B. Kaggwa, J.I. Kilpatrick, J.E. Sader and S.P. Jarvis, *Appl. Phys. Lett.* **93** 011909 (2008)
[11] S.J. O'Shea and M.E. Welland, *Langmuir* **14** 4186 (1998)
[12] W. Hofbauer, R.J. Ho, R. Hairulnizam, N.N. Gosvami and S.J. O'Shea, *Phys. Rev.* B **80** 134104 (2009)
[13] S.J. O'Shea, *Phys. Rev. Lett.* **97** 179601 (2006)
[14] N.A. Burnham, G. Gremaud, A.J. Kulik, P.-J. Gallo and F. Oulevey, *J. Vac. Sci. Technol.* **12** 2 (1996)
[15] S. de Beer, D. van den Ende and F. Mugele, *Appl. Phys. Lett.* **93** 253106 (2008)
[16] H.K. Christenson and C.E. Blom, *J. Chem. Phys.* **86** 419 (1987)
[17] We used the 'Thermal Tune' in the Nanoscope 7.20 software, which takes all the relevant corrections (e.g. temperature, cantilever shape) into account.
[18] J.L. Hutter and J. Bechhoefer, *Rev. Sci. Instrum.* **64** 1868 (1993)
[19] A. Maali, C. Hurth and T. Cohen-Bouhacina, *Appl. Phys. Lett.* **88** 163504 (2006)
[20] R. Proksch, T.E. Schaeffer, J.P. Cleveland, R.C. Calahan and M.B. Viani, *Nanotechnoloogy* **15** 1344 (2004)
[21] R. Garcia and R. Perez, *Surf. Sci. Rep*. **47** 197-301 (2002)
[22] L. Zitzler, S. Herminghaus and F. Mugele, *Phys. Rev.* B **66** 155436 (2002)
[23] H. Hoelscher, *Appl. Phys. Lett.* **89** 123109 (2006)
[24] M. H. Lee and W.H. Jhe, *Phys. Rev. Lett.* **97** 036104 (2006)
[25] S.Q. Hu and A. Raman, *Nanotechnology* **19** 375704 (2008)
[26] A.J. Katan, M.H. van Es and T.H. Oosterkamp, *Nanotechnology* **20** 165703 (2009)
[27] J.E. Sader and S.P. Jarvis, *Appl. Phys. Lett.* **84** 1801 (2004)
[28] X. Xu and A. Raman, *J. Appl. Phys.* **102** 034303 (2007)
[29] C. Jai, T. Cohen-Bouhacina and A. Maali, *Appl. Phys. Lett.* **90** 113512 (2007)
[30] L. Landau and F. Lifshitz, *Fluid Mechanics*, Theoretical Physics Vol. No. 6 (Mir, Moscow, 1971)
[31] J.E. Sader, *J. Appl. Phys.* **84** 64 (1998)
[32] A. Maali, C. Hurth, R. Boisgard, C. Jai, T. Cohen-Bouhacina and J.-P. Aime, *J. Appl. Phys.* **97** 074907 (2005)
[33] J.E. Sader and S.P. Jarvis, *Phys. Rev.* B **74** 195424 (2006)
[34] L.T.W. Lim, A.T.S. Wee and S.J. O'Shea, *Langmuir* **24** 2271 (2008)
[35] S.J. O'Shea, M.E. Welland and J.B. Pethica, *Chem. Phys. Lett.* **223** 336 (1994)

Appendix 5.A

It is well known that the dynamic and static deflection of a cantilever are not the same [20]. However, due to the finite spot-size of the laser this effect is averaged out for small cantilevers. To test this we measured the static and dynamic deflection for cantilevers of various lengths.

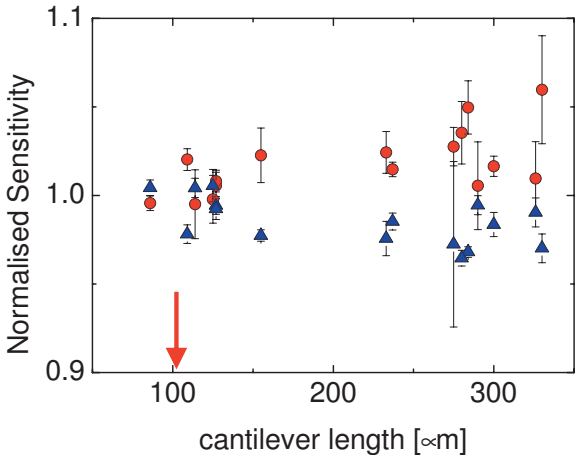

Fig. 1 The normalized static (blue) and dynamic (red) deflection sensitivity for various cantilevers with a different length. The arrow denotes the length of the cantilevers typically used for the experiments described in this Chapter.

In order to compare our data we fitted the extracted interaction stiffness with a decaying cosine function (which is known to describe the oscillatory solvation forces for weakly interaction liquids like OMCTS very well).

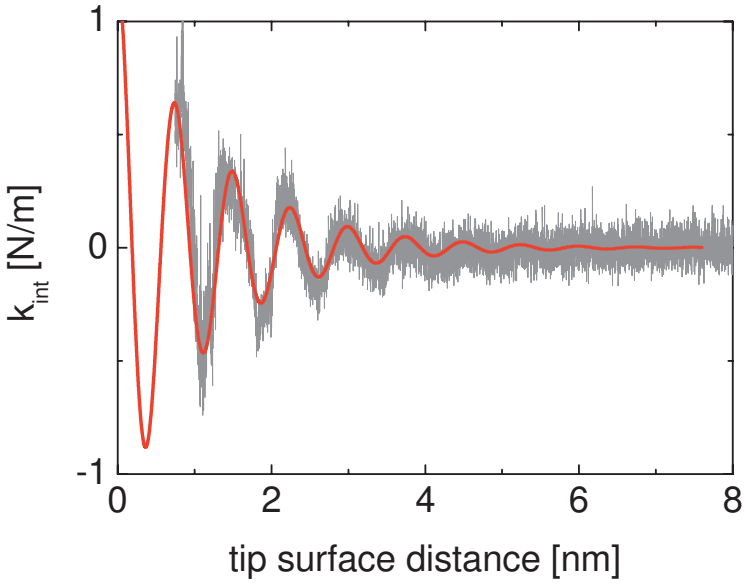

Fig. 2 The extracted interaction stiffness k_{int} fitted with a decaying cosine function to find the amplitude of the stiffness K_{int}.

To test whether the Reynolds squeeze-out damping under the cantilever changes as we approach the surface, we measure the APD curves over a larger distance. Since the amplitude and phase response of cantilever remain constant over this distance, we know that the Reynolds damping under the cantilever does not change (to a measurable extent).

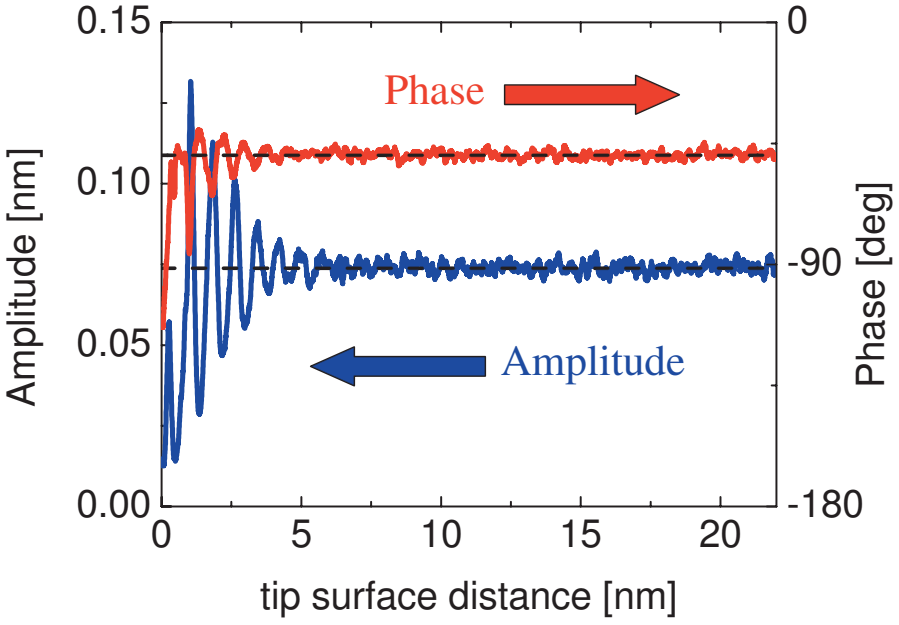

Fig.3 The Amplitude and Phase response of the cantilever over tens of nanometers ($\omega_{res}/2\pi$ = 42 kHz, Au-coated Si cantilever, ω/ω_0 = 0.75). Note that, apart from the oscillations close to the surface, the amplitude and phase response is constant.

In our experiments the biggest contribution to the total error comes from the uncertainty in the calibration constants. These uncertainties are mostly affecting the results on resonance. Note that on resonance the error in the phase is significant and can cause cross-coupling between the conservative and dissipative interaction forces.

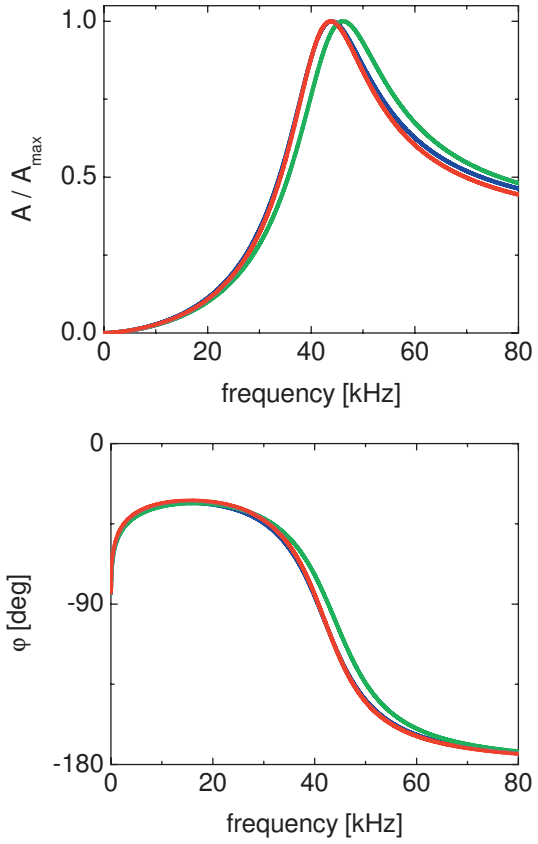

Fig. 4 The effect of an error of 5% in both Q (2.85+5%, red vs blue) and $\omega_{res}/2\pi$ (42 kHz+5%, green vs. blue) on the amplitude (a) and phase (b) response spectra of an acoustically driven cantilever using deflection detection.

Nevertheless, for acoustically driven cantilevers using deflection detection, the sensitivity to tip-sample interactions is approximately equal for low frequencies (15 kHz) and close to resonance (42 kHz). Fig. 5 shows the effect of an increasing interaction damping on the amplitude and phase response. Although the response in the amplitude is less for lower frequencies the response in the phase larger. For the effect of a change in interaction stiffness (an even more pronounced effect) we refer to ref. [15].

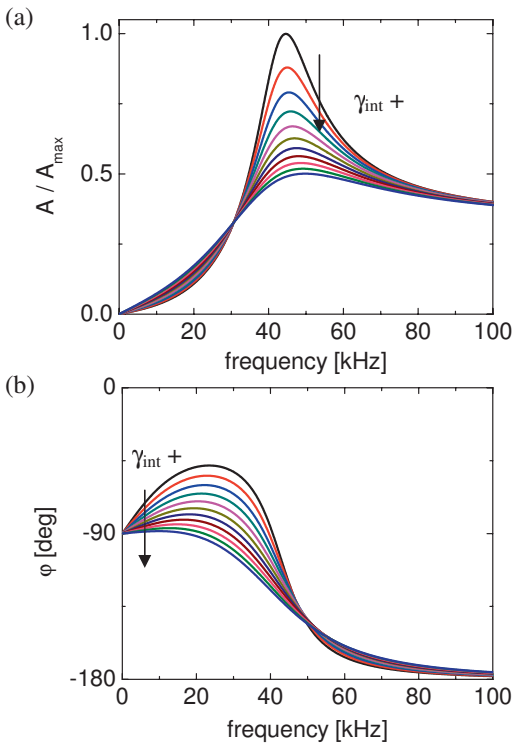

Fig. 5 The effect of a linearly increasing interaction damping (from 0 to 5 10^{-6} kg/s in steps of 0.5 10^{-6} kg/s) on the amplitude (a) and phase (b) response of an acoustically driven AFM cantilever using deflection detection ($\omega_{res}/2\pi$ = 42 kHz, Q = 2.85).

Appendix 5.B

Consider an AFM cantilever [11] consisting of a rectangular beam with length L = 120 μm, width w = 35 μm and at the end a tip with cone-radius R_{cone} = 5 μm and a tip-end with radius R_{tip} = 10 nm. The cantilever is in the vicinity of a solid surface and completely immersed in a liquid with density ρ = 2330 kg/m3 and viscosity η = 2.2 mPa s. The distance between the beam and the surface is $h = d$ + 25μm, between the tip-cone and the surface is $D = d$ + 8 μm, with the distance between the tip and the surface d (~ 1-2 nm).
For each part of the cantilever, there are contributions due to the free oscillation far away from the surface and contributions due to squeeze-out damping close to the surface. The former contain a constant and a frequency-dependent component due to the varying added mass, which is responsible for the reduction of the total damping for large distances at low frequencies (see Fig. 5.5).
The total damping of the cantilever is built up by:

1. Hydrodynamic damping due to viscous drag and the added mass over the beam, $\gamma_{cb} = 0.24 \cdot \left(3\pi\eta L + \frac{3}{4} wL\sqrt{2\rho\eta\omega} \right)$.
2. Hydrodynamic damping due to viscous drag and the added mass at the tip-cone, $\gamma_{cc} = \frac{1}{2}\left(6\pi\eta R_{cone} + 3\pi R_{cone}^2 \sqrt{2\rho\eta\omega}\right)$.
3. Hydrodynamic damping due to viscous drag and the added mass at the tip, $\gamma_{ct} = \frac{1}{2}\left(6\pi\eta R_{tip} + 3\pi R_{tip}^2 \sqrt{2\rho\eta\omega}\right)$.
4. Reynolds squeeze-out-damping under the beam, $\gamma_{Rb} = 0.24\eta \frac{w^3 L}{h^3}$.
5. Reynolds squeeze-out-damping under the cone, $\gamma_{Rc} = 6\pi\eta \frac{R_{cone}^2}{D}$.
6. The interaction damping under the tip, γ_{int}.
    a. Reynolds squeeze-out-damping under the tip, $\gamma_{\mathrm{int}\,R} = 6\pi\eta_{local} \frac{R_{tip}^2}{d}$.
    b. Changes in the hydrodynamic damping due to local changes in the added mass and viscosity under the tip, $\gamma_{\mathrm{int}\,c} = \frac{1}{2}\left(6\pi(\eta_{local} - \eta)R_{tip} + 3\pi R_{tip}^2 \left(\sqrt{2\rho\eta_{local}\omega} - \sqrt{2\rho\eta\omega}\right)\right)$.

We define damping 1-5 as the background damping γ_c and damping 6 as the interaction damping, $\gamma_{int.}$

First of all, using these equations, it is easy to show that due to the change in Reynolds damping between 100 nm and 1 nm tip surface distance, the cantilever's damping γ_c increases with 0.25%. This is far within our experimental error and therefore our assumption that the extracted changes in damping are due to tip-sample interactions is valid. (Remember that the assumption of a constant γ_c is supported by the experimental observation that the APD curves are constant for tip-sample distances varying between 100 and 10 nm.)

Second, note that the damping due to the Reynolds force under tip always results in an increase of the total damping and therefore a positive interaction damping. Consequently the negative interaction damping can only be a result of a change in hydrodynamic damping due to viscous drag and the added mass at the tip. Since the local density (and accordingly the viscosity) under the tip varies around its bulk value, this contribution can be both positive and negative. However, if, in a worst case scenario, the local viscosity under the tip would go to zero, the maximum decrease in the calculated total damping is 0.013%. Our experimentally found decrease in the total damping is much larger and therefore unrealistic.

Chapter 6

Oscillatory solvation forces measured with magnetic actuation

In Chapter 5 we have described our acoustic drive Atomic Force Microscope (AFM) measurements of the conservative and dissipative forces in a confined liquid. However, acoustic drive measurements are often mistrusted because of their sensitivity to modeling errors and the occurrence of spurious resonances. When using a magnetic driving scheme with deflection detection, the motion of the cantilever is directly measured and therefore modeling the cantilever dynamics is more straightforward. So, to assure ourselves that the results described in Chapter 5 are not artifacts due to wrongful modeling, we repeated our measurements using atomic force spectroscopy with magnetic actuation.[1]

[1] This chapter has been published as: S. de Beer, D. van den Ende & F. Mugele, *J. Phys: Condens. Matter* **23**, 112206 (2011).

6.1 Introduction

With the recent trend of down-scaling fluidic devices [1], the surface to volume ratio becomes significantly larger and consequently it becomes more important to characterize liquids close to solid surfaces. Moreover, a thorough understanding of confined liquids is of fundamental importance to industrial engineering with respect to friction, lubrication and wears [2]. Close to a solid surface liquid molecules can organize into layers, which, upon confinement between two solid surfaces, gives rise to oscillatory solvation forces [3]. Although the existence of oscillatory solvation forces is by now well established, the dynamic properties of the layered liquid are still under debate. Surface Forces Apparatus (SFA) measurements of confined octamethylcylotetrasiloxane (OMCTS, a model-liquid with quasi-spherical molecules) have shown that the liquid can abruptly solidify at wall-to-wall distances larger than six molecular layers [4], while SFA measurements performed in other labs on the same system have revealed that the squeeze-out of OMCTS layers is liquid-like and can be described with continuum theory and the bulk properties of the liquid down to the last two molecular layers [5,6]. Recently *acoustic drive* Amplitude Modulation Atomic Force Microscope (AM-AFM) measurements have shown that the damping in confined OMCTS shows features with a periodicity equal to the size of the molecules (and coinciding with either the maxima or the minima of the interaction stiffness) superimposed onto a monotonic increasing damping [7-9]. On the other hand (off-resonance) *magnetic drive* AM-AFM [10] and Frequency Modulation (FM-) AFM [11] measurements have only found the monotonic increase in the damping. However, acoustic drive AFM measurements are frequently mistrusted because of their sensitivity to modelling and analysis errors [11,12] and difficulties to obtain a clean spectral cantilever response without spurious resonances [10]. Yet, for another model liquid (1-dodecanol) recent *magnetic drive* measurements did indicate the presence of non-monotonic features in the dissipation [13].

In this chapter we present distance dependent, *magnetic drive* AM-AFM measurements of the conservative interaction stiffness and the dissipative interaction damping in confined OMCTS. The measurements are carried out close to the resonance frequency of the AFM cantilever, which increases the sensitivity in the phase. We demonstrate that the interaction damping shows indeed features with a periodicity representing the size of the molecules and we discuss possible reasons for the discrepancies between the different measurements performed with different AFM measurement techniques.

6.2 Materials and Methods

As a substrate we used highly oriented pyrolitic graphite (HOPG, Mikromasch ZYB), which was cleaved just before depositing the OMCTS (Fluka, purum ≥ 99.0%, used as received) to obtain an atomically flat and clean surface. The measurements were performed on a Veeco Multimode 8 with Nanoscope V controller equipped with the Veeco EV scanner using Cobalt coated cantilevers (Mikromasch NSC18) with a spring constant k_c = 2-3 N/m and a resonance frequency f_0 = 55-70 kHz in air. Prior to the measurements the cantilevers were rinsed with OMCTS to flush away contamination. After the measurements the tip was characterized using high resolution SEM imaging (yielding tip radii $R_{tip} > 90nm$) and to ensure that the cantilevers were free of contamination (Chapter 11 or [14]). The spring constant was determined in air using the thermal calibration method [15]. The resonance frequency (f_0 = 25-32 kHz) and quality factor Q (2.9-3.2) in liquid were determined by fitting the thermal response of the cantilever with the equation for the spectral response of a simple harmonic oscillator as implemented in the Veeco Nanoscope 8.10 software. For a correct characterization of the added mass and damping of the system, the calibration was performed 100 nm above the sample surface. During the experiments the temperature in the AFM head was measured to be 27°C. However, we have shown in a previous study that close to room temperature the conservative oscillatory forces in OMCTS are independent of the temperature (Chapter 9 or [16]). Nevertheless, we can not rule out that temperature might affect the dissipative forces.

To ensure a clean spectral response of the cantilever without spurious resonances we used a magnetic driving scheme, which was accomplished with the Digital Instruments Magnetic Actuation Drive (MAD) and the glass MAD fluid cell. The fluid cell has a small coil (diameter 8.7mm, height 3mm, ~100 turns, inductance 0.35 mH) and two permanent magnets in line with the cantilever (see also Fig. 6.1(a)) to ensure a magnetization of the Cobalt coating parallel to the cantilever [17]. To obtain a trustworthy spectral response without spurious resonances, we found it was critical to rigidly clamp the cantilever in the holder and to mount the HOPG surface at a distance larger than 25 mm from the (magnetic) scanner using a homebuilt spacer. Before the measurements we characterized the frequency dependent response of the electronics.
Figure 6.1(b) shows a typical measured amplitude (yellow) and phase (red, after correction for the spectral characteristics of the electronics) as well as the thermal response (black) versus frequency of one of the cantilevers used for the measurements described in this paper. Please note that at high frequencies the amplitude becomes very low and therefore the phase becomes undefined (resulting in a strong phase-noise at high frequencies). From the thermal power spectrum we determine the calibration constants (f_0 and Q). Together with k_c, these values are used to calculate the amplitude and phase response (Fig. 6.1(b), grey curves). The calculated spectra show an excellent agreement with the measured amplitude and phase. Yet, since the spectral response is quite noisy, a variation of f_0 and Q by ~3% would also have matched the data.

However, we checked and found that such variations had no effect on the extracted physical properties described below (within the experimental error). The experiments were carried out with more than 50 cantilevers, of which 25 were discarded due to a bad spectral response (non-harmonic response or spurious resonances).

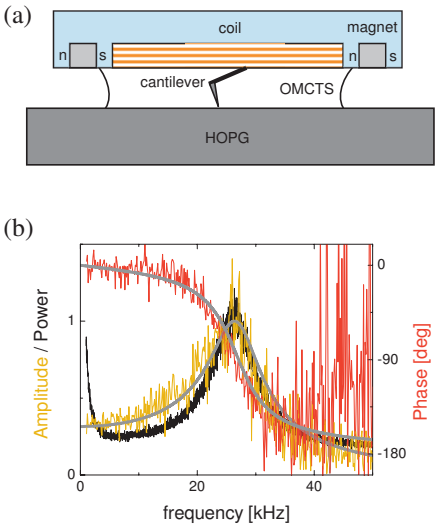

Figure 6.1 The calculated (gray) and measured amplitude (yellow) and phase (red) response as well as thermal power spectrum (black) of a cantilever used in our experiments (k_c = 2.66 N/m, f_0 = 27.06 kHz).

In the experiments we monitor the amplitude and phase response as well as the average deflection of the cantilever upon approach towards the surface (typical approach velocity: 1 nm/s). To extract the physical properties of the confined liquid we convert the amplitude & phase versus distance curves into the conservative interaction stiffness k_{int} and dissipative interaction damping γ_{int} via a simple harmonic oscillator model in the small amplitude approximation (see also Chapter 3.3.1b). This results in:

$$k_{\text{int}} = -k_c + m\omega^2 + \frac{F_0}{A}\cos\varphi$$

$$\gamma_{\text{int}} = \frac{-F_0}{A\omega}\sin\varphi - \gamma_c \ ,$$

where A and φ are the measured amplitude and phase, ω is the drive frequency, F_0 is the driving force, which is determined from the amplitude far away from the surface (~10 nm), m is the mass (cantilever + added mass), which can be found via $m = k_c / \omega_0^2$, where $\omega_0 = 2\pi f_0$ and γ_c is the damping and can be calculated from the calibration constants via $\gamma_c = m\omega_0 / Q$.

6.3 Experimental results

Figure 6.2(a) shows a typical Amplitude (yellow), Phase (red) Displacement (APD) curve upon approach of the cantilever (k_c = 3.2 N/m, f_0 = 31.8 kHz and R_{tip} = 108 nm) towards the surface while the cantilever is driven just below resonance ($\omega / \omega_0 = 0.91$). When the distance z_c between the tip and the surface is more than ~7-8 nm, the amplitude and phase are constant. The cantilevers used in these experiments have a relatively large tip-height (20-25 ∝m) to minimize the changes in added mass and hydrodynamic damping during approach of the cantilever towards the surface [9]. When the cantilever is brought closer to the surface (z_c < 7-8 nm), the amplitude and phase both increasingly oscillate (with a periodicity representing the size of the molecules; $\sigma = 0.79 \pm 0.08$ nm) until the tip touches the surface.

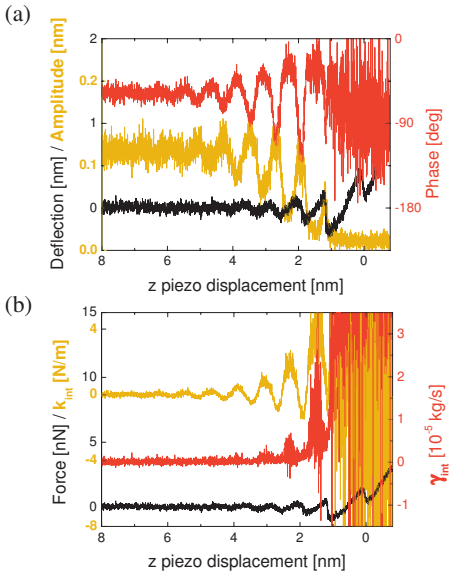

Figure 6.2 (a) Amplitude (yellow) and Phase (red) vs Distance (APD) curves as well as the average deflection (black) measured at $\omega / \omega_0 = 0.91$ (k_c = 3.2 N/m, f_0 = 31.8 kHz and R_{tip} = 108 nm) (b) The interaction stiffness k_{int} (yellow) and interaction damping γ_{int} (red) extracted from the APD curves in (a) as well as the average force calculated from the average deflection by multiplication with k_c.

Every approach (and retract) curve showed oscillations in the amplitude and phase, although the number of visible liquid layers N varied ($N_{av} = 6.9 \pm 2.9$). In the present magnetic drive experiments N_{av} was significantly larger than reported before for the acoustic drive measurements (Chapter 5, $N_{av} = 4.8 \pm 2.2$). Simultaneously with the APD curves we also monitored the average deflection of the cantilever (Fig. 6.2(a) and

(b), black curves). From the deflection we can conclude that, after the amplitude has gone to zero, one more layer of OMCTS is left between the tip and the surface, which will rupture at a force of approximately F_r = 1.2-1.5 nN. This instantaneous rupture is where we position our 'zero' in Fig. 6.2.

Figure 6.2(b) shows k_{int} (yellow) and γ_{int} (red) extracted from the APD curves of Fig. 6.2(a). The conservative k_{int} has the shape of an exponentially decaying cosine, characteristic for the oscillatory forces [3]. When we fit k_{int} with an exponentially decaying cosine (see Chapter 5), the average amplitude of the stiffness $K_{int} = 5.5 \pm 0.6$ N/m. This is approximately 4x as large as the stiffness found in our acoustic drive measurements of Chapter 5. Taking into account the Derjaguin approximation, (F/R and thus K_{int}/R is constant) and the larger tip radius in the present results (Fig. 6.3(a), magnetic drive, R_{tip} = 90-110 nm vs Fig. 6.3(b), acoustic drive, R_{tip} = ~25 nm, see also Chapter 5), we find that the k_{int} presented in this paper is consistent with the k_{int} found in our acoustic drive measurements. The larger absolute values of the force also explain why the number of visible layers (described above) is significantly larger in the present measurements [18].

The dissipative γ_{int} (Fig. 6.2(b), red curve) is zero, within the noise, for z_c > 4-5 nm. However, upon further approach, distinct peaks, similar to our acoustic drive measurements [9], become visible. The maxima in γ_{int} coincide with the maxima in k_{int} (or the repulsive part of the oscillatory forces as shown in the upward bending of the cantilever, Fig. 6.2(b) black curve) and the peaks are superimposed onto a monotonic Reynolds-like increase in the damping.

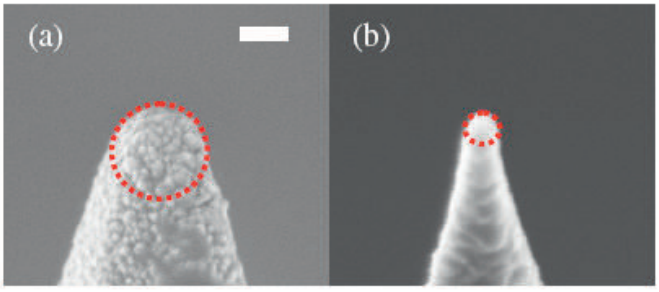

Figure 6.3 (a) SEM image of a tip typically used in the magnetic drive measurements (scale bar is 100 nm) (b) SEM image of a tip used in acoustic drive measurements. The red circles correspond to tip radii of 103nm (a) and 29nm (b).

We repeated the same measurements for various drive amplitudes (0.05 nm < A_0 < 0.2 nm) and approach speeds (0.4 to 6 nm/s). Furthermore, we used drive frequencies close to and well below the resonance frequency (0.05 < ω / ω_0 < 0.95). For all

measurement conditions, we found quantitatively the same results (within the experimental error) for both k_{int} and γ_{int} . Only for $\omega / \omega_0 < 0.15$, a decrease in the signal-to-noise ratio for γ_{int} overshadows the peaks in the dissipation. This latter aspect might explain why no peaks in γ_{int} were observed in very early experiments carried out at low drive frequency ($\omega / \omega_0 = 0.035$) [10].

6.4 Discussion

The present results display an excellent agreement with our earlier acoustic drive measurements (Chapter 5) regarding the absolute value k_{int} and the existence of distance-dependent features in γ_{int} . If we heuristically normalize γ_{int} by the tip radius, then also the height of the dissipation peaks agrees reasonably well with the acoustic drive measurements. Interestingly, however, the position of the peaks in γ_{int} is different for both measurement techniques. While for the acoustic drive measurements the peaks were found at the attractive part of the oscillatory forces, for the measurements described in this paper the maxima in γ_{int} are found at the repulsive part. However, features in γ_{int} have been observed before to vary in position relative to the maxima in k_{int}. Patil et al. [7] found that the maxima in γ_{int} coincide with the maxima in k_{int} at low approach speeds (< 0.5 nm/s), while they found minima in γ_{int} at the maxima in k_{int} at high approach speeds (> 0.5 nm/s). They argue that this might be a jamming effect for higher approach speeds. While our measurements did not display such a dependence on the approach speed, the jamming concept might still provide an explanation for the different relative location of the peaks in the dissipation and the maxima of the conservative force as compared to our earlier acoustic drive measurements: jamming is expected to depend strongly on the geometry, i.e. on the radius and on the roughness of the tip. The present magnetically coated cantilevers display a much larger tip radius than uncoated ones (see Fig. 6.3), which might be expected to favor jamming. However, the high resolution SEM pictures also clearly demonstrate an increased roughness of the tip, which might have the opposite effect. We defer a detailed analysis of the effect of tip radius and tip geometry to a numerical future study using molecular dynamics simulations.

6.5 Summary

In summary, we have presented magnetic drive AFM measurements of the conservative interaction stiffness and the dissipative interaction damping. Our measurements unequivocally demonstrate the existence of peaks in the dissipation related to the layer structure of the confined OMCTS films. The interaction stiffness is consistent with acoustic drive measurements and there are indeed distance dependent features in the damping. However, the maxima in the damping are at a different position compared to our acoustic drive measurements. We suggest that the confinement-volume (or tip-radius) might explain the observed differences.

Acknowledgement

We thank P. Markus, J. Flach, P. de Wolf and S. Lesko (Bruker corporation) for the technical support, supplying the MAD module and the fruitful discussions. We thank K. Smit for the technical support and M. Smithers for the SEM images. This work has been supported by the Foundation for Fundamental research on Matter (FOM), which is financially supported by the Netherlands Organization for Scientific Research (NWO).

References

[1] J.C.T. Eijkel and A. van den Berg, *Microfluid Nanofluid* **1**, 249 (2005)
[2] B.N.J. Persson and F. Mugele, *J. Phys. Condens. Matter* **16**, R295 (2004)
[3] J.N. Israelachvili, *Intermolecular and Surface Forces* (Academic London 1991).
[4] J. Klein and E. Kumacheva, *Science* **269**, 816 (1995)
[5] T. Becker and F. Mugele, *Phys. Rev. Lett.* **91**, 166104 (2003)
[6] L. Bureau, *Phys. Rev. Lett.* **104**, 218302 (2010)
[7] S. Patil, G. Matei, A. Oral and P.M. Hoffmann, *Langmuir* **22**, 6485 (2006)
[8] A. Maali, T. Cohen-Bouhacina, G. Couturier and J.-P. Aimé, *Phys. Rev. Lett.* **96**, 086105 (2006)
[9] S. de Beer, D. van den Ende and F. Mugele, *Nanotechnology* **21**, 325703 (2010)
[10] S.J. O'Shea and M.E. Welland, *Langmuir* **14**, 4186 (1998)
[11] G.B. Kaggwa, J.I. Kilpatrick, J.E. Sader and S.P. Jarvis, *Appl. Phys. Lett.* **93**, 011909 (2008)
[12] S.J. O'Shea, *Phys. Rev. Lett.* **97**, 179601 (2006)
[13] W. Hofbauer, R.J. Ho, R. Hairulnizam, N.N. Gosvami and S.J. O'Shea, *Phys. Rev.* B **80**, 134104 (2009)
[14] B.M. Borkent, S. de Beer, F. Mugele and D. Lohse, *Langmuir* **26**, 260 (2010)
[15] J.L. Hutter and J. Bechhoefer, *Rev. Sci. Instrum.* **64**, 1868 (1993)
[16] S. de Beer, P. Wennink, M. van der Weide – Grevelink and F. Mugele, *Langmuir* **26**, 13245 (2010)
[17] I. Revenko and R. Proksch, *J. Appl. Phys.* **87**, 526 (2000)
[18] We would like to add, that we obtained these consistent results only for 4 out of 26 cantilevers. The remainder of the cantilevers were discarded due to contamination (showing up as large variations in the individual measurements curves and / or an artificial attractive force on top of the oscillatory solvation forces) or an undefined tip geometry (local roughness due to the Co-Cr coating) resulting in a lower force than expected from the Derjaguin approximation. See also L.T.W. Lim, A.T.S. Wee and S.J. O'Shea, *Langmuir* **24**, 2271 (2008)

Chapter 7

Molecular Dynamics Simulations

In Chapter 5 and 6 we have shown that, when we confine a liquid between the AFM tip and a solid surface, the response of the AFM cantilever is entirely different from the response in the bulk liquid. Upon confinement, the discrete nature of the liquid becomes visible, resulting in the observation of the conservative oscillatory solvation forces. Moreover, we observe that, in addition to the change in static behavior, also the dynamic behavior and dissipation in the confined liquid change significantly. When a liquid is confined between an AFM tip and a solid surface, the properties of a particularly small volume are probed (~ zeptoliter = 10^{-21} liter). Within this small volume, we have approximately 100-500 molecules. Because of the small scales and the observation of distance-dependent density variations, it is obvious that at least several aspects of the confined liquid can no longer be described by continuum theory and the bulk properties of the liquid. For that reason, we use Molecular Dynamics (MD) simulations to get a better understanding of the static and dynamic behavior of a confined liquid.

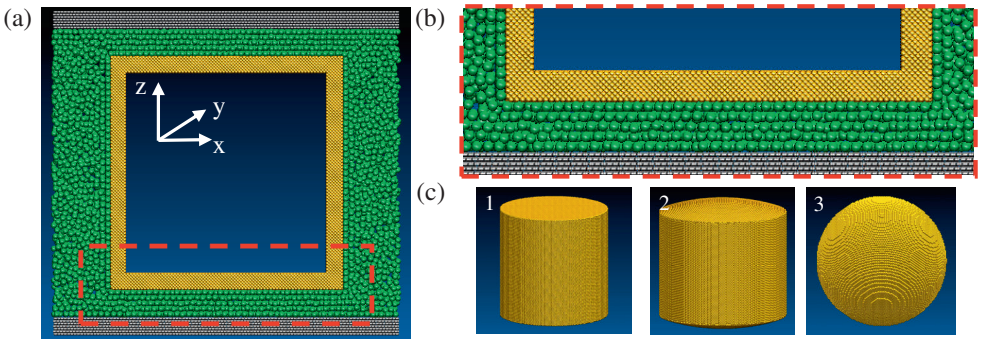

Figure 7.1 The setup of our MD simulations. (a) Sideview of the simulation box for the cylindrical tip. (b) Magnification of the red dashed square in (a). (c) The different tip geometries used for the simulations, 1: cylindrical tip, 2: tip with apex of R = 45nm, 3: spherical tip with radius R = 15nm.

Figure 7.1 shows our simulation setup. The simulation box consists of ~100 000 liquid molecules. In the middle of the box we have placed a fixed tip-shaped object and at the top and the bottom of the box two fixed walls. The molecules confined between the tip and the walls are in equilibrium with the molecules in the bulk. In our simulations we varied the distance between the walls and the tip. At each distance the system was separately simulated. Moreover, we performed simulations with different tip-shaped objects (Fig. 7.1(c)). The results of the simulations can be found in Chapter 8.

In this chapter we will describe the basic principles of MD simulations and the theoretical background that is needed to extract the properties of interest from the simulations.
For a complete overview of MD and further background information we refer to textbooks like [1] and [2].

7.1 Molecular Dynamics

In MD simulations Newton's classical equations of motion are solved for a set of particles. Setting up a MD simulation is very similar to setting up an experiment [3]. In both cases we apply the following procedure: First we decide what we want to measure. Then the sample is prepared. Next the sample is brought into the measurement-device and equilibrated. After that, the sample is measured long enough and with enough repetitions to account for statistical noise. Finally, the measurement-data are analyzed and interpreted, leading to the final results and conclusions. Also the pitfalls are comparable: e.g. the sample is not prepared correctly or the system has not yet reached equilibrium.

Figure 7.2(a) shows the flowchart of our MD program. We start the program with the initialization in which we define the input parameters (e.g. temperature, time step, total simulation time) and the initial positions and velocities of the particles. In the next step, we start the core of the simulation program. The forces on all the particles are calculated (see also Chapter 7.2). Then we solve the equations of motion (Newton's equation, see also Chapter 7.3) and calculate and save the quantities we want to measure (observables, see also Chapter 7.4). We repeat this procedure until the end of the total simulation time. Finally, we save the average values of the observables and the final position and velocity of the particles for in case we want to continue the simulations later on.

The calculation of the force on the N particles is computationally the most expensive part of the program. In this step, we need to find the total force applied on each particle by all the other particles (N x (N-1) calculation steps). However, we can significantly reduce the amount of calculations by using some computation tricks. First of all, we introduce a cut-off of the interaction potential (see also Chapter 7.2), so that particles far away from each other do not interact. Also, we use a grid-list [1], in which we label the particles with respect to their position and subsequently only calculate the interactions between particles which are close to each other. Moreover, since the force between particle i and j (F_{ij}) is the opposite of the force between particle j and i (F_{ji}) (that is $F_{ij} = -F_{ji}$), we only need to calculate half of the total number of interactions: $0.5 \cdot (N \text{ x } (N\text{-}1))$.

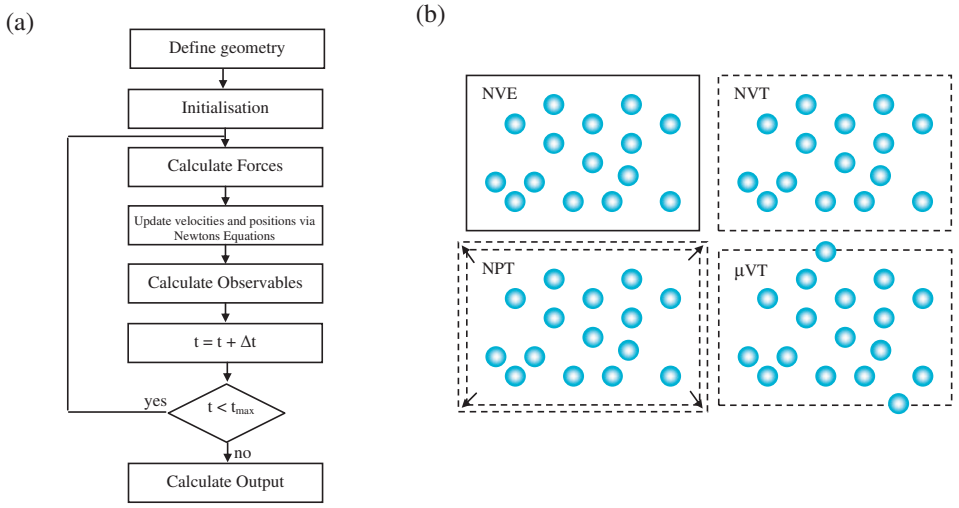

Figure 7.2(a) Flow-chart of a typical Molecular Dynamics program. (b) The different ensembles used in MD simulations (see text for more info).

An MD simulation in its most basic form consists of a system with N particles in a fixed volume V. Since we solve Newton's equations of motion for the trajectories of the particles and since on this level all forces are conservative, also the energy E in the system is conserved. Therefore a conventional MD simulation is equivalent to a micro-canonical (*NVE*) system. An *NVE* ensemble corresponds to an isolated system (Fig. 7.2(b)). However, in most experimental setups, the sample is in equilibrium with its surroundings. Therefore, we may want to perform simulations at a set pressure P and /or temperature T (*NVT* or *NPT* ensemble). In an *NVT* ensemble, the system is allowed to exchange energy with the surroundings, as denoted by the dashed lines in Fig. 7.2(b). When simulating in *NVT*, the velocities v_i of the particles are scaled, such that they represent the correct temperature following the equipartition theorem: $\frac{3}{2}k_BT = \frac{1}{2}m < \vec{v}^2 >$, with k_B the Boltzmann constant and m the mass of the particles, see also Chapter 7.5. Various algorithms have been developed for *NVT* simulations, like the Berendsen [4], Andersen [5] and Nosé-Hoover thermostats [6]. Using the Berendsen thermostat the velocities of the particles are gradually scaled towards the correct temperature using a time constant that defines the rate of change of the velocities. An Anderson thermostat randomly adjusts the velocities of the particles sampling from a Maxwell distribution. The Berendsen and Andersen thermostat are easy to implement and will guarantee a quick equilibration towards the chosen temperature. However, the Berendsen thermostat does not lead to a canonical (Maxwell-Boltzmann) distribution of the velocity. Using the Andersen thermostat the velocities of the particles are randomly adjusted. Therefore, this thermostat is inappropriate if we want to study the transport-properties of the system, like the diffusion of the particles. Also, both thermostats do not conserve the energy in the system. A Nosé-Hoover thermostat is an algorithm to adjust the equations of motion that leads to the correct canonical distribution, while the velocities are gently adjusted. Therefore, using a Nosé-Hoover thermostat, the transport-properties can be more realistically probed then for an Anderson thermostat. However, for the study of transport-properties it is always better to perform the simulations in *NVE* [1], since in *NVE* the dynamics of the system is not affected by the user-set control-parameters.

In isothermal-isobaric MD, or *NPT* MD, both the temperature T and the pressure P are controlled using a thermostat and a barostat respectively. *NPT* MD is equivalent to a piston-closed system that is allowed to exchange kinetic energy with the surroundings. In barostatted MD simulations, the volume of the simulation-box is varied to adjust the pressure in the system, as denoted by the arrows in Fig. 7.2(b). To incorporate a barostat in MD, various algorithms have been developed (see e.g. [8]). Toxvaerd developed an algorithm that minimizes the change in dynamics and leads to the correct fluctuations in the system [9].

In grand canonical, or μVT MD simulations, the chemical potential μ, the volume and the temperature are kept constant. As *NPT* MD, μVT MD corresponds to most lab-situations: The studied system is in equilibrium with the surroundings. The chemical potential can be measured and controlled using the Widom particle insertion method [10]. In this method virtual test particles are inserted in and removed from the

simulation box. The difference in potential energy before and after insertion or removal leads to the excess chemical potential. This method, however, does not work for high density system [1], since virtual particle insertion will lead to large variations in the measured potential energy.

In our simulations we first equilibrate our bulk liquid (bulk liquid: all molecules that are more than five molecular distances σ away from each solid surface) to the same temperature using an Anderson thermostat for 10ps. Then equilibration of the bulk liquid is continued for 58.5ns by controlling the temperature and the pressure using a Toxvaerd thermostat and barostat respectively. The final simulations, from which we extract the static and dynamic liquid properties we want to study, are performed in the *NVE* ensemble, to ensure that we do not affect the system by control-parameters.

7.2 Interaction potential

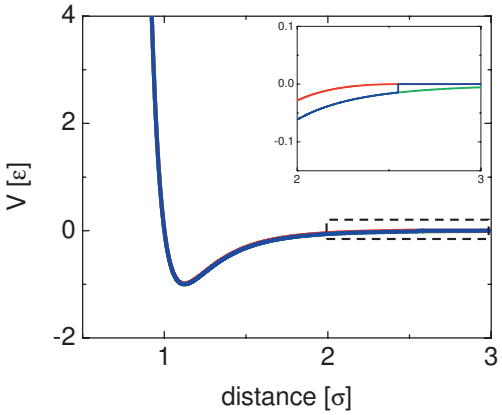

Figure 7.3 The Lennard-Jones (LJ) potential, green: LJ potential, blue: cut-off LJ potential, red: cut-off, shifted and corrected LJ potential. The inset shows a magnification of the potential in the dashed box.

In Molecular Dynamics the particles interact via a pre-defined potential. Depending on the studied system, a variety of potentials can be used, like the hard sphere potential or the square well potential. To take into account the attractive van der Waals forces and the repulsive force due to Pauli's exclusion principle, the Lennard-Jones potential is often used [11]:

$$V_{LJ}(r_{ij}) = 4\varepsilon\left(\left(\frac{\sigma}{r_{ij}}\right)^{12} - \left(\frac{\sigma}{r_{ij}}\right)^{6}\right), \qquad (1)$$

where r_{ij} is the distance between particle i and j, ε is the depth of the potential well and σ is the distance at which the potential is zero.
Figure 7.3(a) (green curve) shows the Lennard-Jones (LJ) potential. To calculate the force between particle i and j we use the derivative of eq. (1): $F = -dV_{LJ} / dr_{ij} = -V_{LJ}^{'}(r_{ij})$.
As mentioned in Chapter 7.1, to reduce the computation time, the potential is cut-off at large distances (in our simulations $r_{cut} = 2.5\sigma$, see Fig. 7.3(a) blue curve). However, this would mean that particles can move in and out the interaction volumes of other particles, resulting in jumps in the potential and thus total energy of the system. Therefore the cut-off potential is shifted upward and corrected, such that both the potential and the force smoothly approach zero (Fig. 7.3(a), red curve), via:

$$V_{shift}(r_{ij}) = \begin{cases} V_{LJ}(r_{ij}) - V_{LJ}(r_{cut}) - V_{LJ}^{'}(r_{cut})(r_{ij} - r_{cut}) & r < r_{cut} \\ 0 & r > r_{cut} \end{cases}. \qquad (2)$$

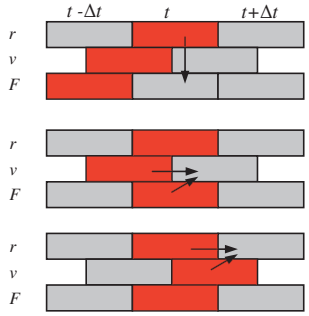

Figure 4 Schematic representation of the leap-frog Verlet algorithm.

7.3 Integration of the equations of motion

Once we know the forces acting on all particles, we can solve the equations of motion. For this we need an algorithm which conserves the energy of the system (and so is time reversible), is computationally inexpensive, is accurate for 'large' time-steps Δt and stable for long times. The most commonly used algorithm in MD is the leap-frog Verlet algorithm [1]. The algorithm is a special form of the original Verlet algorithm [12]. While the position r is calculated at integer time-steps, the velocity v is evaluated at half-integer time-steps:

$$v(t + \Delta t/2) = v(t - \Delta t/2) + \frac{F(t)}{m}\Delta t,$$

$$r(t + \Delta t) = r(t) + v(t + \Delta t/2)\Delta t, \qquad (3)$$

where F is the total force on the particle and m is the mass of the particle.
Figure 7.4 shows the leap-frog Verlet scheme: From the positions of the particles, the interaction forces between the particles are calculated. With the total force on each particle and the velocity at $(t-\Delta t/2)$, we calculate the velocity at $(t+\Delta t/2)$. Finally, from the velocity at $(t+\Delta t/2)$ and the positions at t, we calculate the positions at $(t+\Delta t)$.
The Verlet algorithm is time-reversible, has no drift in the total energy, is computationally inexpensive and is fourth order accurate in the positions and second order accurate in the velocities.

7.4 Periodic boundary conditions

In Molecular Dynamics we want to probe the properties of a macroscopic system or (as in our case) a molecular system in equilibrium with its macroscopic surroundings. Nevertheless, the number of particles that can be handled in MD is limited to maximum a few million. Therefore we need boundary conditions that act as infinite bulk surroundings. This is achieved by applying *periodic* boundary conditions [1, 2].
When we use *periodic* boundary conditions, a particle interacts with all particles within the cut-off distance. In practice this means that, when a particle is situated at the boundary of the box, it interacts with particles on the opposite side of the box (denoted by the red arrows in Fig. 7.5(a)). Moreover, when a particle moves out of the box, it reappears on the other side of the box (denoted by the black arrows in Fig. 7.5(a)). In this way, we simulate an infinite bulk system.

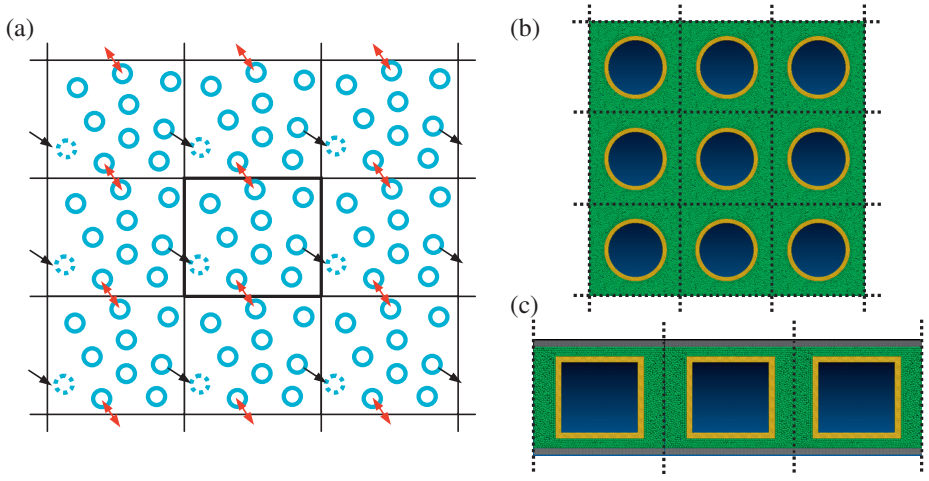

Figure 7.5(a) Schematic representation of the periodic boundary conditions in MD simulations. Topview (b) and sideview (c) representation of our simulation box with our periodic boundary conditions.

In our simulations we use periodic boundary conditions in the *xy* plane. Hence, we simulate an infinite amount of liquid particles between two infinitely large walls and an infinite amount of tips periodically arranged between both walls (see also Fig. 7.5(b) and (c)).

7.5 Observables and Characterization

With the above described techniques we can perform MD simulations. But, we also want to extract data from our simulations. From the positions, velocities and interactions of the particles we can extract the most basic observables: Kinetic plus potential energy $E_{tot} = E_{kin} + E_{pot}$, temperature T, pressure P and force F (e.g. on a built-in AFM tip). These observables are calculated and saved for each time-step to monitor the evolution of the system during equilibration and for the final analysis. Moreover, the calculated temperature and pressure at each time-step are directly used to correct the position and velocities of the particles in *NPT* simulations. The basic observables are calculated as follows [1]:

Energy:
The total energy is given by the sum of the potential energy and the kinetic energy in the system. The potential energy is determined by adding up all the interactions between the particles calculated from the Lennard-Jones potential:

$$E_{pot} = \sum_{i=1}^{N} \sum_{j=i}^{N} V_{shift}\left(r_{ij}\right) . \tag{4}$$

The kinetic energy is calculated from the velocities v_α (α is x, y or z) of all the particles:

$$E_{kin} = \frac{1}{2} m \sum_{i=1}^{N} \left(v_{i,x}^2 + v_{i,y}^2 + v_{i,z}^2\right). \tag{5}$$

Please note that velocity is evaluated at half-integer time-steps (see Chapter 7.3). So to find the kinetic energy at integer time-steps, we need to calculate the velocity at integer time-steps via $v_\alpha = \frac{1}{2}\left(v_\alpha(t - 0.5\Delta t) + v_\alpha(t + 0.5\Delta t)\right)$.

Temperature:
To determine the temperature we use the kinetic energy and the equipartition theorem:

$$T = \frac{2E_{kin}}{k_B N_f}, \tag{6}$$

where $N_f = 3N\text{-}M$ is the number of degrees of freedom, with M the constraints.

Pressure:
For the calculation of the pressure in the liquid we use an expression derived from the virial equation [13]. The stress is evaluated between all particles and in each direction $\alpha\beta$ (= xx, yy, zz, xy, xz and yz) and devided by the volume V:

$$P_{\alpha\beta} = \frac{1}{V}\sum_{i=1}^{N} m v_{i,\alpha} v_{i,\beta} + \frac{1}{V}\sum_{i<j} r_{ij,\alpha} F_{ij,\beta} \,. \tag{7}$$

To run the barostat the average pressure $P = \frac{1}{3}\left(P_{xx} + P_{yy} + P_{zz}\right)$is compared to the setpoint pressure.
The above described thermodynamic observables tell us where in the phase diagram of the system we perform our simulations.
A second class of observables is the characteristics of the local structure and dynamics of the liquid that is studied (e.g. pair distribution function, structure factor, diffusion coefficient, (shear) viscosity) [1].

Pair distribution function
As explained in Chapter 1, the pair distribution function $g(r)$ represents the correlation between the positions of particles due to the intermolecular interactions. To obtain $g(r)$, we calculate the average number density at each distance r of all particles and normalize it by the total average number density in the simulation box:

$$g(r) = \frac{1}{N\rho_{bulk} 4\pi r^2 dr}\sum_{i=1}^{N} N_r(r), \tag{8}$$

where N_r is the number of particles between (r-dr/2) and (r+dr/2) with respect to the position of particle i.
The pair distribution function is of special interest for our study of confined liquids. It will show whether the position-correlation increases within our confined volume. Moreover, the shape of $g(r)$ will indicate whether we can speak of confinement-induced phase transitions: a solid structure will give rise to many sharp maxima in the $g(r)$, while the periodicity between the maxima is no longer equal to the molecular size (see e.g. Chapter 1 of Ref. [14]).

In-plane Nearest neighbors
The pair distribution function will give us a first indication whether our confined molecules are liquid-like or solid-like. However, if we want to know the specific structure when the liquid molecules solidify, we need more information. To make the distinction between a cubic and hexagonal structure, the number of nearest neighbors N_{NN} can be calculated:

$$N_{NN} = \frac{1}{N_c}\sum_{i=1}^{N_c} N_{NN,i} \,, \tag{9}$$

where N_C is the number of particles in the region of interest (e.g. under the tip) and $N_{NN,i}$ is the number of particles within inplane distance d$r = 1.35\sigma$ and height d$z = 0.2\sigma$ of particle i.
Using this method a cubic structure will result in $N_{NN} = 4$, while a hexagonal structure will give $N_{NN} = 6$.

Diffusion
The above discussed observables describe the static properties of the system. To study the dynamic or transport-properties of the system, we use the Mean Square Displacement (MSD) of the particles:

$$MSD = \frac{1}{N}\sum_{i=i}^{N}\left(r(t)-r(0)\right)^2 . \tag{10}$$

For long times the MSD of liquid molecules varies linearly with time. The slope is then given by $2dD$, with d the dimensionality of the system and D the diffusion coefficient.

7.6 Force and Fluctuation-Dissipation Theorem

The above described observables characterize the molecular dynamics simulations and the studied system. However, in order to compare our simulations to the measurements described in Chapter 5 and 6, we need to make a direct link between the simulations and the experiments. In the experiments we measure the effect of the confinement-induced changes in liquid properties on the tip of the cantilever, resulting in variations in the conservative interaction stiffness and dissipative interaction damping. So, to directly compare our measurements with the performed simulations we need to find the conservative and dissipative forces on the simulated tip.

The average conservative force is found by adding up the interaction force between the liquid particles and the particles of the structure that imposes the confinement (e.g. the simulated tip). This is the total force F_α (F_x, F_y or F_z) on the tip applied by the liquid molecules:

$$F_\alpha = \frac{1}{N_t}\sum_{n=1}^{N_t}\sum_{j=1}^{N_{tip}}\sum_{i=1}^{N} F_{\alpha,ij}(t_n), \tag{11}$$

where N_t is the total number of time-steps and N_{tip} is the number of tip-particles.

In early reports of simulations on the dissipative properties of confined liquids, non-equilibrium techniques were used (e.g. the solid surfaces were sheared) [15, 16]. The disadvantage of these techniques is that high (shear) velocities are needed to impose a

motion of the solid surfaces within the short timescales of the simulations (typically nanoseconds).
Instead, to obtain the dissipative forces from equilibrium MD simulations we use the generalized Langevin equation [17]. Under the tip the liquid molecules move around and collide with each other and the tip. This induces force-fluctuations. Affected by these random force-fluctuations, on the larger timescales of typically milliseconds, a tip would come in motion described by [17]:

$$m\ddot{x}(t)+\int_0^\infty \zeta(t')\dot{x}(t-t')dt'+kx(t)=f_B(t), \tag{12}$$

where the m is the mass and k is the spring constant and $f_B(t)$ is the random force, described by:

$$\begin{aligned} &< f_B(t) >= 0 \\ &< f_B(0) f_B(t) >= k_B T \zeta(t). \end{aligned} \tag{13}$$

The last relations directly follow from fluctuation-dissipation [17].
The second term in eq. (12) describes the velocity dependent friction force incorporating the memory of the system. For Markovian times – that is: the motion of the particle is much slower than the decay of the system memory [17] – this term can be approximated by:

$$\int_0^\infty \zeta(t')\dot{x}(t-t')dt' \cong \dot{x}(t)\int_0^\infty \zeta(t')dt' = \gamma\dot{x}(t). \tag{14}$$

Thus:

$$\gamma=\int_0^\infty \zeta(t')dt'. \tag{15}$$

So, to find the damping γ felt by the tip for experimental timescales, we combine eq. (15) and fluctuation-dissipation (eq. 13):

$$\gamma=\frac{1}{k_B T}\int_0^\infty \langle f_B(0) f_B(t)\rangle dt. \tag{16}$$

So, in summary, first, since our simulation tip is fixed, we can calculate the conservative force on the tip via the average force applied by all the liquid molecules on the tip. Second, from the autocorrelation of the force fluctuations we derive the damping the fixed tip would have felt if it would move.

The above described average conservative force and the interaction damping can be compared to our measured conservative interaction stiffness (derivative of the force w.r.t. position) and dissipative interaction damping.

7.7 Rheology

Onsager's regression theorem states that the evolution of a spontaneous fluctuation is identical to that induced by an external disturbance [14]. Therefore $\zeta(t)$ should also be proportional to the step relaxation modulus. If we would oscillate our tip we would apply a strain ε of:

$$\varepsilon(t) = \varepsilon_0 \sin \omega t , \tag{16}$$

where ε_0 and ω are the amplitude and the angular frequency of the modulation respectively.
Consequently, the strain rate $\dot{\varepsilon}$ equals:

$$\dot{\varepsilon} = \omega \varepsilon_0 \cos \omega t . \tag{17}$$

Due to the modulation we create a stress-variation $S(t) = F / A$ (with $F = -3A\mu V/h$ for full slip, where A is the tip area, $\propto$is the shear viscosity, V is the gap volume and h is the gap height) in the system that equals [18]:

$$\begin{aligned} S(t) &= \int_{-\infty}^{t} \zeta(t-\tau)\dot{\varepsilon}(\tau)d\tau = \int_{0}^{\infty} \zeta(\tau)\dot{\varepsilon}(t-\tau)d\tau \\ &= \varepsilon_0 \left\{ \zeta'(\omega)\cos \omega t + \zeta''(\omega)\sin \omega t \right\} \end{aligned} , \tag{18}$$

with:

$$\begin{aligned} \zeta' &= \omega \int_{0}^{\infty} \zeta(\tau)\cos \omega\tau d\tau \\ \zeta'' &= \omega \int_{0}^{\infty} \zeta(\tau)\sin \omega\tau d\tau \end{aligned} , \tag{19}$$

where ζ' and ζ'' are the real and the imaginary part of the complex damping ζ^*. Hence, if we calculate the FFT of $\zeta(\tau)$, the imaginary part will be equivalent to the elastic response (or storage modulus G') and the real part will be equivalent to the dissipative response (or the loss modulus G'').

References:

[1] D. Frenkel and B. Smit, *Understanding Molecular Simulation from Algorithms to Applications*, Academic Press (1996)
[2] M.P. Allen and D.J. Tildesley, *Computer Simulation of Liquids*, Oxford University Press (1987)
[3] D. Frenkel, lecture Dynasoft workshop, Corsica (2010)
[4] H.J.C. Berendsen, J.P.M. Postma, W.F. van Gunsteren, A. Dinola, J.R. Haak, *J. Chem. Phys.* **81**, 3684 (1984)
[5] H.C. Andersen, *J. Chem. Phys.* **72**, 2384 (1980)
[6] W.G. Hoover, *Phys. Rev.* A **31**, 1695 (1985)
[7] W.G. Hoover, *Phys. Rev.* A **34**, 2499 (1986)
[8] S. Nosé and M. Klein, *Mol. Phys.* **50**, 1055 (1983)
[9] S. Toxvaerd, *Phys. Rev.* E **47**, 343 (1993)
[10] B. Widom, *J. Chem. Phys.* **39**, 2802 (1963)
[11] J.E. Lennard-Jones, *Proc. Roy. Soc.* **106**, 463 (1924)
[12] L. Verlet, *Phys. Rev.* **159**, 98 (1967)
[13] J.-P. Hansen and I.R. McDonald, *Theory of simple liquids*, Elsevier (2006)
[14] J.-L. Barrat and J.-P. Hansen, *Basic concepts for simple and complex liquids*, University Press Cambridge (2003)
[15] P.A. Thompson and M.O. Robbins, *Science* **250**, 792 (1990)
[16] J. Gao, W.D. Luedtke and U. Landman, *J. Phys. Chem.* B **102**, 5033 (1998)
[17] D. Chandler, *Introduction to Modern Statistical Mechanics*, Oxford University Press (1987)
[18] W.J. Briels, Linear response theory and Polymer Dynamics, Lecture notes Han-sur-Lesse, January 24-28 (2011)

Chapter 8

Viscous friction in confined liquid films

In this Chapter we present the results of equilibrium Molecular Dynamics simulations of a liquid confined between a solid surface and a tip. We use fluctuation-dissipation to extract the damping on the tip from our simulations. We show that the damping strongly depends on the distance between the solid surfaces, which is in agreement with the results presented in Chapter 5 and 6. Moreover, we observe that the damping strongly correlates with the structure and the diffusivity of the confined molecules. We show that, within the timescale of our simulations (~10ns) the molecular properties show predominantly liquid-like or solid-like behavior depending on the distance between the confining surfaces. Upon examination of the storage and the loss modulus, we find, surprisingly, that the confined liquid behaves quasi-Maxwellian with one or two dominant relaxation times in the probed time range when the damping shows a maximum and gel-like with an algebraically decaying memory function, indicating a series of relaxation times, in between the maxima in the damping.[1]

[1] S. de Beer, W.K. den Otter, D. van den Ende, W.J. Briels and F. Mugele, *submitted*

8.1 Introduction

Understanding the hydrodynamics of confined liquids is essential in numerous technological challenges, like e.g. the downscaling of fluidic devices [1] or the reduction of friction and wear [2]. When a liquid is confined between two solid surfaces, the molecules can assemble into layers. This gives rise to density variations and the conservative oscillatory solvation forces [3-18]. The existence of the oscillatory forces is by now experimentally well-established. However, how the anisotropy of the molecular density affects the hydrodynamics of the confined liquid is not yet clear. In recent Atomic Force Microscope (AFM) measurements, strong variations in the damping of the AFM cantilever were observed, in confined octamethylcyclotetrasiloxane (OMCTS, a simple model liquid) [4-8]. However, others reported visco-elastic effects for the same liquid [9,10] and changes in the relaxation time of the same confined liquid [10]. In addition, a similar variety of phenomena were reported for confined dodecanol [11] and water [9, 10]. On the other hand, confinement induced solidification was observed in Surface Forces Apparatus (SFA) measurements [12]. While others, studying the same system, reported visco-elastic effects [13], stick-slip motion [14] and layer-by-layer squeeze-out, which can be described by continuum theory [15]. All these observations seem to contradict. However, it was recently shown that different SFA measurement techniques (shearing at a thickness of a discrete number of liquid layers versus monitoring the layer squeeze-out) can result in different effective viscosities of the same liquid [16]. This is not surprising regarding the anisotropy and confinement dependent variations of the liquid density.

In this chapter we present Molecular Dynamics (MD) simulations of a Lennard-Jones (LJ) liquid confined between a fixed solid surface and an AFM-tip. Early simulations on the hydrodynamics of confined liquids [17, 18], were performed in non-equilibrium MD or Monte-Carlo. However, these methods were frequently challenged for the high (shear) velocities inherent to short time-scale simulations. In contrast, we employ equilibrium MD and the fluctuation-dissipation theorem [19, 20] to extract the conservative and dissipative forces felt by the confining tip. While previous studies already predicted a liquid-to-solid transition upon increasing confinement for either commensurate [21] or non-commensurate walls [22], we show that the confined molecules can behave liquid-like or solid-like depending on the exact distance between the confining surfaces.

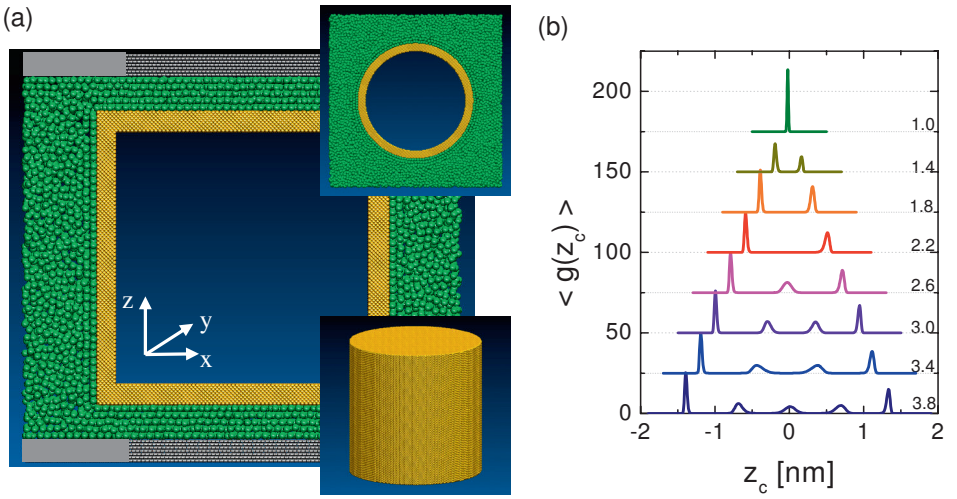

Figure 8.1(a) Side view cross-section of the simulation box at $y = 0$ (origin is in the middle of the box), upper inset: top-view cross-section of the box at $z = 0$, lower inset: cylindrical shaped tip in the middle of the box (H_{cyl} = 30 nm and R_{cyl} = 15 nm). (b) Density profiles between the tip and the solid surface for various tip-surface distances D, indicated by the number on the right. The curves are shifted by n·25 and $z_c = 0$ at $D/2$.

8.2 Materials and Methods

Figure 8.1(a) shows the configuration of our simulation box. The box consists of ~100 000 LJ particles which represent OMCTS molecules [23] (molecular diameter σ_l = 0.77 nm, interaction strength ε_l = 2.85 kJ / mol, density ρ_l = 957 kg / m^3). At the top and the bottom of the box we have built two fixed solid graphite surfaces constructed of LJ particles (honeycomb structure, in plane particle distance 0.142 nm, ε_w = 0.3598 kJ / mol, see e.g. [24]). The graphite was built up using multiple layers separated by σ_w = 0.34 nm. To allow for box-size variations and reduce the computational costs, we created a gradual (cosine-function based) transition from an 'all-atom' wall underneath the central part of the tip, for $r = \sqrt{x^2 + y^2}$ < 10 nm, to a smooth mathematical wall at r > 12.5 nm with the same interaction potential. We did not observe differences in static or dynamic behavior of the liquid particles above the all-atom wall or the mathematical wall. The boundaries were periodic in x and y, i.e. parallel with the walls. In the middle of the box we built a fixed golden tip in the shape of a cylinder with a radius of R_{cyl} = 15 nm and height of H_{cyl} = 30 nm. The tip is also constructed of LJ particles (fcc, lattice constant 0.408 nm, σ_{cyl} = 0.3 nm, ε_{cyl} = 6.84 kJ / mol). All particles interact via the 12-6 Lennard-Jones potential, which was cut off at 2.5 σ (see Chapter 7). For the interactions between different kinds of particles we used the Lorentz-Berthelot combining rules. The liquid particles are non-commensurate with

the solid surfaces. Since we created two confinement-volumes (top and bottom of the box), we performed two simulations in parallel. We are aware that the chosen simulation parameters only approximate an experimental setup. However, our goal is to obtain a qualitative (not quantitative) understanding of the experimental observations.

The equations of motion of the liquid particles were solved using the leap-frog Verlet algorithm [26, 27] with an integration time step of 40 fs. We performed equilibrium simulations for 35 gap widths (D = 0.5, 0.6 … 3.9 nm) between the tip and the surface. This was accomplished by varying the total distance between the two graphite surfaces, while the tip was kept fixed in position and size. Each simulation box, with a new distance D, was equilibrated to the same temperature $T^* = 0.88\ \varepsilon / k_B$ and pressure $P^* = 3.3\ \varepsilon / \sigma^3$ (close to the liquid-solid phase transition) in the bulk liquid for 58.5 ns using the Toxvaerd barostat and thermostat [28]. Particles were assumed to be in the bulk liquid when they were more than 5 σ from all solid surfaces. To adjust the pressure the volume was allowed to change parallel with the walls, i.e. the size of the mathematical wall increases / decreases. During the volume variations, the all-atom part of the walls and the distance between the two walls remained fixed. Equilibration was ensured by monitoring that the changes in total energy, $\langle P^* \rangle$, $\langle T^* \rangle$ and the average force on the tip $\langle F_{cyl} \rangle$ were zero. Next, the static and dynamic properties of the liquid (average number of particles under the tip $\langle N_{gap} \rangle$, diffusion $D_{xy} = (D_{xx}+D_{yy})/2$, number of nearest neighbors $\langle N_{NN} \rangle$) and both the conservative force $\langle F_{cyl} \rangle$ and dissipative interaction damping $\langle \gamma \rangle$ on the tip were extracted from 2-5 subsequent simulations of 16 ns. To eliminate interference of the barostat and thermostat with the dynamic properties of the liquid, these simulations were performed in *NVE* [25].

8.3 Analysis and Results

Figure 8.1(b) shows the equilibrium density profiles between the tip and the surface normalized by the bulk density for various values of the gap width D and averaged over 16ns. The curves have a pronounced oscillatory shape representing the layered assembly of the liquid molecules. As D decreases, the number of oscillations and thus number of layers between the tip and the surface decreases. This is also indicated by the colors and numbering in Fig. 8.2(a). At large D the transition from n to n-1 layers occurs with a periodicity of σ. At the final part of the 2-1 layer transition (D = 1.4 and 1.3 nm), the exact number of layers becomes less clear: Although only one layer fits between the two solid surfaces, the particles hop between the minima of the interaction potentials with both walls, showing up as two (lower) peaks in de density plot (Fig. 8.1(b)).

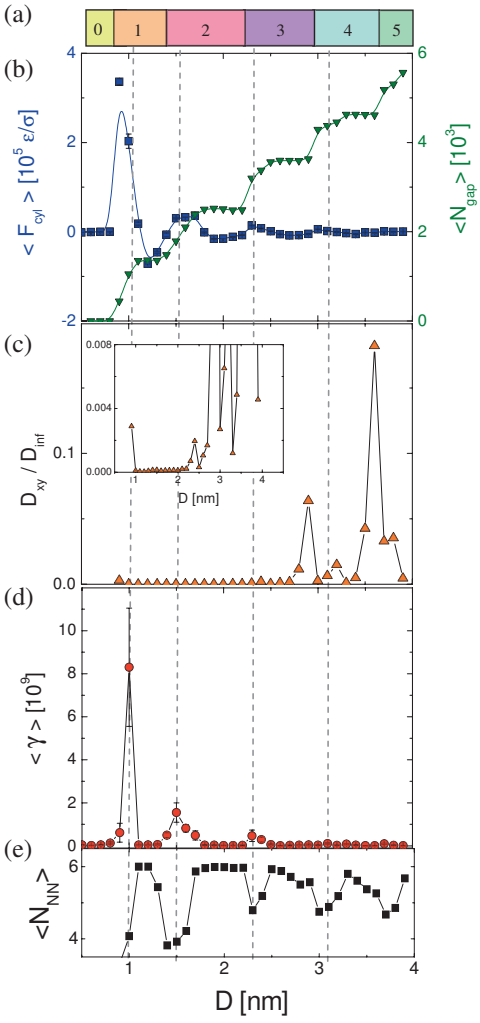

Figure 8.2(a) The number of layers under the tip. (b) The average force in the z direction on the tip $\langle F_{cyl} \rangle$ (blue squares) and the average number of particles under the tip $\langle N_{gap} \rangle$ (green downward triangles). (c) The diffusion coefficient in plane with the solid surfaces normalized by the diffusion coefficient in the bulk liquid. (d) The damping felt by the tip $\langle \gamma \rangle$ (red circles). (e) The average number of nearest neighbors $\langle N_{NN} \rangle$ of the particles under the cylinder. The gray dashed lines are positioned at the maxima of the damping to guide the eye.

8.3.1 Density and Force

The green downward triangles in Fig. 8.2(b) show the number of particles N_{gap} under the tip as D is varied. N_{gap} clearly correlates with the number of layers under the tip. As D is decreased (e.g. starting at D = 2.9 nm) we first observe a plateau in N_{gap}, which means that the particles are compressed in a denser structure. Upon compression of the layers in the plateaus of N_{gap}, the molecules configure themselves in different 3D structures, as indicated by the snapshots of Fig. 8.3.

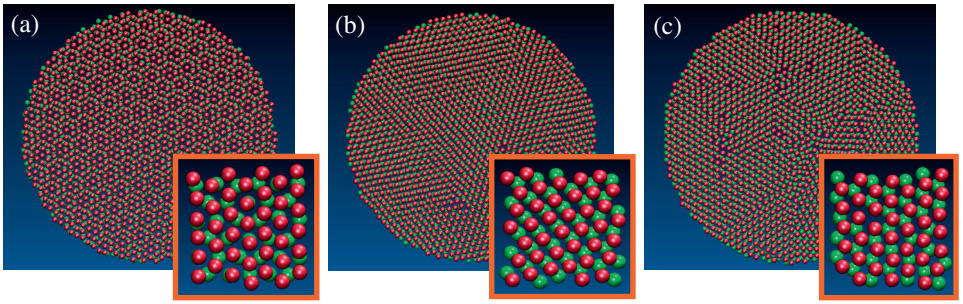

Figure 8.3 Configuration of the molecules confined between the tip and the surface (r < 15 nm) at (a) D = 2.2 nm, (b) 1.9 nm and (c) 1.7 nm. The insets show an amplification of the central region under the tip ($|x| \& |y| < 3.85$ nm).

Figure 8.3(a) shows the configuration of molecules at D = 2.2 nm. There are two layers between the tip and the surface. Each layer has an in plane hexagonal structure. Since σ = 0.77 nm, there is a lot a free space in the gap. At this distance the hexagons of the two layers are rotated with respect to each other. When the distance is decreased from D = 2.2 nm to D = 1.9 nm, N_{gap} remains the same and the molecules are in the same in plane hexagonal structure. However, the orientation of the two layers with respect to each other has changed. The molecules in the top layer mostly reside in between *two* molecules in the lower layer. However, in some regions, the molecules in the top layer are positioned above *three* molecules in the lower layer. When the distance is decreased from D = 1.9 nm to D = 1.7 nm, N_{gap} still remains the same and the molecules are still in the same in plane hexagonal structure. However, almost all molecules in the top layer reside on three molecules from the bottom layer. Moreover, the in plane hexagonal structure is no longer perfect, but shows defects and grain boundaries and in some regions the molecules have positioned themselves in an inplane cubic structure. The plateaus in N_{gap} are always followed by a gradual decrease N_{gap}, which is just before the transition from n to n-1 layers. After the transition we again observe a plateau.

The blue squares in Fig. 2(b) represent the average force on the tip $<F_{cyl}>$, which was determined by adding up the forces of all the liquid particles with the tip particles for

the top and the bottom of the box separately. $\langle F_{cyl} \rangle$ shows a clear modulation varying from attractive to repulsive forces, which is characteristic of the oscillatory solvation forces [3-18]. $\langle F_{cyl} \rangle$ is attractive in the plateaus in N_{gap}. On the other hand, when we observe the gradual decrease in N_{gap} $\langle F_{cyl} \rangle$ is repulsive [21]. The last and second last maxima in the $\langle F_{cyl} \rangle$ correspond to a pressure of 2 GPa and 261 MPa respectively, which is very similar to experimental observations [28].

8.3.2 Diffusion

Figure 8.2(c) shows the in plane diffusion coefficient D_{xy} of the molecules normalized by the bulk diffusion coefficient D_{inf}. D_{xy} and D_{inf} are extracted from the slope of the average Mean Squared Displacement of the particles between the tip and the surface and in the bulk respectively.
In agreement with the results of Landman et al. [21] the diffusion strongly oscillates with the distance between the tip and the surface. We find a maximum in the diffusion for a minimum in the density. Moreover, the diffusion also increases during the gradual decrease in N_{gap}.
Surprisingly, the strong variations in the diffusion coefficient are at large distances (D > 2.5 nm). For small distances the diffusion is close to zero. However, in the experiments we only see changes in the damping of the cantilever at D < 2.5 nm. So, the experimentally found variations in the damping can not directly be related to the diffusion of the molecules. This is not surprising regarding that in the experiment we probe a system property (liquid + confining surfaces), while the diffusion is a liquid property [29].

8.3.3 Damping

In the simulations the average force on the tip is constant. However, due to the discrete nature of the liquid the force fluctuates. The force fluctuations contain information about the dissipation via fluctuation-dissipation [30]. The damping γ, felt by the tip (if it would be able to move), is extracted via integration of the autocorrelation of the force fluctuations or the second theorem of fluctuation-dissipation:

$$\gamma = \frac{1}{k_B T} \int_0^\infty \langle dF(t) dF(t+\tau) \rangle d\tau$$

(see also Chapter 7), with $dF(t) = F(t) - \langle F_{cyl} \rangle$.

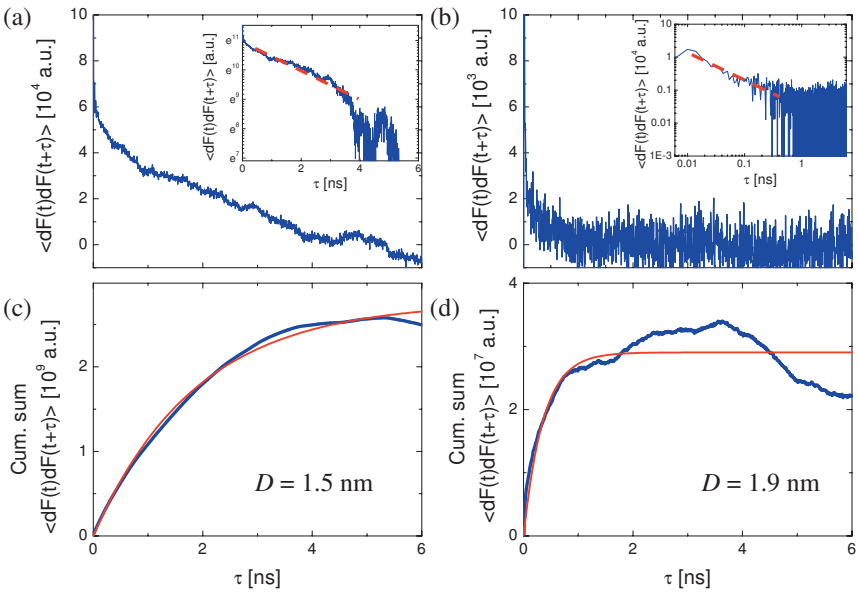

Figure 8.4 The autocorrelation of the force for (a) D = 1.5 and (b) D = 1.9 nm. The insets show the same data on a different scale (ln-lin for (a) and log-log for (b)). The blue curves in (c) and (d) show the cumulative sum of the data of (a) and (b) respectively and the red lines are the fitted curves.

Figure 8.4 shows two characteristic averaged curves of the autocorrelation of the force fluctuations at (a) D = 1.5 and (b) 1.9 nm. The curves are remarkably different. For D = 1.5 nm, $<dF(t)dF(t+\tau)>$ starts at a high initial value and slowly decays towards zero. On the other hand, for D = 1.9 nm the initial value is lower and the decay is much faster. Moreover, both curves decay differently towards zero. While for D = 1.5 nm we find an exponential decay (see insets of Fig. 8.4), for D = 1.9 nm the decay is algebraic. Figure 8.4(c) and (d) show the cumulative sum of the curves in (a) and (b) respectively. To find the damping and the relaxation time the curves are fitted with: $< dF(t)dF(t+\tau) >= \gamma\left(1-\exp(-\tau/\tau_{rel})\right)$, where γ is the plateau value and thus the damping and τ_{rel} is the decay time. Both γ ($2.8\cdot10^9$ a.u. for D = 1.5 nm and $2.9\cdot10^7$ a.u. for D = 1.9 nm) and τ_{rel} (1.9 ns for D = 1.5 and 0.36 ns for D = 1.9 nm) are significantly different in both graphs. In general, when we find a high γ, τ_{rel} is also high. The red circles in Fig. 8.2(d) correspond to the average plateau-values of, at each gap width D, 4-10 independent values of γ extracted from the simulations. The error bars denote the average uncertainty in the individual plateau values at each run and at each D. While the damping is indistinguishable from the noise for larger D, sharp peaks become visible for smaller D (around D = 2.3, 1.5 and 1.0 nm).
This is in excellent agreement with our experimental observations (Chapter 5 and 6), where we also found distinct peaks in the damping of the cantilever.

The maxima in the damping are found at distances where we find a gradual decrease of N_{gap} and where $<F_{cyl}>$ is repulsive. This is just before the transition from n to n-1 molecular layers.

8.4 Discussion

How can we explain these observations? What happens with the liquid molecules when we vary the distance between the tip and the surface?

8.4.1 Structure

Figure 8.5 shows typical snapshots of the configuration of the molecules at 4 different distances D (Fig. 8.5(a) 1.0, (b) 1.1, (c) 1.5 and (d) 2.0 nm). Figure 8.5(a) and (c) show the arrangement of the molecules at the peaks in γ. The molecules are clearly organized in an in-plane cubic formation of different orientations separated by disorganized grain boundaries. On the other hand, the molecules in Fig. 8.5(b) and (d) are perfectly arranged in an in-plane hexagonal structure. The latter snapshots resemble at distances where we find a valley in the damping.

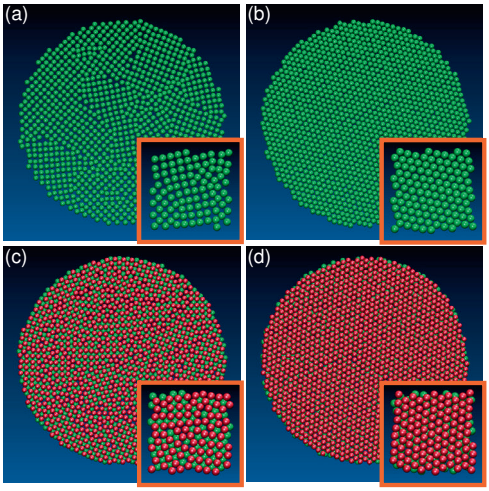

Figure 8.5 Snapshots of the molecules confined between the tip and the surface (r < 15 nm), (a) configuration at D = 1.0 nm, (b) 1.1 nm, (c) 1.5 nm and (d) 2.0 nm. The insets show an amplification of the central region under the tip ($|x| \& |y| < 3.85$ nm).

The relation between the damping and the arrangement of the molecules can be more quantitatively observed in Fig. 8.2(e), which shows the number of nearest neighbors N_{NN} (within dr = 1.35σ and dz = 0.2σ) of each molecule under the tip. For each

maximum in γ, we find a minimum in N_{NN} (close to 4, representing an in-plane cubic structure), while for the valley's in γ we find N_{NN} to be close to 6 (representing an in-plane hexagonal structure). This demonstrates a clear relation between the configuration of the molecules and the damping.
The observation of different configurations of the molecules in confinement was observed before in MD simulations of the squeeze-out of layered liquids [31, 32]. Just before the transition from n to n-1 layers the molecules rearrange from a hexagonal structure to a cubic structure to release the energy stored in the elastically deformable surfaces. In our simulations the walls can not be deformed, but we find the cubic structure at the same position: just before the transition from n to n-1 layers (see also N_{gap} in Fig. 8.2(b)).

8.4.2 Diffusion versus Damping

Figure 8.6 shows the average Mean Squared Displacement <MSD> of the molecules confined between the tip and the solid surface for the same D's as in Fig. 8.5. For D = 1.0 nm the molecules are diffusive in x & y and non-diffusive in z (the latter to be expected for a single layer). While for D = 1.5 nm the molecules are diffusive in both x & y and z.

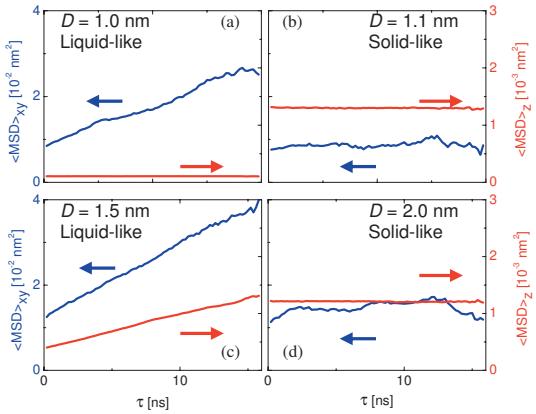

Figure 8.6 The average Mean Squared Displacement (<MSD>) of the molecules under the tip in x & y $<MSD>_{xy} = <MSD>_{xx} + <MSD>_{yy}$ (blue curves) and z (red curves) for (a) D = 1.0 (b) 1.1 (c) 1.5 and (d) 2.0 nm.

Upon examination of the trajectories of the individual molecules, we find that the diffusion at D = 1.0 and 1.5 nm is mainly in the disorganized grain boundaries between the in-plane cubically structured regions and via the growth and shrinkage of the different regions. For D = 1.1 and 2.0 nm the molecules are non-diffusive in x & y and z. Now, by comparing these results with γ (Fig. 8.2(d)), we observe that the

molecules behave diffusive (or liquid-like) when we find a peak in γ and that the molecules do not diffuse (are solid-like) in between the maxima in γ. So, within our simulation time, the confined liquid can behave like a solid or a liquid depending on the distance between the solid surfaces.
These results might explain the different observations in SFA measurement, where solid-like behavior was reported in shear measurements [12, 14] and bulk liquid behavior was found during the squeeze-out of the liquid layers [15, 16]. The shear measurements are performed when the average force is zero where we find an in-plane hexagonal structure and no diffusion. On the other hand, just before the squeeze-out of the liquid layers, the molecules rearrange into a cubic structure [31, 32], where we find liquid-like behavior. Note that we find an increased damping only for the last layers, which is consistent with the reports on the layer squeeze-out [15, 16], that could be described by continuum theory and the bulk properties of the liquid except for the last 2-3 layers.

8.4.3 Rheology

To learn more about the dynamic properties of the liquid, we calculated the storage and loss modulus of the confined molecules (Chapter 7, C' is ζ'' and C'' is ζ').

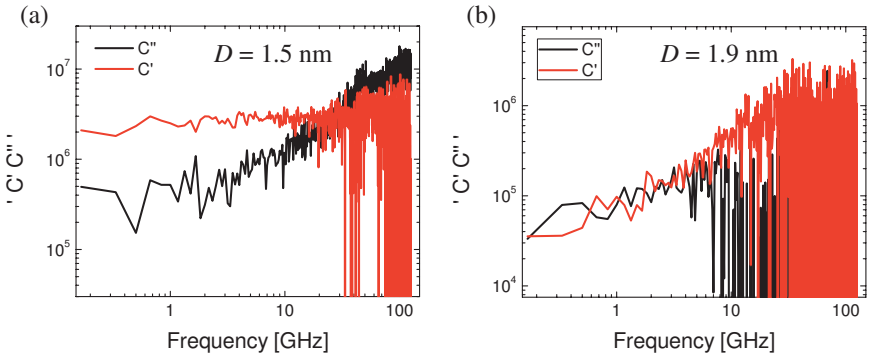

Figure 8.7 The storage C' and loss C'' moduli of the confined liquid for (a) D = 1.5 and (b) 1.9 nm.

Figure 8.7(a) shows the C' and C'' for D = 1.5 nm (in de second peak in the damping, see also Fig. 8.2(d)). The storage modulus, which represents the elastic response of the confined liquid molecules, is approximately constant over this frequency range. On the other hand, the loss modulus, which represents the dissipative properties, increases linearly with slope 1. This response is very close to the typical characteristics a soft glassy material [33]. This conclusion is consistent with the exponential, Maxwellian decay found for the autocorrelation in the force fluctuations (see inset Fig. 8.4(a)), which indicates liquid-like behavior for low frequencies. However, to be sure, we

would need longer simulations in order to also analyze the C' and C'' for lower frequencies.
Figure 8.7(b) shows C' and C'' for D = 1.9 nm (in between the peaks in the damping). Both the storage modulus and the loss modulus increase with a slope of approximately 0.5. This response indicates gel-like behavior and the existence of several relaxation processes. The linear increase of both C' and C'' is consistent with the algebraic decay of the autocorrelation of the force fluctuations.
These results indicate the behavior of the liquid is more complex than just a viscous liquid or an elastic solid. However, to obtain more knowledge on the subject further research and especially longer simulations are required.

8.5 Effect tip shape

The simulations described above were performed with a cylindrically shaped tip. However, experimental tips normally have a more spherical shape. Therefore, we started also simulations with different tip shapes:
1) A cylinder with end-caps that have a constant curvature R_{tip} = 45 nm.
2) A spherical tip with radius R_{tip} = 15 nm.

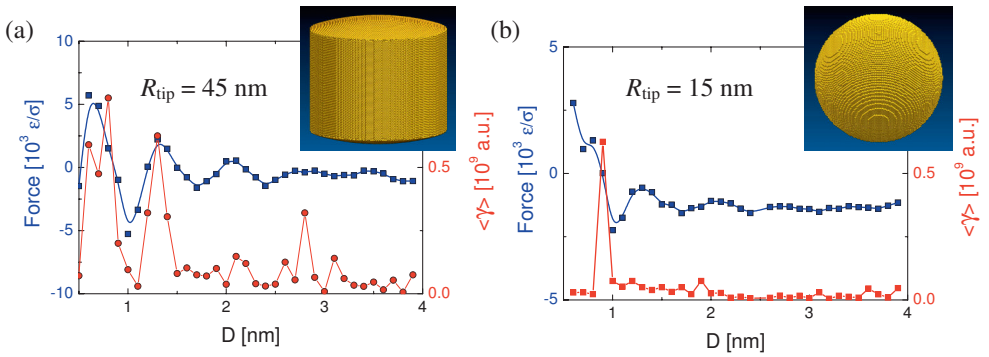

Figure 8.8 The average force on the tip in z direction (blue squares) and the damping γ extracted from the force fluctuations for a tip with radius (a) R_{tip} = 45 nm and (b) R_{tip} = 15 nm.

Figure 8.8(a) shows the average force and damping on a 45 nm tip, extracted from a single *NVE* simulation of 16 ns after equilibration of 41 ns. Although these simulations have not yet been finalized and the statistics is still poor, first qualitative results indicate that both the force and the damping show the same trend as for the cylindrical tip (Fig. 8.2). The average force shows clear oscillations, with a periodicity equal to the molecular diameter σ, which is characteristic for the oscillatory solvation forces. However, since the distance between the tip and the surface depends on the radial position, the force is significantly lower than the force on the cylindrical tip ($F_{cyl} \approx 50 F_{45nm}$). Nevertheless, the damping shows clear peaks with a magnitude of

~1/10 of the peaks for the cylindrical tip. The maxima in the damping are positioned around the maxima in the force.
Figure 8.8(b) shows the average force and damping on a 15 nm tip, extracted from two *NVE* simulations of 16 ns after equilibration of 58.5 ns. Again both the force and the damping show the same qualitative trend as for the cylindrical tip (Fig. 8.2). The average force oscillates as a function distance between the tip apex and the surface. However, since the radial dependent height between the tip and the surface increases more rapidly than for the 45 nm tip, the forces are now even lower ($F_{45nm} \approx 3F_{15nm}$). Although, we can not directly use the Derjaguin approximation (F/R = constant) to compare the forces on both tips, because the 45 nm tip is not a complete half-sphere, this seems to agree surprisingly well.
On the other hand, although the average forces on both tips are qualitatively similar, the peaks in the damping have almost completely disappeared for the 15 nm tip. We only observe one peak in the damping for the last maximum in the force. For this observation we do not yet have an explanation. Nevertheless, this observation would explain why some researchers observed no peaks and only a monotonic increase in the damping [34, 35], while others did observe peaks [4-9, 11].

8.6 Summary

In summary, we have shown that our MD simulations reproduce the peaks in the damping found in recent AFM experiments. Upon closer examination of the behavior of the molecules confined between the tip and the surface, we observe that the molecules are organized in regions with a cubic structure separated by disorganized grain boundaries when we find a maximum in the damping. On the other hand, the molecules are assembled in a perfect hexagonal structure in between the peaks in the damping. Moreover, we find that the molecules behave diffusive for the distances with a maximum damping, while they behave non-diffusive in between the peaks. We conclude that the confined liquid can behave solid-like or liquid-like depending on the exact distance between the confining walls. Moreover, the diffusivity decreases with increasing peak height in the damping.

Acknowledgement

We thank J. Klein, D. Frenkel, M. Müser and M. Schindler for the fruitful discussions at Dynasoft 2010. This work has been supported by the Foundation for Fundamental research on Matter (FOM), which is financially supported by the Netherlands Organization for Scientific Research (NWO).

References:

[1] L. Bocquet and E. Charlaix, *Chem. Soc. Rev.* **39**, 1073 (2010)
[2] B. N. J. Persson and F. Mugele, *J. Phys. Condens. Matter* **16**, R295 (2004)
[3] J. N. Israelachvili, *Intermolecular and Surface Forces* (Academic, London, 1991)
[4] A. Maali, T. Cohen-Bouhacina, G. Couturier and J-P Aimé, *Phys. Rev. Lett.* **96**, 086105 (2006)
[5] S.J. O'Shea, *Phys. Rev. Lett.* **97**, 179601 (2006)
[6] A. Maali and T. Cohen-Bouhacina, *Phys. Rev. Lett.* **97**, 179602 (2006)
[7] S. de Beer, D. van den Ende and F. Mugele, *Nanotechnology* **21**, 325703 (2010)
[8] S. de Beer, D. van den Ende and F. Mugele, *J. Phys. Condens. Matter* **23**, 112206 (2011)
[9] S.H. Khan, G. Matei, S. Patil and P.M. Hoffmann, *Phys. Rev. Lett.* **105**, 106101 (2010)
[10] T.-D. Li and E. Riedo, *Phys. Rev. Lett.* **100**, 106102 (2008)
[11] W. Hofbauer, R.J. Ho, R. Hairulnizam, N.N. Gosvami and S.J. O'Shea *Phys. Rev.* B **80**, 134104 (2009)
[12] J. Klein and E. Kumacheva, *Science* **269**, 816 (1995)
[13] Y. Zhu and S. Granick, *Langmuir* **19**, 8148 (2003)
[14] J.N. Israelachvili, P.M. McGuiggan, and A.M. Homola, *Science* **240**, 189 (1988)
[15] T. Becker and F. Mugele, *Phys. Rev. Lett.* **91**, 166104 (2003)
[16] L. Bureau, *Phys. Rev. Lett.* **104**, 218302 (2010)
[17] P.A. Thompson and M.O. Robbins, *Science* **250**, 792 (1990)
[18] D.J. Diestler, M. Schoen and J.H. Cushman, *Science* **262**, 545 (1993)
[19] L. Bocquet and J.-L. Barrat, *Phys. Rev.* E **49**, 3079 (1994)
[20] K. Falk, F. Sedlmeier, L. Joly, R.R. Netz and L. Bocquet, *Nano Lett.* **10**, 4067 (2010)
[21] J. Gao, W.D. Luedtke and U. Landman, *Phys. Rev. Lett.* **79**, 705 (1997)
[22] Y. Leng, Y. Lei and P.T. Cummings, *Modelling Simul. Mater. Sci. Eng.* **18**, 034007 (2010)
[23] S.A. Somers, A.V. McCormick and H.T. Davis, *J. Chem. Phys.* **99**, 9890 (1993)
[24] N. Choudhury and B.M. Pettitt, *J. Am. Chem. Soc.* **127**, 3556 (2005)
[25] D. Frenkel and B. Smit, *Understanding Molecular Simulation from Algorithms to Applications*, Academic Press (1996)
[26] L. Verlet, *Phys. Rev.* **159**, 98 (1967)
[27] S. Toxvaerd, *Phys. Rev.* E **47**, 343 (1993)
[28] N.N. Gosvami, S.K. Sinha, W. Hofbauer and S.J. O'Shea, *J. Chem. Phys.* **126**, 214708 (2007)
[29] M.H. Müser and M.O. Robbins, *Phys. Rev.* B **61**, 2335 (2000)
[30] D. Chandler, *Introduction to Modern Statistical Mechanics*, Oxford University Press (1987)
[31] B.N.J. Persson and P. Ballone, *J. Chem. Phys.* **112**, 9524 (2000)
[32] U. Tartaglino, I.M. Sibebaek, B.N.J. Persson and E. Tosatti, *J. Chem. Phys.* **125**, 014704 (2006)
[33] E. H. Purnomo, D. van den Ende, S.A. Vanapalli and F. Mugele, *Phys. Rev. Lett.* **101**, 238301 (2008)
[34] G. B. Kaggwa, J. I. Kilpatrick, J. E. Sader, and S. P. Jarvis, *Appl. Phys. Lett.* **93**, 011909 (2008)
[35] S. J. O'Shea and M. E. Welland, *Langmuir* **14**, 4186 (1998)

Chapter 9

Do epitaxy and temperature affect the oscillatory solvation forces?

The changes in the properties of confined liquids are often compared to liquid-solid phase-transitions. Therefore we also studied confined liquids for various temperatures just above the melting point of the bulk liquid. In this chapter we present our temperature dependent Atomic Force Microscope (AFM) measurements in force-distance (contact) mode of confined 1-dodecanol.[1] Upon approach of the AFM-tip towards the Highly Oriented Pyrolytic Graphite (HOPG) surface, the final liquid film - only a few nanometer thin - is squeezed out in discrete layers. We find that both the force needed to squeeze out these layers and the number of structured layers strongly increase as the freezing temperature is approached. Surprisingly the force and the number of layers increase non-monotonically and show a local maximum around 3 degrees and a local minimum at 1 degree above the bulk melting point of the liquid.

[1] This chapter has been published as: S. de Beer, P. Wennink, M. Van der Weide-Grevelink & F. Mugele, *Langmuir* **26**, 13245 (2010).

We attribute this result to changes in epitaxial effects between 1-dodecanol and the HOPG surface close to the melting point of the liquid. To test this hypothesis we performed the same measurements in hexadecane, a similar carbon-chain molecule, and octamethylcyclotetrasiloxane (OMCTS), a quasi-spherical molecule. Hexadecane shows the same maximum in the squeeze-out force and the number of layers at 4-5 degrees and a minimum at 1-2 degrees above the freezing temperature of the liquid, while the squeeze out of OMCTS was found to be independent of temperature.

9.1 Introduction

Confined liquids play an important role in numerous phenomena, like friction, lubrication and the flow in porous media (as in oil recovery), and applications, like the lab-on-chip. On small scales a liquid often behaves different from the bulk. An especially interesting phenomenon is the structuring or layering of liquid molecules close to a solid wall, which gives rise to the oscillatory solvation forces [1]. These oscillatory forces have been studied extensively in both Surface Forces Apparatus (SFA) [1-3] and Atomic Force Microscope (AFM) [4-7] experiments and a lot of progress has been made in understanding their properties. Layering occurs for purely entropic reasons like in a hard-sphere liquid, but is usually also influenced by liquid-surface interactions. For weakly interacting liquids like octamethylcyclotetrasiloxane (OMCTS), the oscillatory forces depend only very little on temperature. The squeeze-out force of layered OMCTS between two mica sheets in a SFA was measured to be temperature independent [8] in a temperature range of 10 ºC above down to 3 ºC below the liquids melting point. Nevertheless, whether or under which conditions the layers are solid- [2] or liquid-like [3] is still under debate. On the other hand, recent AFM measurements in OMCTS on Highly Oriented Pyrolitic Graphite (HOPG) over a wider temperature range (20-60 ºC) have shown that the oscillatory forces strongly (and linearly) decrease for increasing temperature [9]. The latter was attributed to a temperature dependent decrease in the entropic energy-barrier that the system needs to overcome in order to squeeze-out the layers.
The effect of temperature on layering has been measured in other liquids as well. For hexadecane a linear decrease in squeeze-out force was found for increasing temperature [9] (similar to OMCTS), while for ionic liquids a more sudden, but significant, increase of the oscillatory forces was reported at temperatures close to the melting point of the liquid [10]. Furthermore for liquid crystals, which can already show nematic or smectic ordering in the bulk, a surface induced pre-smectic phase was found in nematic and isotropic bulk-phases [11]. Temperature-dependent measurements of the oscillatory forces in dodecanol on HOPG have been performed as well. While Ref. 9 found a constant force (within the experimental error) between 25 and 45 ºC and a decrease in force for higher temperatures, earlier experiments had not shown such an effect [12]. The measurements in hexadecane and dodecanol are particularly interesting, since both alcohols and alkanes are known to interact strongly with HOPG. The carbon chains of these liquid molecules adsorb on the graphite

surface [13]. Moreover interfacial freezing and a layer dependent shift in the melting point have been reported in a number of experimental studies [14-16] and molecular dynamics (MD) simulations [16, 17]. Scanning Tunneling Microscopy (STM) studies of the same systems showed that the configuration of the absorbed layer (from solution) is strongly temperature dependent [18, 19]. How epitaxy and commensurability affect the squeeze-out forces is, however, still not well understood. MD simulations predict stronger layering, monolayer freezing - and consequently much higher oscillatory solvation forces - for commensurate systems [20, 21]. However in SFA measurements different results have been obtained. While some found no measurable effect of epitaxy [2, 22], others reported indirect evidence [23] or even a strong influence of epitaxial (mis-)match [24]. From an experimental perspective, the impact of epitaxial effects on the strength of squeeze-out forces and on the structuring of confined liquid layers is thus not well established. Given the temperature dependence of the molecular ordering observed in STM measurements [19], hydrocarbon chains on HOPG are an ideal model system to study the effect of epitaxy on layering forces.
In this chapter we present detailed measurements of the oscillatory solvation forces in 1-dodecanol confined between an AFM tip and HOPG, upon varying the temperature (22-28 ºC) in the vicinity of the melting point of the bulk liquid. In our experiments we find a strong increase in the squeeze-out force as the bulk melting point is approached. Nonetheless, the force does not increase monotonically, but displays a maximum at 3-4 ºC and a dip at 1-2 ºC above the melting point of the liquid. We argue that this unexpected observation is closely related to the monolayer freezing due to the epitaxial effect between dodecanol and HOPG described above and is a direct result from an order-disorder transition as the bulk liquid starts to freeze. The relevance of epitaxial effects is corroborated by temperature dependent measurements of the squeeze-out forces in hexadecane and OMCTS. Hexadecane shows similar non-monotonic behavior above the melting point, while the force of the non-commensurate liquid, OMCTS, is found to be temperature-independent.

9.2 Materials and Methods

As a substrate we used highly oriented pyrolitic graphite (HOPG, Mikromasch, ZYA quality grade). Just prior to each measurement the HOPG was freshly cleaved using adhesive tape and immediately imaged in air to ensure clean and atomically smooth surfaces. The force distance measurements were performed in 1-dodecanol ($C_{12}H_{26}O$, Fluka, ≥99.8%, measured melting temperature: T_m = 22˚C [25]), hexadecane ($C_{16}H_{34}$, Sigma-Aldrich, anhydrous 99+%, T_m = 18˚C) and octamethylcyclotetrasiloxane ($(SiO)_4(CH_3)_8$, OMCTS, Fluka, purum ≥99.0%, T_m = 17.5˚C). All liquids were taken fresh from the bottle and directly applied to the HOPG surface without further purification. (While the value of T_m for hexadecane and for OMCTS agrees with standard literature data, the T_m for dodecanol (22˚C) is below the most frequently cited value of 24°C, yet within the range given by the supplier (22-26˚C). Interestingly, very

detailed thermodynamic and x-ray scattering studies [26, 27] of neat and hydrated 1-alcohols of variable chain length showed that T_m typically increases by about 2°C upon addition of water to thoroughly dried alcohol. To evaluate the significance of possible water contamination in our experiments, we measured the melting temperature for three different samples of dodecanol: 1) as received, 2) dried with molecular sieve, 3) saturated with water and obtained values of T_m= 22°C, 22°C, and 24°C, respectively. This result is consistent with the ref. 26, 27 and confirms that the degree of water contamination is not substantial in our experiments.)

The measurements were performed on a Veeco Multimode 5 with Nanoscope V controller equipped with a small, low-noise A-scanner (Veeco) and an ultra-low-noise head using deflection detection. We used various cantilevers of different manufacturers, with different shapes, surface materials and spring constants: v-shaped Veeco NP and NPS (spring constant k = 0.2-1.0 N/m), rectangular Mikromasch CSC37, with either a silicon-nitride or gold coating (spring constant k = 0.5-1.3 N/m). The spring constant of each cantilever was determined in air using the thermal calibration method, as implemented in the Veeco Nanoscope 7.30 software. Prior to the measurements the cantilevers were cleaned in a plasma-cleaner (Harrick Plasma) for approximately 1 minute. To determine the tip radius and to make sure that the cantilevers were not contaminated [28] we characterized the tip after the measurements using high resolution SEM (HR- SEM Zeiss LEO 1550) yielding tip radii of $R_{tip} = 10 - 35nm$.

In the experiment we monitored the deflection of the, completely immersed, AFM cantilever upon approach towards the solid surface. We controlled the local temperature using a PID controller (Eurotherm 3508), (water-cooled) peltier elements and a home-built environmental chamber around the AFM. To reduce vibrations the total temperature controller was switched off during the actual measurement-period (<3min.). The temperature was continuously monitored using a Parmer digital sensor with a calibrated T-thermocouple (Fig. 9.1). The exact position of the thermocouple had no effect on the measurement-results and the measured melting point of the liquids. During the measurement the temperature was constant within 0.03 ºC. Under ambient lab conditions, the local 'base-temperature' in the head was measured to be 27-28 ºC, due to local heating caused by the electronics. For each temperature setting a minimum of 25 measurement curves were recorded and analyzed. In some experiments the temperature was decreased to the melting point of the liquid and then slowly increased in steps of ~0.5ºC, while in other experiments the temperature was decreased in steps of ~0.5ºC from ambient temperature down to the melting point of the liquid. We found the same results for both the heating and the cooling route. All approach curves showed characteristic jumps in the deflection due to the solvation forces, although the number of jumps varied from curve to curve (depending also on the temperature). Experiments that did not show these stable results (e.g. due to a bad tip or contamination) were discarded. Apart from a separate experiment where we systematically varied the approach rate (in which we found that the measured force was independent of the approach speed, see also Appendix 9.A), the approach speeds

were kept around 20-50 nm/s. The typical drift was in the order of 0.08±0.03nm/s, as determined from the change in z piezo voltage at tip-surface contact.

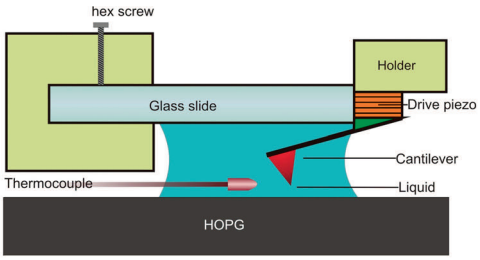

Figure 9.1 Schematic drawing of measurement system. The entire AFM was cooled or heated, while the local temperature at the surface in liquid was continuously monitored with a thermo-couple.

To make sure we squeezed out all the liquid layers and had a real tip-surface contact, we repeated our measurements with conductive AFM (Veeco TUNA module, with a maximum gain of 10^{12} / 1 pA/V) and Mikromasch CSC37 gold-coated cantilevers using a procedure similar to Ref. 29 (see also Appendix 9.A).
After the measurements the results were analyzed by converting the deflection versus z piezo displacement curves into normalized force versus tip-surface distance curves. To allow for comparison between different cantilevers all force distance curves were normalized by the tip radius.

9.3 Experimental results

Figure 9.2 shows four typical normalized force versus distance curves for dodecanol confined between the AFM tip and HOPG. The curves are captured with the same cantilever in the same liquid-drop, but at different temperatures close to the melting point of the liquid. We started the experiment under ambient conditions in the laboratory (Fig. 9.2(a) the base temperature in the head was 27.8˚C). The tip was approached over ~25 nm towards the surface.
Figure 9.2(a) shows the force on the cantilever over the last 5 nm. For a tip surface distance of 5nm or more, the measured force is zero. In the last 2 nm discrete jumps, superimposed over a total increase in the force, show up. As the last 2 nm of liquid film is squeezed out, the layered structure of the liquid molecules becomes visible and a finite force is needed to rupture the layers. The jump-distances are on average 0.45nm, which is close to the width of the dodecanol-molecules (0.43nm). As the number of layers between the tip and the surface decreases, the necessary squeeze-out force increases. These observations are characteristic for measurements of the oscillatory solvation forces [1, 6].

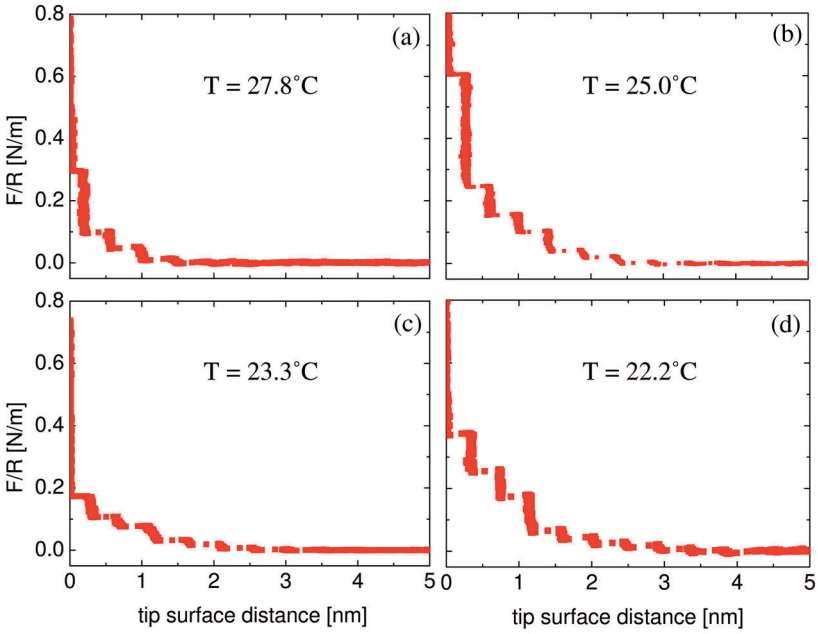

Figure 9.2 Normalized force versus tip-surface distance curves upon approach of an AFM cantilever towards HOPG in dodecanol for 4 temperatures close to the liquids melting point (Mikromasch CSC37 Si_3N_4 cantilever, R_{tip}=30 nm, k=0.66 N/m).

Upon decreasing the temperature the force distance curves strongly alter. Figure 9.2(b) shows a characteristic force distance curve at 25˚C. The number of visible jumps and the squeeze-out forces have significantly increased. Upon comparing Fig. 9.2(a) to Fig. 9.2(b), it becomes immediately visible that in Fig. 9.2(b) the layering already is observable at a larger tip-surface distance (4 nm). Furthermore, in Fig. 9.2(b) the force needed to squeeze out the last layer has doubled in comparison to Fig. 9.2(a).
However, when decreasing the temperature even more to 23.3˚C we observed a surprising trend: The squeeze-out forces decrease again and are even lower then at the base temperature (27.8˚C), while the number of visible layers remains comparable (Fig. 9.2(c)). At this temperature the force-gradient before each jump is also smaller than at other temperatures, which indicates that the layered liquid is more elastic and easier to compress. Finally, Fig. 9.2(d) shows a typical force distance curve closest to the melting point of the liquid. The number of visible layers has slightly increased and the forces are again higher then at 23.3˚C, nevertheless still lower than at 25˚C. Although force-distance curves vary from curve to curve, the above described temperature dependent trend surpasses the measurement uncertainty (Fig. 9.3).

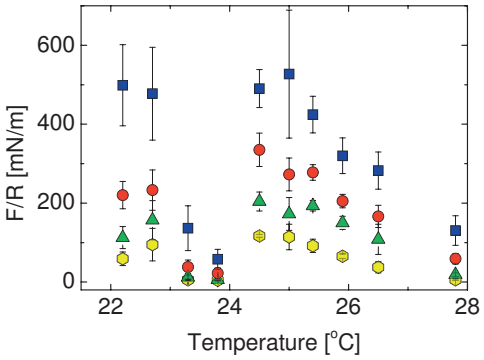

Figure 9.3 Average normalized squeeze-out force for the last 4 layers (blue squares last, red circles second last, green triangles third and yellow hexagons fourth last layer) measured upon approach of the AFM tip towards the HOPG surface in dodecanol for various temperatures close to the melting point of the liquid. Error bars denote the standard error of the mean with a 95% confidence interval.

Figure 9.3 shows the average force needed to squeeze out the last 4 layers [30]. In this figure the clear trend described above is evidently observed. As we approach the melting point of the liquid from 27.8˚C, the force first strongly increases. However, after the force maximum around 25˚C, amazingly the forces again decrease to values even lower than at 27.8˚C. Only very close to the melting point (T<23˚C) the force needed to squeeze out the layers again increases.

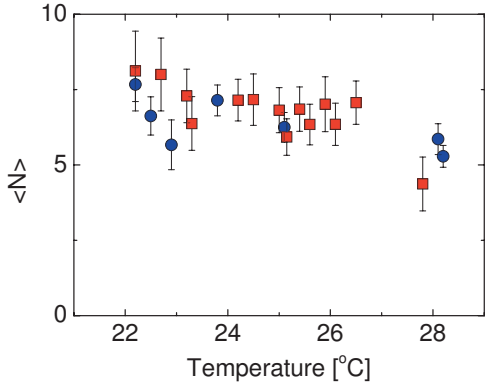

Figure 9.4 Average number of layers <*N*> visible in force distance curves measured in dodecanol upon approach of the AFM tip towards the HOPG surface. The different colors represent independent measurements with different cantilevers (red squares Mikromasch CSC37 Si_3N_4 cantilever, R_{tip} = 30 nm, k = 0.66 N/m, blue circles Mikromasch CSC37 Si_3N_4 cantilever, R_{tip} = 30 nm, k = 0.54 N/m). The error bars denote the standard deviation of the mean.

Figure 9.4 shows the average number of visible layers <*N*> for various temperatures from two experiments with different cantilevers (extracted from at least 25 curves per temperature). For the measurements at the highest temperature (27.8˚C) we find the lowest amount of observable layers <*N*>. Upon decreasing the temperature, <*N*> increases.
We performed the same measurements as described above with several different cantilevers in different experiments and found quantitatively the same results.

9.4 Discussion

This leads to the interesting question: What can cause this peculiar behavior? What can change the properties of the liquid molecules so dramatically over such a small temperature-range?
It is known that carbon chains can adsorb onto graphite surfaces creating several frozen layers. Groszek [13] proposed that, although the molecule has to adjust its configuration, it is energetically more favorable for the molecules to arrange and adsorb onto the hexagonal basal plane of the HOPG surface (as depicted in Fig. 9.5(a) & 9.5(b)).

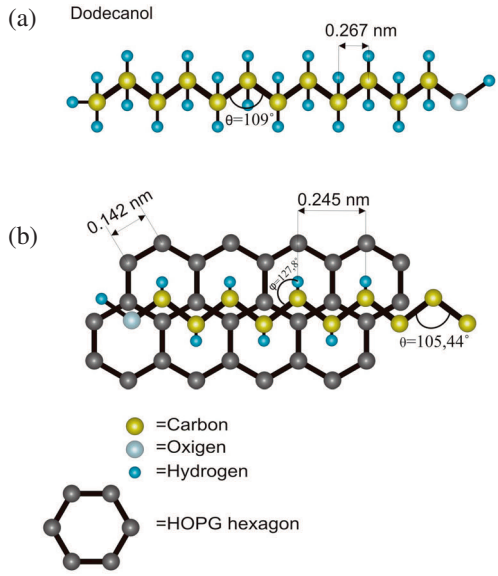

Figure 9.5 Schematic representation of Groszek's model on adsorbed carbon chains at a graphite surface. (a) A 'free' dodecanol molecule. (b) A dodecanol molecule adsorbed onto the HOPG surface. In order to match the hexagonal structure of graphite, the dodecanol molecule needs to adjust the angles in the carbon chain. This new configuration and the adsorption, however, reduces the total potential energy of the dodecanol-graphite system.

Although experiments and simulations have shown that several different adsorption configurations are possible [16], it is generally accepted that dodecanol forms frozen monolayers on HOPG at room temperature. Furthermore, frozen monolayers can melt upon increasing the temperature, as was measured by Ref. 15 using scanning calorimetry (DSC) in combination with neutron scattering. For the different layers with increasing distance above the graphite surface, decreasing shifts in the melting point were reported for linear alcohols [15] (like dodecanol) and alkanes [14]. For example, the melting point of the first layer of dodecanol on graphite was measured to be at $T_{m1} = 67^{\circ}C$, of the second layer at $T_{m2} = 30^{\circ}C$ and of the third layer at $T_{m3} = 23^{\circ}C$. However, in our experiment the squeeze-out force displays the same temperature-dependent trend for all the last 4 layers (Fig. 9.3). Both the dip (around 23-24˚C) and the maximum (at 25˚C) are at the same position for all 4 layers. So, frozen monolayers at the solid liquid interface and the layer dependent shifts in melting points can not explain our results. On the other hand, recently, up to 6 well-ordered layers of dodecanol were imaged at ambient temperature using frequency-modulation AFM [5], which generally requires a solid-like structure. The DSC and neutron data did not display freezing at such large distances [15]. This might indicate that the confinement by the second solid surface, the AFM tip (which is absent in the DSC and neutron measurements) alters the freezing behavior of the dodecanol layers.

The adsorption and structuring of carbon chain alcohols and n-alkanes on HOPG have also been studied with STM [18, 19]. In this study the method of adsorption was different from ours. Their monolayer was deposited from solution, while we measure in a pure liquid. However, in recent MD simulations [16] it was shown that alkanes can adsorb in two configurations: 1) high density configuration and 2) low density configuration. The high density configuration agrees with results obtain with the STM data of Ref. 19. Since we measure in bulk liquid, we will most likely also have a high density configuration. Therefore, we tentatively discuss and compare their results to our.

For the STM study of dodecanol [18] a structure transition in orientation was reported. For temperatures around 30-35˚C the molecules were oriented in a herringbone formation, while at higher temperatures (40˚C) a configuration close to the bulk crystal structure was found. Nonetheless, this change in structural orientation occurs at temperatures outside our measurement range. The structuring of long-chained alkanes ($C_{24}H_{50}$) has been studied with STM [19] over a broader temperature range (from 26 degrees below, up to 15 degrees above the melting point of the bulk liquid, 50˚C). In this study several structure transitions were found. At ambient temperature (24˚C, 26 degrees below the melting point of the liquid) the alkanes were neatly ordered in lamella. Upon increasing the temperature, roughening occurs at the ends of the alkane-chains. The roughening increases for increasing temperature, until the imaged monolayer is completely disordered at the melting temperature of the liquid. Surprisingly, however, the system recovers a structured phase at 6˚C above the melting point of the bulk liquid. The ordering of the monolayer appears different from its formation well below the melting point, but can be stably imaged. Moreover, the

authors of Ref. 19 report the same structural orientation transition several degrees above the melting point of the liquid for shorter alkanes, though closer to the melting point. These observations strengthen the conclusion that confinement by a tip alters the freezing behavior of the structured layers.

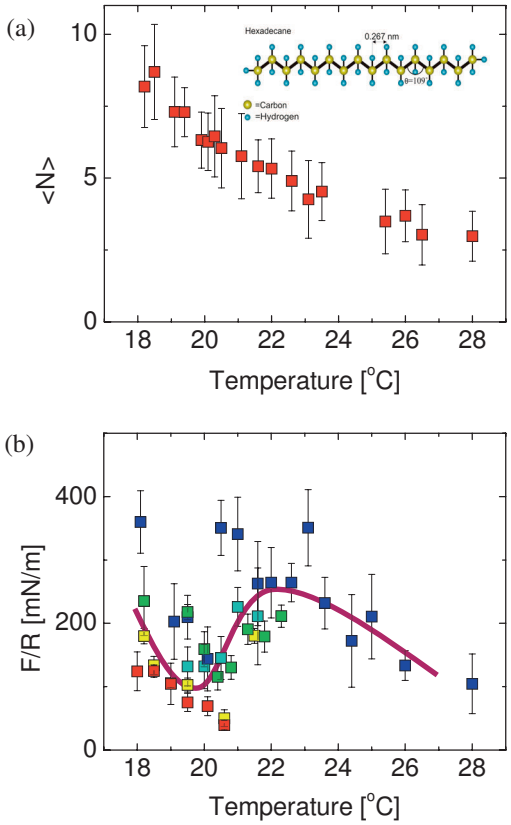

Figure 9.6 (a) Average number of layers <*N*> visible in force distance curves measured in hexadecane upon approach of the AFM tip towards the HOPG surface. The error bars denote the standard deviation of the mean. (b) Average normalized squeeze-out force for the last layer (blue Veeco cantilever k = 0.93 N/m and R = 23 nm, red Veeco cantilever k = 0.65 N/m and R = 25 nm, green Veeco cantilever k = 0.47 N/m and R = 20 nm, yellow Veeco cantilever k = 0.48 N/m and R = 20 nm, cyan Veeco cantilever k = 0.34 N/m and R = 22 nm,) measured in hexadecane upon approach of the AFM tip towards the HOPG surface for various temperatures close to the melting point of the liquid. Error bars denote the standard error of the mean with a 95% confidence interval. The inset in (a): a schematic representation of the structure of hexadecane.

Let us compare these observations to our results. We find a force-maximum at 3˚C and a dip at 1-2˚C above the melting point of the liquid for the squeeze-out of dodecanol on HOPG. This can qualitatively match the disordered state found at the melting point of the liquid and the ordered state found at 6˚C above in the STM measurements for long alkanes. In addition, the carbon chain of dodecanol is much shorter than the alkanes used in the STM experiments, which would shift the structure transition downwards, as reported in Ref. 19. Hence, we attribute the high squeeze-out force to the structuring of the adsorbed dodecanol layers and the dramatic decrease a few degrees above the bulk melting temperature to the disorder in the layers. This conclusion is also supported by MD simulations, which predict a significant increase in rupture force for commensurate systems [21].

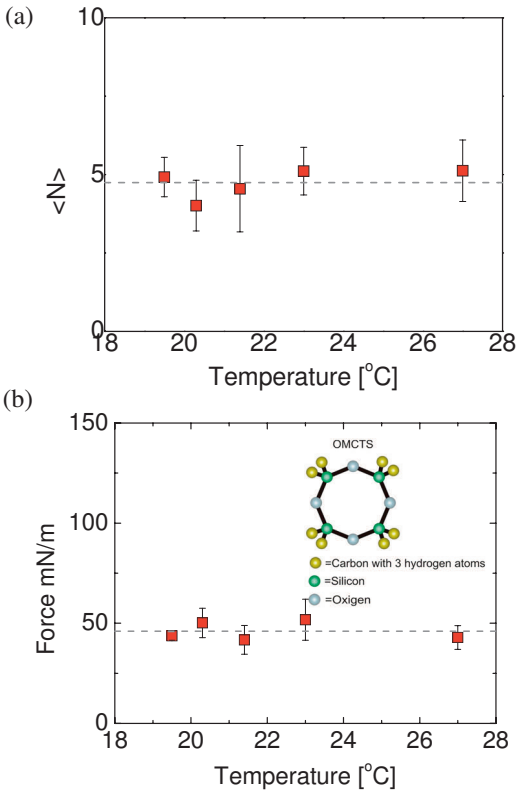

Figure 9.7 (a) Average number of layers <*N*> visible in force distance curves measured in OMCTS upon approach of the AFM tip towards the HOPG surface. The error bars denote the standard deviation of the mean. (b) Average normalized squeeze-out force for the last layer (Veeco v shaped cantilever k = 0.51 N/m. The tip radius was not measured, so we used the value given by the supplier, R = 20nm) measured in OMCTS upon approach of the AFM tip towards the HOPG surface for various temperatures close to the melting point of the liquid.

Error bars denote the standard error of the mean with a 95% confidence interval. The inset in (b): a schematic representation of the structure of OMCTS.

To test whether our observation is related to the adsorption of the molecules on HOPG, we repeated our measurements with hexadecane and OMCTS. Since hexadecane has a similar carbon-chain as dodecanol, we expect to find a similar maximum and dip in the force as a function of temperature. Yet, since hexadecane has a longer carbon chain than dodecanol, the maximum should be found at higher temperatures. In contrast, the OMCTS molecule is much larger than the lattice constant of HOPG and will therefore not display any specifically favorable adsorption configurations that compete with the intrinsic bulk crystal structure. Hence, we expect no significant changes in the squeeze-out force close to melting point of OMCTS.
Figure 9.6 shows the number of layers and the force needed to squeeze-out the last layer of hexadecane between the AFM tip and HOPG for various temperatures close to the melting point of the liquid. The number of layers clearly increases for lower temperatures, while the force shows the same characteristic dip and maximum as in our dodecanol experiment. Moreover, the maximum is (as expected) found at a higher temperature (4-5˚C above the melting point).Figure 9.7 shows the average number of layers and the average normalized force needed to squeeze out the last layer of OMCTS confined between the AFM tip and HOPG for various temperatures close to the melting point of the liquid. Both the number of layers and the force do not depend on temperature within the experimental error.
The observations described above for hexadecane and OMCTS corroborate the conclusion that the dip and maximum in the squeeze-out force of dodecanol on HOPG as a function of temperature can be attributed to a order-disorder transition of the system close to the melting point of the liquid as observed in STM measurements [19].
How can we explain these order-disorder transition observations? We know that above the melting point of the liquid n-alcohols and n-alkanes order and freeze on graphite, since it is energetically more favorable to orient and readjust to the graphite basal plane [13]. However, when the melting point is approached, the system becomes frustrated: on the one hand, the liquid molecules want to match the graphite basal plane. On the other hand, the molecules at the interface should freeze and orient in line with the bulk molecules. We therefore propose the following mechanism to explain our results: there is a critical temperature slightly above the bulk melting temperature (about 2°C for dodecanol; about 3°C for hexadecane) at which the confined liquid switches from surface dominated behavior (at higher temperature) to intrinsically fluid-dominated behavior (at lower temperature). At the transition temperature between the two states, the confined liquid is rather compliant and therefore gets squeezed out at substantially reduced normal forces. The experiments by Rabe et al. [19] corroborate the existence of such structural order-disorder transitions (notwithstanding the differences between adsorption from solution and from the bulk melt).

Unfortunately, our experimental resolution does currently not allow for a direct proof of this hypothesis (e.g. through direct imaging of the adsorbed layers as in ref. 9). Therefore, it is appropriate to discuss possible sources of error. Even at an impurity level of <0.2%, it is conceivable contaminants give rise to appreciable additional forces, as reported in various surface forces studies (see e.g. [31, 32]). Such effects are known to be particularly strong for strongly polar contaminants (in particular: water) on polar surfaces such as mica. The HOPG surfaces in the present study are much less polar and in fact rather water-repellant, as reflected e.g. in the macroscopic contact angle of approximately 90°. Moreover, the test experiments described in the experimental section demonstrate that the degree of water contamination is not substantial in our experiments. Other impurities, such as molecules with a different carbon chain length likely contribute to the 0.2% impurity. Yet, systematic surface forces experiments [31] with mixtures of branched alkanes of different lengths suggest that such polydispersity has a much weaker influence on force curves (on mica) than polar contamination. Even if present, it is not obvious how such trace amounts of contamination should produce the temperature-dependent behavior observed in our experiments.
Additionally we would like to comment on the constant force found in our OMCTS experiment. In principle the oscillatory forces are temperature dependent as shown in numerical simulations [33] in a temperature range from 400-675K. An increase in temperature also decreases the entropic contribution of the energy barrier the system needs overcome for nucleation and rupture of the layer [9, 34, 35], which would make this effect even more pronounced. Yet, given the small temperature window in the present experiments, (19-27˚C or 292-300K), it is not surprising that these effects do not surmount the experimental error.
Finally we would like to remark, that our measurements were performed in a different temperature range then of Ref. 9. However, as a test case, we also heated our hexadecane sample to the same temperatures as described in Ref. 9, at which we found very similar results (see also Appendix 9.A).

9.5 Summary

We measured the number of structured layers and the forces needed to rupture these layers of dodecanol confined between an AFM tip and HOPG. Upon decreasing the temperature towards the melting point of the liquid the forces significantly increase. However, surprisingly the force was found to increase non-monotonically with a local maximum around 3˚C above and a characteristic dip was at 1-2˚C above the melting point of the liquid. We have shown that for measurements using a different carbon chain (hexadecane) the same force maximum and minimum are found, yet at a slightly higher temperature with respect to the melting point. For OMCTS the forces were found to be independent of temperature. The former observations are consistent with the order-disorder transitions measured via STM imaging [19] of carbon-chains on graphite. Combining these results, we tentatively conclude that for ordered layers the

squeeze-out forces are higher then for disordered layers. Moreover, we interpret this order-disorder transition as a structural relaxation driven by the epitaxial mismatch with the substrate and the bulk material, which tends to crystallize upon approaching the melting point.

Acknowledgement

We thank A. Embrechts and W. den Otter for the fruitful discussions. We thank P. Markus and S. Lesko (Veeco) for the technical support, good ideas and supplying the TUNA module. We thank M. Smithers for his help on the SEM images and K. Smit, A. Vermaning and C. Harteveld for the technical support on the environmental chamber. This work has been supported by the Foundation for Fundamental research on Matter (FOM), which is financially supported by the Netherlands Organization for Scientific Research (NWO).

References

[1] J.N. Israelachvili, *Intermolecular and Surface Forces*. 2nd ed.; Academic Press: London, 1992.
[2] J. Klein, E. Kumacheva, *Science* **816**, 269 (1995)
[3] T. Becker, F. Mugele, *Phys. Rev. Lett.* **91**, 166104 (2003)
[4] T.D. Li, J.P. Gao, R. Szoszkiewicz, U. Landman, E. Riedo, *Phys. Rev. B* **75**, 115415 (2007)
[5] W. Hofbauer, R.J. Ho, R. Hairulnizam, N.N. Gosvami, S.J. O'Shea, *Phys. Rev. B* **80**, 134104 (2009)
[6] H.-J. Butt, B. Cappella, M. Kappl, *Surface Science Reports* **59**, 1-152 (2005)
[7] S. de Beer, D. van den Ende, F. Mugele, *Nanotechnology* 21, 325703 (2010)
[8] H.K. Christenson, J.N. Israelachvili, *J. Chem. Phys.* **80**, 9 (1984)
[9] L.T.W. Lim, A.T.S. Wee, S.J. O'Shea, *J. Chem. Phys.* **130**, 134703 (2009)
[10] D. Wakeham, R. Hayes, G.G. Warr, R. Atkin, *J. Phys. Chem. B* **113**, 5961-5966 (2009)
[11] G. Carbone, R. Barberi, I. Musevic, U. Krzic, *Phys. Rev. E* **71**, 051704 (2005)
[12] T. Nakada, S. Miyashita, G. Sazaki, H. Komatsu, A.A. Chernov, *Jpn. J. Appl. Phys.* **35**, 52-55 (1996)
[13] A.J. Groszek, *Proc. Roy. Soc. Lond. A* **314**, 473-498 (1970)
[14] H. Kern, W. v. Rybinski, G.H. Findenegg, *J. Coll. Interf. Sc.* **59**, 301-307 (1977)
[15] L. Messe, A. Perdigon, S.M. Clarke, M.A. Castro, A. Inaba, *J. Coll. Interf. Sc.* **266**, 19-27 (2003)
[16] A. Diama, B. Matthies, K.W. Herwig, F.Y. Hansen, L. Criswell, H. Mo, M. Bai, H. Taub, *J. Chem. Phys.* **131**, 084707 (2009)
[17] J. Gao, W.D. Luedtke, U. Landman, *J. Chem. Phys.* **106**, 10 (1997)
[18] Y.H. Yeo, G.C. McGonical, D.J. Thomson, *Langmuir* **9**, 649-651 (1993)
[19] L. Askadskaya, J.P. Rabe, *Phys. Rev. Lett.* **69**, 1395-1398 (1992)
[20] P.A. Thomson, M.O. Robbins, *Science* **250**, 4982 (1990)
[21] B.N.J. Persson, P. Ballone, *J. Chem. Phys.* **112**, 21 (2000)

[22] J. Klein, E. Kumacheva, *J. Chem. Phys.* **108**, 6996-7009 (1998)
[23] T. Becker, F. Mugele, *J. Phys. Cond. Matt.* **15**, S321-S330 (2003)
[24] P.M. McGuiggan, J.N. Israelachvili, *J. Mater. Res.* **5**, 2232-2243 (1990)
[25] The bulk melting temperature T_m of the liquids was measured using the same calibrated thermocouple as for the temperature-dependent force measurements.
[26] E.B. Sirota, X.Z. Wu, *J. Chem. Phys.* **105**, 7763-7773 (1996)
[27] O. Gang, X.Z. Wu, B.M. Ocko, E.B. Sirota, M. Deutsch, *Phys. Rev.* E **58**, 6086 (1998)
[28] B.M. Borkent, S. de Beer, F. Mugele, D. Lohse, *Langmuir* **26**, 260-268 (2010)
[29] N.N. Gosvami, S.K. Sinha, S.J. O'Shea, *Phys. Rev. Lett.* **100**, 076101 (2008)
[30] To exclude the possibility of systematic changes in the experimental conditions with time, e.g. due to contamination or geometric changes of the tip, the temperature was both increased and decreased during the experiments.
[31] J.N. Israelachvili, S.J. Kott, M.L. Gee, T.A. Whitten, *Macromolecules* **22**, 4247-4253 (1989)
[32] H.K. Christenson, C.E. Blom, *J. Chem. Phys.* **86**, 419 (1987)
[33] L.D. Gelb, R.M. Lynden-Bell, *Phys. Rev. B* **49**, 2058 (1994)
[34] B.N.J. Persson, F. Mugele, *J. Phys. Cond. Matt.* **16**, R295-R355 (2004)
[35] H.-J. Butt, V. Franz, *Phys. Rev. E* **66**, 031601 (2002)

Appendix 9.A

1. Effect Approach speed

If the rupture of liquid layers is nucleation driven [9, 34, 35], the squeeze-out force would strongly depend on the approach speed. We tested the effect of the approach rate on the oscillatory forces in hexadecane and found no effect within the experimental uncertainty and within this range of approach speeds (Figure 1). However, our typical approach speeds are also much smaller than the typical rates used by Ref. 35. Moreover, since the force depends logarithmically on the approach speed this effect is also expected to be small for these small approach speeds.

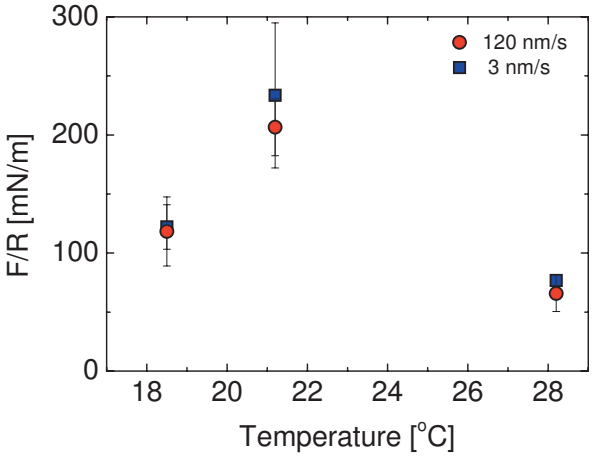

Figure 1 The effect of the approach speed on the normalized squeeze-out force of the last layer of hexadecane on confined between the AFM tip and HOPG (Veeco v shaped cantilever k = 0.61 N/m and R = 20 nm).

2. Tunneling current measurements

To test that we squeezed-out all the liquid layers in our experiments, we repeated our measurements while simultaneously monitoring the tunneling current (Figure 2) (For a more detailed study see Ref. 29) At large distances (> the thickness of the last layer) the tunneling current is close to zero. When only one liquid layer remains between the tip and the surface we see a small but finite tunneling current (20 nA). As soon as the tip makes contact with the surface the current becomes much higher (outside the measurement range). While the force needed to squeeze-out the last layer was comparable to the values in our experiment (~50% higher due to the larger radius of the gold coated tip, 30 nm), we concluded that all the liquid layers had ruptured.

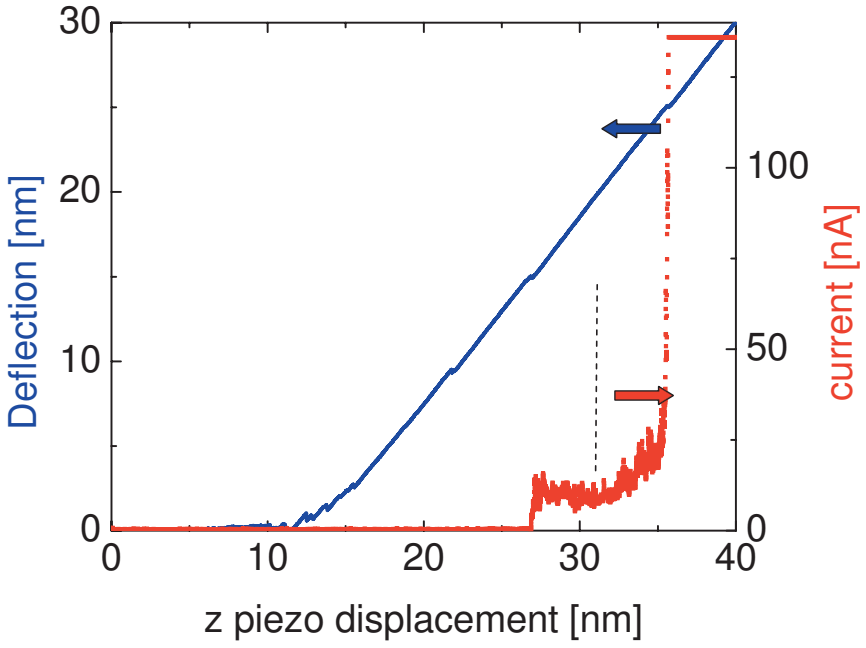

Figure 2 Deflection versus distance (blue) and the tunneling current versus distance (red) upon approach of a conductive AFM cantilever towards the HOPG surface in hexadecane at 19.5˚C (Mikromasch cantilever k = 0.56 N/m).

3. Squeeze-out force hexadecane for higher temperatures

Our experiments are focused on temperature dependent effect close to the melting point of the liquid. However, to compare our measurements to results reported by others [9], we also varied the temperature of hexadecane between 30 and 50 ˚C. In this experiment we found results similar to those reported in Ref. 9.

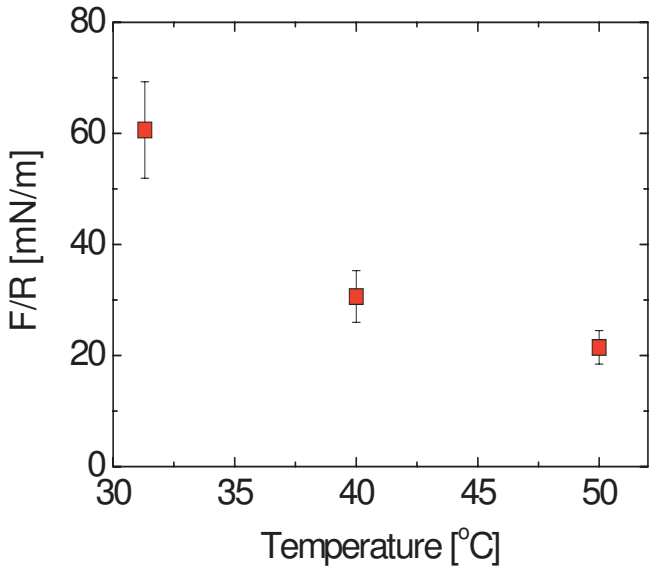

Figure 3 The normalized squeeze-out force of the last hexadecane layer for temperatures between 30-50 ˚C (Veeco v shaped cantilever k = 0.43 N/m and R = 20 nm).

Chapter 10

Instability of confined water films between elastic surfaces

In this chapter we present our study on the behavior of a rapid quench of water films between two elastic surfaces in the Surface Forces Apparatus (SFA). We investigated the dynamics of nanometer thin water films at controlled ambient humidity adsorbed onto two atomically smooth mica sheets upon rapidly bringing the surfaces in contact. Using the SFA in the imaging mode, we found that the water films break up into a distribution of drops with a typical thickness of few nanometers and a characteristic lateral size and spacing of several micrometers. While the characteristic length is found to be independent of the ambient humidity, the characteristic time of the break-up decreases from ~1s to 0.01s with increasing humidity. The existence, of characteristic length and time scales shows that this break-up is controlled by an instability rather than a – for SFA experiments conventional – nucleation and growth mechanism. These findings cannot be explained by a dispersion-driven instability mechanism. In contrast, a model involving the elastic energies for the deformation of both the mica sheets and the underlying glue layer correctly reproduces the scaling of the characteristic length and time with humidity.[1]

[1] This chapter has been published as: S. de Beer, D. 't Mannetje, S. Zantema & F. Mugele, *Langmuir* **26**, 3280 (2010).

10.1 Introduction

Understanding the properties of liquids confined between solid surfaces is of fundamental importance to many applied problems, like friction and lubrication, adhesion, micro- and nanofluidics, and lithography. Upon confinement to a thickness of few nanometers, liquids often behave completely different from the bulk. These nanoscale effects include the layering of the liquid molecules close to a solid surface [1], slip between the solid and the liquid [2, 3], and surface nanobubbles in water on hydrophobic surfaces [4] and sometimes even hydrophilic surfaces [5]. Many experiments and theoretical models also highlight the importance of the interplay between nanoscale fluid properties and the elastic response of the confining surfaces on a larger scale [6], in particular in situations involving soft surfaces. Examples range from adhesion in biological systems to the behavior of tires on wet roads (for a review, see ref 7).

Confined water is of particular interest, because of its ubiquitous presence in Nature both in geological and in biological systems. The Surface Forces Apparatus (SFA) played a pioneering role in elucidating many of the phenomena mentioned above because it allows for detailed studies in a particularly well-defined geometry with atomically smooth walls [8, 9]. Recent experiments with the SFA [9] and with other experimental techniques [10, 11] as well as numerical simulations (see P. Ball, Chem. Rev., 2008, 108, 74. and ref. there) indicate that confined water in the vicinity of hydrophilic surfaces behaves bulk-like down to very few molecular layers. For the equivalent two or three molecular layers Atomic Force Microscopy measurements [11] report anomalies pointing to substantially different mechanical properties, which is qualitatively consistent with strong orientation effects including the formation of ice-like structures [12, 13] found for monolayers of water adsorbed from the vapor phase onto free surfaces.

In this chapter we report an instability of thin adsorbed water films that break up into nanodroplets if abruptly confined by pressing two atomically smooth elastic mica sheets together in a SFA. The basic aspects of this novel phenomenon are illustrated in Figure 10.1.

Frame (a) shows an initially flat water film with a thickness of order 1nm between the two mica surfaces. Frames (b) to (f) show the break-up of the film into a pattern of nanodrops. The dynamics of the break-up display the hallmarks of a linear instability: the drops appear after a characteristic time τ and the drop pattern displays a characteristic length scale λ. By controlling the ambient humidity in the SFA chamber, we systematically vary the initial thickness of the water film and analyze its influence on τ and λ. Surprisingly, we find that τ decreases with increasing humidity while λ remains constant. A linear stability analysis shows that this behavior is incompatible with an instability driven by van der Waals interactions. We argue that our findings can best be understood in terms of a model borrowed from the theory of elastic wrinkling (see e.g. Ref. 14 and 15). This model correctly reproduces the scaling of the characteristic time and length scales, τ and λ, with humidity.

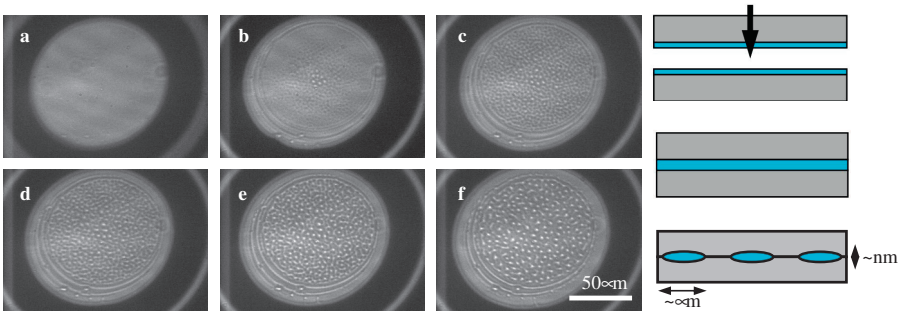

Figure 10.1 Water film confined between two mica substrates becomes unstable and develops into nano-droplets with a typical in-plane diameter of several micrometers and a typical height of a few nanometer. The thin water-film is evaporated (62% RH) onto the mica surfaces before they are pressed together. The first 3 frames (a-c) (Δt = 0.65s) show the initial development. The flat water-film breaks up into droplets. The last 3 frames (d-f) show the long term evolution of the instability (Δt d $\rightarrow$ e 3.0s and Δt e $\rightarrow$ f 8.0s), where the droplets collide and consequently grow in size.

10.2 Materials and Methods

Figure 10.2 shows the measurement setup used for the experiments described in this chapter. In contrast to conventional SFA experiments, in which fringes of equal chromatic order (FECO) are used, the SFA is illuminated with monochromatic light. This configuration allows for two-dimensional imaging of dynamic processes in nano-confined fluids, as demonstrated earlier in the context of layer-by-layer drainage of simple organic liquids [16, 17]. Briefly, monochromatic light is generated by passing white light from either a xenon arc lamp (300W, Mueller Elektronik) or a super-continuum laser (Fianium, SC450, 2W) through a grating monochromator (Lot Oriel). The width of both entrance and exit slits can be adjusted to optimize the intensity and wavelength distribution. The monochromator is calibrated using a spectral calibration lamp (mercury-argon, Lot Oriel). The monochromatic light is sent into the SFA, through the sample in cross-cylinder geometry with the usual two silver-layers acting as mirrors for the Fabry-Perot configuration (Fig. 10.2). With the mica samples in contact an incident wavelength is chosen on the wing of a transmission peak such that the variation of the transmitted intensity inside the contact area is maximum for small variations of the liquid film thickness. Under these conditions, the intensity variations are to a good approximation linearly proportional to liquid film thickness. The transmitted light is collected with a microscope objective (Nikon, 5x, NA = 0.13 WD = 22.5mm or 20x, NA = 0.35 WD = 20.5mm) connected to a CCD camera (PCO, Pixelfly or Photron). The camera signal is read-out and analyzed using a custom-written Matlab program.

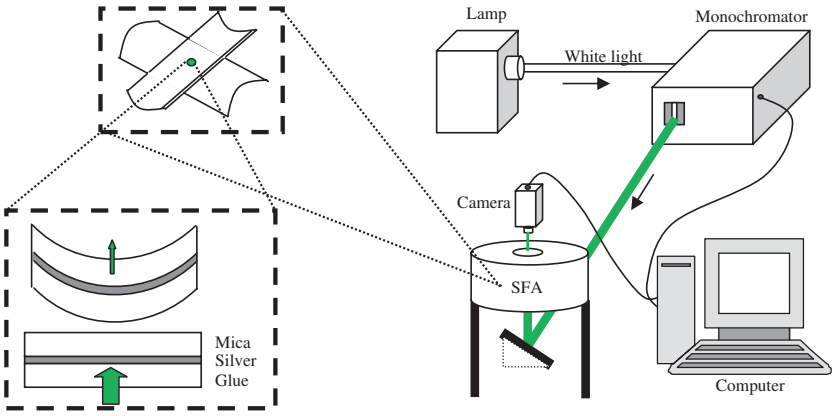

Figure 10.2 The 2D imaging SFA Measurement Setup. Instead of using the FECO technique as in the traditional SFA, monochromatic light is sent into the SFA. When the wavelength is set to the wing of a constructive interference peak of the multilayer system, a change in optical path length will result in a change in transmitted intensity. This makes the 2D imaging of nanoscale fluid flow possible.

Muscovite ruby mica (B & M Mica Co.) is used as a substrate. To minimize any possible contamination the re-cleavage technique [18] is used to prepare the mica surfaces. Prior to silver deposition (45 nm, thermal evaporation) the mica is cleaved up to a thickness of 10 – 20 μm and cut using a Pt-wire into pieces of about 1 cm^2. The silvered substrates are glued to microscope glass (Menzel Glaeser, 12 x 19.5 mm) using a relatively soft UV curable optical glue (Dymax OP29) and mounted onto curved (R = 5 cm) stainless steel sample supports. Just prior to the measurements the mica substrates are then re-cleaved to the final thickness of 1 – 4 μm. A detailed description of the setup and the experimental procedures can be found in ref.19.

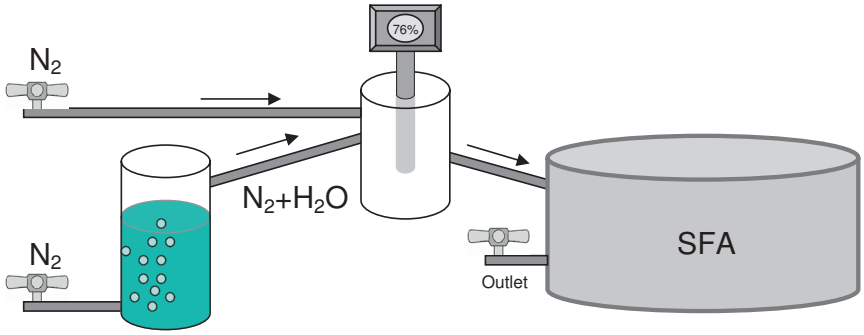

Figure 10.3 Sketch of humidity control. The relative flow of dry and humid (H_20-saturated) nitrogen can be adjusted with the two valves on the left side of the scheme. The humidity of the mixture is measured in the mixing chamber (in the middle of the picture) and then introduced into the SFA.

As soon as the sample supports are mounted into the chamber of the SFA, the chamber is connected to a simple humidity control system (Fig. 10.3), which allows for varying the relative humidity (RH) in the chamber from approximately 4 to 99% (± 3%) by adjusting the relative flow rates of dry and H_2O-saturated nitrogen. The humidity and the temperature of the mixture are measured in the mixing chamber using a commercial sensor (Testo). After changing the flow rates, the humidity is allowed to stabilize for about 50-60 min.

The thickness of the mica substrates is determined using multiple beam interferometry [20]. From the positions of the peaks in the transmission spectra the total mica thickness can be calculated using the Fast Spectral Correlation Method [21]. Reference measurements to determine the thickness of the mica substrates were performed both in dry nitrogen atmosphere and in bulk water, yielding as usual a somewhat smaller value in the latter case. To determine the thickness of the upper and the lower mica substrate individually, Ag was deposited on the top side of both substrates after the experiment. The thickness of the individual substrates was then measured with the same method as described above. The thickness of the samples for the data presented here, are given in Table 10.1.

sample pair	d_m (∝m)	d_{top} (∝m)	d_{bottom}(∝m)
1	8.456	7.044	1.421
2	3.170	1.190	2.010
3	1.015	0.200	0.815

TABLE 10.1 The thicknesses of the 3 mica samples used in this chapter. Abbreviations in the table: d_{m} is the total mica thickness; d_{top}, d_{bottom} are the thickness of the top and bottom sheet; E_{m} is the effective elasticity of the samples.

10.3 Experimental results

The experiments are performed as follows: the samples are first brought in contact with a load of approximately 30 mN. Then the top surface is mechanically pulled back against the spring by approximately 5 mm. At this distance, the system is equilibrated for 3-5 minutes. Then the upper sample is released, whereupon it hits the lower surface and quickly forms a contact area with a typical diameter of 150 - 200 µm, depending on the substrate. From the eigenfrequency of the system and the retraction force, we estimate that the "impact velocity" of the two surfaces is of order 1 cm/s. Simultaneously, the transmitted light in the region of the contact area is recorded with the CCD camera. Figure 10.1 shows snapshots from a typical experiment at finite humidity (62% in the present case). Frame (a) corresponds to a time within a few tens of milliseconds from contact formation [22]. The homogeneous intensity [23] within

the contact area, the round gray area in the center of the image, shows that the spacing of the mica surfaces is homogeneous in this initial phase, as it is for instance under perfectly dry conditions.
Within a few hundred milliseconds (frame (b)), perturbations of the intensity appear in the center of the contact area and grow (frames (c) and (d)). These intensity variations display a characteristic length scale that remains constant in the initial phase and only gradually increases at later stages (frame (e) → (f)). Close to the edge of the contact area, ring-like structures appear. We attribute these features to lateral vibrations in the setup excited upon abruptly forcing the surfaces into contact. In the following, we will disregard them and focus on the intensity variations in the center of the contact area.
The right panel, Fig. 10.1(g), shows our interpretation of these observations: before being brought into contact, both mica surfaces are covered by a water film with a thickness of order ~1 nm, depending on the humidity in the SFA chamber [24, 25]. When the mica surfaces are suddenly brought into contact, they are flattened out and quickly form a contact area with a diameter of approximately 150 µm in the present case. From the approach speed of order cm/s and the typical indentation depth of the Hertzian contact of order 10 nm, we estimate that the contact area forms within a time of order milliseconds, thus leaving essentially no time for squeezing out any liquid. Owing to the high hydraulic resistance experienced by the thin water layer, there is also insufficient time to squeeze out the water from the contact area between the time of contact and the start of the intensity variations over the contact area. This statement is supported by the fact that after the contact area has been formed the average transmitted intensity remains essentially constant until the modulation pattern appears (and in fact even longer). Hence a confined water film of homogeneous thickness is formed, which is subject to elastic normal stresses as well as inter-molecular forces. The experiment shows that this initially flat water film is unstable and breaks up into a pattern of drops, as illustrated in the bottom panel of Fig. 10.1(g). Moreover, movies, such as the one from which the images in Fig. 10.1 are extracted, show that the drops are mobile. At long times, they frequently coalesce, which also explains the coarsening in Fig. 10.1(e) → (f), Finally some drops are expelled from the contact area. The final state, which is stable for hours, still contains many nanodrops. Transmission spectra recorded in this final state reveal that the two mica surfaces are in direct contact in the flat areas in between the nanodrops and that the thickness of the nanodrops ranges between 2 and 4 nm. Hence, any lateral motion of the nanodrops implies separation of the mica sheets at the advancing edge and mica-mica contact formation at the receding edge.
To analyze the dynamics of the nanodrop formation more quantitatively, we calculated the two-dimensional fast Fourier transform (FFT) of the central area of the contact area in the images. This procedure confirms the visual impression from Fig. 10.1. As shown in Fig. 10.4, a ring appears in the FFT images, indicating the presence of a well-defined characteristic wavelength as well as the isotropy of the system. Integration along the azimuthal direction improves the statistics and the position of the peak yields the wavenumber $q = 2\pi / \lambda$ and thus the characteristic length scale λ of the

drop pattern. As one can see in Fig. 10.4, the peak intensity grows with time corresponding to the increasing amplitude of the intensity modulation in Fig. 10.1. At late times, when coalescence processes set in, the peak position slightly shifts towards smaller q-values as expected. The growth of the peak also allows for extracting the characteristic time τ for the development of the instability. (In practice, it turned out that τ could also be extracted more readily by counting the number of frames until the drop pattern became clearly visible in the real space video frames.)

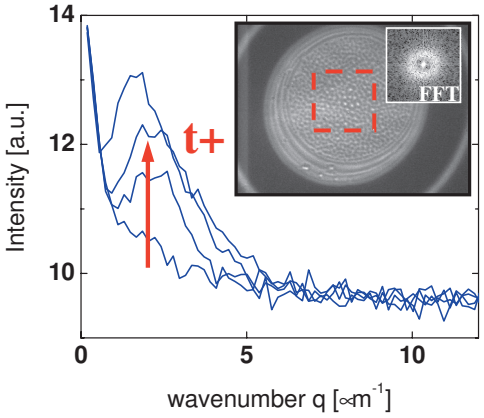

Figure 10.4 Development of the azimuthally averaged intensity of the FFT spectrum (inset) in time (Δt = 0.5 s). As the perturbation develops a clear peak becomes visible in the spectrum. At later times the droplets collide resulting in the inward motion of the peak.

To investigate the origin of the instability in more detail we repeated the same experiment at various ambient humidities ranging from 4% to 99% RH, corresponding to an initial thickness of the adsorbed water films ranging from approximately one to four or five molecular diameters [24, 25]. At humidities below ~55%, the modulation pattern became visible only after the recording time of <1 minute and at humidities below ~40% the pattern was not observable at all. Apparently, modulations do not develop under these conditions, unless their amplitude is below our detection limit of approximately 0.2 nm. At higher humidities, however, the modulation pattern always appears and the films clearly break up into drops on a time scale that decreases substantially with increasing humidity.

Fig. 10.5(a) shows the characteristic length λ as a function of the humidity for the three different mica samples. The graph clearly shows that λ is independent of the humidity (and therefore of the initial thickness of the water film), yet it increases linearly from ≈ 1.7 µm to 5.5 µm from the thinnest to the thickest pair of mica sheets (see Fig. 10.5(b)). (For the sake of comparison, we plot λ not only versus the total mica thickness d_m (crosses), but also versus the thickness of the thinner (diamonds) and the thicker (circles) mica sheet; see discussion section.)

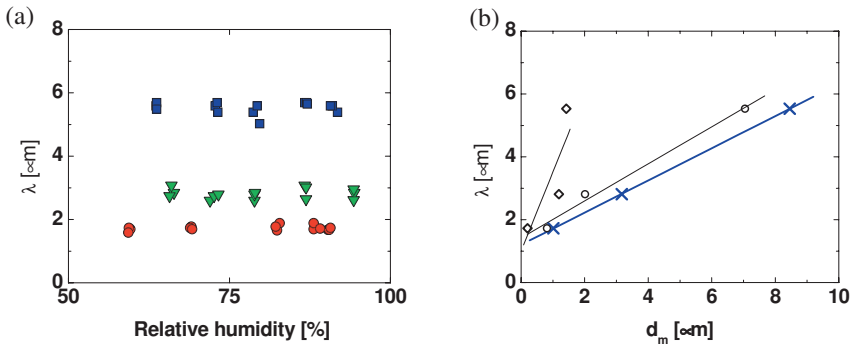

Figure 10.5 (a) Characteristic wavelength λ of the instability versus relative humidity. The different colors represent the different sample pairs used in the experiments (Table 1); blue squares: d_m = 8.5µm, green triangles: d_m = 3.2µm and red circles: d_m = 1.0µm. (b) λ vs. total mica thickness d_m (blue cross). (diamonds and circles: λ vs. thickness of the thinner and thicker mica sheet, respectively. (see text for discussion)

Figure 10.6 shows the corresponding characteristic times τ for the same measurements. At high humidity (thick water-film) the droplets are formed within <0.1s. At lower humidity (thin water-film) it can take up to several seconds for the instability to develop. For thicker samples, the humidity dependence of τ is more pronounced than for thinner ones. The fastest decay was observed for the thinnest samples at the highest humidity. Qualitatively similar results were obtained for a large number of other samples, including some that were prepared using a conventional thermosettling glue, which corroborates the general validity of the findings, in particular the faster break-up at higher humidity.

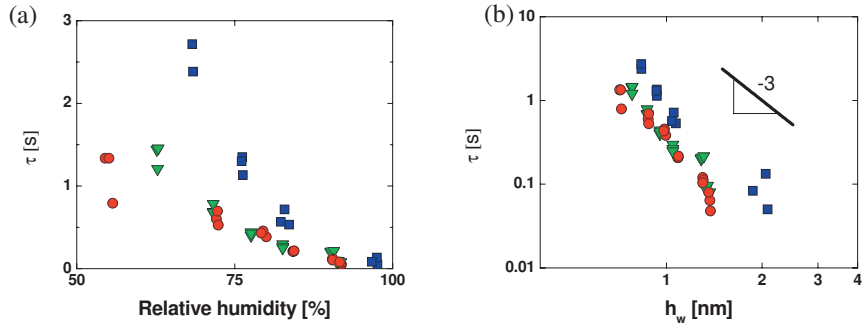

Figure 10.6 (a) Characteristic growth time τ of the instability versus relative humidity for variable mica thickness. Same symbols as in Fig. 10.5. (b) Same data as in (a) but plotted versus the initial thickness of the flat confined water film.

The relevant physical parameter for the instability that changes upon varying the humidity is the thickness of the water films adsorbed to the mica surfaces prior to bringing them in contact. In principle the combined initial water film thickness of both adsorbed layers is accessible from the value of the transmitted intensity in the first movie frame after having established contact relative to the transmitted intensity for direct mica-mica contact in the final state. Such measurements are indeed possible and they confirm that the initial water film thickness (i.e. twice the thickness of the adsorbed water film on a single mica sheet) increases from zero (within error) below 40% R.H. up to 1.5 to 2 nm at the highest humidity. Yet, the variations between consecutive runs under identical conditions are substantial because the measurement relies on the absolute intensity. Therefore, we adopted the approximate procedure of balancing the chemical potentials of the adsorbed water layer due to van der Waals interaction and the chemical potential of the vapor in the surrounding atmosphere to convert the relative humidity (and thus the relative vapor pressure p/p_0) into the thickness of adsorbed water layers on each individual mica surface $h_{ads} = \sqrt[3]{v_m A_{ads} / (6\pi k_B T \cdot \ln(p/p_0))}$, where A_{ads}=2.7 10^{-20} J was used for the Hamaker constant for the adsorption of water on mica in air. k_B is the Boltzmann constant, T is the temperature, and v_m is the molecular volume. (Detailed experiments display deviations from this prediction [24, 25], nevertheless the formula yields a reasonable estimate.) In Fig. 10.6(b), we replot the same data as in Fig. 10.6(a) as a function of the thus obtained initial thickness of the water layer $h_w = 2h_{ads}$ on logarithmic scales. Note that the data are consistent with an algebraic decrease $\tau \propto h_w^{\nu}$ with an exponent $\nu \approx -3.8 \pm 1$. This average value is based on a larger set of data than presented here. Note that the data, which due to the nature of the problem cover only a rather limited range of h_w, is also consistent with a slope -3 as indicated in Fig. 10.6.

10.4 Discussion

What is the physical nature of the observed phenomenon? Under which conditions does it occur? Both the dynamics and the patterns formed in the final stage are completely different from the squeeze-out behavior of strongly layered films of organic liquids that were investigated earlier in great detail [16, 17, 26]. These films clearly decayed by a nucleation and growth scenario driven by the applied external pressure, as first proposed by Tosatti and Persson [27]. (For a review, see ref. 28) Even when several nucleation sites appeared at the same time upon approaching the mica surfaces at (relatively) high speeds, the resulting break-up scenario of the films is qualitatively different from the present experiments (see Fig. 5 of ref. 26). The same applies to the break-up dynamics of somewhat thicker non-layered liquid films squeezed by pressing curved elastic rubber surfaces against flat stiff solid surfaces [28, 29], which also follow a nucleation and growth scenario. In contrast, the present experiments with its well-defined characteristic wavelength and characteristic time clearly point to an instability mechanism, as explained before. There are two main differences between the two situations: (I) The physical system and therefore the

interaction forces between the two mica surfaces are very different. For simple organic liquids (in particular octamethylcyclotetrasiloxane; OMCTS) the interaction is dominated by strong oscillatory solvation forces up to surface separations of several nanometers. For water (with the possible exception of film thickness below two or three molecular layers [30]) the interaction potential displays a single cross over from attractive van der Waals interaction at the smallest separation to repulsive electrostatic interaction beyond about 1 nm, depending on the concentration of ions. The strong structural forces obviously provide stable energetic minima for discrete numbers of liquid layers, which counteract the growth any oscillatory perturbation of the mica surface. (II) The approach speed in the previous experiments with the organic liquids was substantially slower because those experiments were performed in a bulk liquid environment whereas the present experiments are performed in air. As a consequence of the absence of hydrodynamic (Reynolds) damping, the typical approach speed in the present experiments is much higher. This is crucial for entrapping the flat water film in the beginning of the experiment. To verify this idea, we repeated the experiment with the mica surfaces immersed into a bulk drop of water such that the approach speed is slowed down hydrodynamically. In this case, the water was indeed continuously drained out and direct mica-mica contact was observed throughout the entire contact area. This confirms that the high approach speeds are indeed crucial for quenching the system into the unstable initial state.

What is the physical origin of the observed instability? Our observations appear similar to the well-known phenomenon of spinodal dewetting [31], which has been studied extensively, e.g. in the context of thin polymer coatings [32]. Specifically, the present experimental configuration with two elastic mica sheets separated by an initially flat film resembles experiments of Dalnoki-Veress et al. [33], who investigated the (in-)stability of thin flat polymer films covered on both sides by elastic inorganic capping layers upon heating the samples beyond the glass transition temperature of the polymer. The competition between attractive dispersion forces (described by a disjoining pressure $\Pi_{vdW} = -A/12\pi h^3$, where $A>0$ is the Hamaker constant, in our case for the mica-water-mica trilayer), which destabilize the flat film morphology, and the bending elasticity of the capping layers, which tends to restore a flat configuration, determines the stability of the film. For a sinusoidal perturbation $h = h_w + 2\zeta_0 \sin(qx)$ of the film thickness (see Fig. 10.7), it is straightforward to show using linear stability analysis in lubrication approximation, that the system is unstable for perturbations beyond a certain critical wavelength λ_c. In particular, one finds that the wavelength of the fastest growing mode and the corresponding characteristic growth time of the instability are given by $\lambda = 2h_w \sqrt[4]{\pi^5 E_m d_m^3 / (2A(1-\nu^2))}$ and $\tau = 12\eta h_w^3 \sqrt{\pi^3 E_m d_m^3 / (2A^3(1-\nu^2))}$, respectively [33]. ($\eta$: the viscosity of the liquid and E_m: the Young's modulus of the capping layer.) Comparing these expressions to our experimental findings, results in a striking discrepancy. According to the model λ increases with increasing thickness of the initial water film, whereas it remains constant in the experiments. Moreover, τ, which decreases with h_w^{-3} in the experiments, increases with h_w^{+3} according to the model. This contradiction is rather

fundamental: even if one assumes a more complex form of the disjoining pressure (e.g. including electrostatic interactions), any possible interaction would depend strongly on the initial distance h_w between the two mica surfaces. Unless some thickness-dependent variation of the viscosity fortuitously compensates for this distance-dependence, one automatically obtains a characteristic wavelength that depends on the initial thickness of the water layer - in contrast with the experimental results. We are thus left with the challenge of identifying a driving mechanism for the instability that is independent of h_w.

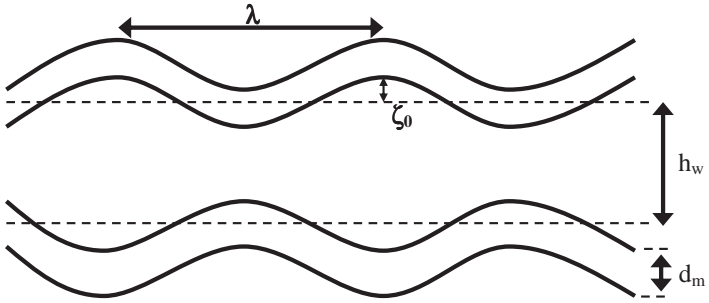

Figure 10.7 Schematic sketch of the developing instability (not to scale; in reality, ζ_0, h_w << d_m, λ). When the mica (with thickness d_m) is perturbed with a small amplitude ζ_0 the thin water film (initial thickness h_w) becomes unstable and breaks up into droplets.

Elastic wrinkling is a common instability mechanism that can lead to spontaneous surface deformations in (visco-) elastic multilayer systems, including in particular stiff thin shells on a softer bulk foundation, such as the mica sheets on the glue layer in the present SFA experiments. (See ref. 15 for a review of recent applications of elastic wrinkling in soft matter systems; a comprehensive overview of the basic physical mechanisms has been given in ref. 14.) If such a multilayer system is exposed to a compressive stress, it may reduce its elastic energy by releasing the energy involved in the compression in the flat configuration and instead assume a buckled configuration. In the present SFA experiments a compressive stress is generated due to the elastic flatting on the originally curved mica sheets within the contact area. In this case, however, the buckling of the supported elastic surface also involves the deformation of the underlying elastic foundation. For a thin mica sheet on a glue foundation that is thick compared to the wavelength of the perturbation, the respective elastic energies (per period), W_m and W_{glue}, for the 2 substrates are given by:

$$\frac{\Delta W}{\lambda} = 2\left(W_m + W_{glue}\right) = 2\left(\frac{1}{4} D q^4 \zeta_0^2 + \frac{1}{6} E_g q \zeta_0^2\right), \qquad (1)$$

where $D = E_m d_m^3 / 12(1-\nu^2)$ is the bending rigidity of mica sheets. ($E_m \approx 200$GPa is Young's modulus of mica for deformations in the a-b plane [34]; $E_g \approx 1$GPa is

Young's modulus of the glue; d_m is the thickness of the mica sheets and ν=0.44 is the Poisson ratio.) The factor 2 accounts for the two elastic surfaces (top and bottom). To determine the energetically most favorable buckling mode, it is important to take into account the fact that the wavenumber q and the amplitude ζ_0 cannot be varied independently since buckling requires the relaxation of the strain u_s imposed by the initial compressive stress. For small amplitudes, the coupling is given by $u_s = \zeta_0^2 q^2 / 4 = const.$ [14]. As a consequence, one can rewrite eq. (1) as:

$$\frac{\Delta W}{\lambda} = u_s \left(2D q^2 + \frac{4}{3} E_g \frac{1}{q} \right). \qquad (2)$$

Minimizing this expression with respect to q results in a characteristic wavelength $\lambda_c = 2\pi d_m \left(E_m / (4E_g(1-\nu^2)) \right)^{1/3}$. This expression is indeed linear in d_m, as seen experimentally (Fig. 10.5(b)). (Note, however, that the model is based on a single deformable sheet, whereas the experimental geometry consists of two mica sheets of different thickness. It is therefore not obvious that the total mica thickness d_m is the relevant quantity to compare to. To account for this uncertainty, we plotted λ in Fig. 10.5(b) also versus the thickness of the thicker and the thinner mica sheet, respectively, expecting that a more complete model would produce some intermediate behaviour.) Moreover, if the driving force for the transition is independent of h_w, the dynamics are determined by a balance of this constant driving force and the hydraulic resistance experienced by the water flowing between the two mica sheets. Since the latter scales as h_w^{-3}, this naturally explains the observed decrease in the characteristic time with increasing h_w. Elastic wrinkling thus successfully reproduces the experimentally observed scaling behaviour corroborating our hypothesis that elastic energies play a crucial role in the observed breakup of the water films.

In spite of this success the above explanation is incomplete. The absolute value of λ_c resulting from the model is about one order of magnitude too large. Moreover, following the standard theory of elastic wrinkling [14], a minimum initial strain of $u_{s,\min} = (\sqrt{2} E_g (1-\nu^2) / E_m)^{2/3}$ is required to induce wrinkling. Even when taking into account the uncertainties due to the poorly known elasticity of the glue layer (which depends also on the efficiency of the UV cross-linking) as well as possible corrections due to the strong anisotropy of mica, the strain derived from the initial curvature of the mica sheets and the diameter of the contact area seems about two orders of magnitude too small to actually cause wrinkling. Mönch and Herminghaus [35] argued in their study of elastic buckling of two PDMS (polydimethylsiloxane) surfaces in close contact that the van der Waals attraction provides an additional q-independent negative contribution to the total energy and thereby renders spontaneous elastic deformations possible. In view of the fixed strain-release requirement of elastic wrinkling, however, it is not obvious whether this argument is applicable in our situation. Experimentally, we occasionally noted that the thin mica sheets display wrinkles close to their edges after UV-curing of the glue. This indicates that a substantial amount of strain is created

during the substrate preparation and might facilitate buckling later in the experiment. A detailed clarification of these aspects has to be deferred to future studies.
Finally, it is also interesting to comment on the equilibrium shape of the nanodrops in the final state. Despite the dominance of the elastic energies in selecting the characteristic wavelength in the initial state of the instability, it is obvious that molecular interaction forces (such as the diverging disjoining pressure due to van der Waals energy and short range adhesive forces) must play an important role in controlling the final shape. Approximate approaches to this problem are described in ref. 36 and 37. A true quantitative analysis, which is outside the scope of the present paper, would require a variational minimization of the total elastic and molecular interaction energy as a function of the shape of the nanodrops under the constraint of constant volume.

10.5 Summary

We have found that nanometer thin water films confined between two elastic smooth surfaces breaks up into nanodroplets if quenched into an unstable initial state by the pressing the confining surfaces together very fast. This is in contrast to conventional experiments with the surface forces apparatus, in which the nucleation and growth processes typically control the break-up of thin liquid films. The instability mechanism described here should also apply in other situations where solid surfaces covered by thin liquid layers are rapidly forced into contact. The elasticity of the substrate walls plays a crucial role in the break-up of the liquid films. While the observed (in-)dependence of the characteristic wavelength and the characteristic time on the initial thickness of the water layer is incompatible with a dispersion-driven mechanism, elastic wrinkling, slowed down by hydrodynamic damping, reproduces the scaling behavior found in the experiments. Yet, a fully consistent model of the break-up process still has to be developed. Once such a quantitative model becomes available, a detailed analysis of the dynamics of the transition provides a novel approach for studying transport properties in ultrathin films of water and other liquids.

Acknowledgement

We thank S. Herminghaus, T. Melsen, H. Rathgen and D. van den Ende for the fruitful and stimulating discussions and C. Harteveld, K. Smit and M. van der Weide-Grevelink for the technical support.

References

[1] J.N. Israelachvili, *Intermolecular and Surface Forces*. 2nd ed.; Academic Press: London, (1992)
[2] E. Lauga, M.P. Brenner, H.A. Stone, *Handbook of Experimental Fluid Dynamics* Springer, New York, (2006).

[3] C. Neto, D.R. Evans, E. Bonaccurso, H.-J. Butt, V.S.J. Craig, *Rep. Prog. Phys.* **68**, 2859 (2005)
[4] J.W.G. Tyrrell, P. Attard, *Phys. Rev. Lett.* **87**, 176104 (2001)
[5] X.H. Zhang, X.D. Zhang, S.T. Lou, Z.X. Zhang, J.L. Sun, J. Hu, *Langmuir* **20**, 3813-3815 (2004)
[6] B.N.J. Persson, *Sliding Friction*. 2nd ed.; Springer Verlag: Berlin, (2000)
[7] B.N.J. Persson, O. Albohr, U. Tartaglino, A.I. Volokitin, E. Tosatti, *J. Phys. Cond. Matt.* **17**, R1-R62 (2005)
[8] J.N. Israelachvili R.M. Pashley, *Nature* **306**, 249-250 (1983)
[9] U. Raviv, P. Laurat, J. Klein, *Nature* **413**, 51-54 (2001)
[10] K.M. van Delft, J.C.T. Eijkel, D. Mijatovic, T.S. Druzhinina, H. Rathgen, N.R. Tas, A. van den Berg, F. Mugele, *Nano Lett.* **7**, 345–350 (2007)
[11] T.D. Li, J.P. Gao, R. Szoszkiewicz, U. Landman, E. Riedo, *Phys. Rev. B* **75**, 115415 (2007)
[12] L. Xu, M. Salmeron, *Studies of Wetting and Capillary Phenomena at Nanometer Scale with Scanning Polarization Force Microscopy* in *Nano-Surface Chemistry*, Rosoff, M., Ed. Marcel Dekker Inc.: New York, (2001)
[13] P.B. Miranda, L. Xu, Y.R. Shen, M. Salmeron, *Phys. Rev. Lett.* **81**, 5876-5879 (1998)
[14] J. Groenewold, *Physica A* **298**, 32-45 (2001)
[15] J. Genzer, J. Groenewold, *Soft Matt.* **2**, 310-323 (2006)
[16] F. Mugele, M. Salmeron, *Phys. Rev. Lett.* **84**, 5796 (2000)
[17] T. Becker, F. Mugele, *Phys. Rev. Lett.* **91**, 166104 (2003)
[18] P. Frantz, M. Salmeron, *Trib. Lett.* **5**, 151-153 (1998)
[19] T. Becker, F. Mugele, *J. Phys. Cond. Matt.* **17**, S319-S332 (2005)
[20] E. Hecht, *Optics*, Addison Wesley Longman Inc. (2002)
[21] M. Heuberger, *Rev. Sci. Instr.* **72**, 1700 (2001)
[22] The accuracy of the contact time is limited by the finite frame rate of the camera. The full contact area appears from within video frame.
[23] The origin of the global intensity variations visible over the contact area is not known a priori, but we speculate that they are most likely an interference-effect. We checked via spectral analysis that they do not represent height changes.
[24] D. Beaglehole, E.Z. Radlinska, B.W. Ninham, H.K. Christenson, *Phys. Rev. Lett.* **66**, 2084-2087 (1991)
[25] T.E. Balmer, H.K. Christenson, N.D. Spencer, M. Heuberger, *Langmuir* **24**, 1566-1569 (2008)
[26] T. Becker, F. Mugele, *J. Phys. Cond. Matt.* **15**, S321-S330 (2003)
[27] B.N.J. Persson, E. Tosatti, *Phys. Rev. B* **50**, 5590-5599 (1994)
[28] B.N.J. Persson, F. Mugele, *J. Phys. Cond. Matt.* **16**, R295-R355 (2004)
[29] P. Martin, F. Brochard-Wyart, *Phys. Rev. Lett.* **80**, 3296-3299 (1998)
[30] R.M. Pashley, J.N. Israelachvili, *J. Coll. Interf. Sc.* **101**, 511-523 (1984)
[31] E. Ruckenstein, R.K. Jain, *J. Chem. Soc. Faraday Trans. 2* **70**, 132 – 147 (1974)
[32] S. Herminghaus, K. Jacobs, K. Mecke, J. Bischof, A. Fery, M. Ibn-Elhaj, S. Schlagowski, *Science* **282**, 916-919 (1998)
[33] K. Dalnoki-Veress, B.G. Nickel, J.R. Dutcher, *Phys. Rev. Lett.* **82**, 1486-1489 (1999)
[34] L.E. McNeil, M. Grimsditch, *J. Phys. Cond. Matt.* **5**, 1681-1690 (1993)
[35] W. Mönch, S. Herminghaus, *Euro Phys. Lett.* **53**, 525-531 (2001)
[36] S. Perkin, L. Chai, N. Kampf, U. Raviv, W. Briscoe, I. Dunlop, S. Titmuss, M. Seo, E. Kumacheva, J. Klein, *Langmuir* **22**, 6142 (2006)
[37] F. Mugele, T. Becker, A. Klingner, M. Salmeron, *Coll. Surf. A* **206**, 105 (2002)

Chapter 11

On the shape of surface nanobubbles

In this chapter we describe our study on surface nanobubbles. Previous AFM experiments on surface nanobubbles have suggested an anomalously large contact angle θ of the bubbles (typically ~160º measured through the water) and a possible size dependence $\theta(R)$. Here we determine $\theta(R)$ for nanobubbles on smooth, highly oriented pyrolytic graphite (HOPG) with a variety of different cantilevers. It is found that $\theta(R)$ is constant within experimental error, down to bubbles as small as R = 20 nm, and is equal to 119 ± 4º. This result, which is the lowest contact angle for surface nanobubbles found so far, is very reproducible and independent of the cantilever type used, provided that the cantilever is clean and the HOPG surface is smooth. In contrast, we find that, for a particular set of cantilevers, the surface can become relatively rough because of precipitated matter from the cantilever onto the substrate, in which case larger nanoscopic contact angles (~150º) show up. In addition, we address the issue of the set-point dependence. Once the set-point ratio is below roughly 95 %, the obtained nanobubble shape changes and depends on both nanobubble size and cantilever properties (spring constant, material, and shape).[1]

[1] This chapter has been published as: B.M. Borkent, S. de Beer, F. Mugele & D. Lohse, *Langmuir* **26**, 260 (2010). In this work SdB performed the measurements and BMB did the data-analysis. Both SdB and BMB worked on the interpretation of the results.

11.1 Introduction

Water in contact with hydrophobic surfaces, the most frequently studied example of a non-wetting system displays various intriguing but poorly understood properties. One of them is spherical caplike soft domains at the solid-liquid interface, which are currently termed "sur-face nanobubbles". Since the first observations through atomic force microscopy (AFM) a-
bout a decade ago, [1-5] ample evidence has been reported on their existence. Most of the AFM studies explored the formation mechanism of nanobubbles and their dependence environmental changes. This yielded characteristics fitting with the interpretation of gas-filled nanobubbles: the features are spherically shaped [6, 7], can merge [6, 8], disappear in degassed water [9], and reappear when the liquid is locally oversaturated (e.g., through the exchange of two solvents [7, 10-14], liquid heating [10], or electrolysis [8, 15]). Although most of these studies were done with AFM in tapping mode, nanobubbles were also inferred from infrared spectroscopy [12-14], neutron reflectometry [16], quartz crystal microbalance [17], and rapid shock-freeze cryofixation experiments [18]. Surface nanobubbles have been found on a variety of substrates[2] with macroscopic contact angles (measured through the liquid) varying between ~50º (Au) and 110º hydrophobized Si) and a roughness ranging from atomically smooth (HOPG) to rough on the nanometer scale (e.g., 3.5 nm rms roughness on polyamide). In contrast, the observed contact angle of the nanobubbles with the substrates is always in the range of 150-170º. Table 11.1 provides an overview of this contact angle discrepancy reported on the literature.

The liquids in which surface nanobubbles have been found usually consist of ultrapure Milli-Q water or DI water, with occasional additions of surfactants [7, 10], salts [7, 15] or acidic solutions [8]. The gas inside the nanobubbles generally comprises air, and sometimes the bubbles are composed of single gases such as N_2 [8, 15], O_2 [15], CO_2 [14]. It is found that these variations do not significantly change the magnitude of the nanoscopic contact angle.

How should the anomalously large contact angle of surface nanobubbles be interpreted?

On one hand, this result has been reproduced in various experiments (Table 11.1). On the other hand, one would expect that for large enough bubbles (contact line radius $R \rightarrow \infty$) the nanoscopic contact angle will approach the macroscopic one. This, however, was never observed: the largest surface bubbles measured through AFM had R values of several micrometers and radii of curvature R_c of several tens of micrometers and still had contact angles of $\theta_{nb} > 160º$ [7, 14] without a noticeable trend toward lower values. This raises a second and related issue as to whether one should expect the nanoscopic contact angle to be size-dependent. Although Zhang et al, [14] were not able to detect such a relation, in contrast, other studies have reported a small decrease in contact angles with increasing nanobubble size, which was attributed to the

[2] For example, bare Si [20], hydrophobized Si [10, 11], polystyrene [6, 16, 27, 43], polyamide [11], gold [21, 44] and HOPG [1, 7-9, 13, 15].

presence of a line tension [19-21]. In one of these studies [19], the bubble shapes were not deconvoluted for the finite size of the cantilever tip, which hinders the extraction of line tension. Contact angles reported for surface nanodroplets, the inverse problem, measured by TM-AFM are either in good agreement with the macroscopic values [22, 23] or any discrepancies could be attributed to surface heterogeneities. [24]

Note that theoretically a line tension is expected to act on a length scale of $\sim \tau / \sigma \approx 10^{-11}$ N / 10^{-1} N / m = 10^{-10} m [25], with τ the typical line tension and σ the liquid-air interfacial tension, which is well below the typical size of a surface nanobubble.

In the discussion on contact angel discrepancy and its possible size dependence, is has always been assumed that the actual topography of the gas-liquid (nanobubble) interface is obtained correctly by the vibrating cantilever tip. However, Zhang et al. [7] concluded that the cantilever tip most likely deforms (or penetrates) the bubble during imaging. How should the crucial premise that the actual shape of the nanobubble can be obtained by TM-AFM be verified?

A possible way to approach this problem is to use cantilevers of different types to determine if their intrinsic properties, such as tip radius, spring constant *k*, and local wetting properties (material), have an effect on the detected nanobubble shape. If the tip penetrates or deforms the bubble during imaging, then one would expect those properties to play a role and thus that different cantilevers will yield different nanobubble shapes.

In addition tunable properties, such as the set-point ratio, free amplitude, and drive frequency of the cantilever, could play a role. From this list, only the effect of the set-point amplitude has been studied: Zhang at al. [7] found that a reproducible nanobubble shape is obtained when using a V-shaped Si_3N_4 cantilever (Veeco) with a spring constant of k = 0.079 N/m for set-point ratios between 0.93 and 0.74. However, for imaging purposes, cantilevers that are a factor of > 4 stiffer are used in ref 7, and it is unclear how this affects the results. Yang et al. [13] showed that the recorded nanobubble shape is a subtle function of the set-point ratio in the case of a rectangular Si_3N_4 cantilever (MikroMasch) with k = 3.8 ± 1.8 N/m: reducing the set-point ratio from 0.89 to 0.78 reduces the apparent nanobubble height with ~10%, where as more drastic morphological changes are obtained for set-point ratios below 0.67. Apart from these studies, little is known.

The aim of this study is to obtain the contact angle of nanobubbles as a function of their size.

As argued, a prerequisite for this measurement is, first, the validation of the assumption that the nanobubble shape is not affected by intrinsic cantilever properties and, second, insight into how the observed nanobubble shape depends on tuneable properties such as the set-point ratio. To this end, we have measured nanobubbles present on HOPG using 15 cantilevers of all kinds, displaying different materials, shapes, and spring constants.

substrate	θ_m or θ_a / θ_r (deg)	θ_{nb} (deg)	Tip correction	Ref.
HOPG	72 ± 11	164 ± 6	Y	7
HOPG	81 ± 3 / 63 ± 3	164 ± 6	Y	9
Si(100) - OTS	110	150 - 170	N	2
Si(100) - OTS	108 ± 5	168 ± 9	Y	7
Si(100) - OTS	110 ± 3	169 ± 3	N	26
Si(100) - OTMS	112 ± 3 / 101 ± 3	174 ± 1	N	12, 14
Si(100) - TMCS	74 / 67	150 – 157	N	19
Si(100) - PFDCS	105 / -	137 – 168	N	10
PS	97	170 – 177	N	27
PS	~ 90	168 ± 10	N	6
Au(100)	40 - 60	166 ± 2	Y	21

Table 11.1 Overview of the contact angle discrepancy in surface nanobubble experiments with TM-AFM where both the static and macroscopic contact angle θ_m (or advancing contact angle θ_a / receding contact angle θ_r) and the contact angle as deduced from nanobubbles θ_{nb} are reported. Substrate abbreviations: PS, polystyrene; OTS, octadecyltrichlorosilane; OTMS, octa-decyltrimethylchlorosilane; TMCS, trimethylchlorosilane; and PFDCS, 1*H,*1*H,*2*H,*2*H*-perflu-orodecyldimethylchlorosilane. Note that the contact angles are not always corrected for the tip radius (see column four for yes = Y or no = N), in which case it is the apparent nanoscopic contact angle θ^I that is reported.

11.2 Materials and Methods

Substrate/Water

As substrates, highly ordered pyrolytic graphite (HOPG, Mikromasch grade ZYA) is used to ensure clean, atomically flat surfaces. Before each experiment, the dry, freshly cleaved (with adhesive tape) HOPG substrate is measured with AFM to ensure that the surface is clean and atomically smooth. Water is purified using a Milli-Q A10 system. To ensure gas-saturated water, the liquid is allowed to equilibrate with atmospheric pressure for several hours. The macroscopic advancing contact angle θ_a of water with the HOPG substrate is 95º, and the receding contact angle is θ_r = 82º as measured with an optical contact angle goniometer (OCA-15+, Data Physics, Germany) with built-in SCA-20 software.

Nanobubble Formation by Entrapment.

To create nanobubbles, the cantilever is mounted in the holder (Figure 11.1(a)) and immersed in a large water droplet deposited by a syringe (Figure 1.1(b)). Second, the holder-cantilever assembly is turned upside down with the droplet hanging underneath the holder. The assembly is then quickly pressed onto the freshly cleaved HOPG surface, already mounted in the AFM head, allowing air to become entrapped between the droplet and the HOPG surface. See Fig.11.1 for the accompanying sketches. We observed that the water droplet should be large enough to create nanobubbles by

entrapment. Presumably, a small droplet is not able to trap air because of its larger curvature.

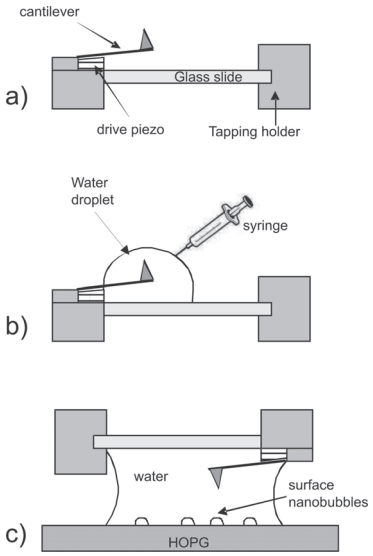

Figure 11.1 Sketch of the dry cantilever holder (a). To create nanobubbles, the cantilever is first immersed in a large water droplet deposited by a syringe (b) while second the holder-droplet assembly is turned upside down and pressed onto the HOPG substrate that is already mounted in the head of the AFM (c)

Atomic Force Microscopy (AFM).
Nanobubble measurements are performed on a Veeco Multimode equipped with a Nanoscope V controller, a low noise head (Veeco), and a piezo-scanner with vertical motor approach (E scanner). The cantilevers vary by manufacturing company (Veeco and Mikromasch), surface material (silicon, silicon nitride, or gold), shape (rectangular or V-shaped), and spring constant. The following cantilever types have been used: Veeco NP-S, Si_3N_4 V-shaped and MPP 22120 Si rectangular, Mikromasch NSC36 Si-rectangular, NSC36 Si_3N_4 rectangular, CSC37 Si rectangular, and CSC37 Si_3 N_4 rectangular.
An overview of the cantilever properties used in this work is found in Table 11.2. Prior to each experiment, the cantilever of interest is exposed to plasma for ~1 min (Harrick Plasma).
The spring constant is determined in air using the thermal calibration method Thermal Tune in the Nanoscope 7.20 software [28]. The resonance frequency in liquid is determined by the same method at a distance of 100 nm above the sample surface for the correct characterization of the added mass of the system. The cantilever is acoustically driven with a frequency just below resonance (without Q control). Acoustic driving of the cantilevers has been realized using a modified cantilever

holder (Veeco Tapping holder air, MMMC), as first described in ref 29, which reduces spurious resonances characteristic of the conventional commercial liquid cell and increases the stability of the measurements.

class	no	symbol	type	Mat.	k	R_t^{spec}	R_t^{SEM}	R_t^{step}	R_t	a (%)	z_{rms} (nm)
A	1	Blue square	MM NSC36[c]	Si	1.6	10	26 ± 4	29 ± 9		5.64	0.94
	2	Left facing black triangle	MM NSC36	Si	2.4	10				2	0.93
	3	Green circle	MM NSC36	Si_3N_4	1.98	20	25 ± 4			1.15	0.7
	4	Magenta diamond	MM CSC37	Si	0.98	10				3.99	2.56
	5	Right facing red triangle	MM CSC37	Si	0.86	10	33 ± 5			0.74	0.99
	6	Magenta triangle	MM CSC37	Si_3N_4	0.63	20	23 ± 4			5.12	1.08
	7	Aqua triangle	MM NSC36[c]	Si_3N_4	2.33	20	35 ± 7			0.78	0.64
	8	Black star	MM CSC37	Si_3N_4	0.71	20				7.96	2.26
B	9	Aqua diamond	V NP-S v	Si_3N_4	0.68	20	N.A.	20 ± 3	20 ± 3	0.42	0.28
	10	Blue circle	MM CSC37[c]	Au	1.14	50	17 ± 3	10 ± 2	13.5 ± 5	0.47	0.26
	11	Green triangle	MM CSC37	Au	0.69	50	22 ± 5	16 ± 3	19 ± 8	0.26	0.2
	12	Magenta square	V MPP22120[c]	Si	0.68	10	15 ± 2	19 ± 3	17 ± 5	[d]	[d]
	13	Right facing black triangle	V NP-S[b] v	Si_3N_4	0.27	10	20 ± 4	N.A.	20 ± 4	0.26	0.22
	14	Blue triangle	MM NSC36	Si	4.8	10	N.A.	N.A.	N.A.	0.71	0.29
	15	Down facing red triangle	V MPP 22120	Si	0.61	10	N.A.	14 ± 3	14 ± 3	0.12	0.19

Table 11.2 Characterization of the cantilevers used in this study: MM denotes cantilevers produced by Mikromasch, which are rectangular in shape. V stands for cantilevers from Veeco, which are rectangular (default) or v-shaped (denoted by v). The values of the cantilever tip radius (in nm) are given as specified by the manufacturer R_t^{spec}, as measured by SEM imaging R_t^{SEM}, as deduced from the measured profile of HOPG steps R_t^{step} and as the mean of the two former values R_t, respectively. R_t is the value used to correct the data. The last two columns depict the roughness of the substrates measured by the cantilevers, quantified by the surface area difference a and the rms value of the surface height z. The symbols refer to Figure 11.8 and 11.9. [b] SEM images of these cantilevers are shown in Figure 11.3. [c] SEM images of these cantilevers are shown in Figure 11.7. [d] No reliable background data because of a too high gain.

The height images are recorded at different amplitude set-point ratios $r_{sp} = A/A_0$, where A is the amplitude set-point during imaging and A_0 is the free amplitude of the cantilever. With the adjusted cantilever holder, the free amplitude is constant over a much longer period of time compared to the commercial liquid cell, allowing long-term imaging with a constant r_{sp}. To find the correct free amplitude, amplitude phase distance (APD) curves are recorded before and after each recorded height image. Typically, $A_0 \approx 30$mV and deflection sensitivities are ~ 40 nm/V, resulting in values of 1 nm $< A_0 <$ 1.5 nm. Hence, the total amplitude of the cantilever, $A_{tot} = \sqrt{(A_0 \sin\varphi)^2 + (A_0 \cos\varphi + A_d)^2}$ is kept at around 1 to 2 nm. Here, A_d is the amplitude of the piezo driving the cantilever base and can be determined through eq 2a of ref 30 and the phase was assumed to ~90 deg at resonance. This low value of A_{tot} is feasible because of the low-noise head, the controller, and the special liquid cell and is

probably much smaller than the ones used in most other previous studies (cf. ref 6); however we are not able to check this because of the lack of reported experimental details. The images obtained are in most cases 2 x 2 μm^2 in size with a resolution of 512 x 512 pixels^2. Typical scan rates are 1 Hz (corresponding to a tip velocity of 4 μm/s).

Image Analysis.

The obtained height images are processed and analyzed using digital image analysis software. First, the images are subjected to second-order flattening (excluding the bubbles) and levelled such that the HOPG surface represents zero height (0 nm). This allows for the identification of individual nanobubbles using a height threshold (typically ~4 nm). In the next step, a 3D fit is applied to each nanobubble separately (to those data points that are above the height threshold), thereby taking into account all information about the recorded nanobubble profile. This results in the apparent radius of curvature $R_c^{'}$ of the nanobubble and its position with respect to the substrate surface. From these parameters, the other relevant geometrical parameters follow: height h, apparent contact line radius $R^{'}$, and apparent contact angle $\theta^{'}$ of the nanobubble; see Figure 11.2(a).

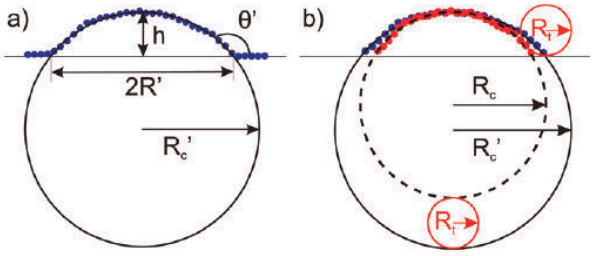

Figure 11.2 (a) Cross-sectional data points (circles) along the scanning direction of a nanobubble present in Figure 11.4 with height h 26.2 nm and apparent radius R^1 = 54.6 nm (without tip radius correction). Note that the bubble resides on a smooth surface and remains spherically shaped when touching the surface (i.e., it does not form a noticeable foot at the triple-contact line). The 3D spherical fit (solid line) gives an apparent radius of curvature of $R_c^{'}$ = 70 nm for the bubble. When the position of the substrate (horizontal line) is known, the other relevant geometrical parameters follow. The apparent contact angle θ' is taken through the water. (b) Same bubble showing raw and deconvoluted cross-sectional data points (blue and red circles, respectively) together with their respective spherical fits $R_c^{'}$ and R_c = 55.0 nm. Alternatively, R_c can be contained using the tip radius R_t (in this case, R_t = 15 nm) through $R_c = R_c^{'} - R_t$.

Tip correction.

The topography image of the solid-liquid interface as obtained by the cantilever tip is a combination of the substrate morphology and the shape of the cantilever tip and

therefore needs to be corrected for the tip shape [31]. In the case of a spherical cap shaped object and a spherical cap shaped object and a spherical tip apex, tip deconvolution simply implies that $R_c = R_c' - R_t$, with R_t being the tip radius [20]. Assuming that the bubble height h is not affected by the tip shape (Figure 11.2(b)), R and θ can be calculated. Note that it is also assumed that the bubble is probed only by the spherical tip apex and not by the tip side walls. This is correct insofar as the bubble makes an angle with the solid wall (through the water) of $\theta_{cutoff} > 90º$ = half-cone angle of the tip. For the cantilevers used in this article, $\theta_{cutoff} = 110º$ (Mikromasch) and $\theta_{cutoff} = 125º$ (Veeco). For the former cantilever, it always holds that $\theta > \theta_{cutoff}$ whereas for the latter we take only those data points into consideration for which this condition is fulfilled. Instead of applying the correction after the 3D fit, alternatively one can also first deconvolute the individual data points and then apply the spherical fit. We checked that this gives no noticeable difference in the corrected radius of curvature as compared to that of the first method; see Figure 11.2(b). Hence it is safe to apply the simple correction $R_c = R_c' - R_t$. Notice that this implies $dR_c = dR_t$, which is further translated into ΔR and $\Delta\theta$ via $\Delta R = (\partial R(h, R_c)/\partial R_c)\Delta R_c$ and $\Delta\theta = (\partial\theta(h, R_c)/\partial R_c)\Delta R_c$. These relations are used to estimate the error in our measurements.

The tip radius R_t has been determined in two ways: using high resolution SEM imaging (HR-SEM Zeiss LEO 1550 equipped with NORAN EDS end WDS) and using the measured profile of a (multiple) step on the substrate. From the SEM images, the tip radius R_t^{SEM} was determined by applying a circular fit to the imaged tip apex (Figure 11.3(a)). In the second method, a step profile of the substrate is averaged along the direction of the (multi)step (to filter out any noise) and interpolated and then a circular fit is applied, yielding R_t^{step} (Figure 11.3(b)). We have checked the reproducibility of R_t^{step} by using as many steps as possible (typically 2-5). The tip radii obtained with these two methods are shown in Table 11.2. The average of both values (if possible) is the tip radius R_t for which our data has been corrected. The experimental error in the tip radius dR_t is anticipated in a worst-case scenario by adding the two error values determined in the two methods, $dR_t = d R_t^{step} + R_t^{SEM}$. In some cases, only one of the two methods could be used because of a broken tip (which became broken after taking the recordings) or the lack of a sufficiently large step. If neither of the two methods could be used, the tip correction is not applied; consequently, those data are not presented in graphs where tip-corrected data are shown.

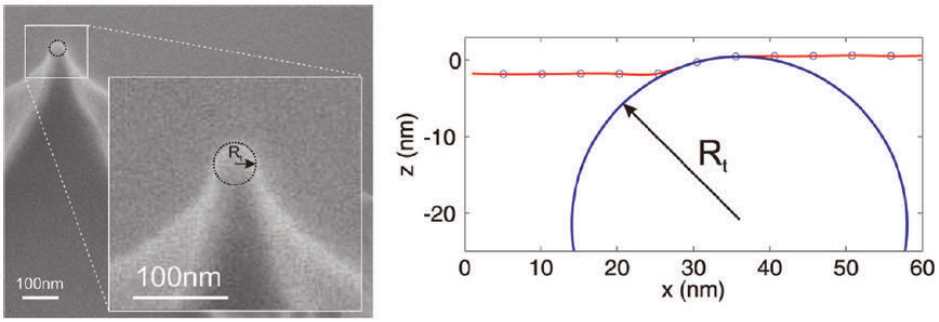

Figure 11.3 SEM picture of the Veeco NP-S Si_3N_4 cantilever tip (left) and circular fit to the measured profile of a step edge in the HOPG (right).

11.3 Results and Discussions

Previous experimental studies showed that no nanobubbles are formed on HOPG unless the water is temporally supersaturated (e.g., through the exchange of two liquids in which the second liquid has a lower gas solubility than the first.) [7, 13] Here, we show that there is an even simpler method of forming nanobubbles on HOPG that requires neither explicit oversaturation of the liquid nor flushing of one liquid with the other but involves just the deposition of a large water droplet on the HOPG substrate. [11] For further description and supporting sketches, see Figure 11.1. After this uncomplicated procedure, images of surface nanobubbles could be obtained through AFM in tapping mode.

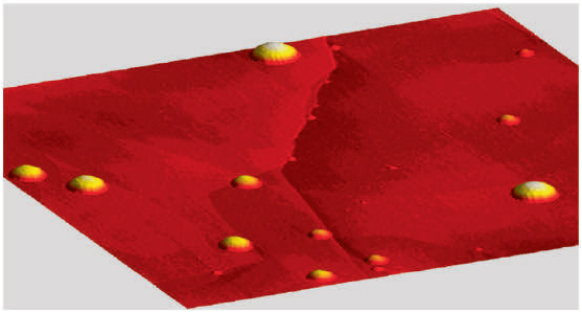

Figure 11.4 Typical 3D image of surface nanobubbles present on a HOPG surface immersed in water. The size of the image is 2000 x 2000 x 40nm^3 and is shown to scale. The nanobubbles show up as perfect spherical caps and have various sizes. They reside both at step edges and on atomically flat terraces. Apart from the step edges, the HOPG surface appears to be very smooth. The picture was taken with cantilever 11 in Table 11.2 and is shown in 2D in Figure 11.5 (second from the top in the right column). No tip correction has been applied.

Properties of Nanobubbles Formed by Droplet Deposition.
A typical result of the water-solid interface is depicted in Figure 11.4 and shows several distinctive features: the bubbles show up as spherical caps, consequently allowing them to be fitted by a spherical cap. Second, the number density of the nanobubbles is relatively low, which allows good analysis of individual bubbles. Because we did not create the bubbles with the help of forced gas over saturation, it is also expected that the number densities are relatively low compared to cases were strong gas over saturation is used (e.g., in refs 7, 10, and 11). Also notice that there are more bubbles residing on the lower side of the HOPG step than on the upper side, in contrast with the observations in ref. 13. A step presumably hinders the air flow while it is escaping in between the substrate and the approaching droplet, and thus some air may become entrapped at this location. Some bubbles are not located at steps but reside on apparently smooth HOPG plateaus. Third, the bubbles have various sizes, which allows the determination of θ (R) from a single image. Notice that this feature is not always the case: in dense surface nanobubble populations, a preferred nanobubble size can be present [6, 32].

Rough and Smooth Surfaces.
To examine whether $\theta(R)$ is dependent on the cantilever properties, experiments are carried out with 15 different cantilevers displaying various shapes, materials, and spring constants. Table 11.2 provides an overview of the cantilevers used and their respective properties. Remarkably, all experiments can be divided into two significantly different classes. In the first class (A), the nanobubbles are present on relatively rough HOPG surfaces, and in the second class (B), the bubbles reside on relatively smooth HOPG surfaces. Figure 11.5 presents height images of eight different experiments and illustrates the categorization based on the roughness present on the HOPG. In the left column, nanobubbles are residing on rough substrates (class A), and the middle column depicts nanobubbles on atomically smooth surfaces (class B). Corresponding line scans of the substrates illustrate the difference in surface roughness (right column).
A quantitative distinction of roughness can be made by comparing the rms values of nano-bubble free areas in the pictures , which gives z_{RMS} = 0.6-2.6 nm for the rough and z_{RMS} = 0.2-0.3 nm for the smooth surfaces present in Figure 11.5.
Another useful measure is the surface area difference a, which is the difference between the actual surface area A_{actual} and the projected surface area A_{proj} in percentage:

$$a = \frac{A_{actual} - A_{proj}}{A_{proj}} \times 100\% \qquad (1)$$

The pictures in the left column of Figure 11.5 show 0.78 % < a < 5.64 %, and the middle column pictures represent 0.12 % < a < 0.47 %. In this way, al 15 experiments can be categorized (Table 11.2): eight experiments were carried out with cantilevers 1-

8 (class A) and show surfaces that are relatively rough (i.e., the nanobubble-free background surface has rms values >0.6 nm and $a > 0.7$ %) whereas the other seven experiments display HOPG surfaces that are relatively smooth (i.e., the nanobubble-free background surface has rms values of < 0.3 nm and $a < 0.7$ %) and correspond to cantilevers 9-15.

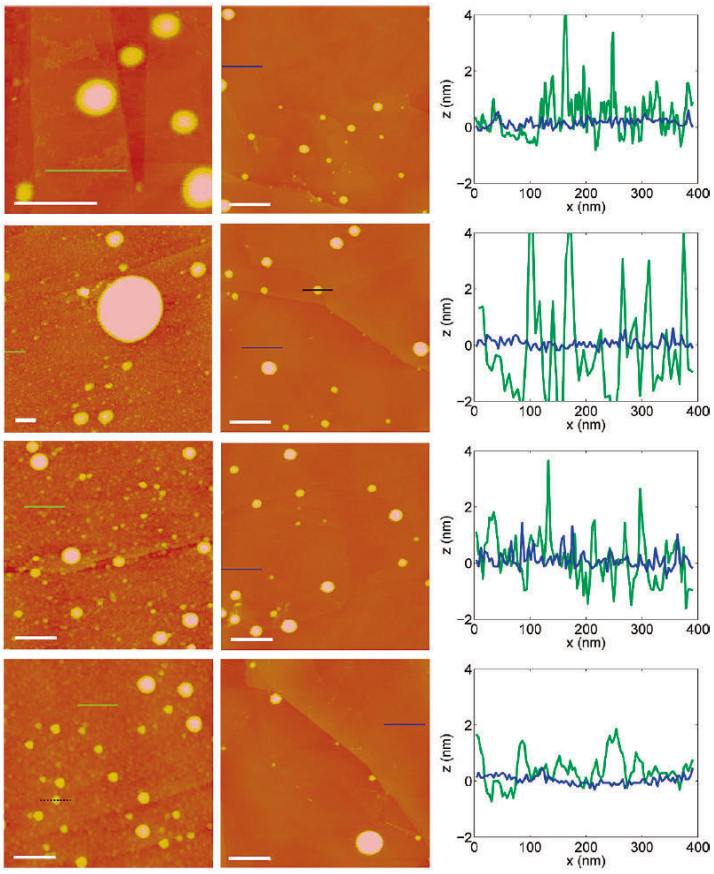

Figure 11.5 AFM height images of eight different experiments. All experiments could be divided into two categories: Images having rough background surfaces (left column) or with smooth background surfaces (middle column). The white scale bar is 400 nm in length, and the color-coded height scale is 50 nm for all images. To show the difference in surface roughness, typical line scans of 400 nm are taken on both the left (green line) and middle (blue line) images and are displayed in the graphs in the right column. Two line scans of a bubble (black dashed and solid lines) in contact with an apparently rough or smooth surface are compared in Figure 11.6. Cantilevers used in these images correspond to nos. 1, 4, 6 and 7 (top to bottom, left column) and 10, 11, 13 and 15 (top to bottom, middle column) in Table 11.2.

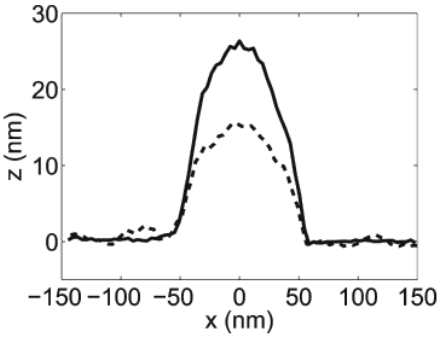

Figure 11.6 Line scans of two bubbles in contact with either an apparently rough substrate (dashed line, taken from the bottom left picture in Figure 11.5) or a relatively smooth substrate (continuous line, taken from the second picture in the middle column of Figure 11.5). The apparent widths of both bubbles are similar, but their heights are markedly different, translating into different contact angles.

Large and Small Contact Angles.

The AFM images, of which some are depicted in Figure 11.5, allow us to extract the contact angles of the bubbles, which is our quantity of interest. We find that the contact angles of two bubbles of equal apparent widths are dramatically different provided that they are residing on substrates of different classes (i.e., rough or smooth). Figure 11.6 illustrates the result using two line scans of equally sized bubbles present either on a relatively rough substrate (dashed line) or on a smooth substrate (continuous line).

What determines the difference? Besides the difference in substrate roughness, the bubbles have also been measured by cantilevers of different types (nos. 7 and 11 in Table 11.2). Therefore, we need to compare all bubbles obtained on all experiments tot give a final answer to the question of what determines the difference in the contact angle. This will be done in a subsequent section; however, first we will consider possible origins of the observed roughness because this will turn out to be a crucial factor.

Contaminated and Clean Cantilevers.

After the AFM experiments, the cantilevers are imaged by high-resolution SEM to obtain their tip radii. Interestingly, the SEM images can be divided into the same two classes. Cantilevers with which nanobubbles on rough surfaces have been measured (class A) are notably contaminated and show distinct staining all over the surface (Figure 11.7 left). The structures look different from dust particles, which are more irregularly shaped. Furthermore, it is known that dark spots on (semi)conducting surfaces in SEM images presumably indicate organic contamination (e.g., siloxane

oil). In contrast, cantilevers with which the smooth surfaces had been measured (class B) look perfectly clean and smooth in the SEM images (Figure 11.7 right).

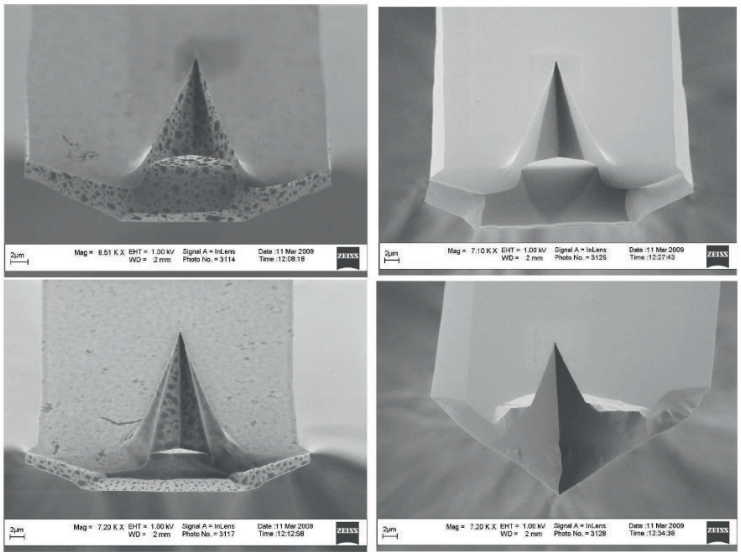

Figure 11.7 SEM images of cantilevers after use, Some cantilevers are stained (left), but others are completely smooth (right). The cantilevers correspond to nos. 1 and 7 (left) and 10 and 12 (right) in Table 11.2.

Origin of Contamination.
All cantilevers are imaged simultaneously, which excludes the SEM chamber itself from being the source of contamination. We have also imaged new (unused) cantilevers from the same batches as the used cantilevers, and they are as clean or contaminated as the ones that were imaged after use. This indicates that the contamination is not measurement induced but originates from the packaging material. Interestingly, MM cantilevers from class A were stored in their gel packages for longer periods of time (months) than MM cantilevers from class B (weeks). Veeco cantilevers did not show the strange contamination, even if they are stored in gel packages for several years, most likely because of the protective seal on top of the gel package. Our result is in line with previous observations of organic contamination on cantilevers arising from the packaging material [33, 34].

Origin of Rough Surfaces.
For all 15 experiments described here, the same experimental preparation procedure has been strictly followed. We checked via AFM that all HOPG surfaces are atomically smooth by preparation. On one day the substrates remained atomically smooth in the experiment, but on another day (using another cantilever) the surfaces appeared to be much rougher. Sometimes, smooth and rough substrates were obtained

on a single day in which nothing was changed except the cantilever. We determined that other possible sources (water, substrate, handling material, or air) did not affect this result. Most importantly, we always find striking agreement between the observation of nanobubbles residing on rough substrates and the cantilevers that were used being contaminated. However, cantilevers with which smooth substrates have been measured are always clean in the SEM images. The most likely interpretation is that the contamination originally present on the cantilever (and presumably the whole chip) precipitates after immersion in water on the HOPG surface, resulting in the observation of nanobubbles on relatively bumpy surfaces. This impression is underlined by some experimental cases in which we could observe the growth of rough features in time, indicating the precipitation process of an unwanted material.

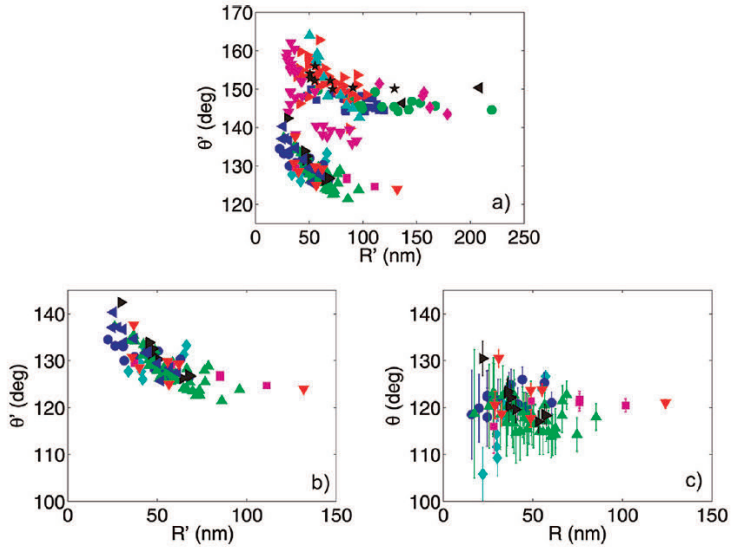

Figure 11.8 Contact angles as deduced from the imaged nanobubbles as a function of their size R. Each symbol refers to a particular cantilever; see Table 11.2. Only images obtained with the largest possible setpoint ratio (typically ~ 95%) are used. (a) Apparent contact angle θ' (not tip-corrected) as a function of R' for all 15 cantilevers. (b) Same data corresponding to 'clean' experiments only (i.e. cantilevers 9-15 in Table 11.2 (class B)); note the different scale on the θ' axis. (c) Tip-corrected data of class B experiments including error bars.

Contact Angle as a Function of Size.

Now we can address the main question of this work: How does the contact angle depend on the nanobubble size?

Figure 11.8(a) shows the apparent contact angle θ' as function of the apparent nanobubble size R' for all 15 experiments, measured with the largest possible set-point ratio (typically ~95%). Each symbol refers to a particular cantilever, see Table 11.2. As touched upon before, two separated regimes are clearly visible: a cloud of large

contact angles in the range of 145-165º, which is similar in magnitude to those reported in the literature (Table 11.1), and another cloud with 120º < θ' < 140º (i.e., much smaller (apparent) contact angles than previously observed). Strikingly, the cloud with the large contact angles contains all data points measured by cantilevers 1-8 (class A), corresponding to the rough substrates and the contaminated cantilevers. Similarly, the relatively small contact angles are obtained by cantilevers 9-15 (class B) (i.e., for experiments with apparently smooth surfaces and clean cantilevers).

Hence, the unwanted roughness, which is probably cantilever induced contamination, in-creases the local contact angle of surface nanobubbles. We notice that the apparent roughness itself is not sufficient to explain the dramatic contact angle increase (i.e., through Wenzel's equation [35] $\cos\theta = r \cos\theta_m$). This indicates that the contamination is hydrophobic in nature. Second, the data points are not scattered but collapse on top of each other, despite differences in the material, shape, and spring constants of the cantilevers. This could indicate that at large enough set-point ratios the vibrating cantilever tip during imaging hardly penetrates into the nanobubble. If it did, then the depth of penetration would depend on the cantilever's local wetting properties, spring constant, and tip radius of curvature and thus the nanobubble shape would be cantilever-dependent, but this is not observed. The good collapse of data points, especially of the lower cloud (class B, Figure 11.8(b)) also means that the shape of surface nanobubbles can be reproducibly obtained on different days and with different cantilevers, provide that imaging conditions are identical. The spread in θ' in the upper cloud is larger than in the lower cloud, in line with the idea of contact angle hysteresis being larger on rough and chemical inhomogeneous surfaces [35]. Third, the apparent dependence of θ' on R' is an effect caused by the finite size of the tip. After application of the tip radius correction, the dependence of θ on R vanishes: θ is constant within the experimental error over a wide range of sizes (Figure 11.8(c)), The error bars originate from the experimental tip radius determination, which has an error of ΔR_t and translates into errors in ΔR_c, ΔR and θ, as described earlier in this article. The mean contact angle of the 85 data points present in Figure 11.8(c) is $\bar{\theta}$ = 119 ± 4º. This is significantly below commonly reported values of ~160º [2, 6, 7, 9, 10, 12, 14, 19, 21, 27] and the lowest contact angle of surface nanobubbles reported so far.

Alternatively, the contact angle can be terminated from the plots of R_c versus R and R versus h, which both show linear relationships (Figure 11.9(a), (b)) and negligible offsets. Because $\cos(\theta - 90) = R/R_c$, the linear relationship $R_c = \alpha R$ gives $\theta = \cos^{-1}(1/\alpha) + 90$ =119.4º, with α = 1.1478 as result of a linear fit. Similarly, $\cos(\theta - 90) = 2hR/(h^2 + R^2)$ can be rewritten, using $R = \beta h$, as $\theta = \cos^{-1}(2\beta/(1 + \beta^2)) + 90$ = 117.7º with β = 1.6546 as the fitted slope. Both values are within the statistical error range of $\bar{\theta}$ = 119 ± 4º. The constant value of θ implies that the line tension is consistent with zero within the precision of our experiments[3].

[3] A least-squares fit to $\cos\theta$ vs 1/R yields $\tau = 1.1 \cdot 10^{-11}$ N. whereas manual fits (as done in Figure 5d of Ref 20) give $-3.2 \cdot 10^{-10} < \tau < -1.9 \cdot 10^{-10}$ N.

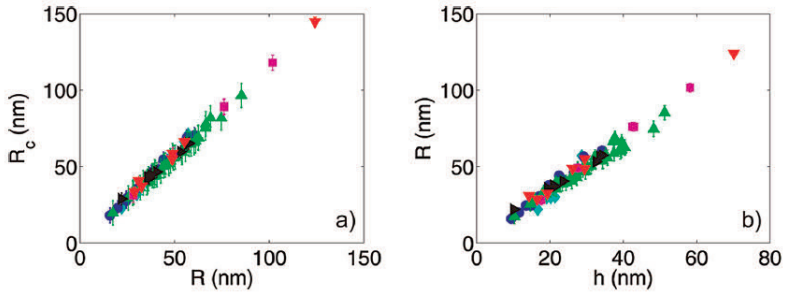

Figure 11.9 Plots of radius of curvature R_c vs radius R (a) and radius R vs height h (b) of class B experiments. Both plots show a linear relationship and go through the origin. The slope can be used to determine the contact angle θ.

Radius of Curvature as a Function of Size.

The plot of R_c versus R (Figure 11.9(a)) reveals another important characteristic of surface nanobubbles: $R_c \rightarrow 0$ as $R \rightarrow 0$, leading to a divergence in the Laplace pressure $p = 2\sigma/R$, with σ being the water –air interfacial tension. Even a 10-fold reduction in surface tension (e.g., due to surface-active solutes or a local super-saturation [36]) still gives an excess pressure of 7.2 bars inside a nanobubble of R_c = 20 nm and should lead to rapid dissolution of the bubble [37, 38].

This puzzling result is a direct consequence of θ being constant. Therefore, there must be a stabilization mechanism that keeps the bubble stable over a period of days. It may be surface contamination on the bubble, blocking the gas outflux, as suggested in refs 39 and 40 and recently by Ducker [41], but further work regarding this issue is necessary.

Set-Point Dependence.

Finally, we address the influence of the set-point ratio on the detected (i.e., not the actual) shape of the bubble. The set-point ratio r_{sp} is the ratio of the set-point amplitude A to the free amplitude A_0 of the oscillating cantilever. As such, it is a measure of the force that the cantilever exerts on the substrate. For solid materials, the detected topography does not change with decreasing r_{sp}, but for soft and deformable surfaces such as surface nanobubbles, it generally does [13]. It is known that the detected surface nanobubble shape changes dramatically for $r_{sp} < 67\%$ [13] whereas for $r_{sp} > 67\%$ little to no changes are ob-served [7, 13]. Here, we show that the observed nanobubble shape can already be deformed at much larger set-point ratios and in a way that depends on the cleanliness of the system, the size of the probed nanobubble, and the specifications of the cantilever.

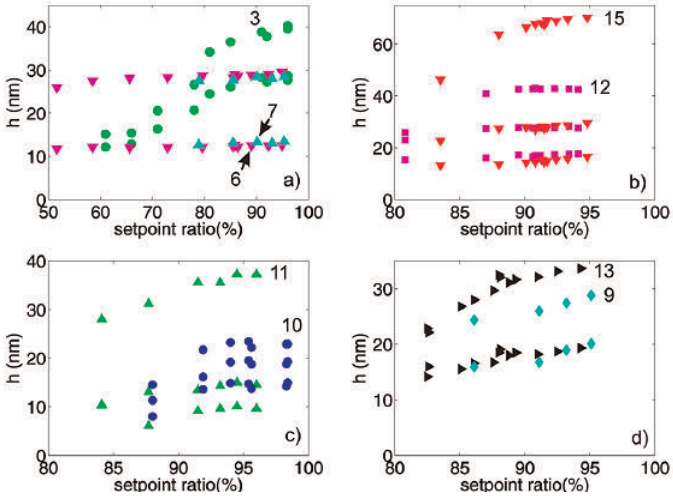

Figure 11.10 Nanobubble shape, parameterized by the height, as a function of the setpoint ration (a) Bubbles measured by cantilevers from class A. (b-d) Bubbles from class B. The symbols and corresponding numbers refer to the cantilevers listed in table 11.2. For each cantilever, the setpoint dependence of two or three bubbles is depicted.

Not unexpectedly, the set-point dependence of the bubbles present on rough substrates (probed by "contaminated" cantilevers 1-8) is irreproducible: cantilevers of the same type sometimes measure a constant nanobubble shape down to $r_{sp} = 50\%$ whereas at other times the detected bubble shape changes dramatically for set-point values $r_{sp} < 90\%$ (Figure 11. 10(a)). This strange behavior cannot be explained by the different spring constants involved because stiff cantilevers sometimes show a weaker set-point dependence (or no set-point dependence at all) compared to that of soft cantilevers, opposite to the expectation (Figure 11.10(a)). We attribute this conspicuous behavior to the uncontrolled presence of contamination, which may not only pin the triple contact line but also could form a skin or a surfactant layer on the nanobubble, thereby changing its response to external forces.

In contrast, clean cantilevers, which probed nanobubbles on smooth surfaces, always show that the observed bubble shape is set-point-dependent. For cantilevers of the same type and spring constant, this dependence is even quantitatively reproducible. For instance, in the case of two rectangular Veeco Si (MPP 22120) cantilevers with comparable spring constants (0.61 and 0.68 N/m), bubbles of equal size show a very similar dependence on the set-point ratio; see Figure 11.10(b). Interestingly, the plot also shows that both cantilevers at relatively low set-point ratios deform the largest bubble to a larger extent than the smallest nanobubbles. This effect also shows up in Figure 11.10(c) (green upward-facing triangles) and Figure 11.10(d) (black right-facing triangles). These results could be an indication that larger nanobubbles are more easily deformable / penetratable than smaller ones, possibly because of the larger

curvature of the menisci or a lower Laplace pressure inside larger bubbles. In Figure 11.10(c), two MM Au (CSC37) cantilevers are used. For $r_{sp} > 94\%$, the shape is identical for different set-point ratios, which shows that the nanobubble shape can be essentially set-point-independent provided that a large enough set-point ratio is chosen. This is also reflected in the corresponding line scans at different set-point ratios depicted in Figure 11.11. However, both cantilevers also show that for $r_{sp} < 94\%$ the detected shape is dramatically altered, with larger deviations in nanobubble size inflicted by the stiffer cantilever. Notice that the changes in morphology are different (in a quantitative sense) compared to Figure 11.10(b), although in both cases spring constants of $k \approx 0.68$ N/m are used. Clearly, more factors influence the set-point-dependent bubble shape than the cantilever spring constant. Figure 11.10(d) is a similar plot for two Veeco NP-S Si_3N_4 cantilevers and shows that for bubbles of equal size the set-point dependence is roughly similar, although here the cantilever spring constants are different (0.27 and 0.68 N/m).

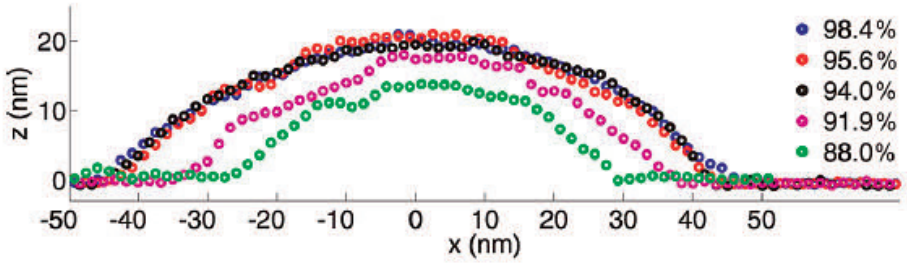

Figure 11.11 Line scans of the bubble topography as measured with different setpoint ratios (see legend), using cantilever 10 (MM Au, $k = 1.14$ N/m, class B).

It is not possible to make all h-r_{sp} curves collapse on top of each other, not even for bubbles of identical sizes. For all cantilevers, it applies that below $r_{sp} \approx 95\%$ the detected nanobubble shape is a subtle function of the set-point ratio and depends on more variables than the spring constant only. Presumably, the tip radius and the local wetting properties play key roles in the way in which the cantilever tip probes the bubble. Force spectroscopy is more suitable method of studying this problem and will be the subject of a forthcoming study.

11.4 Discussion and Conclusions

We have performed a detailed study regarding the question of how the contact angle of surface nanobubbles changes with size. The nanoscopic contact angle of surface nanobubbles has been deduced from spherical cap shaped surface nanobubbles found at the HOPG-water interface. The bubbles were detected by a Veeco AFM system in

tapping mode using very small (total) amplitudes of 1 to 2 nm and large set-point ratios (> 95%). To rule out the possibility that the observed nanobubble shape is cantilever-dependent, experiments were carried out with 15 different cantilevers, displaying different spring constants, shapes, materials (wetting properties), and tip radii of curvature.

We conclude that the contact angle of nanobubbles on atomically smooth surfaces such as HOPG strongly depends on spatial in-homogeneities in the AFM pictures. Data corresponding to an apparent roughness of $z_{rms} > 0.6$ nm and $a > 0.7\%$ display contact angles on the order of 150º. For data with a lower apparent surface roughness of $z_{rms} < 0.3$ nm and $a < 0.7\%$, which reflect as much as possible the ideal situation of nanobubbles on clean HOPG, we found here contact angles of 119 ± 4º despite the different cantilevers involved. Importantly, we found no noticeable θ(R) dependence within the experimental error.

The increased roughness and the different surface chemistries involved, leading to increased contact angles, originates from contamination. Cantilevers concerned with experiments on seemingly relatively rough HOPG showed distinct contamination presumably of an organic type. The origin of the contamination most likely comes from the gel package in which the cantilevers were stored. In contrast, cantilevers involved in the experiments with relatively smooth HOPG did show any source of contamination.

Although the nanoscopic contact angle of 119º is considerably lower than has hitherto been reported, it is still ~24 ± 4º larger than the (macroscopic) advancing contact angle. We speculate that this discrepancy still might originate from the presence of organic material (hydrocarbons) on the subnanometer length scale, as is also recently suggested in ref 41.

After all, we have shown in this study that contamination clearly increases the nanoscopic contact angle, whereas it is also known that ultrapure water-air interfaces and freshly cleaved HOPG easily collect airborne contaminant molecules.

This reasoning implies that if one is able to eliminate contaminants completely then the nanoscopic contact angle can be further reduced tot obtain Young's angle. Thus, from the two main issues associated with surface - nanobubbles extremely large contact angles and long-term stability - only one remains. The observation of an *R*-independent contact angle implies that $\lim_{R\to 0} R_c = 0$. Hence, some stability mechanism, such as the gas passage blocking mechanism caused by surfactants/contaminants as proposed recently [41], has to be identified in order to understand the long lifetime of surface nanobubbles, but also non-equilibrium mechanisms as suggested in ref 42 cannot be excluded.

Another future line of research concerns the complex tip bubble interaction, which, as we have shown, depends not only on the cantilevers' spring constant but also on the nanobubble curvature and most likely also on local wetting properties of the probing cantilever. Also, directly measuring the contamination-dependent surface tension of the nanobubble becomes feasible.

Acknowledgement

We thank Holger Schönherr, Jacco Snoeijer and James Seddon for stimulation discussions and valuable comments on the draft manuscript. B.M.B. acknowledges support from NanoNed, the nanotechnology program of the Dutch ministry of Economic Affairs (gran TMM.6413) and S.d.B. acknowledges support from the Foundation of Fundamental Research on Matter (FOM), which is financially supported by the Netherlands Organization for Scientific Research (NWO).

References

[1] S. Lou, Z. Ouyang, Y. Zang, X. Li, J. Hu, M. Li, F. Yang, *J. Vac. Sci. Technol.* B **18**, 2573 (2000)
[2] N. Ishida, T. Inoue, M. Miyahara, K. Higashitani, *Langmuir* **16**, 6377 (2000)
[3] G.E. Yakubov, H.-J. Butt, O.I. Vinogradova, *J. Phys. Chem* B **104**, 3407 (2000)
[4] A. Carambassis, L.C. Jonker, P. Attard, M.W. Ritland, *Phys. Rev. Lett.* **80**, 5357 (1998)
[5] J.W.G. Tyrrell, P. Attard, *Phys. Rev. Lett.* **87**, 176104 (2001)
[6] A.C. Sominsen, P.L. Hansen, B.J. Kloesgen, *J. Colloid Interface Sc.* **273**, 291 (2004)
[7] X.H. Zhang, N. Maeda, V.S.J. Craig, *Langmuir* **22**, 5025 (2006)
[8] L. Zhang, Y. Zhang, X. Zhang, Z. Li, G. Shen, M. Ye, C. Fan, H. Feng, J. Hu, *Langmuir* **22**, 8109 (2006)
[9] X.H. Zhang, G. Li, N. Maeda, J. Hu, *Langmuir* **22**, 9238 (2006)
[10] S. Yang, S.M. Dammer, N. Bremond, H.J.W. Zandvliet, E.S. Kooij, D. Lohse, *Langmuir* **23**, 7072 (2007)
[11] B.M. Borkent, S.M. Dammer, H. Schönherr, G.J. Vansco, D. Lohse, *Phys. Rev. Lett*. **98**, 204502 (2007)
[12] X.H. Zhang, A. Khan, W.A. Ducker, *Phys. Rev. Lett.* **98**, 136101 (2007)
[13] S. Yang, E.S. Kooij, B. Poelsema, D. Lohse, H.J.W. Zandvliet, *EPL* **81**, 64006 (2008)
[14] X.H. Zhang, A. Quinn, W.A. Ducker, *Langmuir* **24**, 4756 (2008)
[15] S. Yang, P. Tsai, E.S. Kooij, A. Prosperetti, H.J.W. Zandvliet, D. Lohse, *Langmuir* **25**, 1466 (2009)
[16] R. Steitz, T. Gutberlet, T. Hauss, B. Kloesgen, R. Krastev, S. Schemmel, A.C. Sominsen, G.H. Findenegg, *Langmuir* **19**, 2409 (2003)
[17] X.H. Zhang, *Phys. Chem. Chem. Phys.* **10**, 6842 (2008)
[18] M. Switkes, J.W. Ruberti, *Appl. Phys. Lett.* **84**, 4759 (2004)
[19] J. Yang, J. Duan, D. Fornasiero, J. Ralston, *J. Phys. Chem.* B **107**, 6139 (2003)
[20] N. Kameda, N. Sogoshi, S. Nakabayashi, *Surf. Sc.* **602**, 1579 (2008)
[21] N. Kameda, S. Nakabayashi, *Chem. Phys. Lett.* **461**, 122 (2008)
[22] F. Mugele, T. Becker, R. Nikopoulos, M. Kohonen, S. Herminghaus, *J. Adhes. Sci. Technol.* **16**, 951 (2002)
[23] X.H. Zhang, W. Ducker, *Langmuir* **24**, 110 (2008)
[24] A. Checco, P. Guenoun, J. Daillant, *Phys. Rev. Lett.* **91**, 186101 (2003)
[25] L. Schimmele, M. Napiorkowski, S. Dietrich, *J. Chem. Phys.* **127**, 164714 (2007)
[26] A. Agrawal, G.H. McKinley, *Mater. Res. Soc. Symp. Proc.* 899E, (2006)
[27] A. Agrawal, J. Park, D.Y. Ryu, P.T. Hammond, T.P. Russell, G.H. Kinley, *Nano Lett.* **5**, 1751 (2005)
[28] J.L. Hutter, J. Bechhoefer, *Rev, Sci. Instrum.* **64**, 1868 (1993)

[29] A. Maali, C. Hurth, T. Cohen-Bouhacina, G. Couturier, J.-P. Aime, *Appl. Phys. Lett.* **88**, 163504 (2006)
[30] S. de Beer, D. van den Ende, F. Mugele, *Appl. Phys. Lett.* **93**, 253106 (2008)
[31] K.A. Ramirez/Aguilar, K.L. Rowlen, *Langmuir* **14**, 2562 (1998)
[32] B.M. Borkent, H. Schönherr, G. Le Caër, B. Dollet, D. Lohse, *Phys. Rev.* E **80**, 036315 (2009)
[33] Y. Lo, N.D. Huefner, W.S. Chan, P. Dryden, B. Hagenhoff, T.P. Beebe, *Langmuir* **15**, 6522 (1999)
[34] E. Bonaccurso, G. Gillies, *Langmuir* **20**, 11824 (2004)
[35] P.-G. deGennes, F. Brochard-Wyart, D. Quéré, *Capillarity and Wetting Phenomenon: Drops, Bubbles, Pearls, Waves*, Springer New York (2003)
[36] P. Attard, *personal communication*, Leiden, June 2008
[37] P.S. Epstein, M.S. Plesset, *J. Chem. Phys.* **18**, 1505 (1950)
[38] S. Ljunggren, J.C. Eriksson, *Colloids Surf.* A **151**, 129 (1997)
[39] B.D. Johnson, R.C. Cooke, *Science* **213**, 209 (1974)
[40] E. Dressaire, R. Bee, D.C. Bell, A. Lips and H.A. Stone, *Science* **320**, 1198 (2008)
[41] W. Ducker, *Langmuir* **25**, 8907 (2009)
[42] M.P. Brenner, D. Lohse, *Phys. Rev. Lett*. **101**, 214505 (2008)
[43] O.I. Vinogradova, G.E. Yakubov, H.-J. Butt, *J. Chem. Phys.* **114**, 8124 (2001)
[44] M. Holmberg, A. Kuehle, J. Garnaes, K.A. Morch, A. Boisen, *Langmuir* **19**, 10510 (2003)

Chapter 12

Conclusions and Recommendations

In the introduction of this thesis we discussed that we are specifically interested in the following research question:

How does the self-assembly of molecules into layers affect the dynamic properties of a confined liquid?

We addressed this question both with Atomic Force Microscope (AFM) experiments and with Molecular Dynamics simulations.

12.1 Conclusions

Experiments:
Before we could extract trustworthy physical properties of the confined liquid from our experiments, we first needed to characterize our measurement system: the AFM. In Chapter 3 we have shown that, in order to obtain the correct forces from your dynamic AFM measurements, we have to:

1) Determine our actuation and detection method
2) Find the accompanying force inversion formulae (depending on the actuation / detection method used)
3) Take into account the frequency dependent added mass and damping
4) Do a correct calibration (depending on the actuation / detection method used)
5) Shift the phase to the correct value (depending on the actuation / detection method used)

In most of the commercial AFM's the cantilever is driven via acoustic actuation and the deflection is measured via a quadrant photo-detector. In Chapter 4 we have shown that this configuration results in an increased sensitivity in the phase for low frequencies. Moreover, we showed that this implies an increased sensitivity for tip-sample forces at low frequencies. In Chapter 5 we used the model for the cantilever dynamics, presented and discussed in Chapter 4, to extract the conservative and dissipative tip-sample forces from our AFM measurements. We showed that the conservative forces in a layered liquid strongly oscillate in agreement with earlier reports in the literature. However, we also observed that the damping strongly varies as the distance between the tip and the surface is decreased. For a distance smaller than three molecular layers, we found peaks in the interaction damping, where the conservative forces are attractive. At these distances the layered liquid goes from n to n-1 layers. Furthermore, we showed by a rough approximation that the effective 'viscosity' is below 500x the bulk-viscosity for all distances. Nevertheless, acoustic drive measurements are often mistrusted for their sensitivity to modeling errors and for the spurious resonances often observed in the spectral response of the cantilever. Therefore we repeated our measurements using a magnetic driving scheme, of which we presented the results in Chapter 6. In these experiments we showed that the interaction damping displays indeed strong peaks in the damping. However, these maxima in the damping were observed at a different position with respect to the conservative forces compared to our acoustic drive measurements. Yet, the tip shape and structure was also significantly different. Therefore, we suggested that the confinement-volume (or tip-radius) might explain the observed differences.

<u>Conclusion from the experiments:</u>
The dynamic or transport properties of the liquid indeed change when the distance between the confining surfaces is smaller than three molecular layers. These local changes in the dynamic properties of the liquid result in an increased damping of the cantilever, when the liquid is squeeze-out underneath the tip.

Simulations:
In order to understand our measurements and learn what happens with the liquid molecules when they are confined between the tip and the surface, we also performed MD simulations. The results of these simulations were presented in Chapter 8. In the conservative forces extracted from our simulations we found the same characteristic oscillations, when the distance between the tip and the surface is decreased, as in our experimental observations. Moreover, we showed that the damping on the tip displays sharp maxima very similar to our measurements. Furthermore, in our simulations we found that the damping only significantly increases for distances smaller than three molecular layers. The maxima in the damping were found at the tip-surface distance where the layered liquid goes from n to n-1 layers and the largest extracted damping is ~1000x the damping in the bulk (during the transition from 1 to 0 layers). Upon closer inspection of the confined molecules, we observe that the maxima in the damping are strongly correlated to the in-plane structure of the liquid: When the molecules are in an in-plane hexagonal structure, the damping is low. On the other hand, when the molecules configure themselves in a more disordered in-plane cubic structure, the damping is maximum. Moreover, we observed that the molecules are non-diffusive in between the peaks, but behave diffusive in the maxima in the damping. By examination of the rheological properties of the confined molecules we found that the system is probably best described as a soft glassy material. However, the latter result needs further research.

Conclusion from the simulations:
In agreement with our experimental conclusion, we find that the dynamic properties of the liquid indeed change when the distance between the confining surfaces is smaller than three molecular layers. Moreover, we observe that the damping on the tip is strongly related to both the structural and the dynamic properties of the confined molecules.

12.2 Outlook

Although, with the experimental observations and the MD simulations, we have gained insight in the structure and dynamics of the confined liquid, there are still many open questions.

To learn more about the rheological properties of the confined liquid additional and especially longer simulations are needed, such that the storage and loss moduli can be studied over a larger frequency domain and the different relaxation processes can be identified and studied in more detail. Moreover, also the extracted Mean Squared Displacement of the molecules can provide more detailed information on the properties of the liquid and should be studied more closely.

From an experimental point of view, we can employ the technique used in the MD simulations to the fluctuations to extract the damping on the cantilever: By monitoring the response of the cantilever to thermal noise, we can extract both the conservative and dissipative forces. Since Onsager regression theorem states that the response to random fluctuations equals the step-response, we can extract the damping via the autocorrelation of the position of the cantilever. Moreover, this method can be applied in other measurement setups, like the optical tweezers.

From a general perspective, it would be interesting to extend the study on confined liquids, to water. In this thesis, we mainly used model-liquids like octamethylcyclotetrasiloxane, alkanes and alcohols. However, from an applied perspective, water is a more relevant liquid, because of its ubiquitous presence in nature. Moreover, since it was recently shown by the group of Huib Bakker that specific ion-effects can change the relaxation-time of water, varying the ion (-concentration) would be very interesting. Nevertheless, the study of confined water will be more challenging, because of its small molecular diameter. However, by studying the thermal noise (the limit of small amplitudes) as described above, it is most likely feasible.

Furthermore, we have shown in Chapter 9 that solid-liquid interactions and epitaxial effects strongly affect the conservative oscillatory solvation forces. However, we do not know what the effect of these interactions is on the dissipative forces and the dynamic properties of the liquid. Via the experimental methods developed during the course of this thesis, the conservative and dissipative forces can be studied for a wide variety of solid-liquid systems and thus consequently for different solid-liquid interactions.

In view of the recent developments in 3D Atomic Force mapping like Bruker's Peakforce, it would be interesting to extend the force-inversion methods presented in Chapter 3 into a 3D force mapping technique. In this way, the conservative and dissipative forces can be mapped in 3D over an inhomogeneous surface. This method will find applications in many research areas, such as chemistry (force-mapping and energy dissipation on chemically patterned surfaces) or biology, e.g. for studying the forces and dissipation on e.g. DNA or other biomolecules adsorbed on mica.

Summary

In this thesis we describe Atomic Force Microscopy (AFM) measurements and Molecular Dynamics (MD) simulation of the static and dynamic properties of layered liquids confined between two solid surfaces.
Liquid molecules in the proximity of a solid surface assemble into layers. When a fluid is confined between two surfaces, the discrete molecular nature of the liquid becomes observable via the oscillatory solvation forces and can be probed with AFM spectroscopy. Upon approach of an in liquid immersed AFM cantilever – driven with a sub-angstrom amplitude – towards a solid graphite surface, we find that both the amplitude and phase response strongly oscillate as the distance is decreased. From the amplitude and phase response we extract the conservative and dissipative interaction forces. We observe that the conservative forces increasingly oscillate for a decreasing tip-surface distance, as expected for oscillatory solvation forces. For the dissipative interaction forces or the damping on the tip we find pronounced maxima positioned at the transition from 3-2, 2-1 and 1-0 layers. From these observations we conclude that the dynamic transport-properties of the confined liquid significantly change in these transition-regions.
Nevertheless, in AFM measurements we only measure forces. We can not see what happens with the confined liquid molecules. To study the effect of confinement on the dynamics of the molecules and how that will affect the response on the cantilever, we also performed MD simulations. In our simulations the average force on the tip shows the same exponential decaying oscillations as we found in our experiments. Next to the average force, we also monitored the force-fluctuations on the tip. Using fluctuation-dissipation we converted these force-fluctuations in the dissipative force or damping on the tip. The damping on the tip shows pronounced maxima very similar to our experimental results. The maxima are also positioned at the transition regions of 3-2, 2-1 and 1-0 layers. By monitoring the Mean Squared Displacement and the number of

nearest neighbors of the molecules confined under the tip, we find that the damping is closely related to the configuration and the dynamics of the molecules. Regarding these observations one might be tempted to conclude that the confined molecules behave either liquid-like or solid-like depending on the distance between the tip and the surface. However, spectral analysis suggests that the elastic and viscous response of the confined liquid is more complex and would be better described as either a gel or a soft glassy material.

In **Chapter 1** we give a general introduction into the study of confined liquids. We discuss possible applications for this study and introduce the reader to the oscillatory solvation forces. In **Chapter 2** we provide an overview of the current status of the research in confined liquids, focusing on the oscillatory solvation forces. To obtain trustworthy experimental results, we first need to characterize our measurement system. In **Chapter 3** we describe the different small amplitude AFM techniques and the accompanying force inversion procedures. Commercial AFMs are often equipped with acoustic cantilever actuation and deflection detection. In **Chapter 4** we show that this measurement-configuration gives rise to a surprising sensitivity in the phase for low frequencies. With the force-inversion procedures described in Chapter 3 and 4 we extract the conservative and dissipative interaction forces from the amplitude and phase response of the AFM cantilever. In **Chapter 5** we present our measurements of the interaction forces in a confined liquid using an acoustic driving scheme. We show that the conservative forces show the typical characteristics of the oscillatory solvation forces and that the dissipative interaction forces show pronounced maxima. However, acoustic actuation measurements are often mistrusted for their sensitivity to modeling errors and the difficulty of obtained a clean spectral response. Therefore, we repeated our measurements using a magnetic driving scheme of which the results are presented in **Chapter 6**. From these measurements we extracted conservative and dissipative interaction forces very similar to those extracted from the measurements using an acoustic driving scheme, except for the relative position of the maxima in the damping. We contribute this discrepancy to the difference in confinement-volume (tip-radius). To learn more about the static and dynamic response of the molecules confined between the tip and the surface, we also performed MD simulations. The theoretical basics of the simulations are described in **Chapter 7**. In **Chapter 8** we present our results on the conservative and dissipative forces extracted from the simulations. We show that the forces extracted from the simulations are in good agreement with the forces extracted from the measurements. In the last three chapters we describe other research questions that were addressed during the course of this thesis. In **Chapter 9** we present our measurements on the effect of temperature and epitaxy on the oscillatory solvation forces, while in **Chapter 10** we turn our attention to water. In the latter chapter we show that a fast quench of thin water films can cause an elastic instability. Subsequently, in **Chapter 11** we present our study on surface nanobubbles and finally we discuss the conclusions and recommendations of this thesis in **Chapter 12**.

Samenvatting

In dit proefschrift presenteren we atoomkrachtmicroscopie metingen en moleculaire dynamica simulaties van de statische en dynamische eigenschappen van vloeistoffen ingesloten tussen twee harde vlakke wanden.
In de buurt van een vlakke wand organiseren vloeistofmoleculen zich in laagjes. Wanneer de vloeistof wordt opgesloten tussen twee wanden kan men zien dat de vloeistof is opgebouwd uit moleculen via de oscillatorische solvatie krachten. Deze solvatie krachten kunnen gemeten worden met atoomkrachtmicroscopie. Als we het veertje van de atoomkrachtmicroscoop met een sub-angstrom amplitude aandrijven en door de vloeistof naar de wand bewegen, zien we dat de amplitude en de fase van het veertje sterk oscilleren voor afnemende veertje-wand afstand. Vanuit deze amplitude en fase berekenen we de conservatieve en dissipatieve interactiekrachten. Hierin zien we dat de conservatieve krachten steeds sterker afwisselend toenemen en afnemen als we de afstand tussen het veertje en de wand kleiner maken. Dit is een karakteristieke eigenschap van de oscillatorische solvatie krachten. In de dissipatieve krachten zien we sterke maxima op het punt waar de vloeistof van 3 naar 2, 2 naar 1 of 1 naar 0 laagjes gaat. Hierdoor denken we dat de transporteigenschappen van de vloeistof sterk veranderen als we de afstand waarbinnen de vloeistofmoleculen opgesloten zitten veranderen.
Maar in atoomkrachtmicroscopie meten we alleen maar krachten. We kunnen niet zien wat er daadwerkelijk gebeurd met de opgesloten vloeistofmoleculen. Om te onderzoeken wat er met de dynamica van de vloeistofmoleculen gebeurd en hoe dit het veertje van de atoomkrachtmicroscoop beïnvloedt, hebben we ook moleculaire dynamica simulaties gedaan. In de simulaties vinden we dezelfde exponentieel toenemende oscillerende krachten als in de experimenten. Daarnaast hebben we ook de fluctuaties in de krachten onderzocht en via het fluctuatie-dissipatie theorema omgezet naar dissipatieve krachten. In de dissipatieve krachten vinden we maxima die sterk

lijken op de maxima die we in de experimenten vonden. De maxima zaten wederom op de plaatsen waar de vloeistof van 3 naar 2, 2 naar 1 of 1 naar 0 laagjes gaat. Door de gemiddelde kwadratische verplaatsing en de buren van de opgesloten moleculen te bestuderen, vonden we dat de dissipatie sterk afhangt van de dynamica en structuur van de moleculen. Omdat we dit zagen, zou je eigenlijk willen zeggen dat de moleculen zich afwisselend als een vloeistof of als een vaste stof gedragen als we de afstand tussen de wanden veranderen. Maar uit een spectraal analyse volgt dat het gedrag van de vloeistof complexer is en dat je de vloeistof beter zou kunnen beschrijven als een gel of als een zacht glasachtig materiaal.

In **Hoofdstuk 1** geven we een algemene introductie in het gedrag van opgesloten vloeistoffen. We bespreken mogelijke toepassingen van dit onderzoek en waarom de oscillatorische solvatie krachten optreden. In **Hoofdstuk 2** geven we een overzicht van de huidige stand van zaken in het wereldwijde onderzoek naar ingesloten vloeistoffen. Hierin richten we ons specifiek op de oscillatorische solvatie krachten. Om betrouwbare metingen te kunnen doen, moet men eerst het meetsysteem goed begrijpen. In **Hoofdstuk 3** bespreken we verschillende atoomkrachtmicroscopie technieken en de bijbehorende krachtinversie procedures. In commerciële atoomkrachtmicroscopen wordt vaak een akoestische aandrijftechniek gebruikt die is gecombineerd met deflectie detectie. In **Hoofdstuk 4** laten we zien dat deze opzet zorgt voor een sterke sensitiviteit voor interactiekrachten bij lage frequenties. Met de technieken en procedures besproken in Hfdst. 3 en 4 bepalen we de conservatieve en dissipatieve interactiekrachten waarvan we de resultaten voor het akoestische aandrijfmechanisme bespreken in **Hoofdstuk 5**. Maar, omdat metingen via een akoestische aandrijving vaak niet vertrouwd worden vanwege de sensitiviteit voor modelleringsfouten en de slechte spectrale eigenschappen van het systeem, hebben we de metingen nogmaals herhaald gebruik makend van magnetische aandrijving. De resultaten hiervan bespreken we in **Hoofdstuk 6**. De metingen met beide aandrijftechnieken gaven dezelfde resultaten voor de conservatieve en dissipatieve krachten, met uitzondering van de relatieve posities van de maxima in de dissipatie. We denken dat dit verschil komt door de verandering van het insluit-volume.
Om meer te leren over de statische en dynamische eigenschappen van de ingesloten vloeistofmoleculen hebben we ook moleculaire dynamica simulaties gedaan. De theoretische achtergrond die hiervoor nodig is wordt gegeven in **Hoofdstuk 7**. In **Hoofdstuk 8** presenteren we onze simulatieresultaten voor de conservatieve en dissipatieve krachten. We laten zien dat de metingen en simulaties goed overeen komen. In de laatste drie hoofdstukken bespreken we andere onderzoeksvragen die we de afgelopen vier jaar onderzocht hebben. In **Hoofdstuk 9** bespreken we onze metingen van het effect van temperatuur op de oscillatorische solvatie krachten en in **Hoofdstuk 10** bespreken we een elastische instabiliteit die ontstaat als we twee elastische platen met een dunne waterfilm snel op elkaar duwen. Vervolgens presenteren we ons onderzoek naar oppervlaktebelletjes in **Hoofdstuk 11** en sluiten we dit proefschrift af met de conclusies en aanbevelingen in **Hoofdstuk 12**.

Acknowledgement

In this thesis I presented the results of four years of research, which, of course, I could not have done without the help of others. I am very grateful for the help of many people.
First of all, I would like to thank my professor Frieder Mugele:
Frieder, ik vond het fantastisch om voor je te werken. In de afgelopen vier jaar was je niet alleen mijn professor, maar ben je ook een goede vriend geworden. Ik weet dat ik regelmatig boos was om jouw kritiek. Maar dat duurde nooit lang en ik weet dat je het goed bedoelde. Ook al vergat ik dat soms op het moment zelf. ☺ Vaak had je achteraf ook wel een beetje gelijk. ☺ Ik zal onze reizen naar de verschillende conferenties nooit vergeten en ik kijk er naar uit om in de toekomst met je samen te blijven werken.
Secondly, I would like to thank Dirk van den Ende: Dirk, je hebt mij er de afgelopen maanden doorheen getrokken. Op het cruciale moment van de afronding van mijn proefschrift stond je voor mij klaar om het manuscript keer op keer weer te lezen. Ik zal dit nooit vergeten! We hebben nog een aantal leuke projecten samen lopen, waarvan ik hoop dat we die in de komende maanden nog mooi af kunnen ronden.

Next to my daily supervisors, many others helped me. With respect to my Molecular Dynamics simulations: I could not have done this without the help of Wouter den Otter. Wouter, you know everything about computers and programming and more… Thank you for teaching me the basics of MD. Furthermore, I would like to thank Wim Briels. Very often you came with exactly the right comments, questions and answers at exactly the right time. You are a great professor. Also, I would like to thank the nice people of the CBP group for the relaxing coffeebreaks and the nice discussions. Tineke, Li, Igor, Johan, Alessandra and Tom, thank you!
With respect to my experimental results: I could not have done this without the help of the people of Veeco (now Bruker Nano): Jim Flach, Peter de Wolf, Samuel Lesko and

especially Patrick Markus. Patrick, you always know a simple solution to my weird questions and ideas. Thank you! I also would like to thank Klaas Smit for the great technical support. Klaas, you always found simple ways to adjust the AFM setup such that we could seriously improve our measurements. Moreover, you are also just a great guy to drink coffee with. ☺ Furthermore, I would like to thank Mark Smithers for the many high quality SEM images. These images brought us great insights (see Chapter 11) and made it possible to quantify our experimental results. Within our group, I would like to thank the AFM team: Mariska van der Weide, Cock Harteveld and Daniel Ebeling. Especially Mariska: Mariska, je dodecanol metingen waren fantastisch netjes en nauwkeurig! Zo horen AFM metingen te zijn! Ik hoop dat we van de zomer onze samenwerking nog even door kunnen zetten. Over the last four years, I also supervised several students. This was not only very useful (see Chapter 9 and 10), but also a lot of fun to do. By teaching others, you also learn a lot (about) yourself. Telli, Dieter, Sietske, Peter, Aram, Bart, Tom, Mattie, Helmer, Niels en Mariska ☺: Thank you!
Moreover, I would to thank the nice people of our PCF group. You all created a great atmosphere, which made that it was fun working in our group. Helmut, Adrian, Florent, Siva, Tamara, Renske, Eko, Michel, Burak, Gor, Jane, Hao, Rielle, Jolet, Dieter, Huub, Arun, Mariska, Cock, Daniel and Daniel, Dirk, Frieder, Annelies, Tarun, Dileep, Dhirendra, Chandra, Jung, Olga, Agata, Omkar, Pablo and Willem. Thank you! I especially would like to thank Annelies. My organization-skills are a bit underdeveloped. However, you very often arranged everything in great detail (trips, etc.) and reminded me patiently of the administrative stuff I needed to do. You are the best!
I also would like to thank Anika (MTP group) and Kim (Biophysics group). On a regular basis I had coffee breaks with you both (independently). This was not only entertaining, but also very useful. Very often I came back with great new ideas. Moreover, I would like to thank Bram, James, Holger and Detlef for the interesting cooperation and work on surface nanobubbles. Especially Bram: You thought me how to present experimental results and convince supervisors of our ideas.

Finally, I would like to thank my friends and family. Especially Esther and Arjan: De weekenden met jullie zijn altijd fantastisch en een welkome afwisseling van het werk. Ik hoop dat we in de toekomst nog veel weekenden samen weg kunnen gaan.
I also would like to thank my parents, Keesje and Mama. Zonder jullie had ik nu hier niet gestaan. Bedankt voor jullie begrip voor mijn regelmatige afwezigheid en voor de leuke weekenden samen. Mama, extra bedankt voor de tekstuele hulp bij het maken van dit proefschrift.
And last, but certainly not least, I would like to thank Tom Melsen. Tom, je brengt mij elke avond weer terug op aarde. Jouw rust en stabiliteit hebben ervoor gezorgd dat ik vol overgave aan mijn promotie heb kunnen werken. Ik had dit nooit zonder jou kunnen doen. Ik hou oneindig veel van jou!

Publications

During the course of this thesis we published our results in several scientific journals:

Peer reviewed:

Confinement-dependent damping in a layered liquid
S. de Beer, D. van den Ende, F. Mugele,
J. Phys.: Condens. Matt. 23, 112206, 2011

Capillarity-driven dynamics of water-alcohol mixtures in nanofluidic channels
J.M. Oh, T. Faez, S. de Beer, F. Mugele
Microfluidics and Nanofluidics, 9, 123, 2010

Dissipation and oscillatory solvation forces in confined liquids studied by small-amplitude atomic force spectroscopy
S. de Beer, D. van den Ende and F. Mugele
Nanotechnology 21, 325703, 2010

Do epitaxy and temperature affect oscillatory solvation forces?
S. de Beer, P. Wennink, M. van der Weide-Grevelink, F. Mugele
Langmuir, 26, 13245, 2010

Instability of confined water films between elastic surfaces
S. de Beer, D. ‘t Mannetje, S. Zantema, F. Mugele
Langmuir, 26, 3280, 2010

On the shape of surface nanobubbles
B.M. Borkent, S. de Beer, F. Mugele, D. Lohse
Langmuir, 26, 260, 2010

Atomic force microscopy cantilever dynamics in liquid in the presence of tip sample interaction
S. de Beer, D. van den Ende, F. Mugele
Appl. Phys. Lett., 93, 253106, 2008

Other publications:

Small amplitude atomic force spectroscopy
S. de Beer, D. van den Ende, D. Ebeling, F. Mugele
Scanning Probe Microscopy in Nanoscience and Nanotechnology 2, pp 39-58, ed. Bharat Bhushan, Springer-Verlag Berlin Heidelberg, 2011

Plakkende gekko's. Waarom kan een gekko op muren en plafonds lopen?
S. de Beer, A. Klaassen, B. Stel, F. Mugele
Nederlands Tijdschrift voor Natuurkunde 76, 236-240, 2010

Small-amplitude AFM spectroscopy of confined liquid films
S. de Beer, F. Mugele
Microscopy and Analysis 23, 11-14, 2009

About the author

Sissi de Beer was born on the 24th of October in 1979 in Bergen op Zoom. She grew up in Roosendaal, where she also graduated for the HAVO at the Gertrudis College. In 1998 she moved to Eindhoven to follow the Applied Physics Bachelor program at the Fontys University. In Eindhoven she also met Tom, her husband. After graduation for her B.Sc. degree, Sissi worked for over a year at Glaverbel in Tiel as a management trainee. In 2004 Sissi and Tom moved to Enschede, where Sissi continued her study of Applied Physics at the University of Twente. In 2007 she received her Master's degree and started her PhD research at the Physics of Complex Fluids group of Frieder Mugele at the Twente University of which the results were presented in this dissertation.